The Journal of Gemmology

Volume 38 / No. 7 / 2023

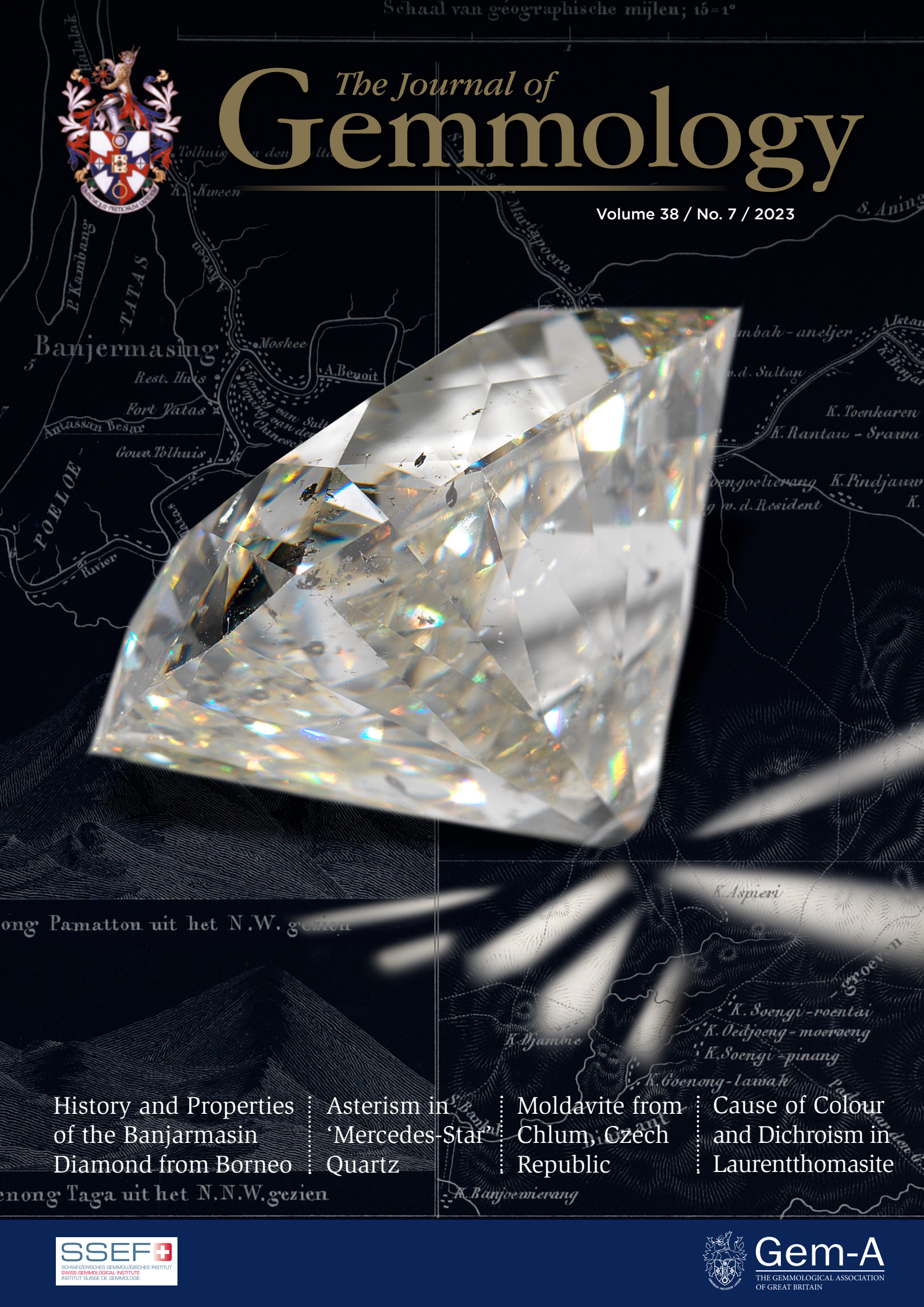

History and Properties of the Banjarmasin Diamond from Borneo

Asterism in 'Mercedes-Star' Quartz

Moldavite from Chlum, Czech Republic

Cause of Colour and Dichroism in Laurentthomasite

SSEF
SCHWEIZERISCHES GEMMOLOGISCHES INSTITUT
SWISS GEMMOLOGICAL INSTITUTE
INSTITUT SUISSE DE GEMMOLOGIE

Gem-A
THE GEMMOLOGICAL ASSOCIATION OF GREAT BRITAIN

SSEF

SCHWEIZERISCHES GEMMOLOGISCHES INSTITUT
SWISS GEMMOLOGICAL INSTITUTE
INSTITUT SUISSE DE GEMMOLOGIE

ORIGIN DETERMINATION · TREATMENT DETECTION

DIAMOND GRADING · PEARL TESTING

EDUCATION · RESEARCH

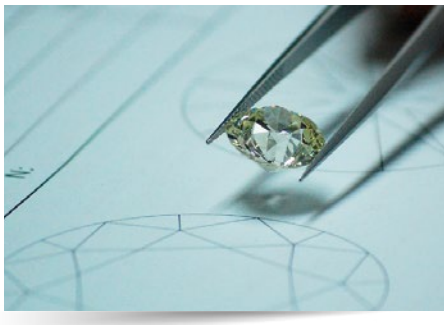

THE SCIENCE OF GEMSTONE TESTING™

Aeschengraben 26, 4051 Basel, Switzerland Tel. +41 61 262 06 40 Fax + 41 61 262 06 41 admin@ssef.ch www.ssef.ch

The Journal of Gemmology

Volume 38 / No. 7 / 2023

Cover photo: *The 38.23 ct Banjarmasin diamond, in the collection of the Rijksmuseum in Amsterdam, the Netherlands, was cut from a 70+ ct octahedral crystal that was reportedly mined in southern Borneo. The rough stone was confiscated by the Dutch from the Sultanate of Banjarmasin in 1860, and it was faceted in Amsterdam in 1870. An article on pp. 662–677 of this issue describes the diamond's history and gemmological properties. The diamond is shown over a colour-inverted image of the old map in Figure 4 of the article. Photo by Frans Pegt; courtesy of Rijksmuseum (inv. no. NG-C-2000-3).*

COLUMNS

Photo by Ozzie Campos & Rosiane Pereira

ARTICLES

Photo by Jan Loun

Photo by Jeff Scovil

The Journal is published by Gem-A in collaboration with SSEF.

Gem-A THE GEMMOLOGICAL ASSOCIATION OF GREAT BRITAIN

SSEF SCHWEIZERISCHES GEMMOLOGISCHES INSTITUT SWISS GEMMOLOGICAL INSTITUTE INSTITUT SUISSE DE GEMMOLOGIE

The Journal of Gemmology

COVERED BY THE FOLLOWING ABSTRACTING AND INDEXING SERVICES:

Clarivate Analytics' (formerly Thomson Reuters/ISI) Science Citation Index Expanded (in the Web of Science), *Journal Citation Reports (Science Edition)* and *Current Contents (Physical, Chemical and Earth Sciences)*; Elsevier's Scopus; Australian Research Council's Excellence in Research for Australia (ERA) Journal List; China National Knowledge Infrastructure (CNKI Scholar); EBSCO's Academic Search Ultimate; ProQuest (Cambridge Scientific Abstracts); GeoRef; CrossRef; Chemical Abstracts (CA Plus); Mineralogical Abstracts; Index Copernicus ICI Journals Master List; Gale Academic OneFile; British Library Document Supply Service; and Copyright Clearance Center's RightFind application.

Science Citation Index Expanded
Web of Science

CONTENT SUBMISSION

The Editor-in-Chief is glad to consider original articles, news items, conference reports, announcements and calendar entries on subjects of gemmological interest for publication in *The Journal of Gemmology*. A guide to the various sections and the preparation of manuscripts is given at https://gem-a.com/membership/journal-of-gemmology/submissions, or contact the Editor-in-Chief.

SUBSCRIPTIONS

Gem-A members receive *The Journal* as part of their membership package, full details of which are given at https://gem-a.com/membership. Laboratories, libraries, museums and similar institutions may become direct subscribers to *The Journal*; download the form from *The Journal*'s home page.

ADVERTISING

Enquiries about advertising in *The Journal* should be directed to advertising@gem-a.com. For more information, see https://gem-a.com/component/edocman/media-kit.

DESIGN & PRODUCTION

Zest Design, London. http://www.zest-uk.com

PRINTER

Park Communications Ltd, London.
http://www.parkcom.co.uk

Mixed Sources
Product group from well-managed forests and other controlled sources
www.fsc.org Cert no. TT-COC-002454
© 1996 Forest Stewardship Council
FSC

ISSN 1355-4565 (Print), ISSN 2632-1718 (Online)

Gem-A
THE GEMMOLOGICAL ASSOCIATION OF GREAT BRITAIN

21 Ely Place
London EC1N 6TD
UK

t: +44 (0)20 7404 3334
f: +44 (0)20 7404 8843
e: information@gem-a.com
w: https://gem-a.com

Registered Charity No. 1109555
A company limited by guarantee and registered in England No. 1945780
Registered office: Palladium House, 1–4 Argyll Street, London W1F 7LD

What's New

INSTRUMENTATION

Dia*Synth* Diamond-detection Device

Italy-based DiaTechPro released its Dia*Synth* device in mid-2023. The instrument employs a combination of 'internal artificial intelligence' (developed in collaboration with the University of Verona) and 'photography of UV induced visible fluorescence'. This methodology reportedly considers about 120 features for each sample to distinguish natural diamond from synthetics (both CVD and HPHT), as well as common simulants such as cubic zirconia and synthetic moissanite. It can accommodate loose stones as well as jewellery such as rings and bracelets. Visit https://www.diatechpro.com.

NEWS AND PUBLICATIONS

CIBJO Congress 2023 Special Reports

Several special reports prepared in advance of the October CIBJO Congress in Jaipur, India, are available for download at https://www.cibjo.org/congress2023-special-reports. They cover issues planned for discussion during the conference by the various CIBJO commissions, and as of early September they included: *Bringing Clarity to the Industry and Consumers by Setting Criteria for Gemstone Variety Names* (Gemmological Commission); *Demand for Coloured Gemstones Is High in Post-COVID Market, but Challenged by Undetected and Undisclosed Treatments* (Coloured Stone Commission); *In Our Ever-Changing Jewellery World, How Can One Compete Successfully?* (Marketing & Education Commission); *Moving Beyond Responsible Sourcing Towards a Shared Understanding of Our Sustainability Impacts* (Sustainable Development Commission); *Protecting Intellectual Property in the Jewellery Industry: Defending Both the Art and the Creative Spirit* (Ethics Commission); *While Geopolitics and Consumer Sentiment are Agents of Change, Industry Standards Remain Grounded in Scientific Discipline* (Diamond Commission); and *While Precious Metals Retain Their Safe Haven Status, Sustainability and Responsibility [Are] More Pressing Issues* (Precious Metals Commission).

Gemmological Society of Japan 2023 Annual Meeting Abstracts

Abstract of Papers Presented at Annual Meeting of the Gemmological Society of Japan

Abstracts of lectures presented during the June 2023 Annual Meeting of the Gemmological Society of Japan are available at https://www.jstage.jst.go.jp/browse/gsj/45/0/_contents/-char/en. The 23 abstracts cover a variety of topics (in Japanese with English summaries), including fluorescent opal, star peridot, Paraíba-type tourmaline, irradiated and 'hybrid' diamonds (CVD synthetic overgrowths on natural diamonds), lustre and fluorescence of akoya cultured pearls, and more. Also available are abstracts from previous GSJ conferences.

LMHC Gemstone Information Sheet 2023 Updates

The Laboratory Manual Harmonisation Committee (LMHC) updated seven of its 13 Gemstone Information Sheets in January and February 2023: No. 2: *Corundum – Lattice Diffusion of Foreign Elements Other Than Hydrogen*; No. 4: *Padparadscha Sapphire*; No. 5: *Emerald – Fissure Filling/Clarity Enhancement*; No. 6: *Paraíba Tourmaline*; No. 8: *Gemstones Where Colour Authenticity Is Undetermined*; No. 9: *Alexandrite and Other Colour-Change Gemstones*; and No. 12: *Organic Fillers (Oil, Resin, Wax) in Gemstones*. Download the sheets at https://www.lmhc-gemmology.org/gemstones.

Natural Diamond Council's *Diamond Facts* Report

Released in April 2023, *Diamond Facts: Addressing Myths and Misconceptions About the Diamond Industry* provides answers to questions such as 'Is it possible to tell a laboratory-grown diamond from a natural diamond?', 'How do I know whether I'm purchasing a natural or a laboratory-grown diamond?', 'Are all laboratory-grown diamonds sustainable?', 'What is the natural diamond industry doing to reduce its carbon footprint and protect biodiversity?', 'What have been the price trends for laboratory-grown diamonds?', 'Do natural diamonds benefit the countries where they come from?' and others. Factual answers to each question can be used to inform consumers and raise confidence in the industry. View the report online at https://www.naturaldiamonds.com/diamond-guide/diamond-facts-full-report or download it at https://www.naturaldiamonds.com/press/diamond-facts-report.

Sarine's CarbonVERO Diamond Traceability Solution

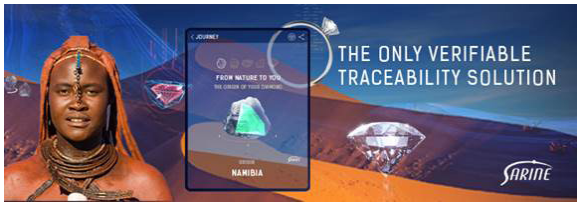

Israel-based Sarine Technologies Ltd introduced its CarbonVERO system in July 2023. It provides a method of recording 'the energy consumption and carbon footprint of each individual diamond' from its mine origin to the polished gem. The data can then be accessed via Sarine's Diamond Journey traceability solution. The system is the result of collaboration with diamond manufacturer and trader Andre Messika Ltd and The Carbon Trust, a renowned authority in carbon emissions assessment. The Carbon Trust created the foundation database, incorporating annual input of materials, energy, transportation, processing, ancillary and waste data, as well as the method of determining carbon footprint. Visit https://sarine.com/carbonvero.

SSEF Update on Irradiation Treatment of Gem Corundum

In July 2023, the Swiss Gemmological Institute SSEF posted a research update on the irradiation treatment of corundum at https://tinyurl.com/mryhkdcs. The report provides preliminary data from SSEF's experiments using a linear accelerator in an attempt to replicate results of recent reports that cancer radiotherapy equipment has been used to enhance the colour of slightly purplish red rubies and pink-to-purple sapphires. SSEF found that not all samples were affected by such irradiation, and most that did react tended to turn an unstable orangey colour; not all of them returned to their original colour with time. To date, no reliable method of detection has been identified.

Trade Alert on Cr-diffused 'Ruby'

In July 2023, a trade alert was posted by Jeffery Bergman of EighthDimensionGems, Bangkok, Thailand, about a 7 ct 'ruby' treated using high-temperature heating combined with surface diffusion of Cr. The stone had abnormally high RIs of 1.772–1.778, and the treatment became apparent when microscopic observation in immersion revealed uneven colour concentrations at the surface. Although this treatment has been known for decades, it is not often encountered today, and this stone was reportedly treated recently. Included with the description of the stone are useful photomicrographs of characteristic surface and internal features. View the report at https://eighthdimensiongems.com/chromium-surface-diffusion-treated-ruby.

OTHER RESOURCES

Rapaport Podcasts

Since the beginning of 2023, Rapaport has released 17 podcasts on a broad range of diamond-related topics. Among these is a 6 July interview with Dr Thomas Hainschwang about the challenges of identifying natural vs colour-treated green diamonds, and an 18 July discussion with Amish Shah (founder of Altr Created Diamonds) about the inaugural Lab-Grown Diamond Symposium that took place on 10 July 2023 in Dubai, United Arab Emirates. This symposium gathered industry members to discuss the economics and marketing of synthetic diamonds, as well as issues such as sustainability and ethics. To hear these and other podcasts, visit https://rapaport.com/type/podcasts.

Tea & Gemstones Podcasts

Jewellery historian Jennifer Sieverling offers an educational but light-hearted look at gems and jewellery on Apple Podcasts in her Tea & Gemstones series. As of this writing, 36 podcasts were available, with five added in 2023: 'The Imitators' (diamond simulants), 'Labradorite', 'Carmen Lucia Ruby', 'History of Birthstones', 'JUSKA (Jewelry U Should Know About): Daniela Villegas' and 'Gemstones of the Zodiac'. Visit https://podcasts.apple.com/us/podcast/tea-gemstones/id1583839944.

MISCELLANEOUS

Collectible Minerals Exhibit in Paris, France

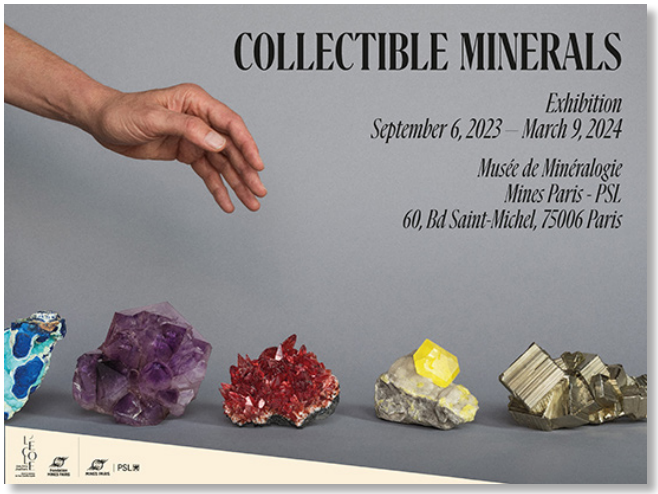

The Musée de Minéralogie, Mines Paris – PSL in Paris, France, is hosting a temporary exhibit titled *Minéraux : Objets de Collection (Collectible Minerals)* until 9 March 2024. It features hundreds of mineral specimens—acquired over two centuries through purchases, field collecting, revolutionary seizures, donations, exchanges and heritage preservation—many of which are not normally on display or assembled in one place. The museum was created in 1794 and has more than 100,000 samples, representing over 1,000 species. Information on the exhibition is available at https://tinyurl.com/msca9a9y, and an informative and well-illustrated catalogue can be downloaded at https://tinyurl.com/yckm4s3y.

Gübelin Gem Museum Opens

In July 2023, the House of Gübelin opened the Gübelin Gem Museum in Lucerne, Switzerland, on the occasion of the 100th anniversary of the Gübelin Gem Lab. The museum houses the lab's reference collection of more than 28,000 gem specimens, many collected at their source by Dr Eduard Gübelin during his travels. In addition to 174 samples from his collection, the museum also includes displays of Gübelin history, watches, jewellery and gemmological instruments, and provides interactive educational experiences. Visit https://www.gubelin-gemmology.com.

What's New provides announcements of instruments, technology, publications, online resources and more. Inclusion in What's New does not imply recommendation or endorsement by Gem-A. Entries were prepared by Carol M. Stockton (CMS) or Brendan M. Laurs (BML), unless otherwise noted.

catawiki

Bid on exceptional gemstones, selected by Catawiki experts

Every day, our in-house experts carefully select a wide range of gemstones from around the world for every collector.

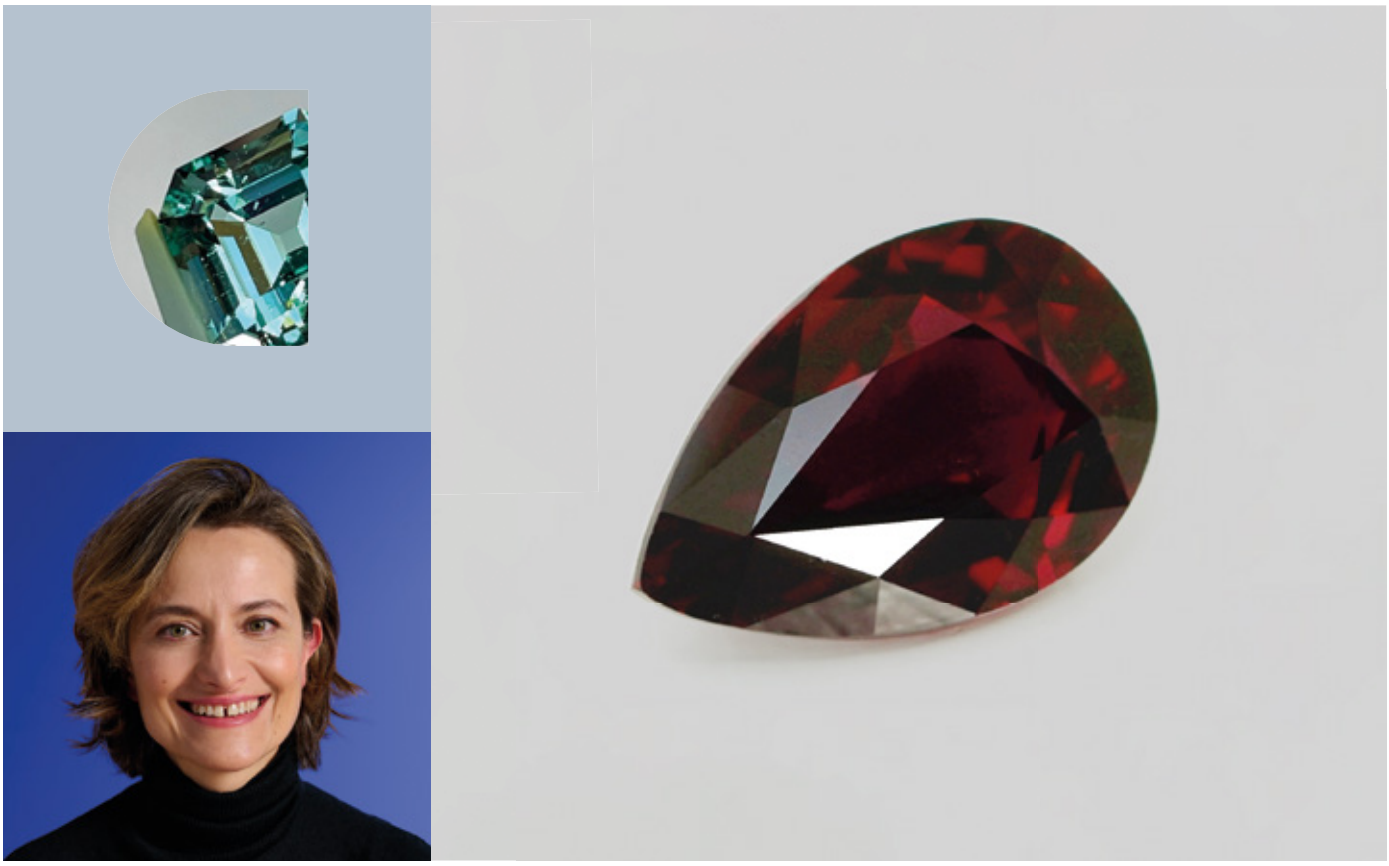

Purificacion Aquino Garcia
Expert Gemstones

Buy and sell on catawiki.com

Download on the App Store

GET IT ON Google Play

Gem Notes

COLOURED STONES

‘Aquafire’ Beryl from Brazil

Figure 1: In 2019, aquamarine containing some interesting inclusions was found in Minas Gerais, Brazil. The broken fragments shown in these images range up to 7 cm long. Photos courtesy of Gems in Gems.

In March 2019, a new find of aquamarine occurred in Minas Gerais, Brazil, which displayed abundant irregular and spotty orangey yellow to yellowish green or brownish orange inclusions (e.g. Figure 1). About 200 kg of rough material were recovered as broken pieces, some with flat areas corresponding to beryl’s poorly developed cleavage on {0001}. The entire production was obtained by Gems in Gems (Seville, Spain), and so far they have faceted about 5,000 carats in sizes up to 23 × 13 mm (e.g. Figure 2). The stones are cut to show their inclusion scenery, particularly the orangey yellow to yellowish green areas, as well as iridescent colours displayed along fractures or on the surfaces of the inclusions (e.g. Figure 3). The appearance of the beryl resulting from the combination of these characteristics inspired Gems in Gems to call it ‘Aquafire’. In order to characterise the material and its inclusions in more detail, Gems in Gems kindly donated three of the stones to Gem-A: a 10.29 ct trilliant, a 5.07 ct cushion-shaped modified cabochon and a 3.26 ct trilliant (again, see Figure 2).

Examination of the stones by authors AC, CW and BW confirmed that all the samples were beryl. They were pale coloured and ranged from aquamarine (greenish blue to green) to goshenite (colourless). The inclusions were characterised in these and in some other Aquafire samples from the collection of author MC-V. The orangey yellow to yellowish green inclusions ranged from a few millimetres to the width of the entire stone, and were sheet-shaped and

Figure 2: The Aquafire beryls shown here were examined for this report. The two trilliants (10.29 and 3.26 ct) are cut with the table parallel to the orangey yellow to yellowish green inclusions (and perpendicular to the *c*-axis), while the 5.07 ct cushion-shaped stone has the table parallel to the *c*-axis. Gift of Gems in Gems; photo by B. Williams.

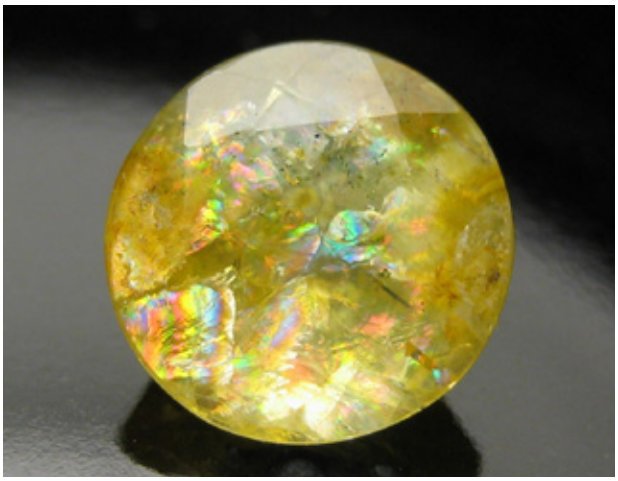

Figure 3: This 2.34 ct Aquafire beryl shows bright iridescent fractures and an orangey yellow appearance due to its inclusions. Photo by Vicky Rodríguez Garrido.

typically oriented approximately perpendicular to the *c*-axis (i.e. parallel to the cleavage direction; Figure 4a). They sometimes displayed a mosaic pattern with many six-sided reflective iridescent surfaces that were capable of producing a sunstone-like effect (e.g. Figure 4b). Associated with the orangey yellow to yellowish green inclusions were small submillimetre-scale platy crystals with a hexagonal shape and a transparent dark green appearance (Figure 4c). These crystals were oriented approximately parallel to the larger yellow to green inclusions. Fractures showing rainbow iridescence were locally present together with the orangey yellow to yellowish green inclusions. Abundant two-phase fluid inclusions were also visible in the stones (again, see Figure 4c). Fine acicular features with a brownish orange appearance were oriented parallel to the *c*-axis and probably consisted of hollow tubes filled with epigenetic material (see Figure 2, centre stone).

Raman spectroscopy of the small dark green inclusions with a Magilabs GemmoRaman-532SG instrument only yielded spectral features of the beryl host. The inclusions in two of the stones (5.07 and 10.29 ct) were then analysed in more detail using a Renishaw inVia Qontor Raman microscope equipped with a 532 nm laser and a 100 × long-working-distance objective. A confocal setup was used for the analyses to ensure high spatial resolution. Raman map data were obtained, and volume imaging and depth profiling were performed on an orangey yellow inclusion in the larger stone. For phase identification, the Raman spectral patterns were compared to Renishaw's reference library. Both the orangey yellow areas and the minute dark green inclusions yielded Raman spectra consistent with goethite, although not with complete certainty. In addition, one of the platy dark green hexagonal-shaped inclusions produced a mixed pattern consisting of signals indicative of goethite along with the host beryl. Although the preliminary identification of goethite is consistent with the frequent presence of Fe-bearing inclusions in beryl, to the authors' knowledge the green colour shown by some of the inclusions has not been documented previously for goethite.

Fe-bearing mineral inclusions in aquamarine were documented by Koivula (2006) in a stone from India and by Danet *et al.* (2012) in samples from Madagascar. Both authors described arrays of flat inclusions—in some cases dendritic—that were oriented in the basal plane of the host aquamarine; these produced aventurescence in the beryl from India. The authors concluded that the black inclusions were usually ilmenite, while the red ones were hematite. Beryl of this type is also known from Brazil, and has been marketed as 'Leopard Aquamarine' (for dark blue stones with black spots) or 'Sunstone Aquamarine' (for light blue gems with lighter-coloured inclusions).

Figure 4: Internal features in the Aquafire beryl consist of: (**a**) sheet-like yellowish green inclusions with irregular borders; (**b**) orangey yellow platelets displaying thin-film interference colours in a mosaic pattern with six-sided reflective iridescent surfaces; and (**c**) dark green platelets and fluid inclusions that are seen here dispersed over a sheet of the orangey yellow mineral. Photomicrographs by Liviano Soprani (a and b; image width 3.5 mm) and B. Williams (c; image width 3.0 mm).

Although Aquafire beryl also hosts Fe-rich inclusions, their non-dendritic structure and their orangey yellow to yellowish green and dark green colouration make it a new variety of aquamarine. Further studies are necessary to better characterise the inclusions mineralogically.

Dr Alessandra Costanzo FGA DGA
(alessandra.costanzo@universityofgalway.ie)
University of Galway, Ireland

Cara Williams FGA *and Bear Williams* FGA
Stone Group Laboratories
Jefferson City, Missouri, USA

Dr Marco Campos-Venuti
Gems in Gems, Seville, Spain

References

Danet, F., Schoor, M., Boulliard, J.-C., Neuville, D.R., Beyssac, O. & Bourgoin, V. 2012. Inclusions in aquamarine from Ambatofotsikely, Madagascar. *Gems & Gemology*, **48**(3), 205–208, https://doi.org/10.5741/gems.48.3.205.

Koivula, J.I. 2006. Gem News International: Cuneiform aquamarine inclusion. *Gems & Gemology*, **42**(1), 70, https://www.gia.edu/gems-gemology/spring-2006-gem-news-international.

Emerald and Green Beryl from Shaanxi Province, China

In China, emeralds have been mined from two deposits: (1) Malipo (or Dyakou) in Yunnan Province, since the late 1980s (Hu & Lu 2019); and (2) Davdar village in south-western Xinjiang, mainly since 2008 (Cui *et al.* 2020). Recently, emeralds have come from a new locality (Figure 5) in central China: the Qinling Mountains in Zhen'an County, Shaanxi Province, where they are associated with a W-Be deposit (Dai *et al.* 2019). In June 2023, author LP received a parcel consisting of 29 pieces of hexagonal prismatic, translucent, heavily included, light-to-moderate green crystals from this locality that weighed 0.07–1.59 g. Eight of them (Figure 6) were selected for analysis at the Antwerp Laboratory for Gemstone Testing (ALGT). Later, some larger crystals of higher clarity were reportedly extracted from a deeper area of the deposit or nearby.

The average hydrostatic SG value for the samples lacking any matrix material was 2.68. Due to the abundant inclusions and surface characteristics of the samples received, it was not possible to obtain an accurate RI measurement. Raman spectra obtained with a GemmoRaman-532SG spectrometer revealed the attached host rock to be mainly quartz, indicating a hydrothermal origin (Giuliani & Groat 2019). All the samples were found to contain significant amounts of oil in surface-reaching fissures, but no dyes or pigments were detected in the oil. None of them showed a red or pink reaction under a Chelsea Colour filter, and all were inert to long- and short-wave UV radiation. All showed yellow-green and green dichroism when viewed with a London dichroscope (Figure 7a). Microscopic examination revealed abundant fractures, and a three-phase inclusion was seen in one of the samples (Figure 7b). In addition, some minute dark solids and tube-like

Figure 5: (**a**) Beryl/emerald crystals from a new deposit in Shaanxi Province are shown embedded in their host rocks. (**b**) This assortment of loose emerald crystals (0.2–7.72 g) is also from the new locality in Shaanxi Province. (**c**) A bluish green emerald from the new occurrence shows relatively high clarity. Photos reproduced with permission.

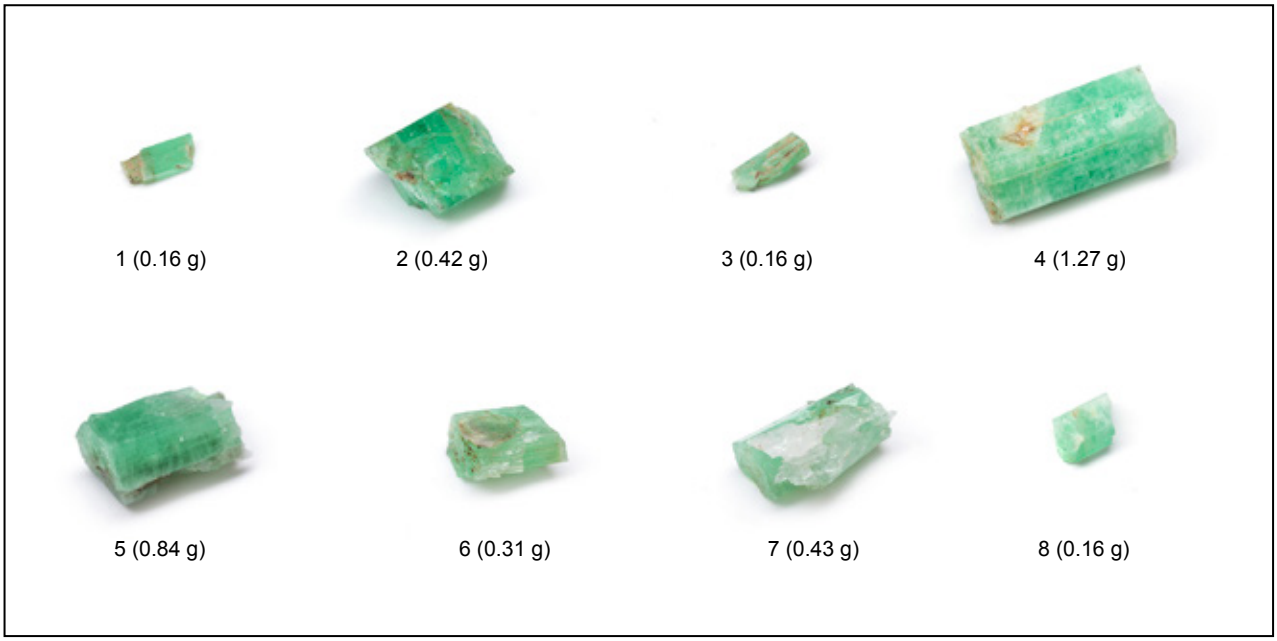

Figure 6: These eight beryl crystals from Shaanxi Province were examined for this report. Composite photo by ALGT.

inclusions were observed.

The chemical composition of five samples was determined by energy-dispersive X-ray fluorescence (EDXRF) spectroscopy using a Thermo Scientific ARL Quant'X instrument. Chromium was below the detection limit, while significant amounts of V and Fe were found in all the samples (Table I). Other trace elements included Cs, Ca, K, Rb and Ga. Ultraviolet-visible-near infrared (UV-Vis-NIR) spectroscopy of seven specimens showed strong Fe^{3+} absorption at 375 nm and Cr^{3+}/V^{3+} absorptions at about 435 and 605 nm (Figure 8).

It is well known that the green colour of emerald can come from a mixture of the chromophores Cr, V and Fe (Hänni 1992). The examined samples from Shaanxi Province were coloured by both V^{3+} and Fe^{3+}. While

Table I: EDXRF trace-element composition of beryl/emerald from Shaanxi Province, China.*

Sample no.	1	2	5	6	7
Element (wt.%)					
K	0.28	0.09	0.05	0.13	0.28
Ca	0.27	0.15	0.04	0.11	0.25
V	0.51	0.37	0.35	0.26	0.62
Fe	0.43	0.23	0.16	0.30	0.43
Ga	0.01	bdl	bdl	0.01	0.01
Rb	0.01	0.01	bdl	0.01	0.01
Cs	0.19	0.34	0.24	0.23	0.36

* Cr was below the detection limit (bdl; approximately 1 ppmw) in all analyses.

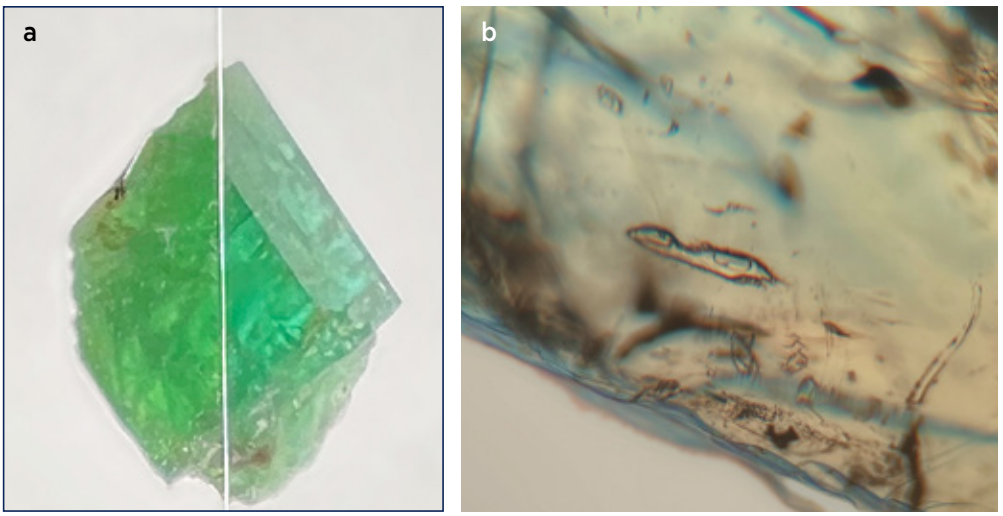

Figure 7: (**a**) Viewed with a dichroscope, the 0.42 g emerald crystal from Shaanxi Province shows yellow-green and green dichroism. (**b**) A three-phase inclusion is present in sample no. 1, as shown here in immersion in benzyl benzoate and magnified 55×. Photomicrographs by Lirui Peng.

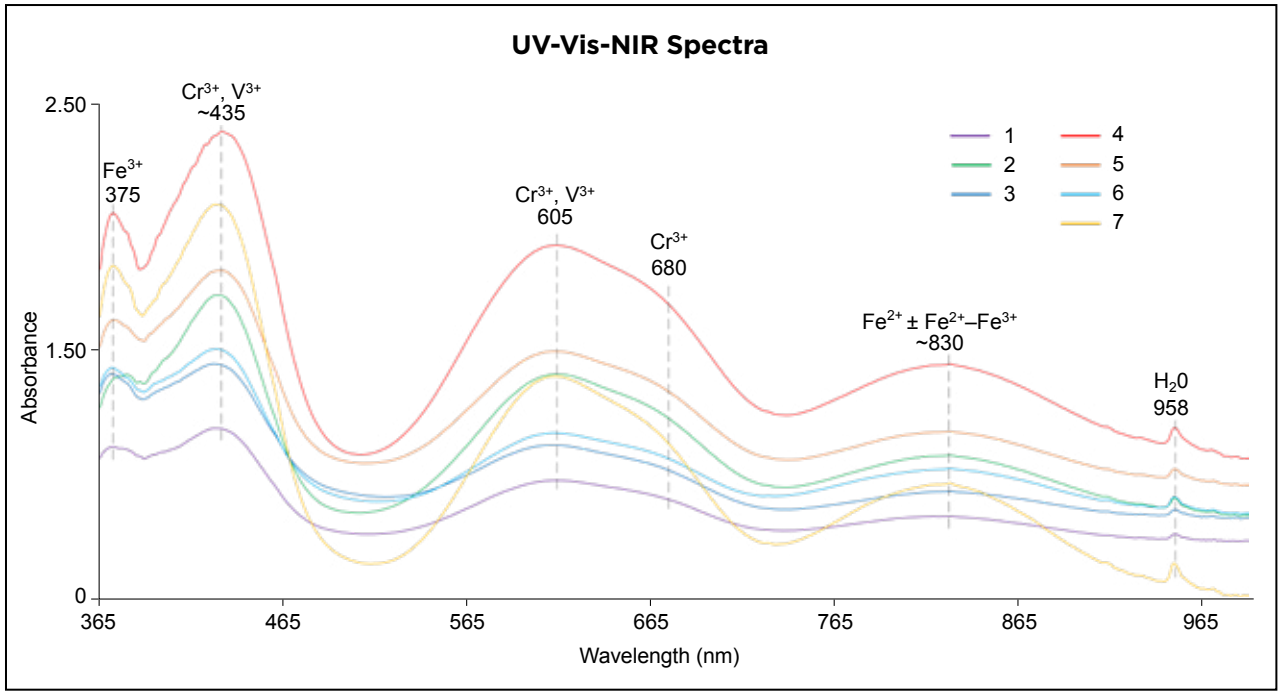

Figure 8: UV-Vis-NIR spectra of seven of the beryl/emerald samples show main absorptions at 375 nm due to Fe^{3+} and at approximately 435 and 605 nm due to Cr^{3+} and/or V^{3+}.

many gemmologists would consider the deeper-coloured samples to be emerald—and would call the paler crystals green beryl—ALGT considers Cr as one of the necessary elements for green colour in emerald, and therefore would classify the studied specimens as green beryl.

Lirui Peng FGA *(lirui.peng@aol.com)*
Antwerp, Belgium

Marc Segers and Mingyue Yang
(info@algtlabs.com)
ALGT, Antwerp, Belgium

References

Cui, D., Liao, Z., Qi, L., Zhong, Q. & Zhou, Z. 2020. A study of emeralds from Davdar, north-western China. *Journal of Gemmology*, **37**(4), 374–392, https://doi.org/10.15506/jog.2020.37.4.374.

Dai, H., Wang, D., Liu, L., Huang, F. & Wang, C. 2019. Metallogenic epoch and metallogenic model of the Hetaoping W-Be deposit in Zhen'an County, south Qinling. *Acta Geologica Sinica*, **93**(6), 1342–1358 (in Chinese with English abstract).

Giuliani, G. & Groat, L.A. 2019. Geology of corundum and emerald gem deposits: A review. *Gems & Gemology*, **55**(4), 464–489, https://doi.org/10.5741/gems.55.4.464.

Hänni, H.A. 1992. Blue-green emerald from Nigeria (a consideration of terminology). *Australian Gemmologist*, **18**(1), 16–18.

Hu, Y. & Lu, R. 2019. Unique vanadium-rich emerald from Malipo, China. *Gems & Gemology*, **55**(3), 338–352, https://doi.org/10.5741/gems.55.3.338.

Unusual Colour-zoned Emerald

Recently, a 3.42 ct green gemstone was submitted to the Gemmological Certification Services laboratory for testing. Initial observations showed an unusual web-like colour distribution (Figure 9). The stone's green colour and RI of 1.570–1.575 suggested that it was an emerald, likely of low iron content. EDXRF chemical analysis and Raman spectroscopy further proved it was emerald. UV-Vis-NIR spectroscopy indicated it had a low Fe content consistent with a Colombian origin. Testing with long-wave UV radiation revealed the presence of significant oiling, supported by prominent oil-related peaks in the infrared spectrum.

The emerald's green colour was concentrated in the

Figure 9: Unusual web-like colour concentrations can be seen through the table of this 3.42 ct emerald. Photo by A. Duffy.

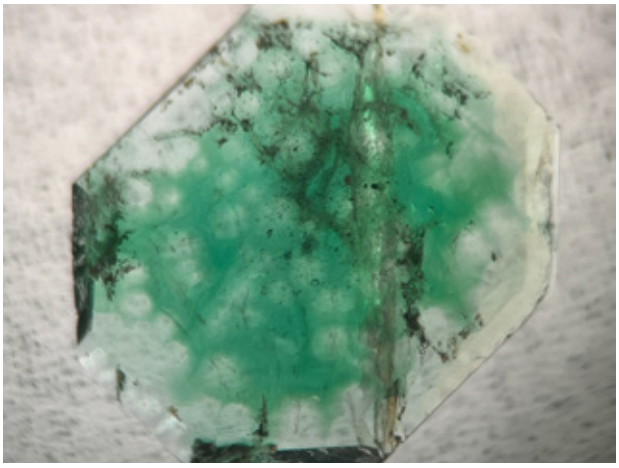

Figure 10: Viewed table-down along the *c*-axis direction with diffused light, areas of green colour can be seen surrounding colourless, roughly hexagonal zones in the emerald. Photomicrograph by A. Duffy; magnified 15×.

lower (pavilion) part of the stone, while the crown appeared near-colourless. This was reflected in the EDXRF trace-element results, which yielded notably greater Cr and V values for the pavilion (1260 and 740 ppm, respectively) compared to the crown (270 and 150 ppm, respectively). In cross-polarised light, a typical uniaxial interference figure was seen through the table, indicating the *c*-axis was oriented perpendicular to the table. The stone also displayed the expected reaction with a dichroscope, with the green areas showing bluish green and yellowish green colouration.

Microscopic examination revealed details of the unusual colour zoning. In immersion and looking through the stone table-down (i.e. down the *c*-axis), a mottled pattern could be seen, consisting of near-colourless roughly hexagonal columnar-like features outlined by interstitial green areas (Figure 10). Viewed at an oblique angle, the hexagonal columns took the form of green-edged jagged peaks (Figure 11).

Similar colour zoning has been noted previously in natural emerald (Gübelin & Koivula 2008; Muyal *et al*. 2015), and was ascribed to a late-stage influx of Cr and V into the growth environment during crystallisation. Thus, it appears that the near-colourless hexagonal columns grew first in a parallel arrangement, and then conditions changed, favouring crystallisation of Cr- and V-bearing beryl (emerald) in the interstitial and surrounding areas.

Despite clearly exhibiting a columnar structure, the stone did not display the *gota de aceite* optical effect that is sometimes associated with Colombian emeralds. The unusual colour zoning seen here is a reminder of the dynamic and changeable conditions under which gems form.

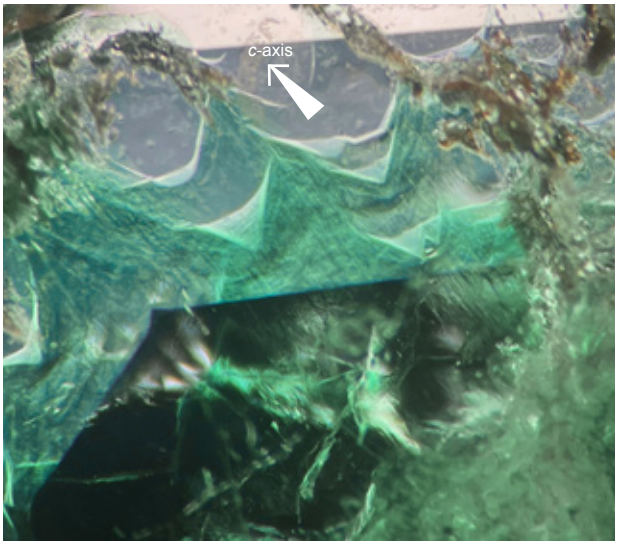

Figure 11: When viewed obliquely to the *c*-axis, the hexagonal growth pattern takes the form of sharp, angular zones. Note the absence of colour at the top of the image, towards the crown of the stone. Photomicrograph by A. Duffy; magnified 40×.

Alexander Duffy FGA DGA
(alexduffy.gcs@gmail.com)
Gemmological Certification Services
London

References

Gübelin, E.J. & Koivula, J.I. 2005. *Photoatlas of Inclusions in Gemstones*, Vol. 2. Opinio Publishers, Basel, Switzerland, 829 pp. (see pp. 433–434).

Muyal, J., Renfro, N. & Cooper, A. 2015. Lab Notes: Colour zoned emerald. *Gems & Gemology*, **51**(3), 314, https://www.gia.edu/gems-gemology/fall-2015-labnotes-color-zoned-emerald.

‘Star of David’ Pattern Produced by a Trapiche Emerald from Colombia

Trapiche emeralds from Colombia are fascinating to many gemmologists and collectors. A notable trapiche emerald weighing 10.77 ct was recently examined at Guild Gem Laboratories (Figure 12). Standard gemmological testing showed properties consistent with those of emerald, with a uniaxial optic character, spot RI of approximately 1.57 and hydrostatic SG of 2.71. Chemical analysis by EDXRF spectroscopy revealed a low concentration of Fe (690 ppmw), high V (1190 ppmw) and low Rb (12 ppmw), which is consistent with values reported for Colombian emeralds (Saeseaw *et al*. 2019).

As usual for trapiche stones, this gem was cut as a cabochon with the basal plane orientated perpendicular to the *c*-axis, and it showed a small hexagonal core with six radiating green arms and dendrites (cf. Pignatelli *et al*. 2015). Microscopic observation revealed classic three-phase fluid inclusions and black carbonaceous material from the surrounding black shale. In addition, abundant transparent striations oriented perpendicular to the sides of the central hexagon were present in each arm. These striations were described by Pignatelli *et al*. (2015) as bundles of straight dislocations oriented perpendicular to the $\{10\bar{1}0\}$ faces, and they are known to produce chatoyancy in cabochons cut from the arms of Colombian trapiche emeralds (e.g. Weldon & McClure 2013; Laurs 2020).

When the emerald was illuminated through either the top or bottom with a focused light source, a six-pointed geometric hexagram, or ‘Star of David’ pattern, was projected on the surface behind the stone (Figure 13). The pattern was clearly visible only at a certain distance (around 5 cm) behind the cabochon. When the stone was tilted, the pattern became narrower. Each edge of the Star of David pattern was oriented perpendicular to the striations within the corresponding arm of the trapiche emerald (Figure 14). Thus, the pattern appears to result from six sharp intersecting chatoyant ‘eyes’ that are produced by the parallel striations within each arm of the trapiche emerald.

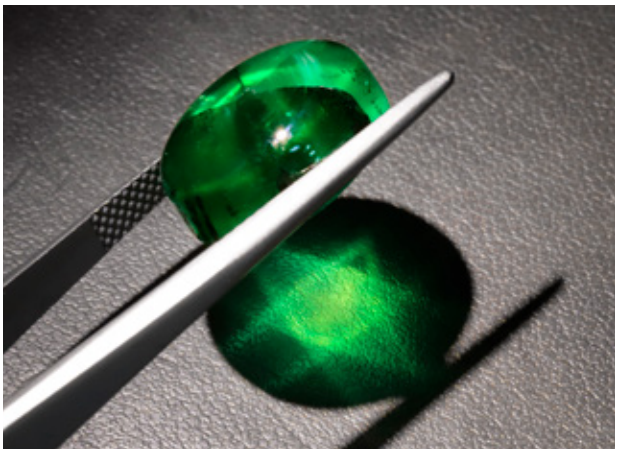

Figure 13: When a focused light source is directed through the 10.77 ct trapiche emerald parallel to the *c*-axis, a Star of David pattern is projected onto the surface behind it. Photo by Huixin Zhao.

Although optical effects such as asterism and chatoyancy are normally seen in *reflected* light when viewing the dome of cabochon-cut stones (e.g. epiasterism), it is

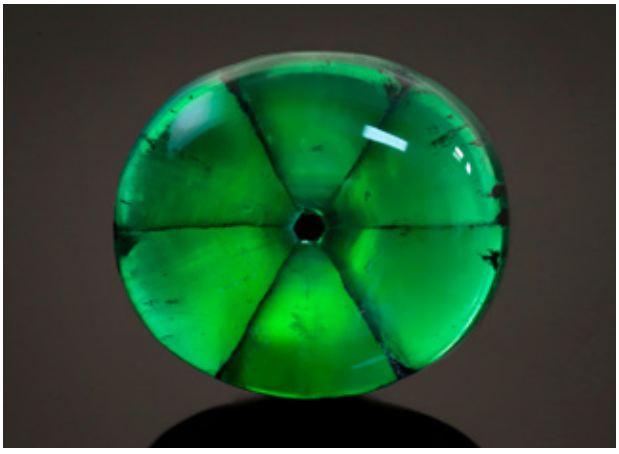

Figure 12: This 10.77 ct trapiche emerald (14.78 × 12.97 × 6.20 mm) exhibits an attractive appearance, but it also proved capable of yielding an interesting optical effect. Photo by Kaiyin Deng.

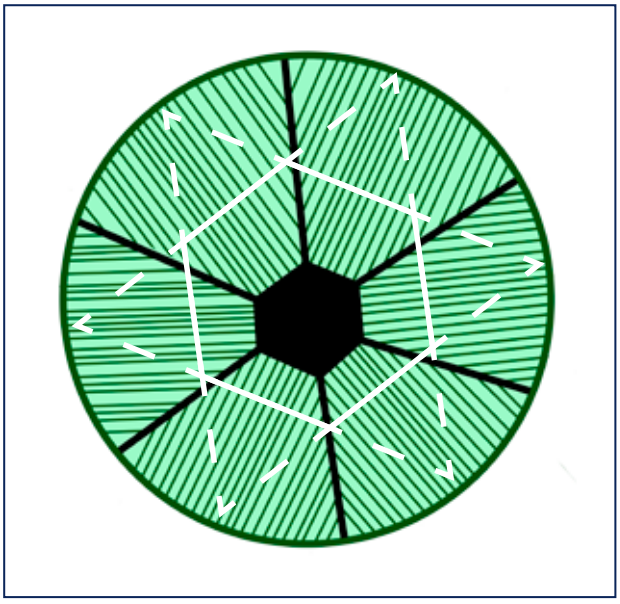

Figure 14: This diagram shows the relationship between the orientation of the striations in the arms of the trapiche emerald and the chatoyant bands (white lines) that are produced by them. The view is parallel to the *c*-axis. Illustration by Xueying Sun.

less common to see these phenomena with *transmitted* light through the gemstone (i.e. diasterism). This optical phenomenon would not have been noticed if the Star of David pattern had not been seen behind the stone while it was being examined. Such projected diasterism has only rarely been mentioned in the literature; an interesting example was documented by Killingback (2007) in a star rose quartz sphere. The trapiche emerald reported here is unusual in that it contains a high-enough density of parallel dislocations to produce chatoyancy while also being *transparent* enough for the multiple cat's-eyes to be transmitted through the stone and manifested in the hexagram-shaped light pattern.

Xueying Sun, Yujie Gao (peter.gao@guildgemlab.com) and Kaiyin Deng
Guild Gem Laboratories
Shenzhen, China

References

Killingback, H. 2007. Star rose quartz by laser light. *Gems&Jewellery*, **16**(3), 10–11.

Laurs, B.M. 2020. Gem Notes: A collection of cat's-eye emeralds from Colombia. *Journal of Gemmology*, **37**(2), 126–127, https://doi.org/10.15506/jog.2020.37.2.126.

Pignatelli, I., Giuliani, G., Ohnenstetter, D., Agrosì, G., Mathieu, S., Morlot, C. & Branquet, Y. 2015. Colombian trapiche emeralds: Recent advances in understanding their formation. *Gems & Gemology*, **51**(3), 222–259, https://doi.org/10.5741/gems.51.3.222.

Saeseaw, S., Renfro, N.D., Palke, A.C., Sun, Z. & McClure, S.F. 2019. Geographic origin determination of emerald. *Gems & Gemology*, **55**(4), 614–646, https://doi.org/10.5741/gems.55.4.614.

Weldon, R. & McClure, S. 2013. Unveiling the cat's-eye effect in a 75 ct Colombian emerald pair. https://www.gia.edu/gia-news-research-unveiling-cats-eye-effect-in-colombia-emerald-pair, 12 July, accessed 23 August 2023.

New Production of Rhodizite-Londonite from Manjaka, Madagascar

Since 2016, the renewal and approval of all mining licences in Madagascar have been blocked, with the official reason that a new mining law is under study. This has created significant administrative confusion in the mining sector there. Nevertheless, in early 2020 some Malagasy government authorities allowed Chinese companies to undertake 'parallel' activities of mining and collecting lithium ore. This resulted in a new mining rush taking place at all of Madagascar's Li-bearing pegmatite fields by thousands of artisanal miners, with no security or sanitary control, and disregarding any pre-existing mining licences. As a by-product of this pursuit of lithium ore, there has been new production of pegmatitic gems, mostly tourmaline. In addition, less-common gem materials have been produced, as described in this report.

In October 2022, a group of scientists from Masaryk University (Brno, Czech Republic) and Goethe University (Frankfurt am Main, Germany) visited several classic mineral and gem localities in the Sahatany Valley of central Madagascar, during a field trip focusing on granitic pegmatites organised by author FP. Among the localities visited was a place known in the literature as Manjaka (Lacroix 1922), which in recent years has been referred to by local miners as Sahananana (from the name of a small village located a few hundred metres south-east of the deposit). This area has been mined since the early twentieth century, mainly for small crystals of vivid red tourmaline. After a long period of inactivity, in early 2020 many tens of miners (expanding to more than 200 miners in early 2022) rushed there to dig for lithium ore. At the time of our visit, about 120 people (miners and their families) were working the pegmatites in numerous shafts using simple hand methods (Figures 15–17). During a more recent visit made by author FP in July 2023, the work was still going on.

The Sahatany Valley pegmatite field is characterised by numerous occurrences of Li-enriched, gem-bearing pegmatites (Pezzotta 2001), occasionally containing large pockets lined with attractive gem-quality crystals of multi-coloured elbaite-liddicoatite, morganite, kunzite, colourless hambergite and yellow rhodizite-londonite and danburite. In the Manjaka area, two major types of pegmatites have been recognised (Gadas *et al*. 2023): (1) A few east-west-trending dykes, of limited length but up to about 2 m thick, that are discordant or parallel to the foliation of the calc-silicate host rocks; and (2) numerous elongated dykes, from 2 to about 20 cm thick, that are typically concordant with the host-rock foliation. In the

Figure 15: An overview of the Manjaka (Sahananana) mining area shows the extent of activity in October 2022, when about 120 people were working the deposit. Photo by M. Novák.

first type, dark (black or brown) tourmaline predominates over pink-to-red tourmaline, which occasionally is found in the central parts of the pegmatites. In the other type, pink-to-red tourmaline significantly predominates and locally grows directly from the contact with the host rock. Associated with this tourmaline are well-formed isometric crystals of yellow rhodizite-londonite (e.g. Figure 18a), some of which contain facetable material (Laurs *et al.* 2002).

As of July 2023, recent mining activities at Manjaka have produced about 2 tonnes of lithium ore weekly (with an average grade of about 30% spodumene), and so far about 200 tonnes of lithium ore have been extracted. Although gem-quality rhodizite-londonite is very rare at the locality, the amount of pegmatitic rock mined for lithium ore is so large that during the past two years there has been a near-constant supply of gem rough, which is mostly faceted and traded at the local market in Antsirabe. Also produced are significant amounts of low-grade red tourmaline, which is mostly traded by West African gem dealers to the Indian market.

The total recent production of rhodizite-londonite is difficult to estimate, but is probably on the order of a few

Figure 16: A closer view of the workings illustrates the simple techniques used by the miners, including primitive windlass systems. Photos by M. Novák.

Figure 17: Local miners and their families are involved with producing lithium ore (and gem materials as by-products) in Madagascar, as shown here at Manjaka. Photo by M. Novák.

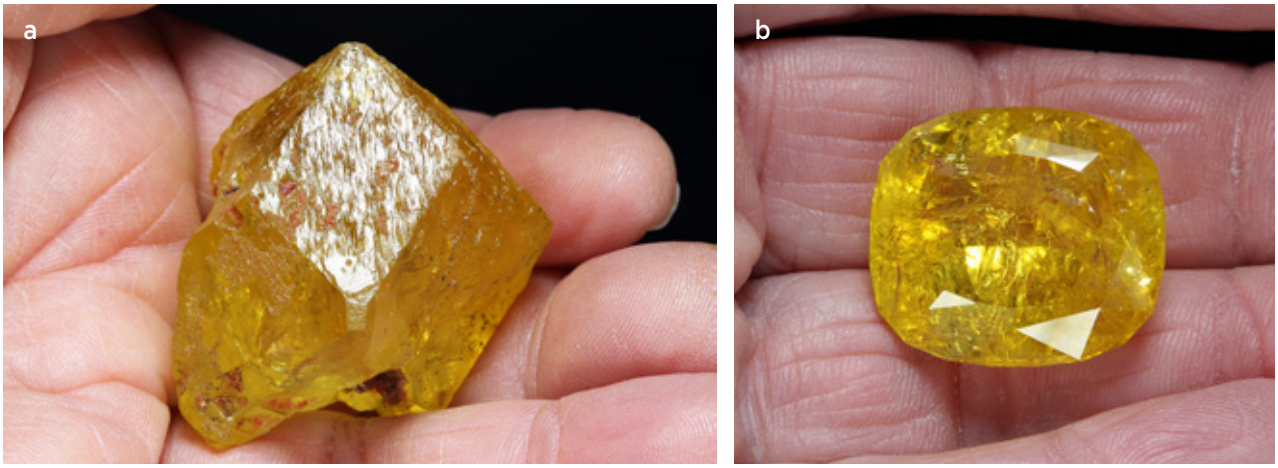

Figure 18: Exceptional examples of rhodizite-londonite recently produced from Manjaka include (**a**) this 65 g crystal (4.1 cm in maximum dimension) and (**b**) this 48 ct cushion-cut gemstone. Both specimens are in the collection of the MIM Museum (Beirut, Lebanon). Photos by Louis Dominique Bayle.

hundred grams of good-quality gem rough. In addition to material from Manjaka—which ranges from very light yellow to vivid yellow—parcels of rhodizite-londonite may contain pieces from other deposits, such as Antsongombato, Manapa and Tetezantsio (which are also being mined for lithium ore). The material from these localities cannot be distinguished, with the exception of the pale bluish to greenish rhodizite-londonite that is exclusive to Tetezantsio. Some attractive faceted stones have been cut from the recent production, including vivid yellow, eye-clean gems weighing up to several carats (very rarely over 10 ct) that have been traded in the local market since 2021. Although gem-quality rhodizite-londonite is quite rare, the mining boom for lithium ore has increased its availability to levels never seen before, and some exceptional specimens have occasionally been produced, including well-formed crystals exceeding 3 cm in diameter and faceted stones of nearly 50 ct (Figure 18).

Dr Milan Novák (mnovak@sci.muni.cz)
Masaryk University
Brno, Czech Republic

Dr Federico Pezzotta
Mineralogical Collection Professionals
Milan, Italy

References

Gadas, P., Novák, M., Vašinová Galiová, M. & Pezzotta, F. 2023. Chemical composition of tourmalines from the Manjaka pegmatite and its exocontact, Sahatany Valley, Madagascar. *Journal of Geosciences* (in press).

Lacroix, A. 1922. *Minéralogie de Madagascar. Tome I: Géologie, Minéralogie Descriptive*. Augustin Challamel, Paris, France, xvi + 624 pp.

Laurs, B.M., Pezzotta, F., Simmons, W.B., Falster, A.U. & Muhlmeister, S. 2002. Rhodizite-londonite from the Antsongombato pegmatite, central Madagascar. *Gems & Gemology*, **38**(4), 326–339, https://doi.org/10.5741/gems.38.4.326.

Pezzotta, F. 2001. *Madagascar: A Mineral and Gemstone Paradise*. extraLapis English No. 1, Lapis International, East Hampton, Connecticut, USA, 97 pp.

Sphalerite from Balmat, New York, USA

Sphalerite (ZnS) is the most important zinc ore and is also known as *zinc blende*. It commonly contains Fe, which causes it to appear dark and opaque, but specimens with low Fe content can appear transparent in near-colourless, yellow, orange, red, brown or green (Bradshaw 2015). Sphalerite has a Mohs hardness of 3½–4 and perfect dodecahedral cleavage, so it is not well suited for jewellery, but it makes an attractive collector's stone that shows high dispersion. The main source of gem-quality sphalerite is Spain (Aliva mine; no longer active), and other localities include Bulgaria (Rhodope Mountains), Canada (Mt St Hilaire

Figure 19: This 9.37 ct sphalerite came from the Empire State mine (former Balmat No. 4 shaft) in 2019. It was faceted by Jay Medici and is the largest cut sphalerite from New York. Dylan Stolowitz collection; photo by Rudolf Van Dommele.

Figure 20: Faceted by Jason Baskin from material mined in 2022, this sphalerite from the Empire State mine weighs 6.49 ct. The diffused lighting emphasises the body colour and not the dispersion. Courtesy of Rocko Minerals; photo by Jeff Scovil.

in Québec), Mexico (Sonora) and the USA (Franklin, New Jersey; Bradshaw 2015).

Over the past several decades, economically important zinc deposits of the Balmat-Edwards zinc mining district in St Lawrence County in the north-west Adirondack Mountains of New York, USA, have occasionally produced sphalerite as well-formed crystals and rare gem rough (Smith & Pressler 1998). The ore bodies are hosted by Proterozoic siliceous dolomitic marble that was metamorphosed during the Grenvillian Orogeny about 1.1 billion years ago, and the mineralisation has been categorised as a massive stratiform sulphide type of sedimentary exhalative deposit (deLorraine & Johnson 1997).

Deposits in the Balmat District were important sources of zinc from 1903 to 2005, and recently all of the historic mines there (i.e. Balmat No. 2, 3 and 4 shafts) were purchased by Titan Mining Corporation and renamed collectively as the Empire State mine. Zinc mining resumed in 2018 at the former Balmat No. 4 shaft, where crystallised cavities were encountered at the 3,800-foot level in the Mud Pond orebody that produced attractive specimens of calcite, halite, pyrrhotite, quartz and sphalerite (Chamberlain & Walter 2020). Since then, several more pockets containing specimen- and gem-grade sphalerite have been found. According to Dylan Stolowitz (Green Mountain Minerals, Beacon, New York), starting in November 2019 additional finds occurred at the 3,800-foot level of the Mud Pond ore body. Over an approximately three-month period, several hundred sphalerite crystals averaging 1 cm (and up to 5+ cm) were recovered, but a large percentage were damaged. Although many of the crystals were facetable, most were colour zoned with dark brown cores. Notably, a small amount of gem-quality 'sulphur yellow' material was found in a separate pocket on this same level (Figure 19).

Stolowitz reported that, most recently in 2022–2023, pockets containing well-crystallised sphalerite were found at the 3,800 and 4,050 foot levels. Several world-class specimens were recovered on a matrix of quartz and calcite. The colour of the sphalerite included yellow, orange and red, and some fine gemstones have been cut (e.g. Figure 20).

Continued zinc exploitation at the Empire State mine is expected to yield additional finds of specimen- and gem-quality sphalerite in the future.

Brendan M. Laurs FGA

References

Bradshaw, J. 2015. Gem Notes: Sphalerite. *GemGuide*, **34**(2), 11–12.

Chamberlain, S.C. & Walter, M.R. 2020. Collector's Note: Balmat mining district update, St. Lawrence County, New York. *Rocks & Minerals*, **95**(5), 463–466, https://doi.org/10.1080/00357529.2020.1744100.

deLorraine, W.F. & Johnson, J. 1997. Geologic field guide to the Balmat zinc mine, St. Lawrence County, New York. *In*: Rayne, T.W., Bailey, D.G. & Tewksbury, B.J. (eds), *Field Trip Guide for the 69th Annual Meeting of the New York State Geological Association*, 85–116.

Smith, A.E. & Pressler, C.D. 1998. A 1946 find of gem sphalerite crystals at the Balmat zinc mine, St. Lawrence County, New York. *Rocks & Minerals*, **73**(6), 404–408, https://doi.org/10.1080/00357529809603080.

Tourmaline from Calabar, Nigeria

Nigeria is an important producer of gem tourmaline, from both primary and secondary deposits associated with granitic pegmatites. The mining areas are distributed across a wide region extending from south-western to east-central Nigeria, mainly in the states of Oyo, Osun, Nasarawa and Kaduna (Olade 2021). Recently, attractive gem tourmaline entered the market from a new deposit that is reportedly situated in the Calabar region of south-eastern Nigeria. Calabar is located in Cross River State near the border with Cameroon, and has not been previously reported as a commercial source of gem tourmaline to this author's knowledge. However, tourmaline-bearing pegmatites are widespread in this region, where they are hosted by basement rocks of the Oban massif and Obudu plateau (Ekwueme & Matheis 1995). Oden *et al.* (2011) reported that in the past, local people have mined tin, tourmaline and beryl from the Iwuru and Akwa-Ibami areas of the western Oban massif.

Figure 21: The rough Calabar tourmaline shown here ranges from approximately 2 to 7 g. Photo by John D. Dyer.

During the February 2023 Tucson gem shows, gem cutter John D. Dyer (John Dyer & Co., North Oaks, Minnesota, USA) obtained a parcel of rough tourmaline from the Calabar region that weighed 470 g. It consisted of broken pieces that appeared to have been cobbed from larger crystals in order to obtain cleaner sections for cutting (Figure 21). Most of the tourmaline was yellowish green to bluish green, with some pink and orangey pink pieces. The rough material ranged from approximately 2 to 7 g, and had an average weight of 3.65 g.

As of July 2023, Dyer had cut 43 stones weighing a total of 150 carats (i.e. 1.75–11.12 ct, mostly in the 2–4 ct range). He reported that the cutting yield was poorer than typically obtained from tourmaline, due mainly to the clarity and shape of the rough. The broken pieces were less well suited for cutting gemstones than the typical triangular or pseudo-hexagonal cross-sections of tourmaline crystals. In addition, the *c*-axis of the green material tended to show an olive hue that, although not over dark, was less appealing (Figure 22). Since the broken pieces tended to be wider on the *c*-axis, orienting the rough to avoid face-up olive colouration also reduced the yield.

Despite the challenges of cutting the material, the finished gemstones display vibrant and attractive colouration (e.g. Figure 23). Dyer reported that there are no significant grey modifiers, resulting in bright hues showing different variations of yellowish green to bluish green and 'seafoam' colours. The pink stones range

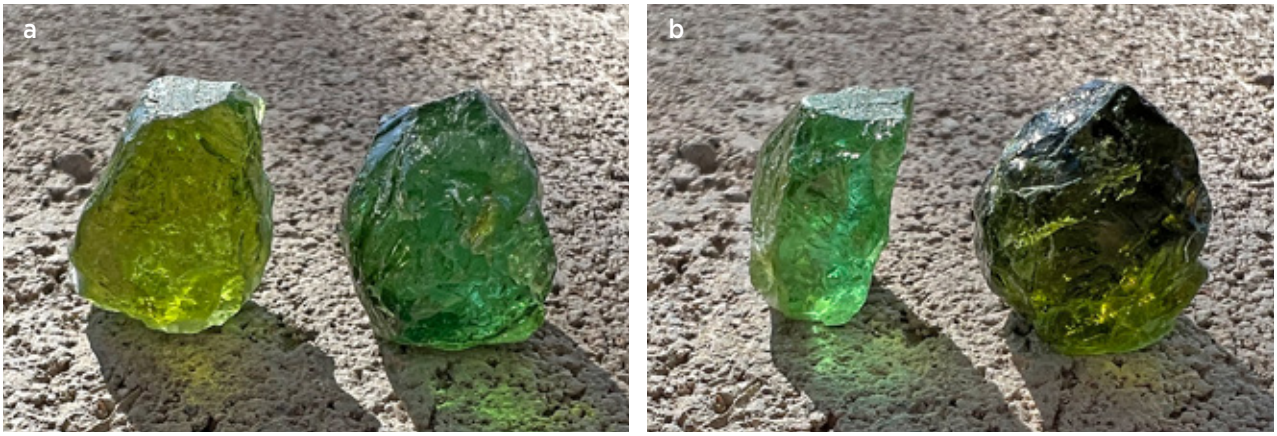

Figure 22: Two pieces of green Calabar tourmaline weighing approximately 5–6 g are shown in different orientations to demonstrate variations in their yellowish green to bluish green colour appearance depending on the viewing direction. The yellowish green colour is seen down the *c*-axis. Photos by John D. Dyer.

Figure 23: This assortment of faceted stones (1.86–11.12 ct) shows the range of colour of Calabar tourmaline. Courtesy of John Dyer Gems; composite photo by Ozzie Campos and Rosiane Pereira.

from deep pink to a paler pink or orangey pink, similar to morganite. The attractive appearance and range of colours shown by Calabar tourmaline make it a welcome addition to the gem trade.

References

Ekwueme, B.N. & Matheis, G.G. 1995. Geochemistry and economic value of pegmatites in the Precambrian basement of south-east Nigeria. *In*: Srivastava, R.K. & Chandra, R. (eds), *Magmatism in Relation to Diverse Tectonic Settings*. A.A. Balkema, Rotterdam, The Netherlands, 375–392.

Oden, M.I., Igonor, E.E. & Ekwere, S.J. 2011. A comparative study of REE geochemistry in Precambrian pegmatites and associated host rocks from western Oban massif, SE – Nigeria. *Global Journal of Pure and Applied Sciences*, **17**(2), 197–208.

Olade, M.A. 2021. Gemstones of Nigeria: An overview of their geological occurrence, provenance and origin. *Achievers Journal of Scientific Research*, **3**(1), 1–22.

TREATMENTS

Faceted Sapphire Coloured Blue by a Polymer Coating

Recently, a ring was submitted to Guild Gem Laboratories containing a 6.81 ct cushion-cut blue sapphire flanked by triangular colourless diamonds (Figure 24). The colour of the sapphire was quite attractive, showing moderate blue saturation with a light tone. Its RI was 1.762–1.770 (birefringence 0.008), which is consistent with corundum. Microscopic examination revealed colourless and transparent prismatic inclusions, which were identified as apatite by Raman spectroscopy. Blurred blue colour zoning was also observed, along with an expanded discoid fracture, which provided evidence of thermal enhancement. Combined with a chalky blue fluorescence reaction to short-wave UV radiation, the stone appeared to be a heated blue sapphire.

UV-Vis-NIR spectroscopy of the sapphire, however, yielded unexpected results (Figure 25). A prominent broad band was centred at 580 nm, along with a sharp peak at 385 nm, but none of the expected features related to iron or Fe^{2+}–Ti^{4+} intervalence charge transfer were present. The reason for this became clear with close microscopic inspection of the stone's surface, which showed evidence of a coating that had locally chipped off the pavilion near the girdle (Figure 26). The edges of the coating displayed uneven blue colour distribution, and in reflected light we could see a lower lustre for the coated areas compared to the underlying sapphire.

Figure 24: The 6.81 ct sapphire in this ring exhibits an attractive blue hue showing moderate saturation and a light tone. Photo by Huixin Zhao.

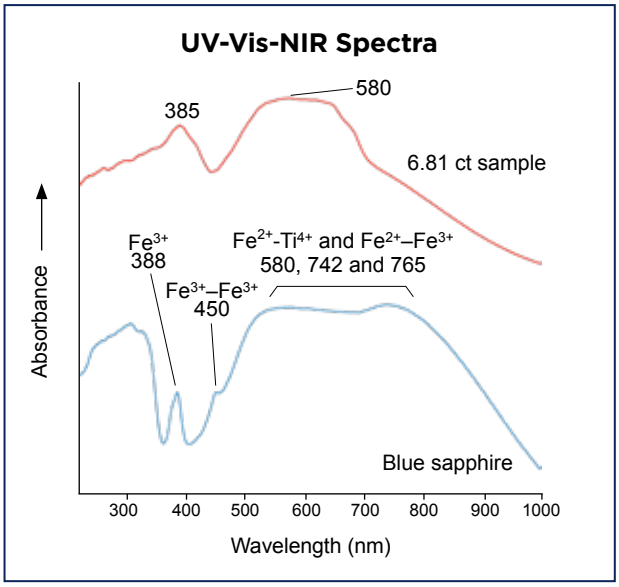

Figure 25: The UV-Vis-NIR spectrum of the 6.81 ct sample shows anomalous features compared to those typically recorded for blue sapphire.

Fourier-transform infrared (FTIR) spectroscopy recorded aspects consistent with corundum, but also revealed prominent features at 2853, 2871, 2926, 2955, 3026 and 3060 cm^{-1} (Figure 27a) that have been attributed to a polymer coating (Lai 2017). In addition, confocal Raman spectroscopy of the coating showed two prominent peaks at 1253 and 1405 cm^{-1} (Figure 27b), consistent with a polymer; the one at 1253 cm^{-1} is related to epoxide vibrations (Vašková & Křesálek 2011). Since the sapphire had no surface-reaching fractures or fissures, the polymer-related features in the spectra must have been due to the coating rather than a filler (i.e. a substance used for clarity enhancement, as is commonly encountered in emerald and aquamarine).

Thus, we identified the blue gemstone in the ring as a heated sapphire with a coloured polymer coating. Although blue sapphires are commonly heated to improve their colour, coating treatments are rarely seen on gem corundum, with only a few cases having

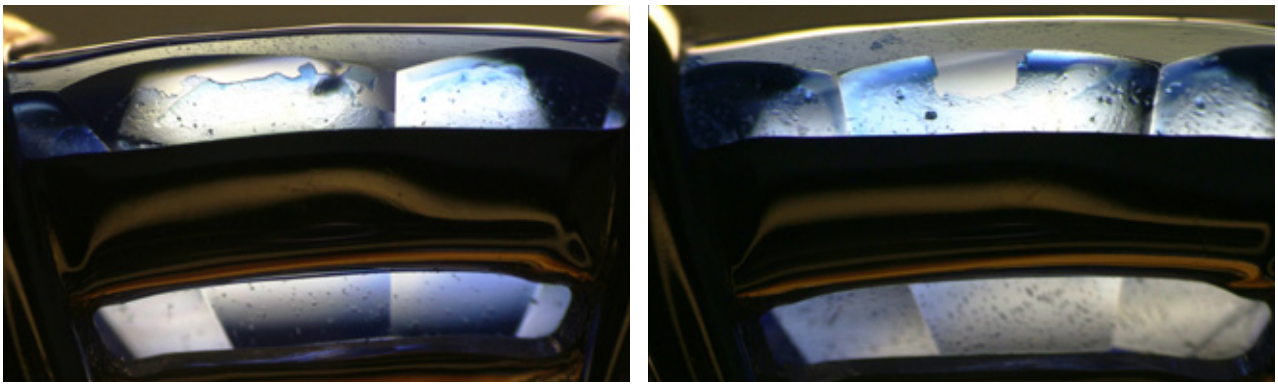

Figure 26: Microscopic examination of the sapphire reveals a blue coating on the pavilion that is locally chipped below the girdle, on both sides of the stone. Photomicrographs by Huixin Zhao; image width 7.35 mm

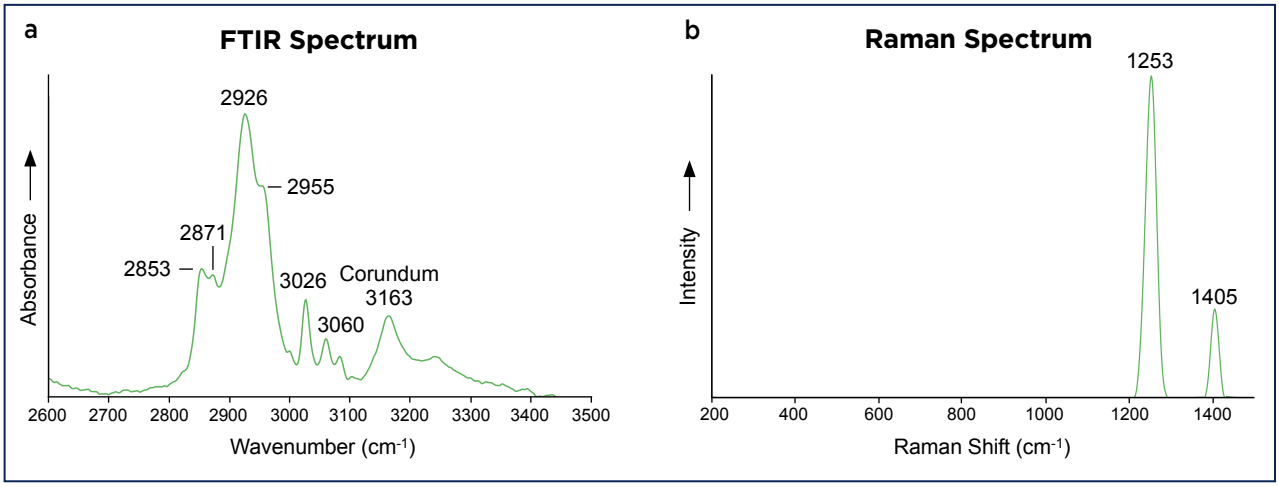

Figure 27: (**a**) The FTIR spectrum of the sapphire displays features associated with a polymer coating at 2853, 2871, 2926, 2955, 3026 and 3060 cm^{-1}. (**b**) Raman spectroscopy of the coating shows two prominent peaks at 1253 and 1405 cm^{-1}, also associated with a polymer.

been reported (e.g. Choudhary 2013; Schneider & Jasso 2019). Such coatings are easy to detect as long as one remembers to check for them.

Yujie Gao, Tiantian Huang (candice.huang@guildgemlab.com) and Yanhua Ni
Guild Gem Laboratories
Shenzhen, China

Chen Zheng
Shenzhen Institute of Technology, China

References

Choudhary, G. 2013. Gem News International: Corundum carving coated with colored polymer. *Gems & Gemology*, **49**(3), 184–185.

Lai, L.T.-A. 2017. Gem News International: Coated beryl imitating emerald. *Gems & Gemology*, **53**(4), 481–482.

Schneider, V. & Jasso, J. 2019. Lab Notes: Cobalt-coated sapphire. *Gems & Gemology*, **55**(3), 421–422.

Vašková, H. & Křesálek, V. 2011. Raman spectroscopy of epoxy resin crosslinking. *13th WSEAS International Conference on Automation Control, Modeling & Simulation (ACMOS'11)*, Lanzarote, Canary Islands, Spain, 27–29 May, 357–361.

MISCELLANEOUS

Mystery Pendant Watch Made by Fabergé?

While conducting an appraisal of an estate containing some stunning pieces of jewellery, this author encountered an intriguing pendant watch (Figure 28). The case contained multicoloured enamelling, tiny rose-cut diamonds and a row of channel-set blue sapphires (Figure 29). The overall shape and winding mechanism were unusual: the watch was wound by rotating the lower half of the case back and forth just like a stem and crown on a wristwatch. The time could be set by pushing a tiny button and again turning the lower half of the case.

Figure 28: This pendant watch (34 × 19 mm) was examined as part of an estate appraisal and is suggestive of Fabergé work. Photo by C. A. Lynch.

Inspection of the watch dial (Figure 30a) revealed a hallmark of Cyrillic lettering (ФАБЕРЖЕ; Figure 30b) that translates to 'Fabergé'. Further examination for Russian hallmarks yielded the Cyrillic initials КФ (for Karl Fabergé) and the initials HW (for Henrik Wigstrom) on the top bail loop (Figure 31). Wigstrom became the senior 'workmaster' for Fabergé in 1903 (Booth 1996), and he presided over the Fabergé workshops during their heyday when thousands of items were produced. Strangely, there were no metal stamps on the opposite side of the bail loop. The pendant watch appeared to be made with platinum, which was confirmed with X-ray

Figure 29: The case of the pendant watch is decorated with enamel, rose-cut diamonds and sapphires. Photo by C. A. Lynch.

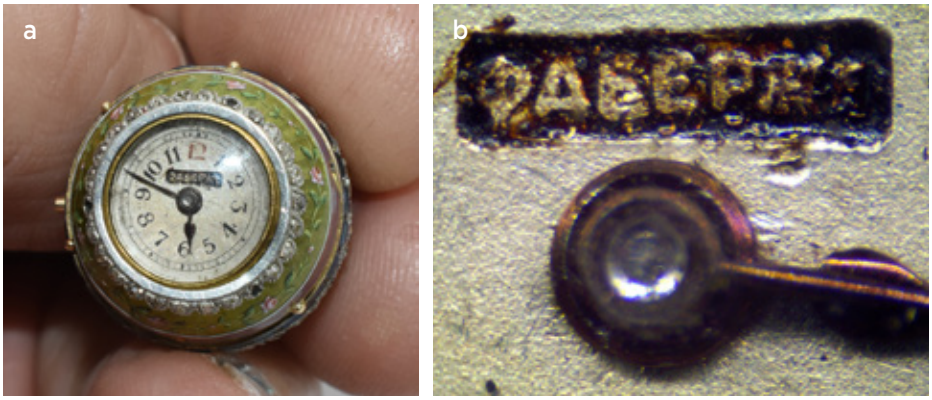

Figure 30: The dial of the watch (**a**) contains a stamp which, at 50× magnification (**b**), can be discerned as Cyrillic lettering that translates to 'Fabergé'. Photos by C. A. Lynch.

fluorescence analysis. Later, a possible reason for the missing metal stamps was discovered: there were no hallmarks for platinum in Russia until 1927 (Whetstone *et al*. 2010).

Upon request, the estate owners provided documentation for the pendant watch in the form of a typewritten letter from the 1960s. The letter detailed how the watch had been gifted to the family and noted its long-standing presence in their lineage. The information appeared credible, adding to the perceived authenticity of the watch as an important Fabergé piece.

However, to confirm this, the author consulted with three Fabergé experts: one who works at a distinguished auction house in London, one in Russia, and another who is a highly regarded watch expert in Europe (all of whom wish to remain anonymous). They were provided with a detailed description and photographs of the pendant watch, and one of the experts also examined it in person. Interestingly, they all concluded that the pendant watch was 'highly unlikely' to be made by Fabergé because the quality of craftsmanship did not match that of a genuine Fabergé piece. They thought it to be Swiss-made in around 1907–1912, when the first 'ball' winding movements were made. They also suggested that the dial and loop bail were replacements added after the watch's original creation. With closer examination (again, see Figures 29, 30b and 31), it is possible to see what the experts were referring to. For example, in the guilloché enamelling on the case, the linear patterns are good but not of the perfection seen on authentic Fabergé pieces. In addition, the dial of the watch is dull looking rather than showing bright enamel work, and the lettering of the name 'Fabergé' is crudely incised into the dial, as opposed to the beautiful black enamel script typically seen on authentic Faberge pieces.

Figure 31: The top bail of the pendant watch carries the stamped letters ΚΦ and HW—presumably for Karl Fabergé and Henrik Wigstrom, respectively. Photomicrograph by C. A. Lynch, magnified 70×.

Although this pendant watch was most likely not manufactured by Fabergé, it is still a fascinating piece and was nevertheless a joy to encounter during an appraisal of this estate.

Craig A. Lynch (craig@ouellet-lynch.com)
Ouellet & Lynch Appraisal Services
Phoenix, Arizona, USA

References

Booth, J. 1996. *The Art of Fabergé*. Wellfleet Press, Secaucus, New Jersey, USA, 192 pp. (see p. 57).

Whetstone, W.B., Niklewicz, D.V. & Matula, L.L. 2010. *World Hallmarks, Volume I: Europe, 19th to 21st Centuries*, 2nd edn. Hallmark Research Institute, 396 pp. (see p. 246).

Banjarmasin Diamond: War Booty from Borneo in Amsterdam

Suzanne van Leeuwen and J. C. (Hanco) Zwaan

ABSTRACT: The 38.23 ct Banjarmasin diamond in the collection of the Rijksmuseum in Amsterdam plays a questionable role in the history of the Dutch occupation of southern Borneo. Confiscated from the Sultanate of Banjarmasin, the original 70+ ct rough diamond arrived in the Netherlands in 1862. This marked the beginning of a 40-year-long political debate on the fate of this former piece of state regalia, as well as consideration of whether or not to cut and sell it. It was eventually faceted in 1870, but efforts to sell it were unsuccessful, and in 1902 it was finally transferred to the Rijksmuseum as a permanent loan from the Ministry of Colonies. Past publications have focused mainly on the colonial history of the diamond, and its properties have not been studied in detail until now. As one of the few large diamonds found in the alluvial deposits of Kalimantan, the results of this study contribute to the recognition of Borneo as an historically small but important diamond source.

The Journal of Gemmology, **38**(7), 2023, pp. 662–677, https://doi.org/10.15506/JoG.2023.38.7.662

The Banjarmasin diamond (Figure 1) is one of the largest diamonds found in southern Borneo (i.e. today's South Kalimantan, Indonesia). It has been in the collection of the Rijksmuseum in Amsterdam since 1902 and is the only unset cut gemstone on permanent display there. It remains a symbol of the controversial history of Dutch colonial rule in this part of modern Indonesia. In its original rough octahedral form, the diamond was considered to have great personal meaning to Sultan Adam Al-Watsiq Billah (Figure 2) and his family (Müller 1839–1844, 1857). The death of the sultan marked the beginning of the Banjarmasin War (1859–1864), a conflict over succession during which the Dutch colonial government decided to dissolve the century-old sultanate (van Rees 1865a, b; Stutje 2022a, b). The diamond and other 'voluntarily' ceded regalia were sent to the Governor-General of Batavia (Jakarta) in June 1860 and, for unknown reasons, the diamond was sent to Amsterdam in December 1861.[1]

When the diamond arrived in the Netherlands aboard the war steamer *Zr. Ms. Ardjoeno* four months later, it merited special mention in local newspapers, and its value was estimated at 400,000 guilders (Anonymous 1862).[2] In the meantime, the Dutch government was not sure what to do with this rough diamond. Plans to offer it to King William III of the

Figure 1: The Banjarmasin diamond (38.23 ct; approximately 21.86 × 17.37 × 13.86 mm) was cut from a 70+ ct octahedral crystal that was confiscated from the Sultanate of Banjarmasin in 1860 and reportedly came from southern Borneo. It currently resides in the Rijksmuseum, Amsterdam (inv. no. NG-C-2000-3), where it is on permanent display. Photo by J. C. Zwaan.

Figure 2: Sultan Adam Al-Watsiq Billah (1782–1857) owned the original rough Banjarmasin diamond. His death precipitated the war that resulted in the transfer of the diamond to the Dutch colonial government. *Portrait of Sultan Adam Al-Watsiq Billah* by Auguste van Pers, circa 1844. Leiden University Libraries, Collection of the Royal Netherlands Institute of Southeast Asian and Caribbean Studies (inv. no. 36A143).

Netherlands (1817–1890), either as a personal gift or as part of the state regalia to be placed in the coronation crown, fell through. One reason was that the cutting costs were deemed too high.[3] Then the diamond was offered to the Museum of Natural History in Leiden, but they declined because it did not fit into their collection and they could not properly secure it.[4] Between 1869 and 1898, three attempts to sell it failed, first in its rough state and later as a cut stone. In August 1902, the Banjarmasin diamond was finally transferred to the Rijksmuseum as a permanent loan from the Ministry of Colonies. The government of the Netherlands is still the official owner today (Stutje 2022b).

Since 2019, the Banjarmasin diamond has been one of the objects under discussion in a research project focusing on the fate of colonial objects in Dutch museum collections. In March 2022, the Rijksmuseum, in collaboration with the NIOD Institute for War, Holocaust and Genocide Studies, and the National Museum of World Cultures, presented the results of this research in an initiative titled 'Pilotproject Provenance Research on Objects of the Colonial Era' (PPROCE; Stutje 2022a, b). With possible restitution claims in mind, the project aims to 'develop a research methodology and make recommendations for the organisation and policy surrounding provenance research into colonial collections' (for further information, see https://www.niod.nl/en/projects/pilotproject-provenance-research-objects-colonial-era-pproce). The Dutch government can use, share and supplement this information in cooperation with foreign governments in case of future restitution claims. The Banjarmasin diamond may become the subject of one of these claims.

Prior to the PPROCE project, much was written on the history of this famous diamond (Brus 1987a, p. 38; Brus 1987b, p. 12; Akkerman 1989; Brus 1989, p. 36; Bari & Sautter 2001, pp. 96–101; Zandvliet 2002, pp. 302–305; Fleet 2005, p. 27; Balfour 2009, pp. 44–45; Drieënhuizen 2017), but a gemmological study had never been conducted. The diamond is not only important for its role in colonial history but also from a material point of view, as it is one of the few historical examples of large diamonds found in Borneo. In addition, the way the Banjarmasin diamond looked before and after it was cut greatly affected its (historic) value and the way it was treated by the Dutch government. The first part of the present article focuses on sources that describe the rough diamond and the cut gem. Until recently it was unknown when, where and by whom the diamond was cut, but the PPROCE project

[1] The other regalia were transferred to the Royal Batavian Society of Art and Sciences as 'archaeological rarities'. They were listed in an 1868 catalogue (Norman 1868, pp. 95–98) and are now part of the collection of the National Museum of Indonesia in Jakarta (Stutje 2022a, b).

[2] Equivalent to a current value of about EUR4.5 million.

[3] As reported in The Hague, National Archives (NL-HaNA), Ministry of Colonies 1850–1900, accession number 2.10.02, inv. no. 1158, 10 March 1862, no. 6, minutes 10-6, p. 4. In the accompanying minutes and correspondence between the Minister of the Colonies and the Governor-General of Batavia, the Koh-i-Noor diamond was briefly mentioned in comparison with the Banjarmasin diamond. The Koh-i-Noor was 'a feat of the British Indian Army' (*eene hulde van 't Brits-Ind. Leger*) and therefore was placed under the state regalia. According to the Dutch government, the same applied to the way the Banjarmasin diamond was acquired.

[4] Indicated in a letter from the Minister of Internal Affairs to the Minister of the Colonies (NL-HaNA, Ministry of Colonies 1850–1900, accession number 2.10.02, inv. no. 1272, 3 December 1862, no. 23); see also Stutje (2022a, p. 9).

Figure 3: This map of the Banjarmasin–Martapura region of South Kalimantan shows the location of the diamond mining areas of Karang-intan and Goenong Lawak. The inset image (adapted from Wikimedia Commons) shows the positions of the two main diamond-mining regions on the island of Borneo.

yielded valuable new information. The second part of this article then focuses on the stone's gemmological properties and their consistency with the assumed Borneo origin of the Banjarmasin diamond.

HISTORY

Borneo Diamonds

The diamond deposits of Borneo are, together with the Indian deposits, the earliest worked diamond mines in the world. On the island, diamonds have been found at two main localities: the Martapura area of South Kalimantan and the Landak District of West Kalimantan (Spencer *et al.* 1988; see also Figure 3). The Dutch first came into contact with diamonds from Borneo in the early seventeenth century (Content 2020). Following in the footsteps of Chinese and Portuguese traders, the Dutch East India Company (*Verenigde Oostindische Compagnie* or VOC) brought back a small quantity of these diamonds from their first voyage to Asia in 1604 (Ikuko 2010). They acquired the stones from Succadana (or Sukadana), a diamond-trading centre in western Borneo, where both the VOC and the British East India Company established a trading post ('factory') soon after (Ogden 2005, 2018). While the British East India Company focused on the Indian diamond mines, the Dutch traders purchased 400–500 carats of rough Kalimantan diamonds yearly between 1610 and 1615. In 1620, they sent more than 1,000 ct of diamonds back to Amsterdam.[5]

[5] See Ikuko (2010), pp. 169–172. After 1620, the VOC ventured into India, where it purchased small quantities of diamonds from Kollur, the Coromandel Coast and Surat. After the 1660s, the Dutch diamond trade with India started to decline, and although the Dutch continued to import Indian diamonds, by the eighteenth century the trade was no longer significant (see Ikuko 2010, p. 183).

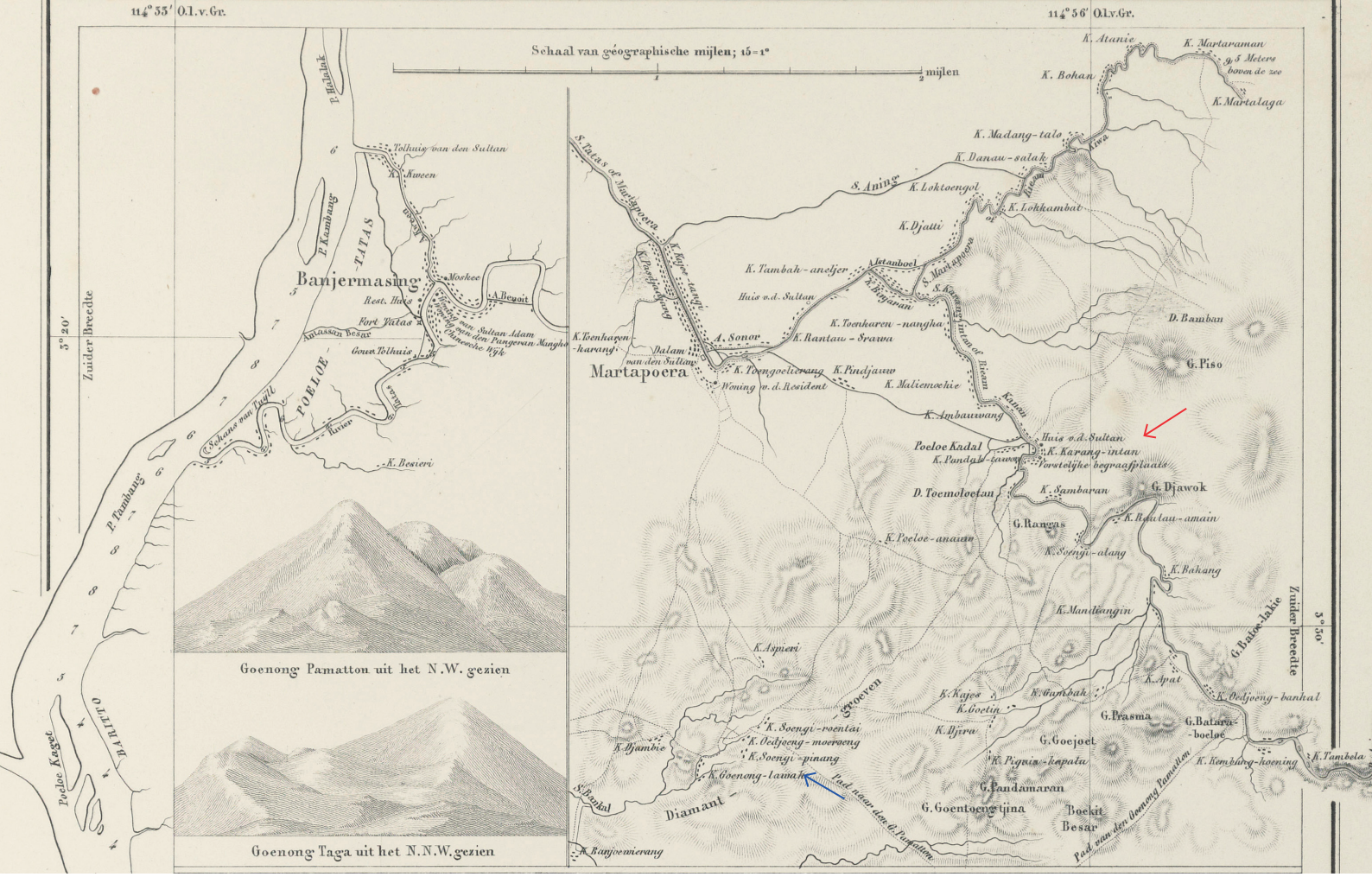

Figure 4: This map of the Banjermassing (Banjarmasin) and Martapoera (Martapura) areas appeared in a book by Müller (1839–1844; on p. 590 of the downloadable PDF file), and covers approximately the same area shown in Figure 3. The diamond localities of Karang-intan and Goenong Lawak are indicated by the red and blue arrows, respectively.

The Rough Banjarmasin Diamond

In September 1829, an unnamed Dutch resident of the town of Banjarmasin travelled upstream to Martapura (Figure 4) to visit the official residence, or *kraton*, of the Sultanate of Banjarmasin and the diamond quarries in that area.[6] The detailed account of his journey describes a moonlit trip on a narrow boat with 30 rowers that took him and his fellow travellers inland with the help of the incoming tide (Anonymous 1829). After arriving in Martapura the next morning, they were taken to the diamond quarries, where they saw 'yellow clay' being washed in wooden troughs/basins in search of diamonds (Figure 5), still a familiar sight in modern Martapura.[7] The next day, the group visited Sultan Adam who, for the occasion, showed them the biggest 'brilliant' ever found in the open-pit mines of this region.[8] Reportedly, a narrow golden band enclosed a 77 ct rough diamond that the sultan would wear on a simple black cord around his neck during festivities (Anonymous 1829).

This account is the earliest of several nineteenth-century sources describing a diamond in the possession of Sultan Adam that seem to refer to the rough Banjarmasin. Other descriptions were published in newspapers and in travel accounts of scientists and explorers visiting the sultanate (Anonymous 1833; Korthals 1836, 1837; Anonymous 1838; Müller 1839–1844; Teenstra 1852a, pp. 442–452; van Rees 1865a, p. 28). Some details vary in the accounts prior to 1848, including the weight, but we believe all these refer to one and the same diamond, the Banjarmasin. However, these sources must be used with some caution because the Banjarmasin was not the only large diamond owned by the royal family.[9] Publications

[6] Other diamond quarries were located at Goenong Lawak to the south of Martapura (Figure 4, blue arrow). This area corresponds to the modern Cempaka diamond fields in the Martapura region.

[7] This 'yellow clay' refers to the layer above the quartz-rich conglomerate that contained most of the diamonds. For a detailed historic description of the diamond mining along the river, see Schwaner (1853, pp. 61–69).

[8] The term *brilliant* was used frequently in nineteenth-century Dutch sources to describe diamonds in general.

[9] In preparing this article, preliminary information came to light that perhaps more large Borneo diamonds found their way to the Netherlands via Jakarta in this period. Whether they have a direct relation to the Sultanate of Banjarmasin remains to be investigated.

Figure 5: Local inhabitants search for diamonds in the Martapura area, as depicted in J. C. Rappard's *Delving for Diamonds Along the Sungai Lawak River*. Colour lithograph from Perelaer (1888, see plate between pp. 132 and 133).

after 1848, for example, mention a (rough) diamond larger than 100 ct (Bleckmann 1850; Teenstra 1852b, p. 831). W. A. van Rees, a former major in the Dutch colonial army, also mentioned a 120 ct diamond as part of the regalia (van Rees 1865a, p. 28). In a region that, in the middle of the nineteenth century, apparently still regularly produced diamonds above 5 ct (Müller 1843, p. 13)[10], a regular-shaped octahedron weighing 70+ ct was still exceptional and one of the reasons why it is described as the sultan's most prized possession (Müller 1839–1844, 1857; Zandvliet 2002, pp. 302–305).[11] The fact that this diamond was mentioned in numerous independent sources, despite discrepancies in the colour of the cord or the exact weight, illustrates its importance. Oral descriptions, non-standardised diamond weights and eyewitness accounts of people with no diamond expertise help explain some of the inconsistencies. That being said, because no drawings or photographs of the diamond are known to exist before 1898, these eyewitness accounts are a valuable source of information about the appearance of the rough diamond.

The first description to mention the shape of the rough diamond was written by German zoologist Salomon Müller (1804–1836).[12] In the 1820s and 1830s, he and a group of other European naturalists travelled through the Dutch East Indies on behalf of the 'Committee for Natural History of the Netherlands Indies' to collect specimens of local flora and fauna (Weber 2019). In 1836, his last stop before returning to the Netherlands was the south-east part of Borneo, where he and two colleagues spent 4½ months. A few days after their arrival in the town of Banjarmasin, they travelled upstream to Martapura and visited Sultan Adam. Müller was intrigued by the dilapidated state of the residence and, at the same time, the portable wealth that was displayed by the royal family (Müller 1839–1844, pp. 419–420; Müller 1857, pp. 268–269). Around his neck the sultan wore two pieces of jewellery, a gold medal set with diamonds and an almost regular octahedron that Müller reported weighing 77 ct which was suspended on a simple cord.[13]

One of the colleagues accompanying Müller in Borneo was the Dutch botanist P. W. Korthals (1802–1897). Previously unpublished parts of his diary from August 1836 and a short article from a year later describe his visit with Sultan Adam (Korthals 1836, 1837).

[10] Officially, diamonds above 5 ct had to be ceded to the sultan and his family for a small compensation.

[11] According to Max Bauer (1904, p. 219), the Malay considered regular octahedra as 'the perfect stones' because they required little or no cutting.

[12] In past publications, this account was often cited as the first nineteenth-century source mentioning the Banjarmasin diamond.

[13] The gold medal was presented to Sultan Adam by Governor-General of the Dutch East Indies, J. van den Bosch (1780–1844), as a token of their alliance. The medal was inscribed in Malaysian and Dutch: *Het Nederlandsche Gouvernement aan zijnen getrouwen bondgenoot den Sultan van Banjermassing* ('The Dutch Government to its faithful ally the Sultan of Banjermassing'. See Müller 1839–1844, p. 420; Müller 1857, p. 269).

Korthals' diary describes both the sultan's clothes and the diamond in detail. He mentioned that the sultan was a man of 'normal' size, tastefully dressed in green silk trousers, with gold galloon on the seams and a white vest set with diamond buttons increasing in size near the neckline. His yellow headscarf was 'folded curiously with at least a dozen points' (see Figure 2).[14] He wore multiple finger rings set with gemstones, and diamond studs in his ears, and Korthals also described the gold medal set with diamonds.[15] The sultan's eldest son and heir to the throne, Abdul Rachman (1825–1852), was sitting next to him on a chair covered with yellow silk. He wore a yellow headscarf with a silver galloon trim, white trousers and a black velvet *samaar* (tabard) decorated with flowers in gold thread. Korthals described three diamonds *aan de hals* (on the neck) of the *sultan moeda* (sultan's son), one of which was a 40 ct *cut* diamond.[16]

After 'lukewarm and weak tea accompanied with local pastry', Sultan Adam showed Korthals and his colleagues the diamond, reported as weighing 76 ct (Korthals 1836).[17] The fairly regular octahedral-shaped diamond was colourless, and through one of its faces Korthals spotted some black dots. Colour-wise he called the stone 'pure'. He further wrote that, although the four sides of one part of the octahedron were fairly uniform, the other part was not in perfect condition, since the point was broken off and one of the sides was damaged.[18] On the damaged side, Korthals (1837) reported, was a little hole, probably used for fixing the thin gold band that surrounded the rough diamond.[19] An 'emerald'-coloured piece of string was attached to the gold band, which allowed the sultan to wear the diamond as a necklace. The stone was reportedly found during the reign of Sultan Adam's father, Sultan Sulaiman Saidullah (1761–1825), in the 'mines' of Karang-intan (Figures 3 and 4).[20]

After Sultan Adam died in November 1857, he was succeeded by his grandson, Tamdjiddillah al-Watsiq Billah (1817–1867), the first son of the deceased crown prince Abdul Rachman (Stutje 2022a, b). His installation marked the beginning of a period of political and social turmoil that would eventually lead to the Banjarmasin War. In June 1859, Tamdjiddillah resigned under heavy pressure from the Dutch government, and he surrendered the regalia of the Sultanate of Banjarmasin, including the diamond, shortly thereafter. Sometime in the following year the regalia were transported to the civil warehouses in Batavia. In July 1861, they were offered to the Bataviaasch Genootschap (Royal Batavian Society of Art and Sciences)[21], except for the diamond that would sail to the Netherlands a few months later. [22]

Arrival in Europe and Cutting

The first 'official' examination of the rough Banjarmasin took place on board the war steamer *Zr. Ms. Ardjoeno*, two days before the ship left the port of Batavia on 16 December 1861. A Muslim diamond expert, Said Adbulla Alaijderves, determined a weight of 70 ct for the gem in its setting, which he described as *in zilver gevatten steen of ruwen diamant* ('stone or rough diamond set in silver'; Figure 6).[23] Apparently nothing was recorded about the form of the rough. The diamond was then wrapped in paper and sealed in a yellow palm-wood

[14] In Dutch: *Zijn geele hoofddoek was op eene zonderlinge wijze gevouwen en had zeker een tiental punten* (Korthals 1836, p. 60).
[15] Sultan Adam told Korthals that this medal was set with diamonds because it was *Soeka Sa(e)kili* (he liked it very much; Korthals 1836, p. 61).
[16] This cut diamond, which was worn by the son of the sultan (*sultan moeda* or *pangerang Ratoe*), is not mentioned in any of the other nineteenth-century sources (Korthals 1836, p. 61).
[17] A year later, Korthals described the diamond as a 72 ct octahedron (Korthals 1837, p. 245).
[18] In Dutch: *Hij is een vrij regelmatige octaëder, waar van de 4 hoekig goed uitloopen, de andere vierhoek is daarentegen onregelmatiger door het afbreken der punt en eene zijde der 4. kanten, hier is ook een klemgaatje in denzelven, en aan der punten ziet men een zwart vlekje; de steen is wat de kleur aangaat zuiver. Hij is gevat tusschen een gouden vatsel die de kanten bedekken en hangt daardoor aan een smarag pennenkoord, hetwelk de plaats van ketting bekleed* (Korthals 1836, diary entry 7 August).
[19] In Dutch: *een tamelijk regelmatige achthoek met een gaatje aan een der kanten* (Korthals 1837, p. 245).
[20] Korthals wrote that the diamond was a *prosakka* (*pusaka* or *poesaka*) of Sultan Sulaiman. This term refers to specific objects that have a strong bond with the family ancestors and are considered valuable heirlooms (Korthals 1836, p. 62). The mines of Karang-intan are situated on the right side of the map in Figure 4 (see red arrow), between 'a house of the sultan' (*Huis v.d. Sultan*) and the royal cemeteries (*Vorstelijke begraafplaats*).
[21] See Bestuursvergadering, 13 July 1861 (van der Chijs 1862, pp. 122–125).
[22] It was proposed that the Minister of the Colonies should gift the diamond to the Dutch King William III (1817–1890) as an ornament for his crown (Stutje 2022a, p. 349).
[23] NL-HaNA, Colonies, 1850–1900 (2.10.02), inv. no. 1158, 10 March 1862, proceedings of 14 December 1861.

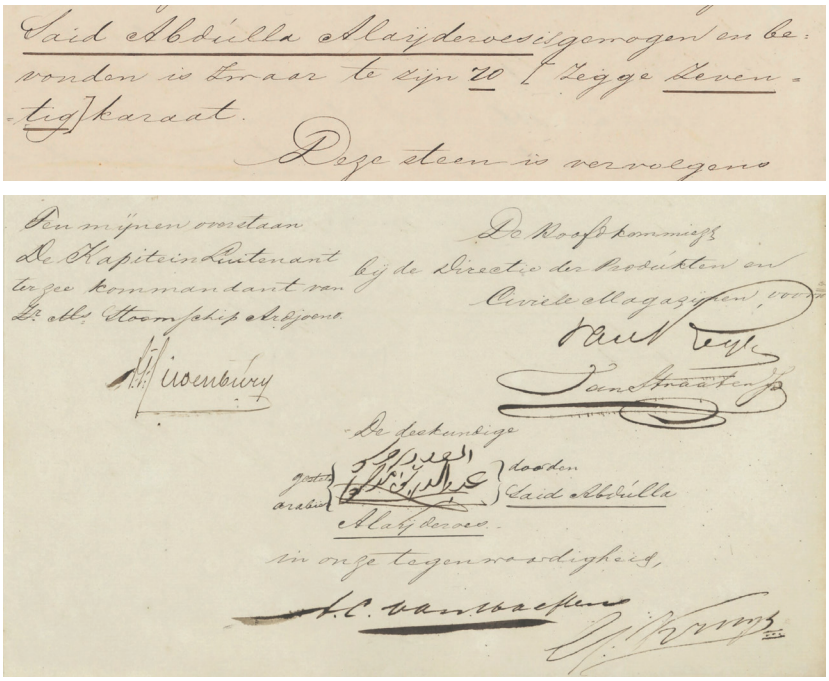

Figure 6: A signed document from 14 December 1861 mentions a weight of 70 ct (top image) and also describes the Banjarmasin as a 'stone or rough diamond set in silver'. The document bears the names and signatures of the Muslim diamond expert Said Abdulla Alaijderves, Captain A. F. Siedenburg and two officials of the warehouse in Batavia (bottom image). From NL-HaNA, Colonies, 1850–1900 (2.10.02), inv. no. 1158, 10 March 1862, proceedings of 14 December 1861.

box. Upon arrival at the Ministry of Colonies in The Hague in April 1862, the diamond was unpacked to be authenticated, after which it remained there for another two years. In February 1864, Amsterdam diamond broker Emanuel Vita Israel (1831–1915) examined and weighed the stone (recording 69⅞ ct) before it was transferred to De Nederlandsche Bank in Amsterdam.[24]

It took another five years before a decision was made to sell the diamond, and in October 1869 the Nederlandsche Handel-Maatschappij (Netherlands Trading Society or NHM) valued the Banjarmasin at 300,000 guilders (a devaluation of 100,000 guilders over seven years). NHM, which specialised in trading colonial products from the Indies, was asked to suggest the best way to sell the diamond without disclosing from whom and how the Ministry of Colonies had acquired it.[25] Amsterdam jewellers Benten & Zonen sent a clear message to NHM: because of the diamond's rough form and its imperfect clarity, they did not expect an offer of more than 100,000 guilders. In fact, they suggested aiming for a sale price of 70,000–80,000 guilders.[26] Benten & Zonen was unable to secure any serious offers in the following months, and in May 1870, Meijer Moses (Martin) Coster (1818–1880), director of Coster Diamonds in Paris, France, advised the ministry to have the diamond cut.

The stone was sent to Abraham Eliazer Daniels (1801–1880) and his son, Alexander Daniels (1832–1911), managing directors of Coster Diamonds in Amsterdam (Figure 7).[27] This company was responsible for the cutting of the Koh-i-Noor and the Star of the South diamonds in, respectively, 1852 and 1856–1857 (Smith & Bosshart 2002). By August 1870, the Banjarmasin had been faceted into a modified Old Mine cut of 37⅜ ct. However, NHM wrote to the ministry that the diamond did not show a 'clear brilliance', as expected, but instead had a yellowish tint.[28] This would have a negative influence on its value, which NHM lowered to 45,000 guilders.[29] With its financial gain diminished, the Banjarmasin diamond was then described as 'a valuable memorial of an important event in the history of the Dutch East Indies' and put back in the safe of NHM.[30]

[24] NL-HaNA, Colonies, 1850–1900 (2.10.02), inv. no. 1441, 22 February 1864, no. 9, minutes of transfer from the Ministry of Colonies to the Dutch national bank.
[25] NL-HaNA, NHM, 2.20.01, inv. no. 428, minutes of the board meeting, no. 72, 8 October 1869.
[26] NL-HaNA, NHM, 2.20.01, inv. no. 428, minutes of the board meeting, no. 93, 20 December 1869.
[27] NL-HaNA, NHM, 2.20.01, inv. no. 428, minutes of the board meeting, no. 27, 9 May 1870, and NL-HaNA, Colonies, 1850–1900 (2.10.02), inv. no. 6010, minutes of 6 May 1870 E5.
[28] In Dutch: *een min of meer geelachtigen tint, die van nadeeligen invloed is op de waarde van het juweel*.
[29] NL-HaNA, Colonies, 1850–1900 (2.10.02), inv. no. 6013, letter from NHM to the Minister of Colonies, 27 August 1870.
[30] In Dutch: *a kostbaar gedenkteeken van een belangrijke gebeurtenis in de geschiedenis van Nederlands-Indië*; NL-HaNA, Colonies, 1850–1900 (2.10.02), inv. no. 2779, minutes of 21 April 1875, no. 19.

Figure 7: The Coster diamond factory on the Amstel River in Amsterdam (depicted here) was where the rough Banjarmasin diamond was faceted into a modified Old Mine cut in 1870. *Amstel 1-13*, watercolour on paper in 1852 by Cornelis Springer (1817–1891); Amsterdam city archives (inv. no. 010097015145).

Early Display and Documentation

Although it is often stated that the cut Banjarmasin diamond was first shown to the public after its transfer to the Rijksmuseum in 1902, it seems that it was put on public display almost 20 years earlier. In 1883, Amsterdam hosted the International Colonial and Export Exhibition at what is now the Museumplein. In addition to displays showcasing 'marvels' from the Dutch colonies, there were pavilions to impress the international visitor with the splendour of Amsterdam's industries. Its renowned diamond-cutting industry was showcased in its own pavilion close to the main building (Figure 8). The diamond exhibition was extensively covered by Dutch newspapers after the exhibition's opening in May 1883. In one detailed review, specific mention is made of a 'beautiful brilliant from Borneo weighing 37½ carats' that was loaned by NHM for the showcase of diamond broker Emanuel Vita Israel (Anonymous 1883), who had examined the Banjarmasin almost 20 years earlier and knew of NHM's involvement. Because there are no images of the pavilion's interior or its showcases, we do not know the context in which the diamond was displayed, although it is probably safe to assume the Sultanate of Banjarmasin was not mentioned as its previous owner.

The first known photographs of the Banjarmasin diamond date from 1898 and were included in a Dutch auction catalogue (Figure 9). The auction was organised by Emanuel Vita Israel and his brother. The catalogue lists the Banjarmasin as the first lot and describes it as *Un Brilliant ancient, qualité supérieure, provenant des mines de Bornéo* (Henriques de Castro *et al*. 1898). Its weight was listed in both carats ($37^{7}/_{32}$) and grams (5.450), and three photographs illustrated different views of the diamond. In previews of the 23 March event, to be held at auction house De Brakke Grond, advertisements in Dutch newspapers raised awareness of the various diamonds, pearls and other pieces of jewellery that were to be offered. Although most of the announcements were rather general, one from the 23 January 1898 edition of the *Algemeen Handelsblad* specifically mentions a 'Borneo brilliant' of 39 ct, presumably the Banjarmasin (Anonymous 1898, p. 12; see Figure 10). Despite these efforts, the diamond once again failed to be sold. Emanuel Vita Israel kept the Banjarmasin until August 1902, when it was transferred as a permanent loan to the Rijksmuseum, although it was not properly registered until the year 2000 (Stutje 2022b).

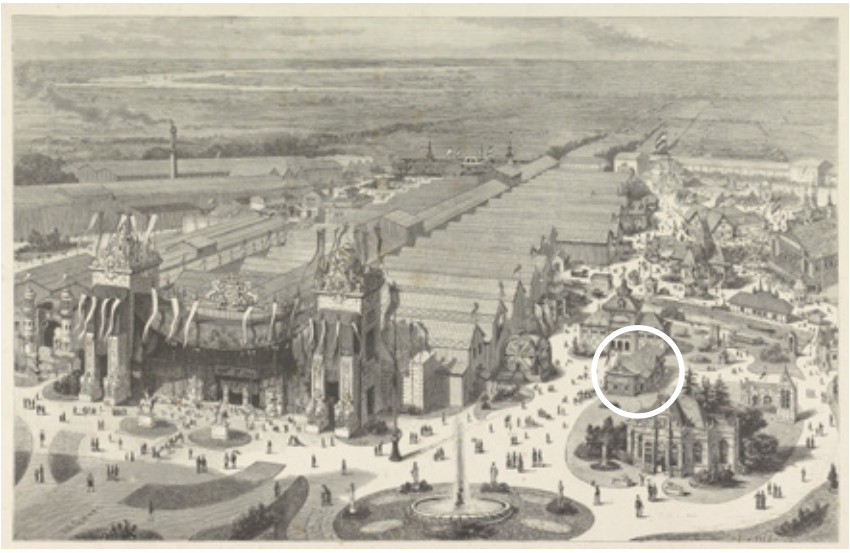

Figure 8: At the 1883 International Colonial and Export Exhibition in Amsterdam, the Banjarmasin was displayed in a pavilion where the diamond-cutting industry of Amsterdam was showcased (circled building). *The International Colonial and Export Exhibition in Amsterdam in 1883*, woodcut by E. & A. Tilly after Johan Conrad Greive, 1883, Rijksmuseum, Amsterdam (inv. no. RP-P-OB-89.774).

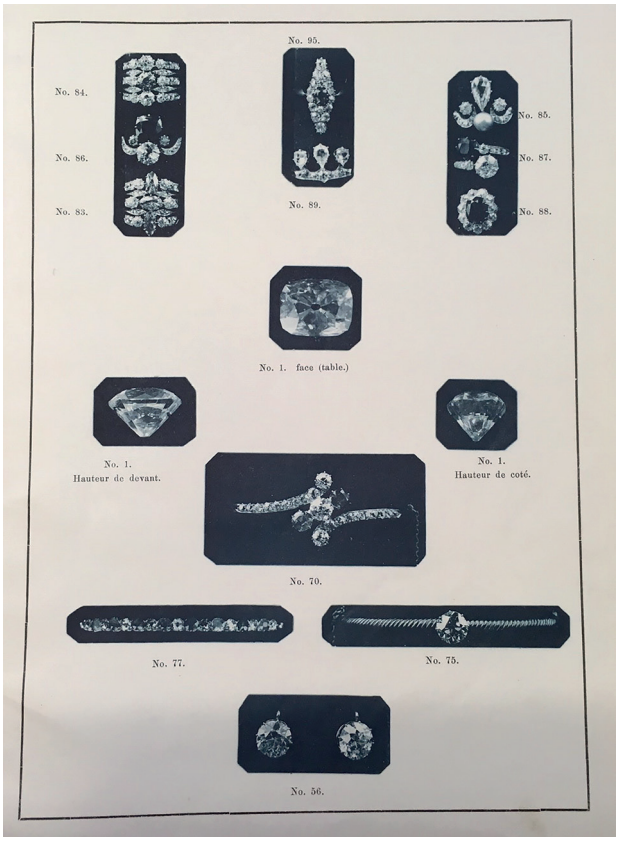

Figure 9: The Banjarmasin diamond is listed as item no. 1 in three views on this page from the *Catalogue d'une très belle Collection de Diamants, Bruts et Taillés, Perles et Pierres de Colours...* at De Brakke Grond on 23 March 1898 (Henriques de Castro *et al.* 1898). The diamond failed to sell at the auction.

METHODS

Analyses of the Banjarmasin diamond took place at both the Rijksmuseum and the Netherlands Gem Laboratory, and included standard gemmological testing, ultraviolet-visible-near infared (UV-Vis-NIR), Fourier-transform infrared (FTIR) and Raman spectroscopy, and DiamondView imaging. The colour was graded using a CIBJO master stone set of round brilliant-cut diamonds and a Dialite Pro daylight-equivalent fluorescent lamp (6500 K). Internal features were observed with a standard gemmological microscope, a Hirox Digital Microscope KH-7700 and a Nikon Eclipse E600 POL polarising microscope.

Inclusions were analysed by Raman spectroscopy using a Thermo DXR Raman microscope with 532 nm laser excitation. Raman spectra were collected in confocal mode to enable analyses of individual inclusions on a micron scale (1–2 µm).

Mid-IR spectra were obtained with a Thermo Nicolet iS50 FTIR spectrometer. UV-Vis-NIR absorption spectra were collected with a Thermo Scientific Evolution 600 spectrometer in the 280–850 nm range.


VOORLOOPIG BERICHT.

De Makelaars **VITA ISRAËL** zullen in **de 2de helft der maand Maart** e. k. in het Lokaal *DE BRAKKE GROND*, ten overstaan van de Notarissen Mr. J. F. **WERTHEIM** en **POLLONES & SMITS** in veiling brengen:

Eene Partij **losse** en **gezette Diamanten, Paarlen** en **gekleurde Steenen,** waaronder uitmunten: een zeldzaam groote en heldere, geslepen **oude Borneesche Brilliant van ongeveer 39 karaat,** Paarlen Colliers, met Brillanten en Diamanten bezette Broches, Oorringen, Ringen, Horloges etc. etc. (1555)

Figure 10: A newspaper announcement of the March 1898 auction at De Brakke Grond (see Figure 9) mentions a 'rare and clear cut old Borneo brilliant of approximately 39 carats'—presumably the Banjarmasin diamond—being offered along with other pieces of jewellery. From Anonymous (1898, p. 12).

Long- and short-wave UV lamps were used in a darkened room to observe luminescence, and growth patterns were observed with a DiamondView fluorescence imaging instrument, which uses ultra-short-wave UV radiation (< 230 nm).

RESULTS

The properties of the Banjarmasin diamond are summarised in Table I. It weighs 38.23 ct and is faceted as a modified Old Mine cut, with ten bezel facets on the crown and ten pavilion facets (Figures 1 and 11), instead of the usual eight bezel and eight pavilion facets. (On the long sides of the diamond there was enough space to add extra facets to improve its sparkle and brilliance.) Apart from the typically high overall depth and large culet, the stone has a fairly large table as compared to the usually small table of an Old Mine cut. The outline of the diamond is sharp with a thin, faceted girdle. Three naturals are present: one on the girdle (Figure 12) and two on the edges of two bezel facets.

Table I: Properties of the Banjarmasin diamond.

Weight	38.23 ct
Measurements	21.86 × 17.37 × 13.86 mm
Colour	E (exceptional white)
Clarity	SI_2
Cut	Modified Old Mine cut
Depth	79.8%
Table	59%
Symmetry	Good
Polish	Good
Girdle	Faceted, where present
UV fluorescence	Very weak blue (long-wave) or inert (short-wave)
Phosphorescence	None
Diamond type	IaAB

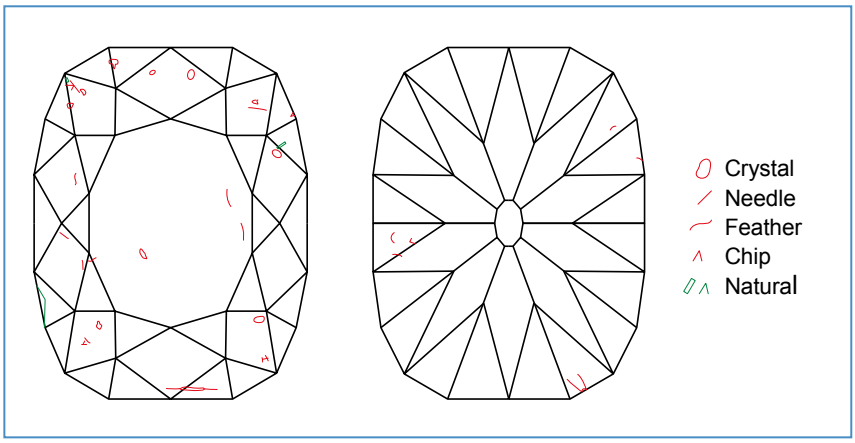

Figure 11: A schematic drawing of the Banjarmasin diamond (modified Old Mine cut) shows ten bezel facets on the crown and ten pavilion facets on the pavilion. A plot of major internal (red) and external (green) features illustrates why it received a clarity grade of SI_2.

The E colour grade (also known as 'exceptional white') was determined by viewing the diamond table down, through the pavilion, at different angles, but especially with its long and short axes at about 45° to the observer. The stone was oriented in this way so that its outline most closely resembled that of the round-brilliant master stones and showed the best visual 'average' for the amount of colour observed (cf. King *et al.* 2008).

Numerous dark inclusions were easily visible to the unaided eye. A schematic plot of the most prominent inclusions reflects their relative size and position (again, see Figure 11). Comparing the sizes of the inclusions and their reflections to the size of this diamond, and relating these characteristics back to a smaller, more average-sized diamond (e.g. 1 ct), we assigned a clarity grade of SI_2.

Many of the dark inclusions were needle-like and oriented in specific directions (Figure 13), which appear to be largely controlled by the octahedral growth of the host diamond. Also observed were transparent colourless inclusions associated with stress haloes that were filled with a black material (Figure 14). The colourless inclusions were identified as forsterite (olivine) by Raman micro-spectroscopy. Because the Raman signal of the host diamond was very strong, the spectral features of these inclusions were barely visible. But by scanning specifically in the 1000–600 cm^{-1} range, the characteristic spectral features of forsterite became apparent (Figure 15). The black inclusions could not be identified by Raman micro-spectroscopy.

FTIR spectroscopy yielded features consistent with those of type IaAB diamond (Figure 16). Strong absorption in the 1300–1100 cm^{-1} region indicated the presence of both A centres (a pair of nitrogen atoms substituting for carbon atoms, producing a peak at 1282 cm^{-1}) and B centres (a carbon vacancy surrounded by four nitrogen atoms, substituting for carbon atoms, causing a peak at 1175 cm^{-1}). A strong platelet peak (caused by extended planar defects in {100} lattice planes, consisting of arrays of carbon interstitials) was present at 1367 cm^{-1}, and a minor peak at 3107 cm^{-1} was related to the presence of hydrogen (cf. Collins 1982, 2001, 2003; Goss *et al.* 2003). The spectrum also contained a small feature at 1522

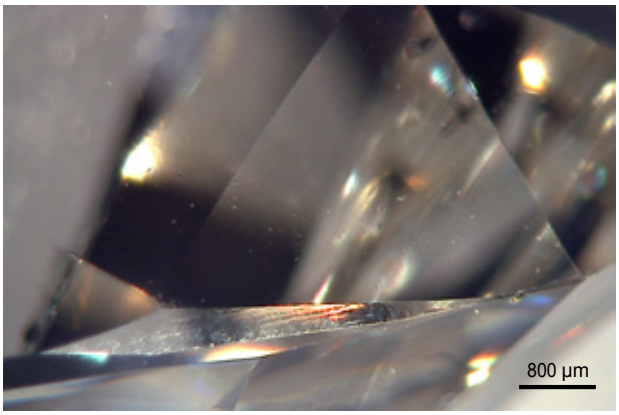

Figure 12: One of the naturals on the Banjarmasin diamond is located along a thin, faceted portion of the girdle. In many places, the girdle is absent and the crown-pavilion junction is razor sharp (see right-hand side of this image). Photomicrograph by J. C. Zwaan.

Figure 13: Many black needle-like inclusions are present in the Banjarmasin diamond, and they are commonly oriented in specific (mainly octahedral) directions. Photomicrograph by J. C. Zwaan.

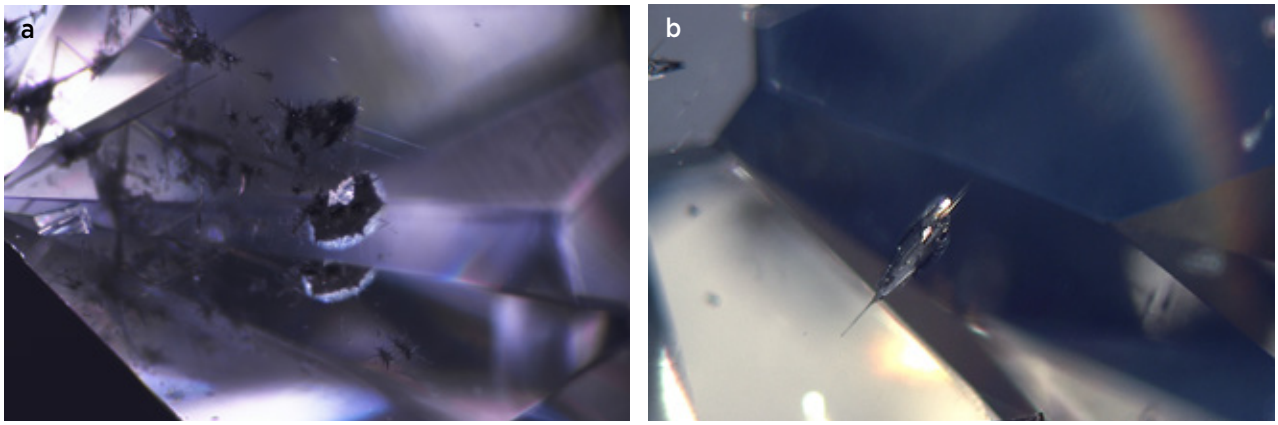

Figure 14: Colourless, transparent olivine inclusions in the Banjarmasin diamond display surrounding stress haloes filled with a black material. Photomicrographs by J. C. Zwaan; image widths (**a**) 3.7 mm and (**b**) 6.6 mm.

cm^{-1}, which is occasionally detected in natural untreated diamonds (e.g. Dobrinets *et al.* 2013).

UV-Vis-NIR spectroscopy showed an absorption edge at 325 nm and a peak at 415 nm due to N3 centres (three nitrogen atoms surrounding a vacancy; cf. Collins 1982; Figure 17). The 415 nm peak and the related absorption near 380 nm only attained approximately 0.9 absorbance unit, which is very weak, and with no typical cape absorption at 478 nm, virtually no yellow colouration was present (i.e. E colour grade). So, like most gem diamonds (cf. Anderson & Payne 1998), the Banjarmasin contains a mixture of A and B centres, together with a low amount of N3 centres that is just a fraction of the concentrations of A and B centres.

Fluorescence to long-wave UV radiation was very weak blue, and the stone was inert to short-wave UV. The long-wave UV fluorescence appeared patchy when viewed from the pavilion (Figure 18). DiamondView imaging clearly revealed the diamond's growth patterns (Figure 19), with blue luminescence. A complicated growth structure was visible in the core, surrounded by regular octahedral growth zones. The core area generally fluoresced only slightly stronger blue. The contact between the core area and the outer zone appeared jagged due to resorption after an early growth phase (cf. Wiggers de Vries 2013). Small displacement zones or slip lines (at left in Figure 19) indicate plastic deformation during an episode of later octahedral growth. Viewed from the pavilion side, mainly octahedral growth zones could be observed, with the same core structure near the culet as seen from the table side.

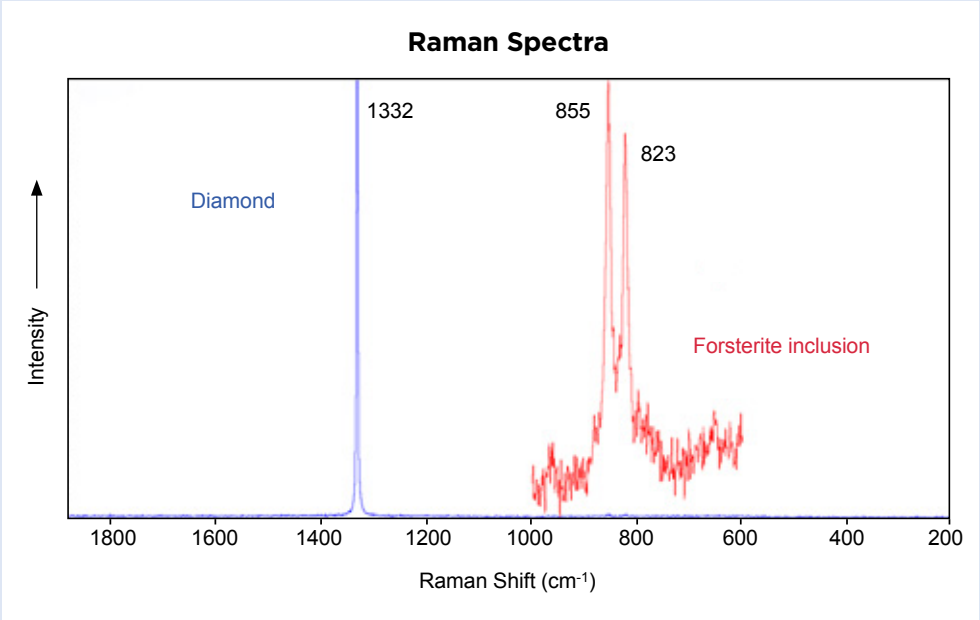

Figure 15: The strong Raman signal of the host diamond at 1332 cm^{-1} makes the features of an analysed inclusion difficult to detect (blue trace). Scanning the specific region between 1000 and 600 cm^{-1} makes the forsterite spectrum more apparent (red trace).

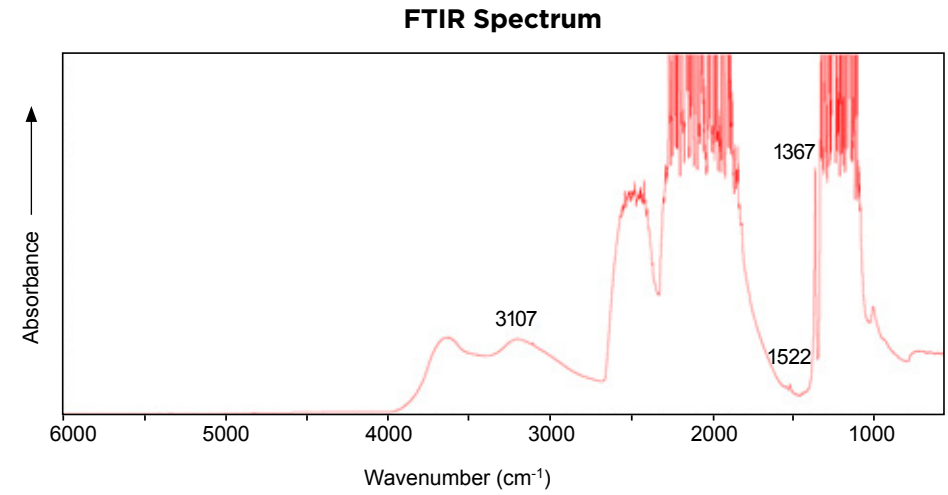

Figure 16: The FTIR spectrum of the type Ia Banjarmasin diamond supports the presence of a mixture of A and B centres in the 1300–1100 cm^{-1} region, along with a strong platelet peak at 1367 cm^{-1}.

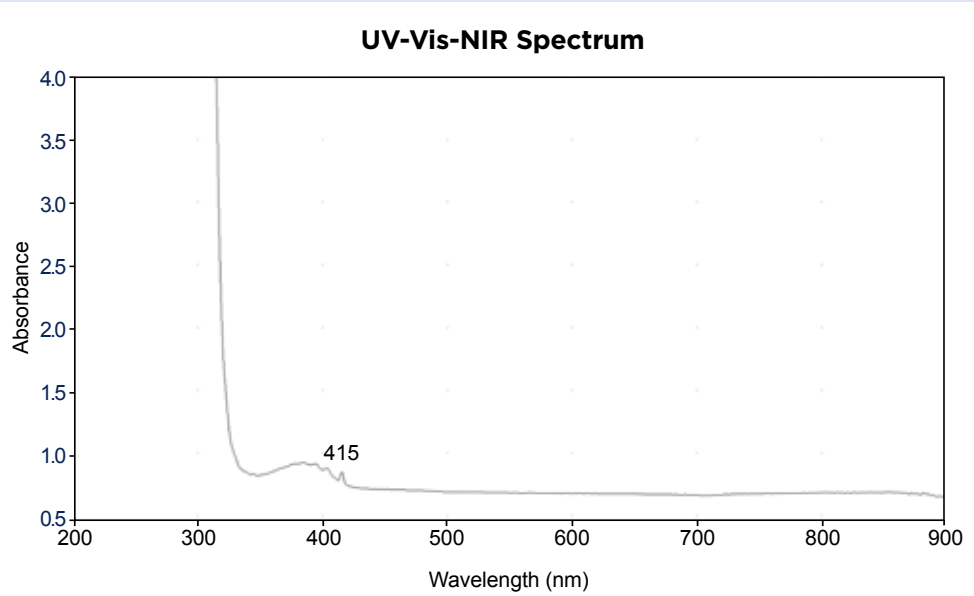

Figure 17: The UV-Vis-NIR spectrum of the Banjarmasin diamond shows only a weak N3 paramagnetic absorption (with a 415 nm zero-phonon line), corresponding to its virtual lack of colour.

DISCUSSION

Black inclusions are poor Raman scatterers, so the ones in this diamond could not be identified with certainty. Such black inclusions commonly consist of sulphides (pyrrhotite or pentlandite) and graphite, although highly reflective chromite has also been identified (e.g. Harris 1972; Harris *et al.* 1972; Koivula 2000). The needle-like black inclusions (Figure 13) look very similar to patterns of small black platelets and needles that form distinct clusters or directional arrays along diamond cleavage planes, and have previously been identified as graphite (Harris 1972). The black material in the fractures around the forsterite inclusions may consist of graphite or sulphides. This material is hosted by tension fractures that are caused by the greater volumetric expansion of olivine than diamond during a decrease in pressure that took place after the diamond's formation (Harris *et al.* 1972).

As mentioned in the History section of this article, the Banjarmasin diamond reportedly originated from southern Kalimantan on the island of Borneo, one of the oldest-mined sources of diamonds. However, most diamonds from Kalimantan are relatively small (averaging about 0.30 ct; Spencer *et al.* 1988), which could raise the question of whether the Banjarmasin originated elsewhere. For instance, India has historically been known as an important source of large 'white' and pink 'Golconda' diamonds (e.g. Bari & Sautter 2001, pp. 96–101). However, large Golconda diamonds have often

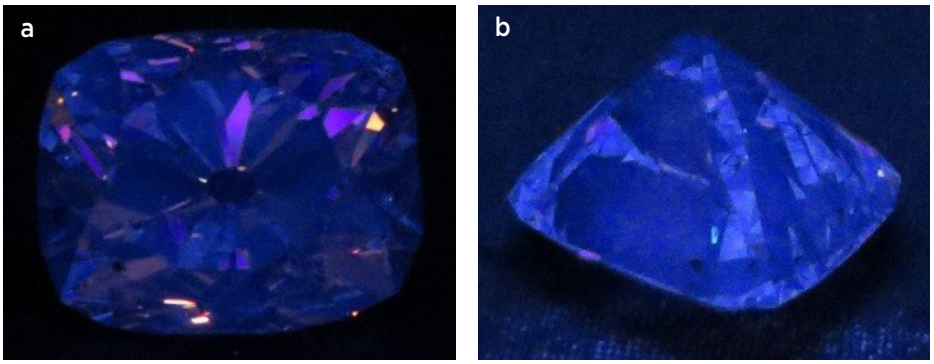

Figure 18: (**a**) The 38.23 ct Banjarmasin diamond fluoresces very weak blue to long-wave UV radiation. (**b**) The blue luminescence appears patchy when viewed on the pavilion side of the stone. Photos by J. C. Zwaan.

been characterised as the rare type IIa, which does not contain nitrogen (e.g. King *et al*. 2008), so India seems a less likely source for the Banjarmasin. Also, there is some evidence of large diamonds coming from Kalimantan. In 1789, the 367 ct Matan diamond was reportedly found in the Landak River of western Kalimantan (Ball 1931), and several diamonds exceeding 100 ct once belonged to the Malay Prince of Landak (Bauer 1904). A more recent find from Kalimantan, in 1965, of the 166.85 ct Tri Sakti diamond (subsequently faceted into a 50.53 ct emerald cut; Spencer *et al*. 1988) also confirms that large diamonds have been found in this region.

Since diamonds are formed in the earth's mantle, their properties cannot be used to provide convincing evidence for a specific geographic origin (cf. Smith *et al*. 2022). The Banjarmasin diamond has characteristics that are commonly seen in many diamonds from all over the world, consistent with those of other diamonds from Kalimantan. Most Kalimantan diamonds are of good gem quality, are generally colourless or pale brown (less commonly pale yellow), typically have simple octahedral zonation and may show plastic deformation (with rare cases of more complex internal structures and episodes

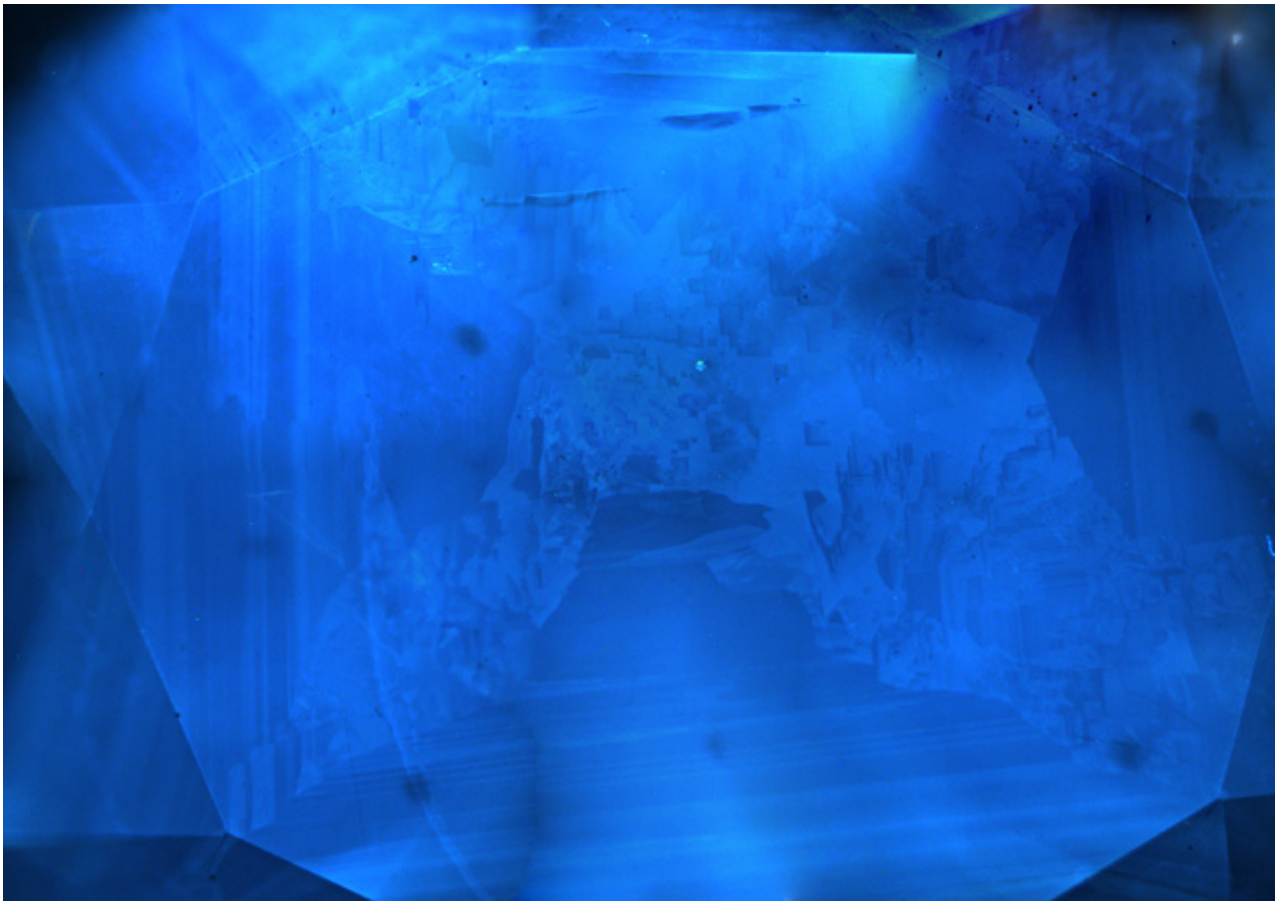

Figure 19: A DiamondView fluorescence image of the Banjarmasin diamond reveals a combination of complicated early growth patterns and later regular octahedral growth. Photo by J. C. Zwaan; image width 15.9 mm.

of resorption). Many are well-aggregated type IaAB (implying a long-term mantle residence time and/or high temperatures of formation), contain detectable hydrogen impurities, and have inclusion parageneses that are 68% peridotitic (containing forsterite; Smith *et al*. 2009). The Banjarmasin diamond shows consistent features: it is colourless, shows octahedral growth zoning and displacement zones indicating plastic deformation, and contains forsterite inclusions. Strong absorption in the 1300–1100 cm^{-1} indicates the presence of aggregated nitrogen in A and B forms. Other indicators that both A and B aggregates are present in comparatively large concentrations are the very weak fluorescence, indicating the presence of A aggregates quenching the fluorescence caused by N3 centres (cf. Collins 1982), and the strong platelet peak, which has an intensity proportional to the absorption produced by the B aggregates (Collins 2001; Smith *et al*. 2009).

CONCLUSION

The Banjarmasin diamond in the collection of the Rijksmuseum in Amsterdam reportedly originated from southern Borneo (in today's South Kalimantan, Indonesia), and was confiscated by the Dutch from the Sultanate of Banjarmasin. It therefore is a symbol of the controversial history of Dutch colonial rule in this part of Indonesia. As a rough diamond weighing 70+ ct, it arrived in the Netherlands in 1862. In 1870, it was faceted into a modified Old Mine cut weighing 38.23 ct. Over the next three decades, there were several unsuccessful efforts to sell it. Ultimately, the diamond was transferred to the Rijksmuseum in 1902. During recent examinations of the diamond as reported in this article, it was graded as E colour and SI_2 clarity. It is a type IaAB diamond, contains forsterite and probable graphite inclusions, and is one of the few historical examples of large diamonds found in southern Borneo.

REFERENCES

Akkerman, K.M. 1989. Een hart, extraordinair groot: de geschiedenis van de grootste diamant in Oranjebezit. *Antiek*, **24**(5), 277–296.

Anderson, B. & Payne, J. 1998. *The Spectroscope and Gemmology*. Robert Hale Ltd, London, 269 pp.

Anonymous 1829. Correspondentie. *Javasche Courant*, No. 127, 29 October, pp. 2–3, https://resolver.kb.nl/resolve?urn=ddd:010502655:mpeg21:p002, accessed 24 February 2023.

Anonymous 1833. Het Eiland Borneo (Vervolg en Slot van Nommer 377). *Nieuwe Amsterdamsche Courant en Algemeen Handelsblad,* Amsterdam, The Netherlands, 17 January, p. 4, https://www.delpher.nl/nl/kranten/view?coll=ddd&identifier=ddd:010068985:mpeg21:p004, accessed 24 February 2023.

Anonymous 1838. Borneo. Eenige reizen in de Binnenlanden van dit Eiland, door eenen Ambtenaar van het Gouvernement, in het jaar 1824. Van Banjermassing naar Tabenio. *Tijdschrift voor Neêrland's Indië*, **1**, 401–413, https://tinyurl.com/2wf7t6cj.

Anonymous 1862. Binnenland. *Nieuwe Rotterdamsche Courant*, Rotterdam, The Netherlands, p. 2, https://resolver.kb.nl/resolve?urn=ddd:010110554:mpeg21:p002, accessed 24 February 2023.

Anonymous 1883. De Diamant-nijverheid op de Tentoonstelling. II. *Nieuwe Amsterdamsche Courant. Algemeen Handelsblad*, No. 16655, Amsterdam, The Netherlands, 9 May, p. 5, https://www.delpher.nl/nl/kranten/view?coll=ddd&identifier=ddd:010165493:mpeg21:p005, accessed 24 February 2023.

Anonymous 1898. Voorlopig bericht. *Nieuwe Amsterdamsche Courant. Algemeen Handelsblad*, No. 21788, Amsterdam, The Netherlands, 23 January, p. 12, https://www.delpher.nl/nl/kranten/view?coll=ddd&identifier=ddd:010162150:mpeg21:p012, accessed 27 February 2023.

Balfour, I. 2009. *Famous Diamonds*, 5th edn. Antique Collectors' Club, Woodbridge, Suffolk, 335 pp.

Ball, S.H. 1931. Diamond mining in Borneo. *Engineering and Mining Journal*, **132**(5), 200–202, https://archive.org/details/sim_engineering-and-mining-journal_1931-09-14_132_5.

Bari, H. & Sautter, V. 2001. *Diamonds: In the Heart of the Earth, in the Heart of Stars, at the Heart of Power*. English edition transl. by M. Hing, Vilo International, Paris, France, 351 pp.

Bauer, M. 1904. *Precious Stones: A Popular Account of Their Characters, Occurrence and Applications, with an Introduction to their Determination, for Mineralogists, Lapidaries, Jewellers, etc. with an Appendix on Pearls and Coral*. Charles Griffin and Company Ltd, London, xvi + 627 pp., https://doi.org/10.5962/bhl.title.55326.

Bleckmann, G.M. 1850. Een bezoek van de steenkolenmijn van Pangaron. *Natuurkundig tijdschrift voor Nederlandsch Indië*, **1**, 319–340, https://www.biodiversitylibrary.org/item/110300#page/7/mode/1up.

Brus, R. 1987a. Diamanten uit Kalimantan. *Orion*, **3**(5), 38–39.

Brus, R. 1987b. Waar bleef de Lombok-schat? *Vorsten: Maandblad Over Alle Vorstenhuizen*, **12**, October, 10–13.

Brus, R. 1989. Dutch mystery stories: The hidden Bandjermasin [*sic*] gem and the disappearing treasure. *Diamond World Review*, **51**, January–February, 36.

Collins, A.T. 1982. Colour centres in diamond. *Journal of Gemmology*, **18**(1), 37–75, https://doi.org/10.15506/JoG.1982.18.1.37.

Collins, A.T. 2001. The colour of diamond and how it may be changed. *Journal of Gemmology*, **27**(6), 341–359, https://doi.org/10.15506/JoG.2001.27.6.341.

Collins, A.T. 2003. The detection of colour-enhanced and synthetic gem diamonds by optical spectroscopy. *Diamond and Related Materials*, **12**(10–11), 1976–1983, https://doi.org/10.1016/s0925-9635(03)00262-0.

Content, D.J. 2020. A concise history of diamonds from Borneo. *In:* Balakrishnan, U.R. (ed) *Diamonds Across Time.* The World Diamond Museum Ltd, London, 137–174.

Dobrinets, I.A., Vins, V.G. & Zaitsev, A.M. 2013. *HPHT-Treated Diamonds: Diamonds Forever*. Springer-Verlag, Berlin, Germany, xix + 257 pp., https://doi.org/10.1007/978-3-642-37490-6.

Drieënhuizen, C. 2017. Een 'lelijk vuil ding': een diamant in het Rijksmuseum en de doorwerking van koloniaal denken. Koloniaal Verleden, Voortdurende Erfenis. Indonisë en Nederland, https://tinyurl.com/y7fayrd9, 26 September, accessed 8 August 2023.

Fleet, A. (ed) 2005. *Diamonds: The World's Most Dazzling Exhibition*. Natural History Museum, London, 60 pp. (see p. 27, no. 10).

Goss, J.P., Coomer, B.J., Jones, R., Fall, C.J., Briddon, P.R. & Öberg, S. 2003. Extended defects in diamond: The interstitial platelet. *Physical Review B*, **67**(16), 165–208, https://doi.org/10.1103/PhysRevB.67.165208.

Harris, J.W. 1972. Black material on mineral inclusions and in internal fracture planes in diamond. *Contributions to Mineralogy and Petrology*, **35**(1), 22–33, https://doi.org/10.1007/bf00397374.

Harris, J.W. & Vance, E.R. 1972. Induced graphitization around crystalline inclusions in diamond. *Contributions to Mineralogy and Petrology*, **35**(3), 227–234, https://doi.org/10.1007/bf00371217.

Henriques de Castro, E., Vita Israel, E., Vita Israel, I.J., Vita Israel, J. & Wertheim, J.F. 1898. *Catalogue de tres-beaux diamants…dont la vente aux enchères publiques….* Emrik & Binger, Haarlem, The Netherlands.

Ikuko, W. 2010. Diamond trade by the Dutch East India Company in seventeenth-century India. *In*: Nagazumi, Y. (ed) *Large and Broad: The Dutch Impact on Early Modern Asia: Essays in Honor of Leonard Blussé*. Toyo Bunko, Tokyo, Japan, 166–187, https://tinyurl.com/6av32xcw.

King, J.M., Geurts, R.H., Gilbertson, A.M. & Shigley, J.E. 2008. Color grading "D-to-Z" diamonds at the GIA Laboratory. *Gems & Gemology*, **44**(4), 296–321, https://doi.org/10.5741/gems.44.4.296.

Koivula, J.I. 2000. *The Microworld of Diamonds: A Visual Reference Guide.* Gemworld International Inc., Northbrook, Illinois, USA, 157 pp.

Korthals, P.W. 1836. *Wetenschappelijk Archief van Pieter Willem Korthals (1807–1892)* [*Scientific Archive of Pieter Willem Korthals (1807–1892)*]. DW.E.04.017.038.004, Naturalis Biodiversity Center, Leiden, The Netherlands, https://hdl.handle.net/21.12107/313819336.

Korthals, P.W. 1837. Aanteekeningen over Borneo's Zuidooskust. *Algemeene Konst- en Letterbode*, No. 47, 244–249, https://books.google.be/books?vid=GENT900000034371.

Müller, G. 1843. *Proeve eener geschiedenis van een gedeelte der west-kust van het eiland Borneo*. H.W. Hazenberg, Leiden, The Netherlands, 123 pp., https://tinyurl.com/4ssvy427.

Müller, S. 1839–1844. *Verhandelingen over de Natuurlijke Geschiedenis der Nederlandsche Overzeesche Bezittingen*, Vol. 1: Land-en Volkenkunde. S. en J. Luchtmans en C.C. van der Hoek, Leiden, The Netherlands, viii + 472 pp. + 486 pl., https://doi.org/10.5962/bhl.title.114730.

Müller, S. 1857. *Reizen en onderzoekingen in den Indischen archipel: gedaan op last der Nederlandsche Indische regering, tusschen de jaren 1828 en 1836*, Vol. 1. Frederik Muller, Amsterdam, The Netherlands, vii + 326 pp., https://tinyurl.com/bdhvyh9c.

Norman, L. 1868. *Katalogus der Ethnologische Afdeeling van het Museum van het Bataviaasch Genootschap van Kunsten en Wetenschappen*. Lange & Co., Batavia, Dutch East Indies (Jakarta, Indonesia), 133 pp., https://tinyurl.com/y766shbm.

Ogden, J. 2005. Diamonds, headhunters and a prattling fool: The British exploration of Borneo diamonds. *Gems&Jewellery*, **14**(3), 67–69.

Ogden, J. 2018. *Diamonds: An Early History of the King of Gems*. Yale University Press, New Haven, Connecticut, USA, 408 pp., https://doi.org/10.12987/9780300235517.

Perelaer, M.T.H. 1888. *Het kamerlid van Berkenstein in Nederlandsch-Indië*, Vol. 2. A.W. Sijthoff, Leiden, The Netherlands, 200 pp., https://books.google.com/books?id=FnVdAAAAcAAJ.

Schwaner, C.A.L.M. 1853. *Borneo: beschrijving van het stroomgebied van den Barito en reizen langs eenige voorname rivieren van het zuid-oostelijk gedeelte van dat eiland, door Dr C. A. L. M. Schwaner*, Vol. 1. P.N. van Kampen, Amsterdam, The Netherlands, 234 pp., https://books.google.com/books?id=LwVdAAAAcAAJ.

Smith, C.P. & Bosshart, G. 2002. Star of the South: A historic 128 ct diamond. *Gems & Gemology*, **38**(1), 54–64, https://doi.org/10.5741/gems.38.1.54.

Smith, C.B., Bulanova, G.P., Kohn, S.C., Milledge, H.J., Hall, A.E., Griffin, B.J. & Pearson, D.G. 2009. Nature and genesis of Kalimantan diamonds. *Lithos*, **112**(S2), 822–832, https://doi.org/10.1016/j.lithos.2009.05.014.

Smith, E.M., Smit, K.V. & Shirey, S.B. 2022. Methods and challenges of establishing the geographic origin of diamonds. *Gems & Gemology*, **58**(3), 270–288, https://doi.org/10.5741/gems.58.3.270.

Spencer, L.K., Dikinis, S.D., Keller, P.C. & Kane, R.E. 1988. The diamond deposits of Kalimantan, Borneo. *Gems & Gemology*, **24**(2), 67–80, https://doi.org/10.5741/gems.24.2.67.

Stutje, K. 2022a. The diamond from Banjarmasin: A story in facets. *Rijksmuseum Bulletin*, **70**(4), 340–355, https://doi.org/10.52476/trb.13473.

Stutje, K. 2022b. *Provenance Report Regarding the Banjarmasin Diamond*. Pilotproject Provenance Research on Objects of the Colonial Era, No. 13, Royal Netherlands Academy of Arts and Sciences, Amsterdam, The Netherlands, 11 pp., https://pure.knaw.nl/portal/en/publications/provenance-report-regarding-the-banjarmasin-diamond, 11 pp., accessed 8 August 2023.

Teenstra, M.D. 1852a. *Beknopte beschrijving van de Nederlandsche overzeesche bezittingen voor beschaafde lezers uit alle standen, uit de beste bronnen en eigen ervaring in Oost- en West-Indiën geput*, Vol. 2. J. Oomkens, J. Zeen, Groningen, The Netherlands, 412 pp., https://tinyurl.com/yh2rbm3y.

Teenstra, M.D. 1852b. *Beknopte beschrijving van de Nederlandsche overzeesche bezittingen voor beschaafde lezers uit alle standen, uit de beste bronnen en eigen ervaring in Oost- en West-Indiën geput*, Vol. 3. J. Oomkens, J. Zeen, Groningen, The Netherlands, 346 pp., https://tinyurl.com/3sxnznza.

van der Chijs, J.A. 1862. *Tijdschrift voor Indische taal-, land- en volkenkunde*, Vol. 12. Lange & Co., Batavia, Dutch East Indies (Jakarta, Indonesia), 620 pp., https://books.google.com/books/about/Tijdschrift_voor_Indische_taal_land_en_v.html?id=8JJUAAAAcAAJ.

van Rees, W.A. 1865a. *De bandjermasinsche krijg van 1859–1863*, Vol. 1. D.A. Thieme, Arnhem, The Netherlands, 346 pp., https://books.google.com/books/about/De_bandjermasinsche_krijg_van_1859_1863.html?id=JRQ5AQAAIAAJ.

van Rees, W.A. 1865b. *De bandjermasinsche krijg van 1859–1863*, Vol. 2. D.A. Thieme, Arnhem, The Netherlands, 417 pp., https://tinyurl.com/bdak9mff.

Weber, A. 2019. Collecting colonial nature: European naturalists and the Netherlands Indies in the early nineteenth century. *BMGN–Low Countries Historical Review*, **134**(3), 72–95, https://doi.org/10.18352/bmgn-lchr.10741.

Wiggers de Vries, D.F., Bulanova, G.P., De Corte, K., Pearson, D.G., Craven, J.A. & Davies, G.R. 2013. Micron-scale coupled carbon isotope and nitrogen abundance variations in diamonds: Evidence for episodic diamond formation beneath the Siberian craton. *Geochimica et Cosmochimica Acta*, 100, 176–199, https://doi.org/10.1016/j.gca.2012.08.034.

Zandvliet, K. 2002. *The Dutch Encounter with Asia, 1600–1950*. Rijksmuseum/Waanders Publishing, Amsterdam, The Netherlands, 463 pp.

The Authors

Suzanne van Leeuwen FGA
Rijksmuseum, Postbus 74888, 1070 DN Amsterdam, The Netherlands
Email: s.van.leeuwen@rijksmuseum.nl

Dr J. C. (Hanco) Zwaan FGA
Netherlands Gem Laboratory – Naturalis Biodiversity Center, Postbus 9517, 2300 RA Leiden, The Netherlands

Acknowledgements

We thank Dirk van der Marel for assistance in drawing the modified Old Mine diagram and stitching separate DiamondView images into one overview image for Figure 19. We thank NIOD historian Dr Klaas Stutje, and jewellery historians René Brus and the late Erik Schoonhoven, for sharing and discussing valuable source material on the Banjarmasin diamond. Collections archivist Karien Lahaise of Naturalis kindly shared scans of the unpublished diaries of P. W. Korthals.

Clues to Understanding the Enigma of the Unusual Asterism in 'Mercedes-Star' Quartz

Jean-Pierre Gauthier, Emmanuel Fritsch, Thanh Nhan Bui and Jacques Fereire

ABSTRACT: 'Mercedes-star' quartz contains abundant long, narrow, randomly oriented rutile inclusions, and is notable for its unusual asterism. In particular, it displays weak three-rayed stars, with rays that meet at the centre as in the Mercedes-Benz emblem. In the classical theory of asterism such stars cannot exist, and they have not been seen in any other gem materials. We examined three samples (two spheres and one egg shaped) of 'Mercedes-star' quartz from Brazil. Ideally, this material displays six three-rayed stars located along two latitude planes parallel to the equatorial plane (perpendicular to the *c*-axis). In addition, six faint four-rayed stars are located along the equatorial plane. Therefore, in total, this quartz may display 18 stars located on three coaxial circles. The rays of all the stars consist of a path of reflective segments of unknown illumination origin, but which appear to result from double reflection of the light beam, first by Brazil-law twin planes and then by the rutile needles, making the phenomenon uncommon. In addition to the abovementioned stars seen in reflected light (epiasterism), more-transparent 'Mercedes-star' quartz may also show two six-rayed stars with transmitted light (diasterism) when illuminated from behind and viewed parallel to the *c*-axis.

The Journal of Gemmology, **38**(7), 2023, pp. 678–695, https://doi.org/10.15506/JoG.2023.38.7.678

Quartz is one of the most abundant minerals on Earth. It occurs in many varieties, not just colour-wise (e.g. amethyst, citrine, prasiolite, pink quartz and smoky quartz) but also inclusion-wise (Hyršl & Niedermayr 2003). Of all quartz inclusions, rutile is relatively common, and it occurs in some spectacular varieties (e.g. Gübelin & Koivula 2005, pp. 627–631). Many of these are artistically highlighted by lapidaries.

Several types of inclusions are responsible for various optical phenomena in gems, such as aventurescence, iridescence, chatoyancy and asterism. Chatoyancy in quartz is produced by a network of parallel acicular inclusions oriented along a particular crystallographic direction of the quartz host (see, e.g., Kane 1985; Koivula 1987; Choudhary & Vyas 2009). Relatively parallel coarse rutile needles sometimes produce pseudo-cat's-eyes (Johnson & McClure 1997). Asterism in quartz is typically caused by several networks of acicular inclusions lying in the basal plane that produce six-rayed stars and, less frequently, 12-rayed stars (Johnson & Koivula 1999). Additional inclusion networks outside the basal plane result in multi-asterism, mainly consisting of four- and six-rayed stars (Schmetzer & Glas 2003).

Here we examine so-called Mercedes-star rutilated quartz (e.g. Figure 1), which displays three-rayed asterism with branches that meet at the centre of the star (like the emblem of the famous German car manufacturer), and exhibits features that are contrary to the most commonly accepted theory of asterism (cf. Gübelin *et al.* 1982; Weibel 1982). This kind of asteriated quartz was briefly described by Gübelin and Koivula (2005,

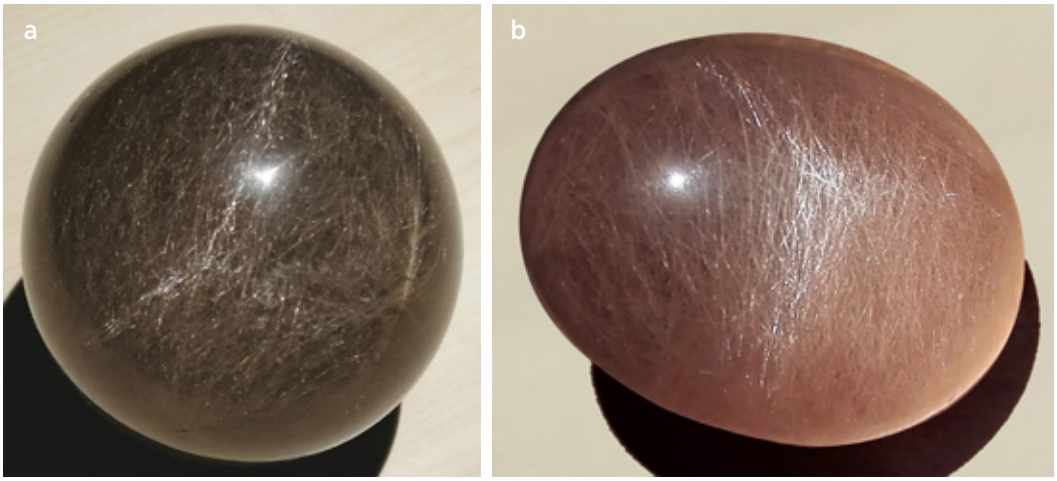

Figure 1: These two samples of Mercedes-star quartz were examined for this study: (**a**) a large sphere (1,470 ct; 60 mm in diameter) and (**b**) an egg-shaped specimen (252.5 ct; 41 mm long × 30 mm diameter). Collection of E. Fritsch; photos by J.-P. Gauthier.

pp. 548, 822) and later encountered by Hainschwang (2007) in five samples from Brazil. More recently, it was reported by Steinbach (2017), as well as by Schmetzer and Steinbach (2022, 2023), in rutilated quartz also from Brazil (apparently similar to the samples described here). The arrangement of the stars located at various positions relative to the optic axis of the host quartz is documented in the present article using polished specimens of rutilated quartz from Brazil, one of which was sacrificed to study the cause of the three-rayed asterism. We report a number of observations not previously described for Mercedes-star quartz, and also propose some ideas to explain the formation of its unique asterism.

MATERIALS AND METHODS

The three Mercedes-star quartz samples examined for this study all came from Bahia State, Brazil. The first was an opaque sphere of 60 mm diameter (1,470 ct; Figure 1a). This sample was used for most of the observations, because the stars were easiest to see and all 18 (12 three-rayed and six four-rayed) stars were visible. The second was an egg-shaped specimen measuring 41 mm long and 30 mm diameter (252.5 ct; Figure 1b), which was semi-transparent in transmitted light, making it ideal for observing any diasterism. The third sample was a 28-mm-diameter sphere that was somewhat translucent, due in particular to its smaller size (150 ct; Figure 2). This last sample was sliced to prepare petrographic thin sections for observation between crossed polarisers.

To describe the asterism in our samples, it was necessary to develop a protocol to locate the centres of all the stars. The following procedure was used on the large sphere (Figure 1a). First, the light source (such as the sun) and the observer faced the same direction. In this orientation, the specular reflection (the image of the light source reflected by the surface of the sphere as seen by the observer) was approximately in the centre of the spherical surface (Figure 3a). Then, the centre of a star was moved (by rotating the sphere) to coincide with this specular reflection (Figure 3b), and a small disc of paper was affixed to indicate this position (Figure 3c). This was done for the centre of each star. For the purpose of this study, these positions of the star centres are called *star spots*. They should not be confused with *light spots*, as previously described for star rose quartz spheres (e.g. Schmetzer & Krzemnicki 2006; Killingback 2008).

The relative angular positions of the star spots on the

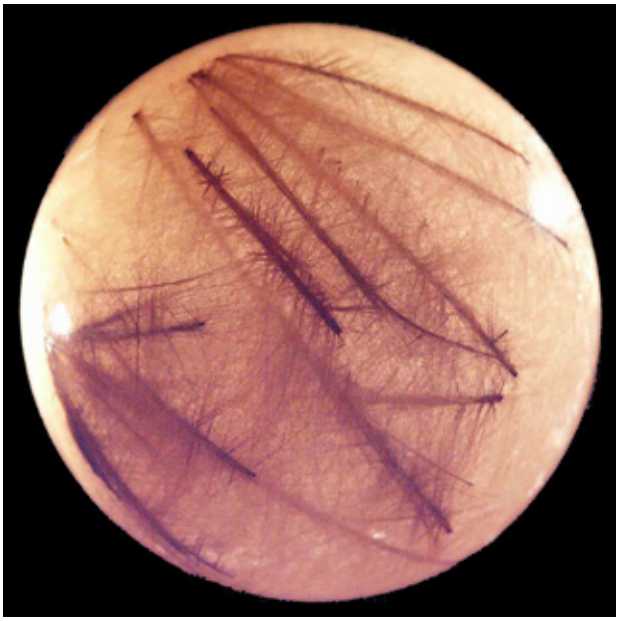

Figure 2: A smaller Mercedes-star quartz sphere measuring 28 mm in diameter (150 ct) was also examined for this study. It is shown here in transmitted light to highlight the interesting form of its inclusions. Photo by J.-P. Gauthier.

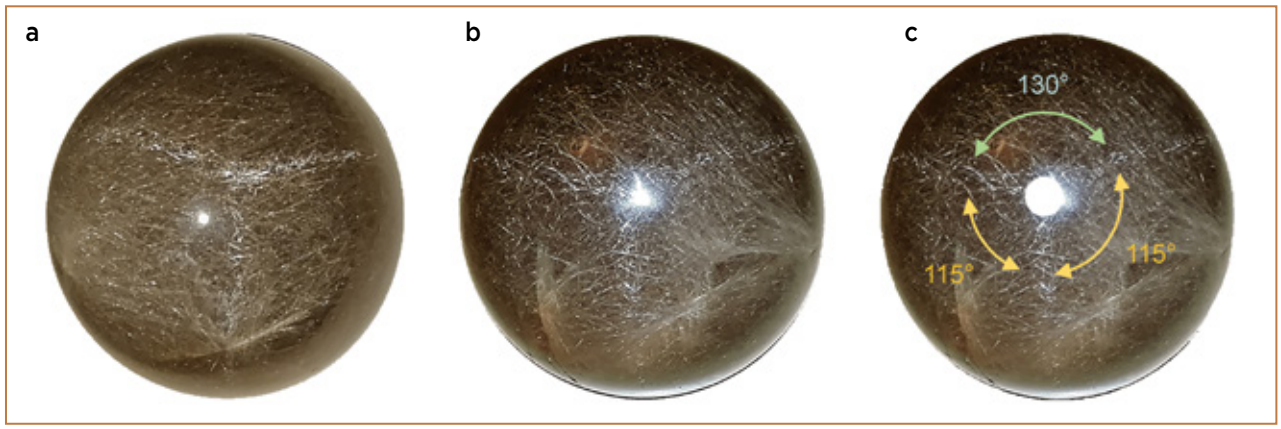

Figure 3: The positions of 'star spots' on the large quartz sphere were determined using the following procedure: (**a**) First the light source and the eye of the observer are aligned with the sphere's centre, so the specular spot becomes centred on the sphere. (**b**) Then the sphere is rotated slightly to bring the centre of a star in coincidence with the specular spot. (**c**) The position of the star spot is marked with a disc of sticky paper. Angle values between branches are about 130° (green arrow) and 115° (yellow arrows). Photos by J.-P. Gauthier.

large sphere were then recorded with a Tri-Mesures MC 1004E three-dimensional coordinate measuring machine (manufactured by MétroVali, Villedieu-sur-Indre, France) equipped with Wenzel WM/Quartis metrological software. Experimentally, five non-coplanar points on the sphere first defined the sphere's centre (denoted Ω). The coordinates of each star spot were obtained in relation to this origin. The next step was to calculate the coordinates of the north pole (P) and south pole (P') of an axis passing through the diameter of the sphere, making it possible to evaluate the angular positions of the spots. (Note: Due to the positional symmetry of the spots as described below, the quartz *c*-axis was determined and chosen as the reference axis P–P'.) We could then calculate the angular positions (with respect to the *c*-axis and/or the equatorial plane) of the radii joining the sphere centre Ω to the different star spots. Due to uncertainty in positioning the star spots (discussed further below), the angular values were rounded to the nearest half degree.

To identify the acicular inclusions in the quartz, we used a Jobin Yvon T64000 high-resolution Raman spectrometer coupled with an Olympus binocular microscope (up to 100 × magnification). With 514 nm excitation from an Ar^+ laser, we employed a triple-subtractive configuration to eliminate the effect of the excitation line, along with a diffraction grating (600 lines/mm), confocal mode and a resolution of approximately 4 cm^{-1}.

RESULTS

Macroscopic Observations

General Features of the Asterism. Viewed in reflected light, 18 star spots were identified on the large quartz sphere, which were distributed on three coaxial circles (Figures 4 and 5a). A set of six four-rayed star spots lay along the median ('equatorial') plane, and two symmetric sets of three-rayed star spots were located along parallel ('latitude') planes on either side of this equatorial plane. This arrangement strongly suggests that the normal to all of these circles is the quartz *c*-axis (optic axis), which is vertical in Figures 4a and 5, and perpendicular to the plane of the photo in Figure 4b.

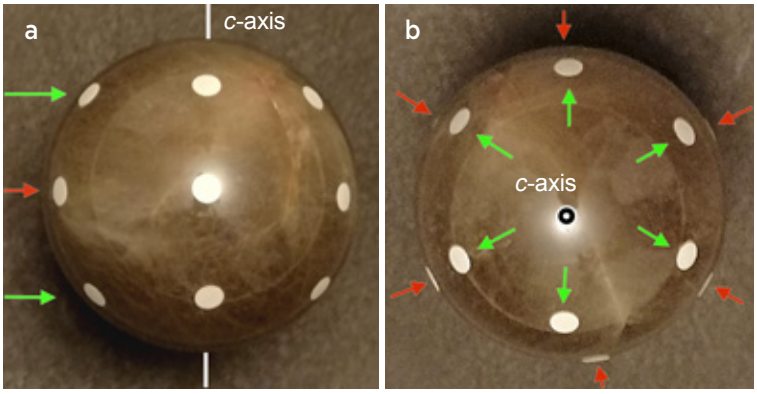

Figure 4: (**a**) When the large quartz sphere is positioned with the quartz three-fold *c*-axis lying in the plane of the figure, there are six three-rayed stars in the upper and lower hemispheres (green arrows) and six four-rayed stars along the equatorial plane (red arrow). These three sets lie on three parallel circles coaxial with the quartz *c*-axis. (**b**) A view along the quartz three-fold axis (*c*-axis) shows the arrangement of the six star spots of the three-rayed stars (green arrows). The star spots of the six equatorial four-rayed stars (barely visible around the perimeter of the sphere) are indicated by red arrows. Photos by J.-P. Gauthier.

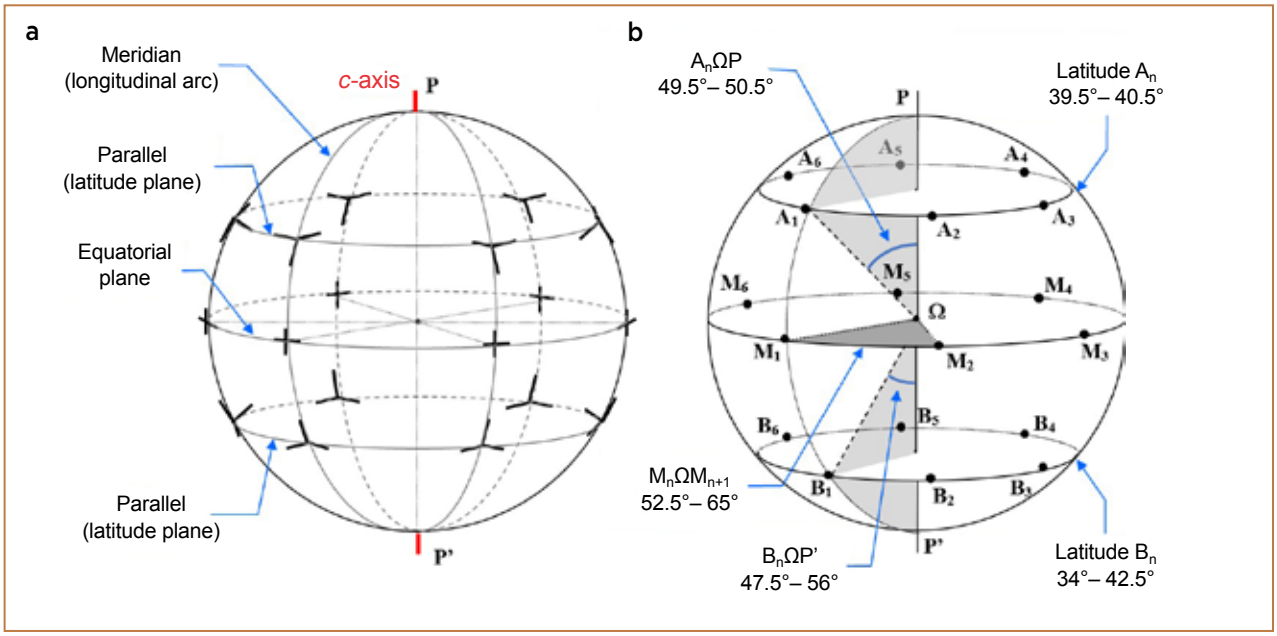

Figure 5: (**a**) The locations of the 18 star spots seen on the large quartz sphere are shown on this diagram. The labels P and P' show the positions of the north and south 'poles' of the *c*-axis, respectively. (**b**) A corresponding diagram is labelled with the nomenclature of the star spots relative to their angular positions on meridians (longitudinal arcs connecting the poles) and parallels (or latitude planes) of the quartz sphere. The labels A_n and B_n correspond to three-rayed stars, while M_n refers to the four-rayed stars along the equatorial plane.

This could not be verified directly on the large sphere, which was much too thick to be transparent between crossed polarisers, but it was later confirmed using the small sphere (see below).

The appearance of the three-rayed stars in Mercedes-star quartz stands out when compared with typical asterism because of two main characteristics. (1) As seen in Figures 1 and 3, each ray of the star seems to be made of a multitude of reflective points or segments. The branches are relatively wide and diffuse—appearing as shiny, intermittent lines made up of reflections from rutile needles—rather than continuous, sharp and linear rays as in star corundum, for example. (2) The branches of the three-rayed stars meet at a central point, rather than crossing each other to form a classic six-rayed star.

However, as for every asteriated stone, the stars move when one of the three entities—stone, light source or observer—shifts while the other two are fixed. Rotating the stone causes the branches of the star to move in the same direction. However, if the lamp or the observer moves, the star shifts in the opposite direction (cf. Gübelin *et al.* 1982). In addition, the arms of the stars are linked together in a network (Schmetzer & Steinbach 2023) that moves as the stone rotates relative to the light source, as in typical asterism exhibited by a multi-star network, such as seen in garnet (Walcott 1937; Schmetzer & Bernhardt 2002) or quartz (Schmetzer & Glas 2003).

Position and Shape of the Stars. The 18 star spots are distributed as follows: six of them are located on each of three parallel circles centred on the same axis, and three of them are on each of six meridians positioned at about 60° of longitude from each other (Figure 5a). Each meridian contains two three-rayed stars opposite in latitude on either side of an equatorial four-rayed star.

Each equatorial four-rayed star has a weak vertical branch (following a meridian) and a much weaker horizontal branch (Figure 6). The lack of visibility of the latter branch is likely the reason why these four-rayed stars were not mentioned in previous publications about Mercedes-star quartz (Steinbach 2017; Schmetzer & Steinbach 2022) until recently (Schmetzer & Steinbach 2023).

The three-rayed stars have one branch along a meridian (joining the vertical branch of a nearby four-rayed star). The other two branches make an angle of about 115° with the meridian branch and an angle of 130° to one another (Figure 3c). This means that the cause of the meridian branch differs from that of the other two. Of course, there is no need for the Mercedes-star branches to be evenly spaced at 120°, since in quartz there is no three-fold axis of rotation other than the one connecting the two poles (i.e. the *c*-axis, as typical hydrothermal α-quartz is trigonal). The presence of six stars on each of the parallel circles

gives a pseudo-hexagonal distribution, reflecting the pseudo-hexagonal symmetry of quartz. This suggests that: (1) the quartz *z* faces are as prominent as the *r* faces, or (2) twinning has occurred with parallel axes of two trigonal domains inducing the six-fold axis (Frondel 1962).

Table I lists the positional data for the 18 star spots recorded for the large sphere using the three-dimensional coordinate measuring machine. (To identify each star spot, the nomenclature shown in Figure 5b was adopted). The latitude values of the six three-rayed star spots in the 'northern hemisphere' were very similar, with values of 40° ± 0.5°. Those of the southern hemisphere, which would be expected to have symmetrical latitude values, showed greater variation (34°–42.5°). There was also some variation from the expected latitude of 0° for the four-rayed stars along the equatorial plane (0.5°–4.5°). In longitude, the angular spacing between consecutive four-rayed star spots should approach a theoretical value of 60°, but some measurements were quite far away from it, ranging from 52.5° to 65° (again, see Table I).

The deviations from the expected values are probably due to the uncertainty of marking the star spots on the surface of the sphere (estimated at 2–3 mm), and not from the measuring machine (with an uncertainty of about 10 µm). The marked positions of the star spots were imprecise for two reasons. First, the observer's head obscures the sphere unless it is slightly away from the theoretical line defined by the illumination source (e.g. the sun) and the observer in order to see the specular reflection. A similar situation exists if the light source is a lamp placed directly in line between the observer's eye and the sample: the observer will be unable to see the specular reflection unless the sphere is moved slightly to one side of the lamp. Second, the star branches are wide and consist of intermittent lines, so the star spots themselves are not well defined. Due to the resulting inaccuracy in the positions of the spots, the angular deviation $\Delta\theta$ with respect to an ideal position can reach up to $\Delta\theta = (\Delta d/R) \times (180/\pi)$ degrees, or about 6° for $\Delta d = 3$ mm (linear deviation at the surface of the sphere of radius R) and R = 30 mm (as for the large sphere) with the constant $\pi = 3.1416$.

Figure 6: The four-rayed asterism on the large quartz sphere is difficult to capture in a photograph. The vertical ray is somewhat visible here, but only part of the horizontal ray is relatively easy to see (yellow arrow). Compare this to the sample in the centre of figure 19 in Hainschwang (2007). Photo by J.-P. Gauthier.

Table I: Latitude and longitudinal angle values (in degrees) for all 18 star spots on the large Mercedes-star quartz sphere.*

Angles $A_nΩP$	**$A_1ΩP$**	**$A_2ΩP$**	**$A_3ΩP$**	**$A_4ΩP$**	**$A_5ΩP$**	**$A_6ΩP$**
	50	50	49.5	50	50.5	49.5
Latitude of A_n	40	40	40.5	40	39.5	40.5

Angles $B_nΩP'$	**$B_1ΩP'$**	**$B_2ΩP'$**	**$B_3ΩP'$**	**$B_4ΩP'$**	**$B_5ΩP'$**	**$B_6ΩP'$**
	51	49	47.5	56	54	53
Latitude of B_n	39	41	42.5	34	36	37

Angles $M_nΩP$	**$M_1ΩP$**	**$M_2ΩP$**	**$M_3ΩP$**	**$M_4ΩP$**	**$M_5ΩP$**	**$M_6ΩP$**
	89.5	89	88.5	88	85.5	86.5
Latitude of M_n	0.5	1	1.5	2	4.5	3.5

Angles $M_nΩM_{n+1}$	**$M_1ΩM_2$**	**$M_2ΩM_3$**	**$M_3ΩM_4$**	**$M_4ΩM_5$**	**$M_5ΩM_6$**	**$M_6ΩM_1$**
	56.5	65	52.5	60	62	62

* The darker tinted boxes indicate data that deviate most significantly from their expected values.

Movement of the Stars with Rotation of the Sphere. The sketch in Figure 7 shows how the stars move upon rotation of the sphere in various directions. In all cases in Figure 7, the light source and the observer are perpendicular to the drawing plane. On each circle representing a projection of the sphere, black points show the positions of the star spots, and various manifestations of the three- and four-rayed stars are shown as shaded bands. Two directions of rotation are shown in a series of five steps:

1. In Figure 7a, the sphere is rotated around a horizontal axis, starting with the *c*-axis perpendicular to the plane of the drawing (parallel to the direction of the light source and the observer). Initially, the set of six star spots forms a virtual hexagon, with no visible optical effect. They move towards the top of the sample as the rotation progresses, and a three-rayed star appears at the bottom after about 30° of rotation. At 50°, the centre of this star is positioned at the centre of the sphere. Further rotation of about 70° causes it to disappear at the top of the specimen, giving way to a cat's-eye-like line occupying the entire height of the sphere. A four-rayed star then appears at the bottom, whose centre eventually occupies the centre of the sphere after a 90° rotation.
2. In Figure 7b, the sphere is rotated counter-clockwise around the vertical *c*-axis, starting from the last position in Figure 7a. The four-rayed star moves away to the right and then disappears, and then another four-rayed star appears from the left.

Additional Stars Visible with Transmitted Light (Diasterism). The distribution of the three-rayed star spots on the egg-shaped sample indicated that its P–P' axis is the quartz *c*-axis. Two unexpected (and not previously described) six-rayed stars were observed at each pole of the egg when this somewhat transparent specimen was illuminated from behind with a standard white-light torch parallel to the *c*-axis (Figure 8). To see the six-rayed diasterism, the lamp had to be held a few tens of centimetres from the opposite end of the egg. Bringing the lamp closer to the egg caused the star to disappear. Using the same light source, we did not observe any such six-rayed stars on the sample by reflection at either the top or the base of the egg.

Precessional movement of the lamp around the axis induced movement of the star that was exactly as observed for a rose quartz sphere that displayed

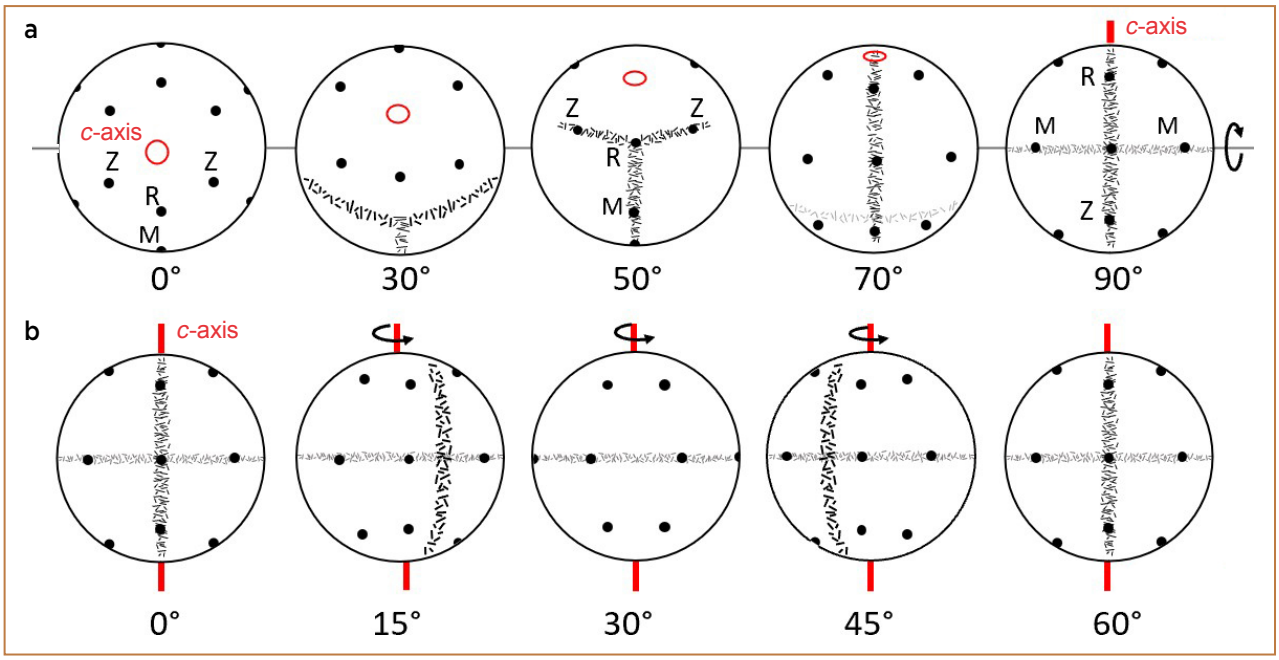

Figure 7: Sketches of the different aspects of the asterism on the large Mercedes-star quartz sphere are shown with the source and observer fixed in the same direction perpendicular to the drawing plane. The black points represent the star spots and the shaded bands correspond to the branches of the stars. (**a**) At 0° (far left), the sphere is positioned with the *c*-axis (red circle) of the quartz crystal perpendicular to the drawing plane. Rotation is then carried out around a horizontal axis with angular values of 30°, 50°, 70° and 90° (from left to right). A three-rayed star, absent at 0°, appears near the bottom of the sphere at about 30°, reaches specular reflection at 50° and then disappears near 70°, where a four-rayed star begins to rise up to, at 90°, the centre of the hemisphere. (**b**) Starting from the last position above, rotation around the vertical three-fold axis (*c*-axis) at angular values of 15°, 30°, 45° and 60° (from left to right) shows the movement of a four-rayed star. Star spots marked with the letters M, R and *Z* are located on the poles *m*, *r* and *z* of a quartz crystal, as indicated later in the Discussion section.

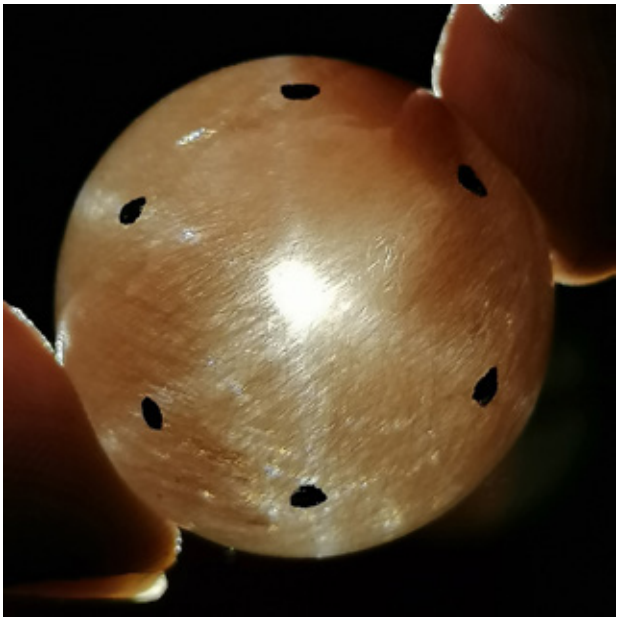

Figure 8: A six-rayed star appears when the semi-transparent egg-shaped quartz is illuminated from behind (diasterism), with the light direction parallel to the *c*-axis (perpendicular to the plane of the image, which is also the symmetry axis of the egg). The black points mark the positions of three-rayed star spots. The diameter of the egg's cross-section is 30 mm. Photo by T. N. Bui.

similar diasterism (Killingback 2006). When the lamp was moved to the right of the axis, the star moved to the left. However, the star disappeared with further angular deviation of the lamp from the *c*-axis.

When the six-rayed star was centred on the *c*-axis, its branches lay along the same meridians as the Mercedes-star spots (again, see Figure 8). The six-rayed diasterism is also apparently created by illumination of rutile needles, as for the three- and four-rayed stars. However, the exact cause of the six-rayed diasterism needs further investigation.

Microscopic Observations

Inclusions. All three quartz samples contained abundant more- or less-curved needles, which we assumed to be typical rutile inclusions. This was confirmed by Raman spectroscopy.

The large sphere shown in Figure 1a appears dark brown, probably due to the large amount of brown rutile inclusions present. The egg-shaped sample is lighter in colour and looks somewhat reddish. Although the host quartz is transparent, the density of the rutile inclusions restricts visibility through the interiors of the stones. The rutile needles have many different aspects, but most are gently curved and look like 'Venus hairs' (i.e. fine golden to reddish curved needles), scattered randomly in the quartz matrix (Figure 9a). Some straighter ones sometimes cross at a node (Figure 9b). Others are roughly aligned in 'combs' that form two perpendicular planes joining along a coarser crystal, as in 'platinum quartz' (Koivula & Tannous 2003; Figure 9c), consistent with the tetragonal nature of the central rutile crystal. Interestingly, healed fractures sometimes transect many rutile needles or 'hairs' (Figure 9d). Rutile inclusions can also be accompanied by two-phase fluid inclusions decorating healed fractures (Figure 9e). Because of the random orientation of the rutile needles, one might assume *a priori* that, despite their abundance, they have little to do with the asterism. Nevertheless, due to their high density, the possibility that they could play a role should not be overlooked.

Water-Drop Test. The water-drop test is typically performed on flat or even unpolished surfaces to detect chatoyancy or asterism (Gauthier 2011). The test consists of applying a small drop of water on the surface of the stone using a syringe fitted with a hypodermic needle. Observing the sample through the curved surface of the water drop allows one to check for an optical effect due to a possible network of very fine, oriented inclusions, invisible under an optical microscope, which could justify classical asterism.

We repeated this experiment on several parts of the large sphere, including on arms and nodes of the stars, and at the ends of the *c*-axis. All of the tests proved negative, ruling out the possibility of a classical scattering phenomenon due to sets of tiny parallel needles.

Reflections from the Rutile Needles. As mentioned above, the branches of the stars do not appear continuous, as for normally chatoyant and asteriated stones. Instead, they consist of concentrations of illuminated segments of randomly oriented acicular rutile inclusions, giving the appearance of the bright reflective dots or lines mentioned above and seen in Figure 10a. The bright lines seem to be due to reflections from the needles' surfaces. The needles act like a multitude of mirrors giving the shiny aspect to the branches of the stars. The needles are not illuminated along their entire length, for at least two reasons: (1) even if the incident rays come from a parallel beam of light, the rays refracted in different points of the sphere are no longer parallel and arrive in different orientations on a rutile needle, and (2) many of the rutile needles are curved.

The cross-sections of the individual needles are significantly smaller than those found in typical coarse rutilated cat's-eye quartz (Johnson & McClure 1997;

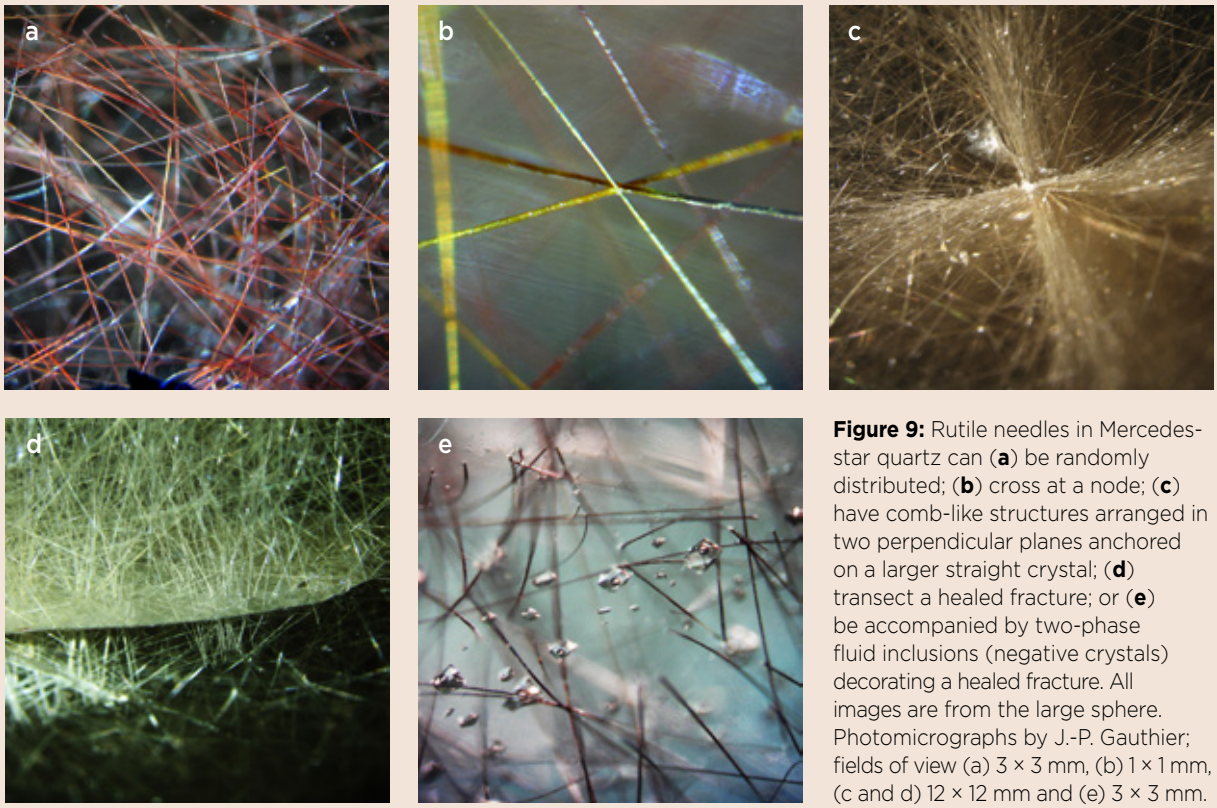

Figure 9: Rutile needles in Mercedes-star quartz can (**a**) be randomly distributed; (**b**) cross at a node; (**c**) have comb-like structures arranged in two perpendicular planes anchored on a larger straight crystal; (**d**) transect a healed fracture; or (**e**) be accompanied by two-phase fluid inclusions (negative crystals) decorating a healed fracture. All images are from the large sphere. Photomicrographs by J.-P. Gauthier; fields of view (a) 3 × 3 mm, (b) 1 × 1 mm, (c and d) 12 × 12 mm and (e) 3 × 3 mm.

Koivula & Tannous 2004). In our samples, the width of these rutile needles, measured on enlarged photomicrographs taken with a binocular microscope at 80 × magnification, is about 50 µm and never exceeds 100 µm. The reflections from the needles are actually composed of very thin luminous striae, as seen only at high magnification (Figure 10b).

Brewster Fringes in the Quartz. The smaller Mercedes-star quartz sphere was sliced parallel to two planes at 90°: (1) along the equatorial plane perpendicular to the *c*-axis and (2) parallel to the *c*-axis. When the curved surface of a resulting quarter-sphere sample (Figure 11a) was illuminated from above parallel to the *c*-axis, we observed iridescent colours (Figure 11b).

With transmitted lighting and crossed polarisers, we observed rectangular or parallelogram-shaped domains underlined by interference colours at different levels within the sample (Figure 11c, d). These features correspond to Brewster fringes, and are due to alternating twin lamellae seen between crossed polarisers, as reported in amethyst (see, e.g., Lu & Sunagawa 1990; Notari *et al*. 2001; Schmetzer 2017). However, they do not have the same sectorial appearance as seen in amethyst.

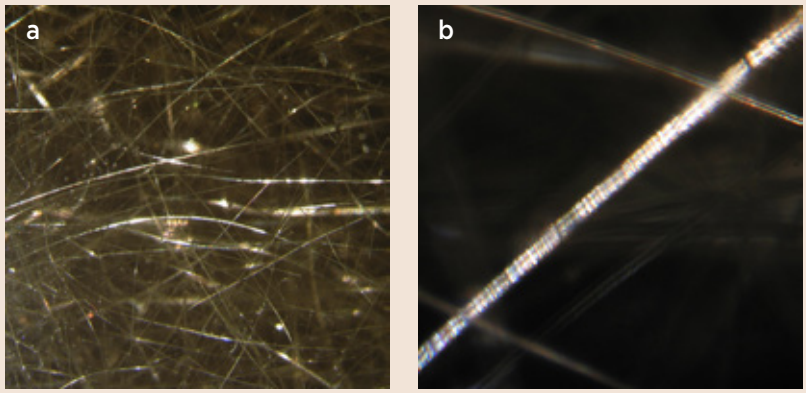

Figure 10: (**a**) Rutile needles in the large quartz sphere are mainly illuminated in a direction that is roughly parallel to the star branch (here, in a horizontal direction). The orientations of the reflections are best observed by slightly squinting when looking at the picture. (**b**) At high magnification, the shiny reflective segments of the rutile needles show a striated appearance. Photomicrographs by J.-P. Gauthier; fields of view (a) 10 × 10 mm and (b) 1 × 1 mm.

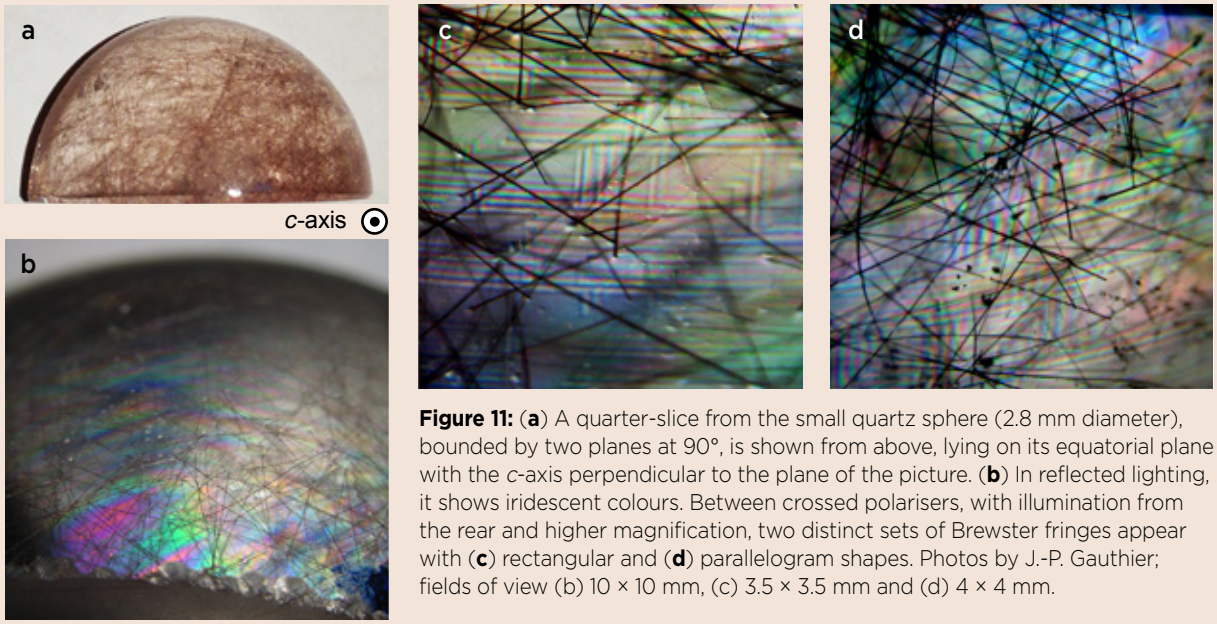

Figure 11: (**a**) A quarter-slice from the small quartz sphere (2.8 mm diameter), bounded by two planes at 90°, is shown from above, lying on its equatorial plane with the *c*-axis perpendicular to the plane of the picture. (**b**) In reflected lighting, it shows iridescent colours. Between crossed polarisers, with illumination from the rear and higher magnification, two distinct sets of Brewster fringes appear with (**c**) rectangular and (**d**) parallelogram shapes. Photos by J.-P. Gauthier; fields of view (b) 10 × 10 mm, (c) 3.5 × 3.5 mm and (d) 4 × 4 mm.

Nevertheless, they reveal the presence of superimposed domains of left-handed and right-handed quartz, corresponding to Brazil-law twinning.

Crystallographically Oriented Thin Sections. To better document the internal structure of the Mercedes-star quartz, two petrographic thin sections (each about 30 µm thick) were cut from the smaller sphere, parallel to the two slices described above. This yielded a full disc parallel to the first slice (S1, oriented perpendicular to the quartz *c*-axis at the equatorial plane) and a half disc cut from one of the remaining hemispheres (S2). Thus, the perimeter of S1 contained six four-rayed star spots, and the hemispherical circular edge of S2 contained two three-rayed and two four-rayed star spots, as well as the *c*-axis (Figure 12a).

With transmitted light, and without polarisers, no remarkable features stood out within the quartz matrix, except for randomly oriented segments of rutile needles (Figure 12b). By rotating the slices between crossed polarisers, both samples became uniformly dark. Then, when rotating the analyser about 1° further, a

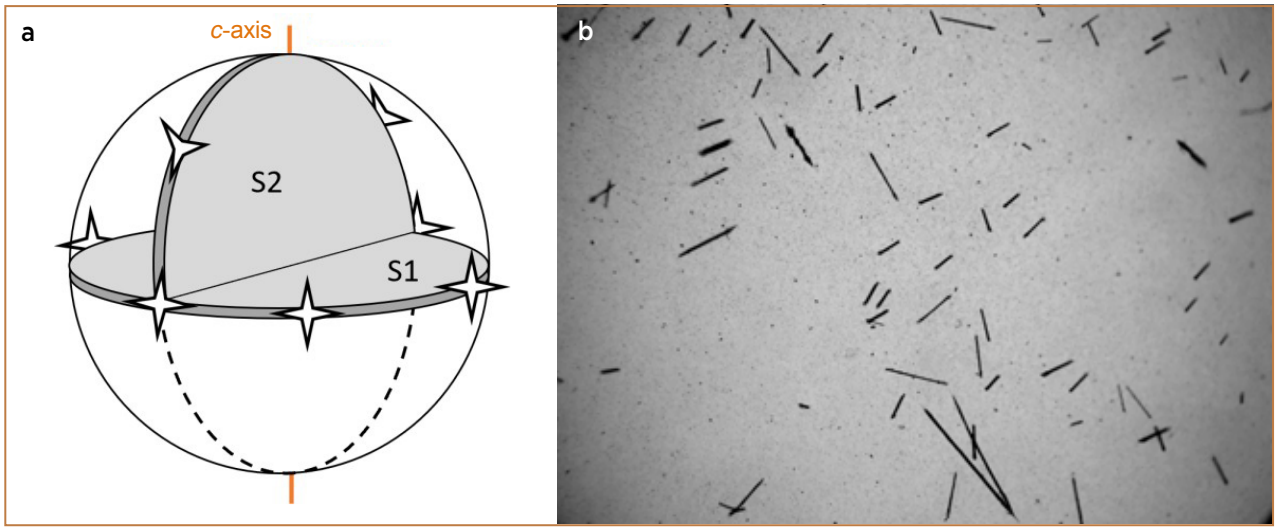

Figure 12: (**a**) A diagram shows the orientation of two slices cut from the small Mercedes-star quartz sphere, with star spots schematically represented along their rims. Slice S1 was cut perpendicular to the *c*-axis along a plane containing six four-rayed star spots. Slice S2 was cut perpendicular to S1 along a meridian containing two three-rayed star spots and two four-rayed star spots. (**b**) The general appearance of these slices, seen illuminated from behind and without light polarisation, shows only randomly oriented segments of rutile needles (here, in slice S1). Photomicrograph by J.-P. Gauthier; field of view 4 × 3 mm.

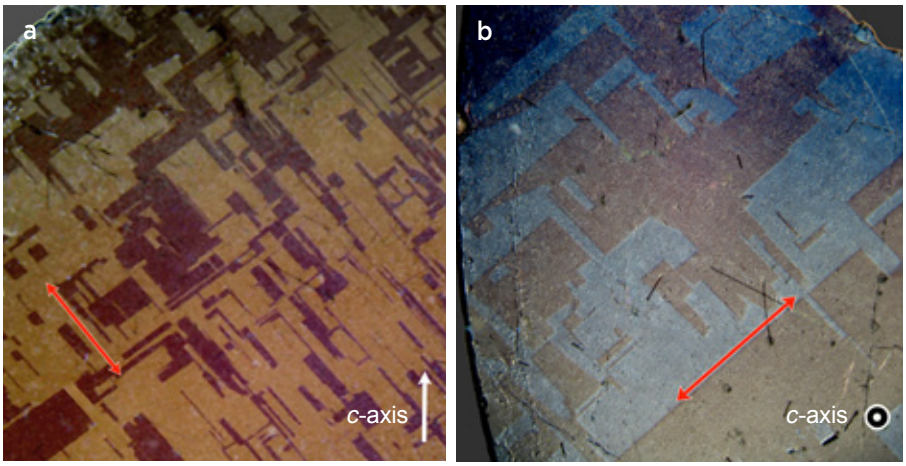

Figure 13: Viewed between crossed polarisers, a slight rotation of the analyser from the extinction position reveals tiling in quartz slices S2 (**a**) and S1 (**b**) that is typical of Brazil-law twin structure made up of right- and left-handed quartz. Contrast was enhanced to make the structures more distinct. The double red arrow indicates the position of the analyser at extinction. Photomicrographs by J.-P. Gauthier; fields of view (a) 10 × 10 mm and (b) 5 × 5 mm.

chequerboard pattern with dark and bright tiles appeared (Figure 13). The pattern reversed when the analyser was rotated in the other direction. This behaviour is expected for Brazil-law twin structure made up of right- and left-handed quartz.

This process is further illustrated using the slice cut parallel to the quartz *c*-axis (S2). In Figure 14a, the polariser is initially parallel to the base of the half-disc (that is, perpendicular to the *c*-axis). The crossed polarisers are then rotated until the sample shows extinction (Figure 14b). Finally, a slight rotation of the analyser reveals the tiles and twin boundaries (Figure 14c), which are oriented at around 50° from the horizontal. This is very close to the inclination of the *r* or *z* planes of the rhombohedron (i.e. 51°27′; Frondel 1962, p. 340).

Unfortunately, there is no crystallographic reference for the horizontal slice (S1). We simply note that extinction occurs when the analyser is parallel to the twin edge (Figure 13b).

It is interesting to note that the tilt angle of the normal (with respect to the horizontal) to the twin boundaries is approximately 40° (again, see Figure 14c), which is also the latitude of the three-rayed star spots (see Table I).

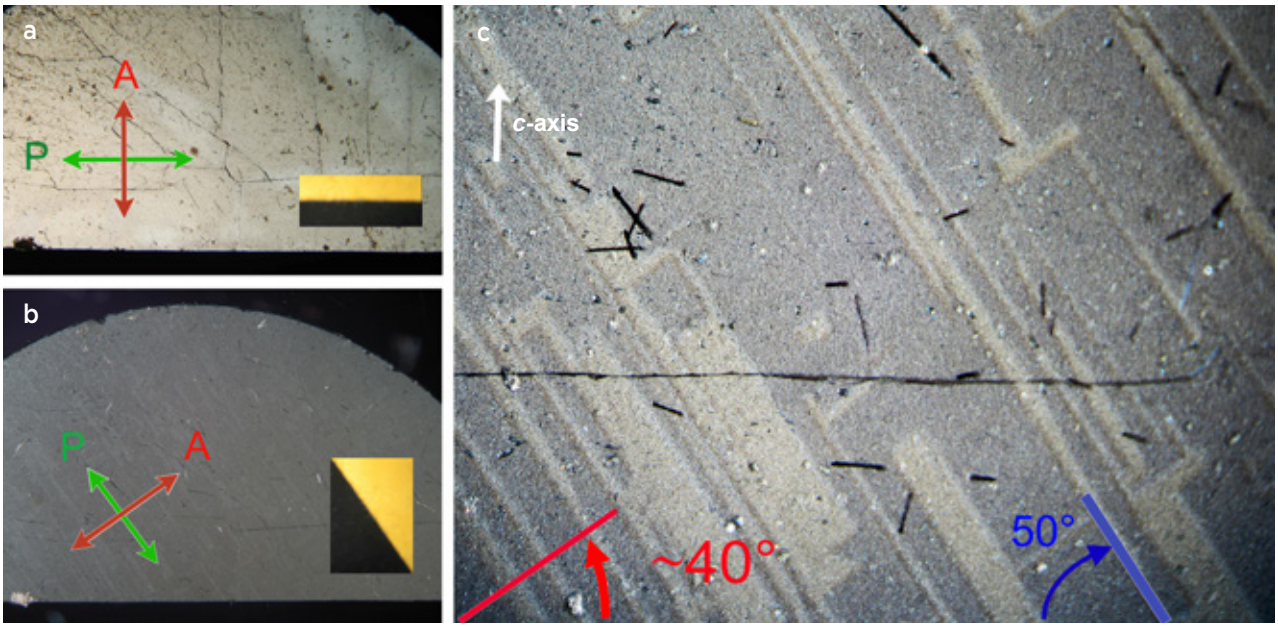

Figure 14: Observation between crossed polarisers of quartz slice S2 reveals: (**a**) when the polariser axis (P) is first aligned with the horizontal diameter (28 mm) of the half disc, the area appears bright, but (**b**) by turning the crossed polarisers about 50°, the area becomes almost uniformly dark. (The yellow self-adhesive birefringent tape in a and b shows the rotation angle of the polariser.) (**c**) By further rotating the analyser (A) by a few degrees, a tiled geometric structure becomes visible. The elongated direction of the structural elements is parallel to the direction of the polariser in Figure 14b. The 40° angle between the red arrow (analyser) and the horizontal corresponds to the latitude of the three-rayed star spots (see Table I), as well as the normal to the rhombohedral faces. The red arrow in a and b indicates the position of the analyser. Photomicrographs by J.-P. Gauthier; field of view 3.5 × 2.65 mm for image c.

DISCUSSION

Proposed Mechanisms of Asterism in Mercedes-Star Quartz

Since we have excluded the presence of sets of invisible parallel fibres leading to a scattering effect, and because randomly oriented rutile needles alone cannot explain a directional optical effect, we must consider a more complex mechanism for the network of stars seen in Mercedes-star quartz, involving both of the following elements highlighted by the experimental observations described above:

1. The presence of Brazil-law twin planes, as revealed both by Brewster fringes and by tiling inside the samples. Not directly visible without polarisers, these can act as reflecting planes due to the change in chirality of the quartz (from left to right, for example), resulting in a slight change in refractive index at the interface.

2. The illumination of some needles, thus playing an obvious role in the formation of the star branches. As the bright reflective markers of the branches, we presume they operate in a second step to produce the asterism.

Figure 15a shows a set of parallel Brazil-law twins (in white) acting as mirrors, and a meridian plane that is perpendicular to this set. With the light source and observer positioned above the quartz sphere, any vertical ray (blue or red) entering this meridian plane will be reflected, by any twin of this set, within this meridian plane. Now consider another set of randomly oriented reflecting planes, none other than the mirror planes observed on rutile needles. The preceding blue and red rays can only be reflected back to the observer by the planes of the rutile needles whose normal lies in the meridian plane (optical paths in blue and red). In any other situation—such as for rutile reflecting planes whose normal is not in the meridian plane, or for incident rays entering outside the meridian plane—the twice-reflected rays usually will not reach the observer.

These conditions are very restrictive, but all rays reaching the observer must cross the sphere on the rim of a meridian plane, giving rise to a luminous branch corresponding to multiple small planes of reflection.

Figure 15b shows, diagrammatically, three sets of primary reflectors (blue), which are required to produce a three-rayed star (yellow) on the rim of the three meridian planes (grey) associated with these stars.

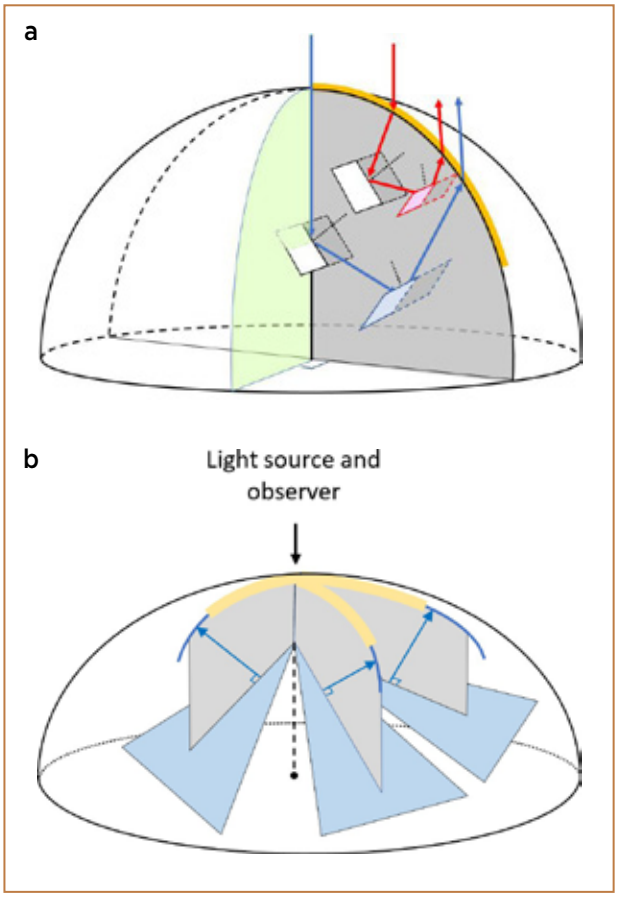

Figure 15: (**a**) This diagram shows the optical path of light rays propagating in a meridian plane that is perpendicular to a set of twin planes (white) in Mercedes-star quartz. A second reflection on a plane (red or blue; belonging to a rutile needle) perpendicular to the meridian plane is necessary for the rays to reach the observer (red or blue paths). The set of rays propagating in (or close to) the meridian plane towards the observer gives rise to a branch of a star (in yellow). (**b**) A general model is depicted for producing a three-rayed star (in yellow) due to the reflection of light from three sets of mirrors (in blue) and then from small planes belonging to the needles (not shown here). The branches of the star lie along three great circles (meridian planes in grey) containing the incident beam and the normals (blue arrows) to the reflecting planes. In Mercedes-star quartz, the three-rayed stars are not seen along the three-fold axis (*c*-axis), but they are visible at an angle of about 50° from it.

So that the branches do not extend beyond the top of the hemisphere—otherwise a six-rayed star would result from the three sets of reflectors—there must be no reflector plane behind the plane perpendicular to the meridian plane, shown in green on Figure 15a. We discuss later if this condition may be satisfied.

Which Planes Are Involved? For the large quartz sphere studied here, the only crystallographic information is the position of the *c*-axis. However, three sets of reflecting planes are needed that are suitable to explain

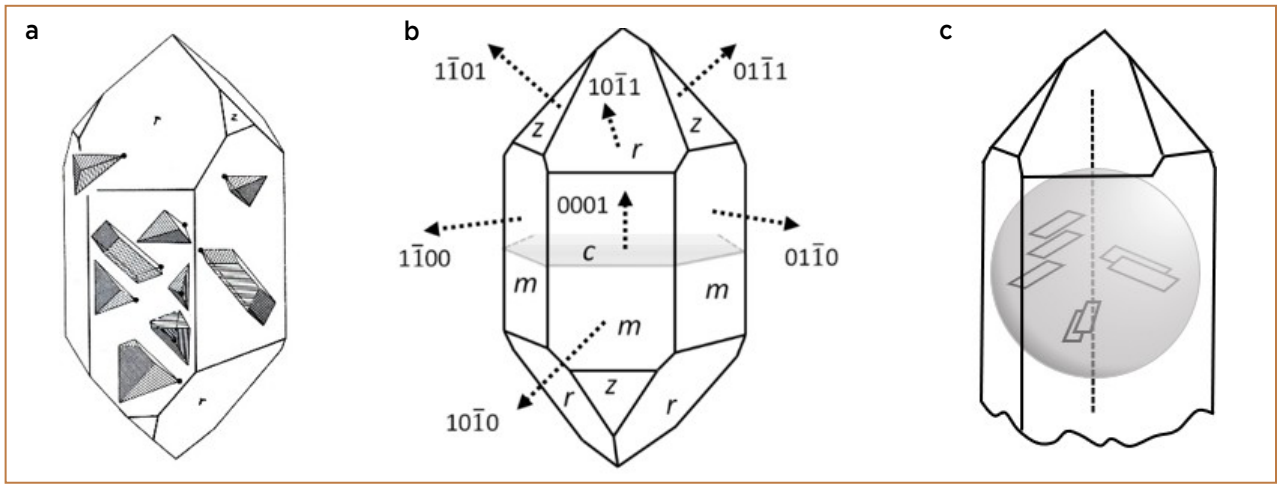

Figure 16: (**a**) This sketch illustrates Brazil twin domains inside a quartz crystal, after Frondel (1962, p. 387). (**b**) A crystal model displays the main faces that develop on quartz and their normals. Twin planes with the same orientations lie within the crystal. (**c**) When 'cutting' a sphere from single-crystal Mercedes-star quartz, it is assumed that the Brazil twin planes do not extend beyond the central axis.

the observed three-rayed stars (again, see Figure 15b), and four planes for the four-rayed stars. It is worth remembering that the three-rayed stars are not viewed down a three-fold axis (*c*-axis) of the quartz.

Brazilian quartz (as well as quartz from other sources) is known to exhibit 'Brazil twins', also called chiral or optical twins (see, e.g., Schmetzer 1987; Lin & Heaney 2017). This is one of two categories of twins with parallel axes known in quartz that is involved here, as shown by the observations between crossed polarisers (Figures 13 and 14). The faces of the twinned volumes shown in Figure 16a are crystallographic planes belonging to the first-order prism *m* {10$\bar{1}$0}, positive rhombohedron *r* {10$\bar{1}$1}, negative rhombohedron *z* {01$\bar{1}$1} (see Figure 16b), basal plane *c* {0001} and triangular dipyramid *s* {11$\bar{2}$1}. Very often, they are manifested in the form of thin, repetitive plates (polysynthetic twins parallel to *r* or *z* planes; Frondel 1962, p. 387). In particular, the lamellar structures in Figure 16c strongly resemble those described by Sunagawa *et al.* (2009), showing the parallelograms that are seen in Brewster fringes.

The most frequently encountered and largest crystallographic planes in quartz usually correspond to the faces of the rhombohedra *r* and *z* and the first-order prism *m*. These are, therefore, the planes that we preferably choose to explain the Mercedes-star quartz asterism. This choice was not made at random. Indeed, as mentioned above, in quartz the angle between the rhombohedral planes *r* or *z* and the basal plane *c* is 51°47′, very close to the angular position of the three-rayed star spots relative to the poles, north or south, at about 50° (Table I).

In addition, it has been assumed that each set of reflecting planes lies on only one side of the vertical sphere diameter (as shown in Figures 15 and 16c) to explain the fact that the branches end at the star centre. It is not possible to have an equivalent reflecting plane (either rhombohedral or prismatic) on the other side of the *c*-axis, simply because it is not also a binary (two-fold) axis. So the plane on the other side is necessarily of a different nature, and thus cannot reflect light the same way. Also, it is probable that within a quartz prism, the lapidary will cut a sphere that is centred within the crystal, if only to obtain the maximum yield (Figure 16c).

Demonstrating the Involvement of These Planes. Consider the observations between the rotation angles 0° and 50° shown in Figure 7a. In the first case, the observer and the light source are in the direction of the quartz's three-fold axis (the *c*-axis). The observer does not see any optical effect. By rotating the sphere upwards by 50° around the horizontal axis in the plane of the drawing, a three-rayed star appears, with a light beam entering perpendicular to the surface of the sphere, thus not deflected by refraction.

According to the description above, the branches of the star will follow the meridians associated with three great circles containing the incoming beam and each of the normals to the reflecting planes. It is then necessary to see if, after rotation by 50°, the chosen planes can explain the appearance of the branches of the three-rayed star in the observed directions.

Stereonet for Three-Rayed Stars. Stereographic projection (Box A) is a method of projecting points and angles onto a circle on a two-dimensional diagram called a stereonet (also known as a Wulff diagram; Bloss 1971;

BOX A: STEREOGRAPHIC PROJECTION ON A STEREONET

This box focuses on angular displacements of the normals to the twin planes when a quartz sphere is rotated around an axis. Stereographic projection can help follow the paths of the ends of normals that originate at the centre Ω of a virtual sphere, with their ends Q on the external surface of this sphere (assumed to have a very large diameter compared to the size of a quartz crystal). As described below, the south pole P' of the sphere plays a special role for points in the northern hemisphere (and by analogy, the north pole P has a similar role for points in the southern hemisphere), making it possible to confine all projections inside the stereographic circle.

By definition, the stereographic projection of the end N of any normal ΩN of the northern hemisphere is located at point Q, which is at the intersection of the equatorial plane and the line joining N to the south pole P' of the sphere (Figure A-1). In Figure A-1a, if we consider all the points N on the circle (C) perpendicular to the west-east direction (W–E), characterised by an angle NΩE = α, their stereographic projection is represented in the equatorial plane by the curved red line Q–Q'. Note that the stereographic projection of a great circle (C') is a line following the diameter of the equatorial plane.

In Figure A-1b, for a point N on a great circle (D) passing through the diameter W–E and tilted by β with respect to the horizontal plane, its stereographic projection Q is located on a curved green line, joining W to E.

On the stereonet (Figure A-1c), the two types of lines (green and red) corresponding respectively to

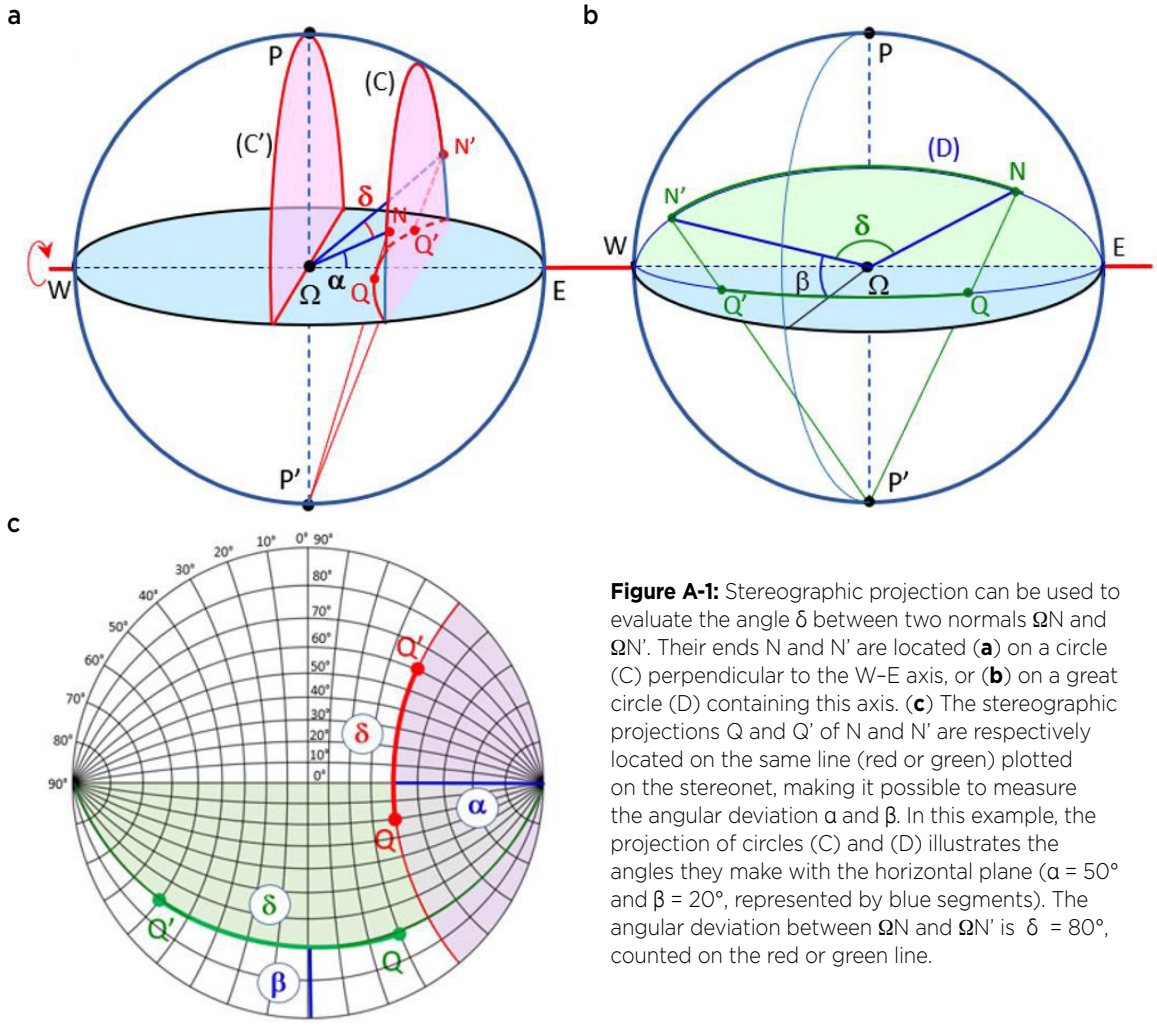

Figure A-1: Stereographic projection can be used to evaluate the angle δ between two normals ΩN and ΩN'. Their ends N and N' are located (**a**) on a circle (C) perpendicular to the W–E axis, or (**b**) on a great circle (D) containing this axis. (**c**) The stereographic projections Q and Q' of N and N' are respectively located on the same line (red or green) plotted on the stereonet, making it possible to measure the angular deviation α and β. In this example, the projection of circles (C) and (D) illustrates the angles they make with the horizontal plane (α = 50° and β = 20°, represented by blue segments). The angular deviation between ΩN and ΩN' is δ = 80°, counted on the red or green line.

α and β (represented by blue segments showing angles α = 50° and β = 20°) are shown on a circle gridded at 10° intervals (more detailed stereonets are gridded at 2°, as in Figure 17 in the text). As an example, if Q' is the projection of N' obtained after rotation from ΩN to ΩN', each projection line provides the corresponding values of the angular deviations δ between ΩN and ΩN' (i.e. rotation of δ = 80° shown in red and green, respectively, in Figure A-1c).

The network of curves in a stereonet makes it straightforward to follow the displacement of the normals to the growth planes or twin planes as a sample is rotated.

Shelley 1985). For this discussion, the light source and the observer are always directed along the vertical axis of the projected sphere (i.e. perpendicular to the plane of Figure 17). We assume that the quartz *c*-axis <0001> initially coincides with this direction, represented by the centre of the stereonet. The other three axes of the quartz are labelled a_1, a_2 and a_3 along the edges of the projection disc (the a_3-axis is omitted from Figure 17 for clarity).

Figure 16b shows the crystal faces that are most likely to be present within a quartz crystal as reflecting twin planes. These are the *r* and *z* rhombohedral faces and *m* faces of the first-order prism. With respect to the *c*-axis, the normals to the faces projected on the stereonet in Figure 17a—from left to right, *z* $(1\bar{1}01)$, *r* $(10\bar{1}1)$ and *z* $(01\bar{1}1)$—make an angle of about 51°47′ with respect to the *c*-axis (Frondel 1962, p. 340) and are, before the rotation, on the same projection circle as the red points in Figure 17a. The projection of the first-order prism face *m* $(10\bar{1}0)$ is also labelled in red at the edge of the stereonet.[1] The situation in Figure 17a is similar to that of Figure 7a for the 0° angle, where the black points represent the star spots.

Starting from this configuration, rotation of the quartz sphere around its a_2-axis from bottom to top by 50° is equivalent to the 50° position in Figure 7a. Then, the poles (initial positions in red on Figure 17) of the *r* and *z* faces move along 'parallels' of the stereographic projection (red arrows on Figure 17a), along which it is possible to count 50° and fix their new positions. We see that the pole *r* (in green) is then at the centre of the stereographic projection in Figure 17a (i.e. facing the direction of the

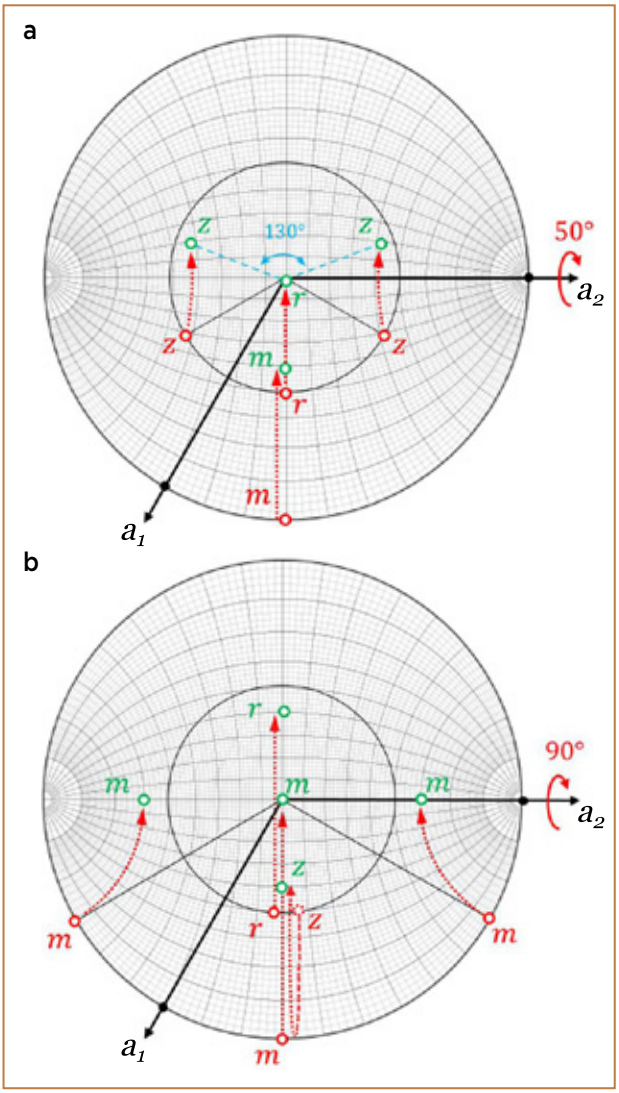

Figure 17: In order to illustrate the correlation between star spots and twin plane directions in Mercedes-star quartz, these stereonets show the movement of the *m*, *r* and *z* poles of a quartz crystal when rotated about the a_2-axis, from an initial position (in red) such as that drawn in Figure 7a (at 0°). (**a**) A 50° rotation brings the poles of faces *m* and *z* (in green) into the same position as shown in Figure 7a (at 50°) with pole *r* at the centre of the diagram (i.e. in the direction of the light source and observer, and coinciding with the centre of the three-rayed star). (**b**) Similarly, a 90° rotation brings pole *m* into the centre of the diagram, coinciding with the centre of a four-rayed star in Figure 7a (at 90°). Arrows indicate the movement of the different poles.

[1] With rotation of 60° around the *c*-axis of the quartz, an analogous situation would occur first with faces *r*, *m* and *r*, and then with the *m* face of the first-order prism. Therefore, if the three-ray star spot at A_1 (longitude 0° for instance) in Figure 5b is produced by a set of *z*-*m*-*z* faces, the next star spot A_2 (thus at the longitude 60°) will be produced by a set of *r*-*m*-*r* faces. Thus, the use of stereographic projection is valid for each three-rayed star.

incident light beam), and that the segments joining it to the two poles *z* make an angle of about 130°. This is exactly the situation in Figures 3c and 7a (centre), where the star spot of a three-rayed star is at the centre (position of green *r*) and the star branches are located on three great circles containing the incident beam and each of the normals to the reflecting planes. The intersection of these three great circles corresponds to the normal to the *r* plane. Note also that the angle of 130° between the branches is not distorted by the stereographic projection, which allows measurement of the real angles on a photograph taken perpendicular to the sphere surface at the centre of a star (again, see Figure 3c).

Given the experimental errors, we propose that the approximate measured value of 50° for the angular positions of the three-rayed stars (points A_n and B_n in Figure 5b) with respect to the north (P) and south (P') poles fits the theoretical angular value of 51°47′ of the *r* and *z* faces of the rhombohedra, with respect to the horizontal (Frondel 1962, p. 340). Importantly, we have shown that the normal to one face of the rhombohedron is coincident to the direction of the light beam, when looking at the star spots. Similarly, the angular value of about 50° measured between crossed polarisers on the twin planes with respect to the horizontal in Figure 14c is close to the experimental value corresponding to the tilt of the rhombohedral faces.

This demonstrates that our measurements are consistent with light reflection on the twinned rhombohedral and prism faces, a rare phenomenon that we propose is responsible for the three-rayed stars through secondary reflections by appropriately oriented portions of the rutile needles.

Stereonet for Four-Rayed Stars. Now consider rotation around the a_2-axis by 90° instead of 50°—that is, from the 0° to 90° position in Figure 7a. The pole of the front first-order prism *m* moves to the centre of the stereographic projection (Figure 17b), and the corresponding plane becomes perpendicular to the incident beam (like the *r* plane in the previous configuration). The poles *m* of lateral planes of the first-order prism migrate on the horizontal axis along the parallels (red arrows). The pole of face *r* is replaced by that of the lower face *z* (initially in the same position on the stereographic projection, but in the southern hemisphere, represented by a dashed red arc), and becomes symmetrical to it with respect to the horizontal axis.

As shown in Figure 17b, the normals to the four planes around the centre (*r*, *z*, *m* and *m*) are on great circles passing through the direction of the incident beam (centre of the stereographic projection). Thus, the four-rayed stars are due to reflection on two non-adjacent *m* faces and a couple of *r* and *z* faces, followed by secondary reflections from the rutile needles. Regarding the weak intensity of the horizontal branch, we assume, without being able to prove it, that the prism faces of the twin interfaces are poorly developed in (or perhaps absent from) the earlier-described Mercedes-star quartz specimens, and constitute only the edges of the twin lamellae.

Finally, the stereonets in Figure 17 show the strong correlation of star spot positions on Figure 7a (at positions 0°, 50° and 90°) with the normals to the *m*, *r* and *z* twin planes.

Reflection of Light by Rutile Needles

To the naked eye, the needles considered in the proposed mechanism appear to shine continuously. At higher magnification, the illumination of the rutile needles reveals segments of closely spaced bright striae. The brightness of the rutile segments is due to the reflection of light on planar features that are perpendicular or oblique to the axis of a needle (Figure 18). This effect can be emphasised by illuminating the inclusions with

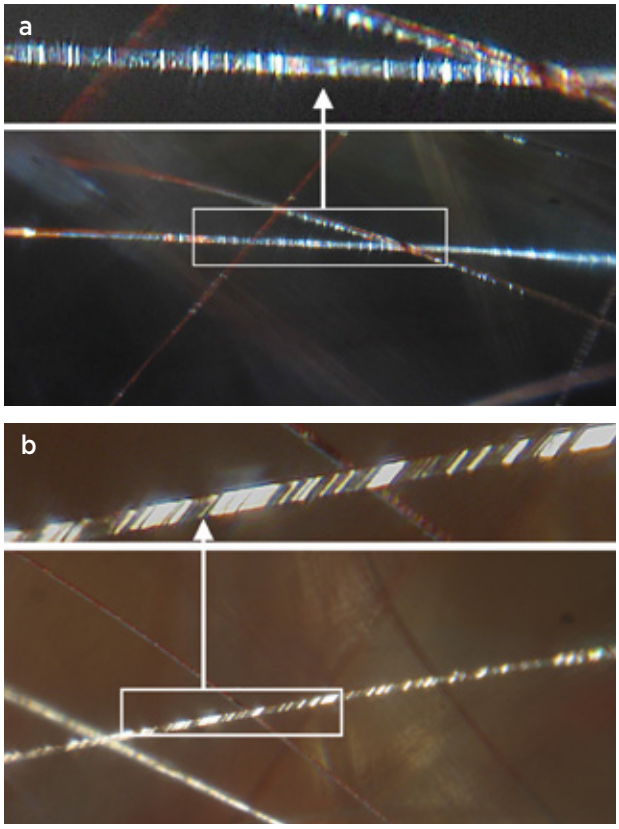

Figure 18: The reflections from the rutile needles consist of striae that are numerous and close together. Depending on the orientation of the needles relative to the light source, they are striated (**a**) almost parallel to the cross-section or (**b**) tilted. Photomicrographs by J.-P. Gauthier; image widths 1.66 mm (a), 1.89 mm (b) and 0.67 mm for both insets.

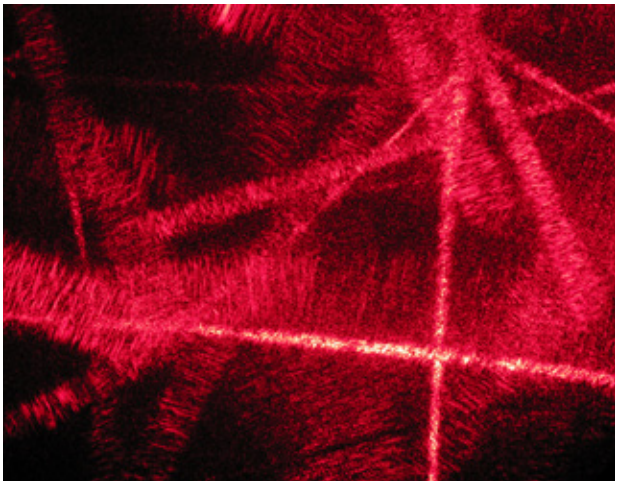

Figure 19: Illumination of the rutile needles with a laser pointer emphasises their reflectivity. Photomicrograph by J.-P. Gauthier; image width 2 mm.

a laser pointer (Figure 19).

Even at high magnification, it is difficult to identify the nature of the tiny reflecting planes on the needles. Are they small facets on the surfaces of the needles, glide planes or planar defects? The answer would require further investigation beyond the scope of this article. For now, it is sufficient to say that these features contribute, as reflectors, to the asterism in Mercedes-star quartz.

Very often, the axis of a needle lies in the direction of the light source (Figure 20) and along a branch of the star. When that happens, the reflections of the striae appear to be perpendicular to the needle axis (Figure 18a). Otherwise, the reflections are oblique (Figure 18b) when a needle axis deviates from the orientation of the light source.

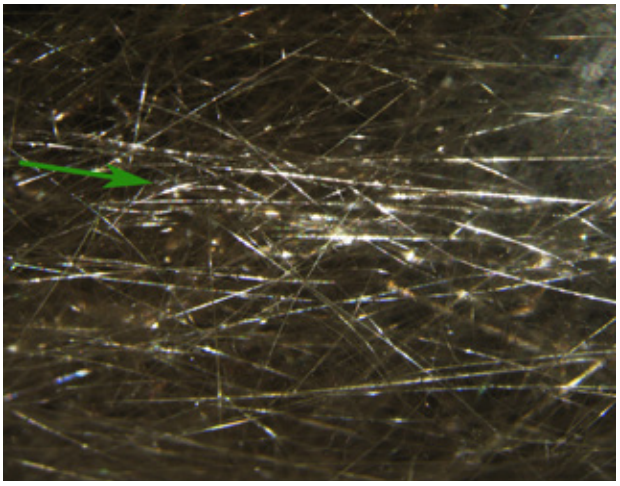

Figure 20: The many illuminated rutile needles in this sub-horizontal star branch are oriented roughly in the same direction (see green arrow). In this case, the mirror striations lie perpendicular to the axis of each needle, as in Figure 18a. Needles that deviate from the general direction indicated by the arrow correspond to the case of Figure 18b. The sample is illuminated from the top of the photo, approximately perpendicular to the arrow. Photomicrograph by J.-P. Gauthier; image width 2.5 mm.

The same kind of striae were seen with transmitted light on the needles in the egg-shaped quartz. Without further analysis, we suspect a similar cause for the diasterism in that specimen, this time involving both *r* and *z* faces, with light directed along the quartz *c*-axis.

In summary, the asterism in Mercedes-star quartz is due to a rare combination of properties. In addition to the characteristics of the rutile needles, the host quartz must be finely Brazil-law twinned, with twinned sectors exhibiting rhombohedral and prism faces. Figure 21 shows the faces involved in the first reflection from the twins, for three-and four-rayed stars. In Figure 21a, the normal to face *r* (in grey) is in the direction of a three-rayed star spot, and the corresponding star branches are produced by the primary reflections of twin planes *z*, *z* and *m* (in orange). In Figure 21b, the face *m* (in grey) is in the direction of a four-rayed star spot, whose branches are produced by the lateral *m* planes and by the upper and lower planes *r* and *z*, respectively (in orange). If the quartz is rotated by 60°, the same observation will be made for the two types of stars, simply by inverting the *r* and *z* notations.

CONCLUSION

The unusual asterism observed in Mercedes-star quartz seems to exist only with the simultaneous presence of Brazil-law twins and rutile needles. We therefore propose a plausible mechanism that we can at least partially

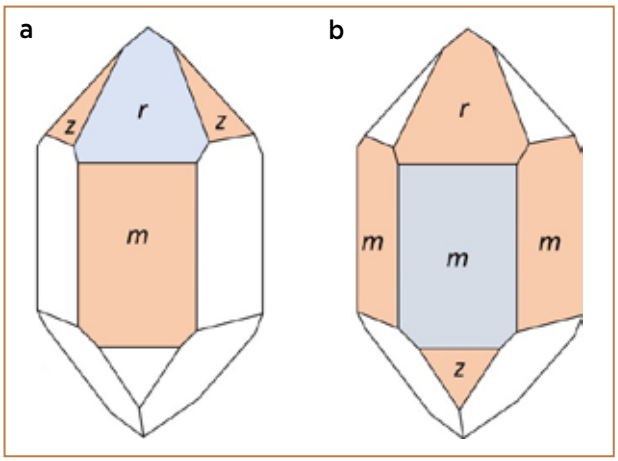

Figure 21: Twin planes participating in the first reflection needed to produce (**a**) three-rayed stars and (**b**) four-rayed stars are shaded orange. When a three- or four-rayed star centre is positioned at a star spot, the respective grey planes are perpendicular to the incident beam of light.

validate through crystallographic observation and reasoning. This unusual asterism arises from a double-reflection mechanism based on the following observations:

- Classical chatoyancy—light scattering on sets of oriented acicular inclusions—was ruled out due to the absence of parallel needles (even at sub-microscopic scale, as validated using the water-drop test) and by the fact that the branches stop at the centre of each three-rayed star.
- The existence of 'optical twins' in Mercedes-star quartz was visible in slices and thin sections cut from one of the samples through the presence of Brewster fringes and tiling (Figures 11 and 13). The occurrence of these twins induces the presence of flat reflective surfaces due to the change of chirality at the interface between the twin planes.
- This type of asterism has never been documented in transparent quartz containing Brazil twins but without rutile needles. Thus, the needles play a key role in this phenomenon.
- While light scattering on oriented acicular inclusions induces a six-rayed star in minerals with a three-fold symmetry axis, the present phenomenon first requires three sets of reflective planes not related to three-fold symmetry, but which are due instead to Brazil twins.
- Randomly oriented rutile needles can intercept the light reflected from the twin planes and send it back towards the observer, provided that the entire light path is in or near a meridian plane of the quartz sphere. The secondary reflection inducing the asterism is not due to the total surface area of rutile needles, but from numerous, discrete, parallel small reflective elements of the needles, the exact nature of which we could not identify by optical microscopy.
- The locations of star spots, supported by stereographic projections, showed a strong correlation with the directions of the normals to the *r*, *z* and *m* planes.
- Due to the random angular distribution of the rutile needles and, thus, of their reflective elements, a high needle density is required to produce enough reflections towards the observer to create the epiasterism in Mercedes-star quartz. However, when very high inclusion density makes the stone opaque, diasterism cannot be observed.

This study represents a major step towards the understanding of Mercedes (three-rayed) stars in quartz. This relatively rare and particularly complex optical phenomenon is related not only to inclusions, but also to the twinned nature of otherwise transparent quartz. The requirement of both a sufficient density of inclusions and Brazil twins means that specimens are generally large (i.e. multi-centimetre sized). Although less attractive than the usual asteriated gems due to the diffuse appearance of the stars, Mercedes-star quartz is certainly an interesting curiosity for collectors.

REFERENCES

Bloss, F.D. 1971. Crystal projections. *In*: *Crystallography and Crystal Chemistry*. Holt, Rinehart and Winston Inc., New York, New York, USA, 70–298.

Choudhary, G. & Vyas, M.B. 2009. 'Multiphenomenal' quartz from India. *Gems&Jewellery*, **18**(1), 10–12.

Frondel, C. 1962. *Dana's System of Mineralogy, Vol. 3: Silica Minerals*, 7th edn. J. Wiley, New York, New York, USA, xii + 334 pp.

Gauthier, J.-P. 2011. Amusantes et instructives variations sur le thème de la détection de la chatoyance. *Revue de Gemmologie A.F.G.*, No. 178, 21–24.

Gübelin, E.J. & Koivula, J.I. 2005. *Photoatlas of Inclusions in Gemstones*, Vol. 2. Opinio Publishers, Basel, Switzerland, 829 pp.

Gübelin, E.J., Weibel, M. & Wuthrich, A. 1982. Elucidating the optical theory of asterism. *Journal of the Gemmological Society of Japan*, **9**(1), 18–21, https://doi.org/10.14915/gsjapan.9.1_18.

Hainschwang, T. 2007. Gem News International: An unusual type of phenomenal quartz. *Gems & Gemology*, **43**(3), 261–262.

Hyršl, J. & Niedermayr, G. 2003. *Magic World: Inclusions in Quartz*. Bode Verlag, Haltern, Germany, 240 pp.

Johnson, M.L. & McClure, S.F. 1997. Gem Trade Lab Notes: Quartz, cat's-eye effect caused by large rutile needles. *Gems & Gemology*, **33**(1), 59.

Johnson, M.L. & Koivula, J.I. (eds) 1999. Gem News: Twelve-rayed star quartz from Sri Lanka. *Gems & Gemology*, **35**(1), 54–55.

Kane, R. 1985. Gem Trade Lab Notes: Quartz, very dark reddish gray cat's-eye. *Gems & Gemology*, **21**(2), 112–113.

Killingback, H. 2006. Diasterism in rose quartz. *Gems&Jewellery*, **15**(3), 64.

Killingback, H. 2008. The positions of light spots on rose quartz star spheres. *Journal of Gemmology*, **31**(1–2), 40–42, https://doi.org/10.15506/jog.2008.31.1.40.

Koivula, J.I. 1987. Gem News: Phenomenal quartz from Brazil. *Gems & Gemology*, **23**(3), 175–176.

Koivula, J.I. & Tannous, M. 2003. Gem News International: "Platinum quartz". *Gems & Gemology*, **39**(4), 334–335.

Koivula, J.I. & Tannous, M. 2004. Lab Notes: Three rutilated quartz cat's-eyes. *Gems & Gemology*, **40**(1), 63.

Lin, X. & Heaney, P.J. 2017. Causes of iridescence in natural quartz. *Gems & Gemology*, **53**(1), 68–81, https://doi.org/10.5741/gems.53.1.68.

Lu, T. & Sunagawa, I. 1990. Structure of Brazil twin boundaries in amethyst showing Brewster fringes. *Physics and Chemistry of Minerals*, **17**(3), 207–211, https://doi.org/10.1007/bf00201451.

Notari, F., Boillat, P.-Y. & Caplan, C. 2001. Quartz α-SiO_2: Discrimination des améthystes et citrines naturelles et synthétiques. *Revue de Gemmologie A.F.G.*, No. 141/142, 75–80.

Schmetzer, K. 1987. Microscopic observation of twinning microstructure in natural amethyst. *Neues Jahrbuch für Mineralogie, Monatshefte*, No. 1, 8–15.

Schmetzer, K. 2017. Distinction of natural and synthetic ametrine by microscopic examination—A practical approach. *Journal of Gemmology*, **35**(6), 506–529, https://doi.org/10.15506/JoG.2017.35.6.506.

Schmetzer, K. & Bernhardt, H.J. 2002. Star garnets from Ilakaka, Madagascar. *Australian Gemmologist*, **21**(5), 202–206.

Schmetzer, K. & Glas, M. 2003. Multi-star quartzes from Sri Lanka. *Journal of Gemmology*, **28**(6), 321–332, https://doi.org/10.15506/JoG.2003.28.6.321.

Schmetzer, K. & Krzemnicki, M. 2006. The orientation and symmetry of light spots and asterism in rose quartz spheres from Madagascar. *Journal of Gemmology*, **30**(3), 183–191, https://doi.org/10.15506/JoG.2006.30.3.183.

Schmetzer, K. & Steinbach, M.P. 2022. Gem News International: Three-rayed asterism in quartz. *Gems & Gemology*, **58**(2), 249–252.

Schmetzer, K. & Steinbach, M.P. 2023. Gem Notes: Three-rayed asterism in quartz: A multi-star network. *Journal of Gemmology*, **38**(6), 552–553, https://doi.org/10.15506/JoG.2023.38.6.552.

Shelley, D. 1985. *Optical Mineralogy*. Elsevier, New York, New York, USA, 321 pp.

Steinbach, M.P. 2017. *Asterism: Gems with a Star*. MPS Publishing and Media, Idar-Oberstein, Germany, 896 pp. (see pp. 649–651).

Sunagawa, I., Iwasaki, H. & Iwasaki, F. 2009. Morphology of natural quartz crystals. *In*: *Growth and Morphology of Quartz Crystals Natural and Synthetic*. Terrapub Scientific Publishing Company, Tokyo, Japan (see chapter 6, pp. 125–132).

Walcott, A.J. 1937. Asterism in garnet, spinel, quartz and sapphire. *Geological Series of Field Museum of Natural History*, **7**(3), 39–57, https://doi.org/10.5962/bhl.title.3353.

Weibel, M. 1982. Wie entsteht der Stern? Asterismus und Chatoyance bei Edelsteinen. *Lapis*, **7**(10), 25–27, 30, 38.

The Authors

Prof. Jean-Pierre Gauthier and Jacques Fereire
Centre de Recherches Gemmologiques,
U.F.R. des Sciences et des Techniques,
Université de Nantes,
2, rue de la Houssinière,
44072 Nantes Cedex 3, France

Dr Emmanuel Fritsch FGA
Institut des Matériaux Jean Rouxel CNRS
(UMR 6502), University of Nantes,
BP 32229, F-44322, Nantes Cedex 3, France
Email: emmanuel.fritsch@cnrs-imn.fr

Thanh Nhan Bui
Rue du Compas, 47/4, 1070 Brussels, Belgium

Moldavite from Chlum, Czech Republic: Mining and Gem Properties

Tom Stephan, Štěpán Jaroměřský, Lukáš Zahradníček and Stefan Müller

ABSTRACT: One of the most well known and popular natural glasses is moldavite, which formed during a meteorite impact about 14.8 million years ago. Today, moldavite is mainly obtained from the Czech Republic. In spring 2022, the authors visited the largest mine currently in operation, a sand-and-gravel quarry near the small village of Chlum in the southern Czech Republic, where moldavite is found as a by-product. This article reviews the formation and distribution of moldavite, gives an overview of current mining activities and reports the gemmological characteristics of samples collected by the authors.

The Journal of Gemmology, **38**(7), 2023, pp. 696–707, https://doi.org/10.15506/JoG.2023.38.7.696

Tektites (from the Greek *tektos* = molten) are natural glasses that formed by meteorite impacts on the earth's surface. One of the most well-known tektite varieties is moldavite (Figure 1), which is named after the main occurrence along the Vltava (or *Moldau* in German) River in the Czech Republic. This tektitic glass originated during a meteorite impact around 14.8 million years ago in the region of today's Nördlinger Ries in Germany (Schmieder *et al.* 2018). The impact created temperatures that melted the rocks on the surface and blasted the glassy droplets eastward over 400 km to the upper reaches of the Vltava River and into Moravia in today's Czech Republic. Occasionally, moldavites have also been found in Austria, Germany and Poland (Brachaniec *et al.* 2014; Schmieder *et al.* 2018).

Moldavite has been used by humans since prehistoric times, as sharp-edged pieces for numerous tools and as amulets. The earliest finds were in Austria in the Gudenus cave near Krems, as well as near Willendorf; they date back to Palaeolithic time (Bayer 1921).

During the modern era, moldavite was particularly popular during the Art Nouveau period (1890–1910). Subsequently interest declined, coincident with the increased use of green bottle glass as an imitation. Later, during the early 1950s and 1960s, moldavite experienced a renaissance as a gem and collectable material, which spurred exploration to discover additional mining sites in what is today the Czech Republic. As a result of this geological survey, the sand-and-gravel layers near Chlum nad Malší (hereafter,

Figure 1: This moldavite shows a valuable 'hedgehog' shape and comes from the Besednice locality in the South Bohemian Region of the Czech Republic. Photo by Jan Loun.

Figure 2: The main moldavite deposits in the Czech Republic lie in the southern part of the country in the regions of South Bohemia and South Moravia. Moldavite occurrences are also known in Germany, Austria and Poland. Map adapted from Wikimedia Commons (https://commons.wikimedia.org/wiki/File:Czech-regions.svg).

simply 'Chlum'; Figures 2 and 3) in the South Bohemian Region were identified as a source of moldavite (Bouška *et al*. 1985).

Today, a large sand-and-gravel pit is actively being operated near Chlum, and moldavite is recovered there as a by-product. In addition, another smaller quarry was opened in 2022 just north of the nearby village of Besednice, where moldavite is the only product that is mined (Dr Vít Kršul, pers. comm. 2023).

In May 2022, the authors had an opportunity to visit the Chlum deposit in order to witness the mining process and collect samples. In this article, we review the formation of moldavite and its main localities, and then examine the current mining techniques and describe the results of our examination of the collected samples.

MOLDAVITE FORMATION

Moldavite most likely originated during the meteorite impact responsible for the Nördlinger Ries crater in Bavaria, Germany. This crater formed approximately 14.8 million years ago, during the Miocene (Bouška & Konta 1999; Böhme *et al*. 2002; Di Vincenzo & Skála 2009; Schmieder *et al*. 2018; Schwarz *et al*. 2020). Gentner (1971) performed age determination using the K/Ar method, and showed that moldavite and the Ries event both have the same age, thus linking their origins. Graup *et al*. (1981) geochemically identified the pre-impact sediments as upper freshwater molasse (i.e. terrestrial clastic sedimentary rocks).

According to Pösges and Schieber (2009), the Ries crater resulted from the impact of a meteorite with a diameter of around 1 km that hit with a speed of about 70,000 km/h, corresponding to the energy of 250,000 Hiroshima bombs. The impact body and the surrounding rock were compressed to about a quarter of their previous volume, creating a pressure of 4 Mbar and temperatures up to 30,000°C. Melted rock materials were ejected from the crater, and a mushroom-shaped ash cloud formed to a height of 100 km. A total of 1,000 km^3 of material was moved by the impact, with 150 km^3 of rock ejected ballistically at up to 25 times the speed of sound. While in flight, the ejected molten rock droplets cooled rapidly and solidified into a glassy substance (moldavite) that was thrown as far as 400 km eastward in the direction of today's Czech Republic. The resulting crater had a diameter of about 15 km and an original depth of 4 km, but it filled relatively quickly due to gravitational collapse that occurred during subsequent basement uplift and displacement by vertical and lateral movements (see also Stöffler *et al*. 2013).

MOLDAVITE DEPOSITS AND MINING

The moldavite deposits are located in southern Bohemia, western Moravia and the Cheb Basin in the Czech Republic, Lusatia in Germany, Waldviertel in Austria (Trnka & Houzar 2002; Hanus 2016) and Lower Silesia in Poland (Brachaniec *et al*. 2014). The largest deposits

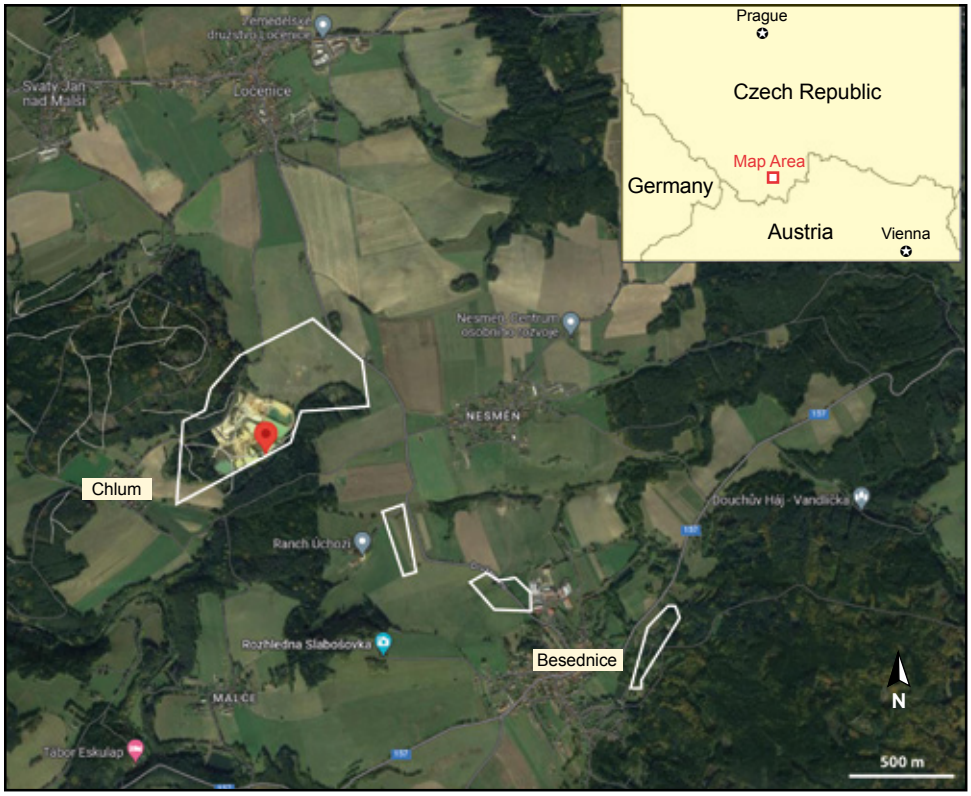

Figure 3: This satellite image (from Google Maps) shows the locality of the sand-and-gravel quarry (red pin) near Chlum. The additional white outlines indicate officially recognised moldavite deposits in the Chlum-Besednice area (taken from a map supplied by Dr Vít Kršul, July 2023). The illegal mining pits mentioned in this article were seen in the forest at the top-centre of the image.

are spread over the regions of South Bohemia and South Moravia (Figure 2).

The most important moldavite deposits form a belt of separate occurrences between Písek and Nové Hrady (again, see Figure 2). The stones were concentrated by gravity and water on the south-west margin of the South Bohemian basin. They occur in sedimentary deposits such as the Koroseky sands and gravels (KSG) in southern Bohemia (e.g. Chlum; see Figure 4) and the Vrábče beds (VB; Trnka & Houzar 2002). The dating of individual sedimentary deposits that contain moldavite is a matter of debate, as are the topographical, morphological and chronological connections among the sites. The deposition of the moldavite-bearing sediments possibly occurred during the Pliocene and early Pleistocene (Bouška & Konta 1999), but the Miocene is often mentioned (Trnka & Houzar 2002). Most of the sediments are colluvial-fluvial sandy clays and/or clayey sands, which fill stream depressions and ravines or form dejection cones. Their thickness is usually around a few metres. The main components of these sediments are quartz and feldspar. At the Chlum site, there is a broader association of moldavite with gravel layers containing 'heavy minerals' such as zircon, rutile, leucoxene and kyanite, while those discovered at Besednice include andalusite, tourmaline and kyanite (Trnka & Houzar 2002).

Various shapes and morphologies are typical for moldavite from different localities. Stones from the KSG deposits in southern Bohemia (e.g. Chlum and Besednice) appear to be less rounded than those from northern KSG locations such as Koroseky. The average weight of VB stones is approximately 2 g, whereas KSG moldavites tend to be larger. Alluvial transport of the moldavite from the original point of impact affected the size and, often, shape of the material. This transport effect can also be observed on coexisting quartz pebbles, which vary from angular fragments to rounded shapes (Trnka & Houzar 2002). This leads to the assumption that the KSG deposits are a polygenetic formation that includes material of different origins. Moldavite from the VB deposits typically shows deeper surface corrosion lines and depressions formed by the chemical action of groundwater in an acidic, permeable environment. A simplified explanation is that after deposition in the host sediments, the less-resistant zones of the moldavite surfaces experienced greater etching due to the influence of differently saturated waters (see Bouška *et al.* 1985).

Thus, the overall shape of moldavite pieces results from a combination of the original fragmentation of the melt, aerial flight, alluvial transport and, finally, post-depositional chemical etching. A rare and quite valuable shape of moldavite from the Besednice locality resembles that of a hedgehog (again, see Figure 1), which mainly results from post-depositional chemical etching. The distinctive surface features of many moldavites are especially useful because careful observation of them

Figure 4: (**a**) The sand-and-gravel quarry near Chlum is expansive. The sediments lie on top of gneissic bedrock (exposed as the dark area on the far side of the smaller pit to the left). (**b**) Mining involves the use of excavators and trucks. A claystone horizon (indicated by the arrow) forms a darker brown layer in the pit wall in the foreground. (**c**) Moldavite is found in subhorizontal gravel layers. (The vertical lines are from the excavator used to mine the sediments.) Photos by T. Stephan.

can help distinguish genuine moldavite from the many glass imitations (e.g. Tay 2007; Tay *et al*. 2008; Hyršl 2015; Hanus & Hyršl 2018).

Today, moldavite specimens are housed in various museums, research facilities and private collections worldwide. The world's largest public collection of moldavite is found at the National Museum in Prague (see Box A).

Moldavite Deposit near Chlum

The small village of Chlum nad Malší is located about 200 km south of Prague (Figure 2). North-east of the village is a quarry where sand and gravel are mined (again, see Figures 3 and 4). The approximately 700 × 400 m pit contains several layers of sand and gravel, tens of metres thick, lying on gneiss bedrock. The sand-and-gravel layers are crossed by a claystone horizon at several metres depth, but which does not run horizontally throughout the deposit. Moldavite is always found above this horizon.

The sand-and-gravel layers are dug with excavators and taken by trucks to a nearby washing plant. There the material is transported by conveyor belts to various washing and sieving stations for sorting into different grain-size fractions for industrial uses (Figure 5a). After removing the smaller fractions, the moldavite is hand-picked at an intermediate facility (Figure 5b), which we were not allowed to visit.

According to the on-site geologist, about 100,000–150,000 tonnes of sand and gravel materials are mined annually from the quarry. The average moldavite recovery is 2.5–3 g/tonne, although the grade of the different horizons varies. Most of the moldavite specimens weigh 0.1–15 g each, but about 20% of them are larger.

On the day of our visit, we were allowed to search a particular area of the pit to a depth of about 5 m below the surface. The sand layer in this area was interspersed with several coarser-grained gravel horizons with clast sizes up to about 1.5 cm (Figure 6). We found moldavite specimens in these layers, and also on the surface, especially along the transportation routes of the trucks. Within 90 minutes of searching, we collected about 150 g of moldavite samples, consisting of fragments of

BOX A: MOLDAVITE IN THE NATIONAL MUSEUM OF THE CZECH REPUBLIC

The National Museum in Prague contains the largest public collection of moldavite in the world. Currently, its tektite collection includes 20,702 moldavite specimens from South Bohemia and 1,988 samples from Moravia. It is valuable not only for the great number of specific localities represented (140), but also for showing such extensive variability in morphology, colour and size. Here we review the history and the most interesting moldavite specimens in the permanent exhibition there, as well as some samples that are stored in depositories. Another (private) moldavite museum is located in Český Krumlov, close to the moldavite deposits, and is highly informative.

The tektite collection of the National Museum was founded in 1930 by the purchase of František Hanuš's collection of about 6,000 moldavites of excellent quality from Bohemian and Moravian localities (Velebil 2020). Until then, the museum had only a few moldavite specimens, including the oldest documented one in the collection: a 38 g specimen from Dolní Chrášťany that was acquired by Josef Kořenský (1847–1938). This moldavite is curiously perched on a flat pebble with which it was allegedly found (Figure A-1). An open cavity on one side of the moldavite is apparently the remnant of a large gas bubble.

In 1936, the purchase of 350 moldavites from Arnošt Hanisch of Třebíč expanded the National Museum's collection significantly with specimens from Moravia. In subsequent years, additional Moravian moldavites were purchased from collectors J. Fiala and J. Krejčí, also of Třebíč. It is important to realise that, at this time, moldavites were mostly regarded as mere glass, so they did not become very valuable until the mid-1960s. This is why the collection continuously added fine specimens (e.g. Figure A-2) during most of the twentieth century, including the acquisition of 1,972 moldavite specimens collected in 1972–1974 by B. Hrabě of České Budějovice. In the following decades—during the 1980s and especially after the millennium—donations and purchases of moldavites from collectors and mining companies became less frequent. Nevertheless, one of the most valuable of these donations took place in 2005 by collector S. Langer, who provided 16 Moravian moldavites, including some relatively large specimens.

Figure A-1: The oldest documented moldavite specimen in the National Museum's collection is a 38 g specimen from Dolní Chrášťany, sitting on a pebble. Reportedly, the piece was found like this. Collection of Josef Kořenský; photo by D. Velebil.

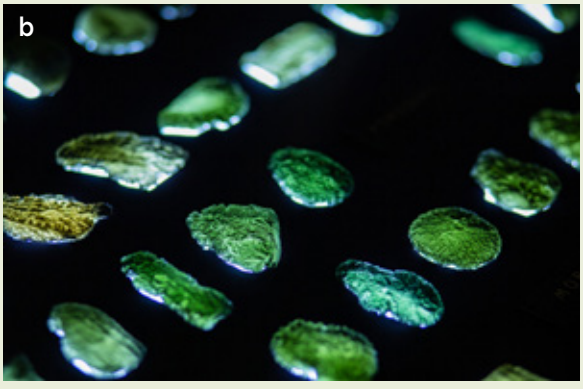

Figure A-2: (**a**) Many of the moldavites at the National Museum are displayed in their original showcases, which have been restored. (**b**) The backlit specimens seen here are a small sample of the more than 20,000 moldavites in the museum's collection (image width approximately 13 cm). Photos by L. Zahradníček.

The National Museum's best moldavite specimens are on display in its Hall of Meteorites (e.g. Figure A-2). The largest South Bohemian moldavite in the collection is a 111 g specimen from Strpí, near Vodňany (collection of B. Hrabě, 1972). The largest Moravian moldavite in the collection weighs 235 g (collection of S. Langer, 2005) and comes from Kožichovice. The next largest Moravian moldavites are also from Kožichovice: 147 g (collection of A. Hanisch, 1942), 124 g (collection of S. Langer, 2005) and 104 g (collection of K. Žebera, 1980). Three noteworthy moldavites in the National Museum's collection were found (and thoroughly documented) in Central Bohemia: two came from the Kobylisy sand quarry in Prague, and the third came from another sand quarry in Jeviněves near Mělník. These are extremely uncommon localities for moldavite.

Moldavite most likely initially became popular during the Land Jubilee Exhibition in Prague in 1891, which featured a display of jewellery set with faceted moldavite and complemented with pearls from the Vltava and Otava rivers. Unfortunately, interest in faceted moldavite promptly declined because jewellery manufacturers in the 1890s did not take the gem seriously. In addition, they often confused moldavite with cut green bottle glass. Because of this, there are relatively few (42) faceted moldavites in the National Museum's gem collection (Figure A-3a). Their largest cut Bohemian moldavite weighs 48.25 ct and the largest faceted Moravian one is 27.25 ct.

Unfortunately, it is now difficult for the museum to acquire better cut moldavites, because collectors keep most such gems for themselves, and the museum does not have the budget to purchase fine specimens when they become available. Interestingly, during a review of the collection in 2016–2022, several samples of cut bottle glass were discovered, with typical air bubbles and star-shaped flux inclusions (Figure A-3b, c).

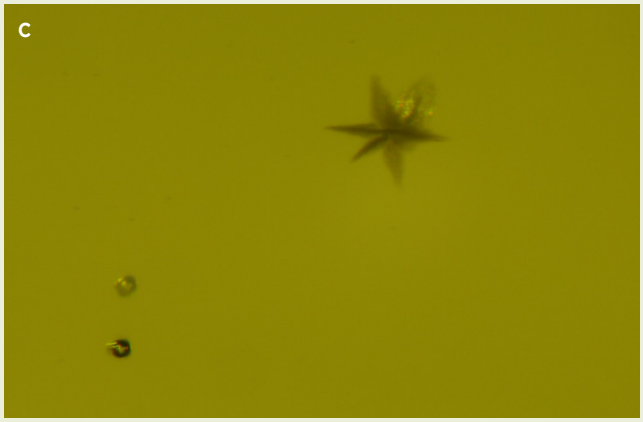

Figure A-3: (**a**) The entire collection of cut moldavites at the National Museum consists of these 42 stones. (**b**) These two faceted samples (15.02 and 19.45 ct) were identified as bottle glass in 2018 during a review of the collection. (**c**) Typical inclusions in bottle glass are gas bubbles and star-like devitrification features (magnified 50×). Photos by L. Zahradníček.

Figure 5: (**a**) The mined sediments are processed in this washing and sorting plant. (**b**) After screening out smaller size fractions, the moldavites are hand-picked in the green building. Photos by T. Stephan.

a few millimetres to pieces 4–5 cm long. Notably, we found some flat, disc-shaped specimens, always with the etched surfaces mentioned above. Special highlights were a teardrop-like piece and a curved sample (Figure 7), shapes which are relatively rare.

Illegal Mining

Moldavite is one of the most sought-after stones in the Czech Republic. The deposits are located relatively close to the surface, so it is easy to reach the moldavite-bearing layers using hand tools. Also, it is not uncommon to find moldavite on the surface of farmed fields, especially after ploughing or heavy rains. These conditions are ideal for illegal mining. Moldavite is classified as state property in the relatively few deposits recognised by mining authorities that have been documented by official geological surveys. Elsewhere, moldavite mining is not directly forbidden, but in the Czech Republic digging is not allowed without official government permission, even on one's own private property. In short, without permits, mining is not allowed. Despite these regulations, surface disturbances related to the informal extraction of moldavite are common (e.g. Figure 8).

In some agricultural fields and, especially, in the surrounding forests, moldavite is mined by digging shallow pits up to 2–3 m deep. The pits are dug vertically until the moldavite-containing layer is reached, and then excavated horizontally. Since the pits are dug in soft sediments, the workings are quite unstable. Furthermore, they are not properly reclaimed after digging. The excavations also damage the roots of forest trees, causing them to die and/or be uprooted by the wind. In addition, wild animals may fall into the deeper pits and be unable to escape. There were so many illegal pits in some areas that the nearby communities decided to go through legal extraction procedures and then restore the disturbed areas.

Illegal mining is a punishable offence, and police

Figure 6: (**a**) The authors were allowed to search for moldavite around the rim of the pit as deep as 5 m below the surface, where we focused on areas of coarser grain size. (**b**) The dark specimen seen here is a 2.5-cm-wide moldavite, shown where it was found *in situ*. Photos by T. Stephan.

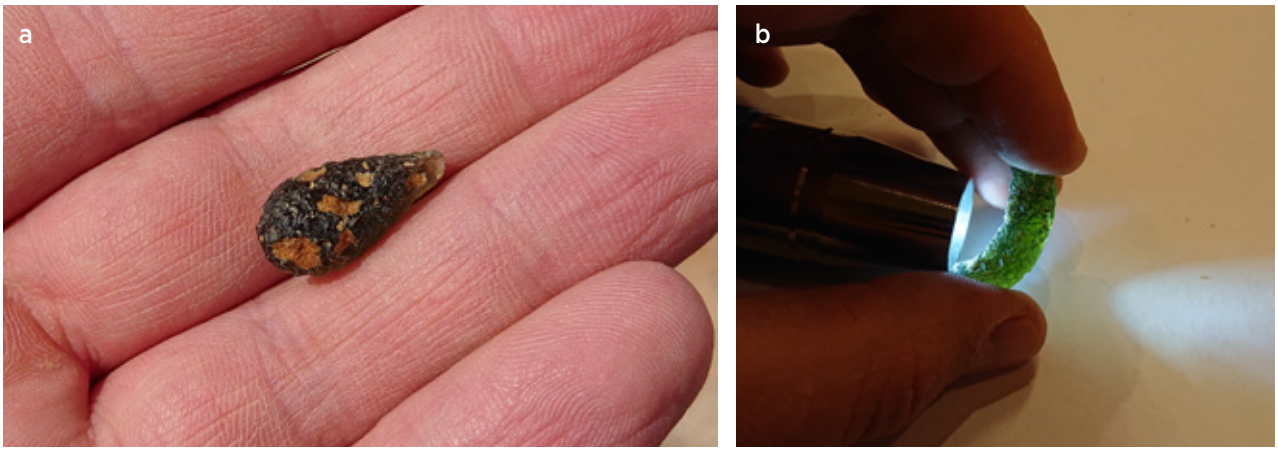

Figure 7: Among the moldavites recovered on the day of the authors' mine visit were (**a**) one drop-shaped and (**b**) one curved moldavite. These shapes are relatively rare. Photos by T. Stephan.

officers frequently patrol the moldavite-bearing localities. In addition, the sand-and-gravel quarry near Chlum has a modern security system. Penalties are mostly in the form of bans.

MATERIALS AND METHODS

Four moldavite samples collected during the field trip described above were polished on one side to measure RIs with a standard refractometer. Their SGs were determined hydrostatically, and microscopic observations were undertaken with a gemmological microscope equipped with Zeiss Stemi2000 optics and an immersion cell containing paraffin oil. Ultraviolet-visible-near infrared (UV-Vis-NIR) spectra were recorded with a PerkinElmer Lambda 950S spectrometer in the range of 200–2500 nm. Chemical composition was measured by energy-dispersive X-ray fluorescence (EDXRF) using a Thermo Scientific ARL Quant'X spectrometer.

For comparison, several other samples from the reference collection of the German Gemmological Association (DGemG) were studied by the same techniques described above, including four faceted moldavites, three artificial green glasses (two faceted and one rough), a green artificial glass that was donated to DGemG as 'green transparent obsidian' and two pieces of greenish slag glass (Figure 9).

RESULTS AND DISCUSSION

Standard Gemmological Properties

Refractive index measurements of the moldavite varied from 1.480 to 1.500, and SG values were 2.33–2.35. The RI values were in the known range for moldavite (1.480–1.525), while the SGs were slightly low (cf. 2.36–2.44 g/cm^3 density; Henn *et al.* 2020). By comparison, the RI and SG values of the artificial glasses were 1.510–1.522 and 2.42–2.51, respectively, and for the slag glasses 1.622–1.629 and 2.80–2.84, respectively.

The inclusions in moldavite are unique and distinct from those in other natural and artificial glasses (see,

Figure 8: Illegal mining for moldavite is a widespread problem, especially in the forests. (**a**) Hand-dug pits up to 2–3 m deep are excavated vertically and horizontally, (**b**) causing damage to trees as well as leaving hazards for wildlife. Photos by T. Stephan.

Figure 9: Samples from the DGemG reference collection analysed for this report include: one uncut (31.32 g) and two cut (2.79 and 7.65 ct) artificial glasses (left); four cut moldavites (top centre, 8.67–33.34 ct), as well as four rough moldavites (polished on the back side, 0.61–5.97 g) that were collected during the 2022 field trip (bottom centre); two pieces of pale green slag glass (top right, 5.88–7.68 g); and one artificial glass that was donated to DGemG as obsidian (bottom right, 14.22 ct). Photo by T. Stephan.

e.g., Bouška *et al*. 1985). Our study samples often contained tiny gas bubbles, usually smaller than 1 mm diameter, but also some as large as 1 cm or more. The gas bubbles were usually round, but some were oval to elongated (Figure 10a–d). They were usually distributed irregularly, but sometimes followed the swirls described below. According to Žák *et al*. (2012), the gas inside the bubbles is usually composed of carbon monoxide (CO), carbon dioxide (CO_2) and hydrogen (H_2), with minor amounts of other gases also present.

Often seen in the moldavites were distinct swirls (i.e. flow structures, Figure 10a, b) that indicate variations in chemical composition (Okrusch & Matthes 2014). Also common were round to elongated, partial zig-zag to curl-like inclusions of the silica glass lechatelierite (Figure 10a–c and e), which are diagnostic of moldavite (see, e.g., Bouška *et al*. 1985) and are not found in imitations. The lechatelierite inclusions represent molten quartz grains and indicate temperatures of glass formation above 1,730°C (Okrusch & Matthes 2014). The lechatelierite inclusions were more obvious when viewed with crossed polarisers, and were often surrounded by a dark cross-like extinction pattern (Figure 10f).

The inclusions in the artificial glasses consisted of typical round to oval gas bubbles as well as swirl marks. The slag glasses were almost opaque, but gas bubbles were observed close to and at the surface, as well as a swirly colour distribution.

UV-Vis-NIR Spectroscopy

The colour of moldavite is due to iron (Bouška *et al*. 1985). Depending on the Fe content, the colour varies from green to brownish green to brown. Most other tektites are richer in Fe and are, therefore, typically dark brown to black.

The optical spectrum of moldavite (Figure 11) is dominated by a strong Fe^{2+} absorption band centred around 1100 nm. Towards the UV range the absorption increases strongly, and the two broad absorption features form a transmission window at about 550 nm in the green spectral region. By comparison, artificial glasses resembling moldavite may show a much different absorption spectrum (Hyršl 2015; Hanus & Hyršl 2018), although some artificial glasses have spectral features very similar to those of moldavite (again, see Figure 11).

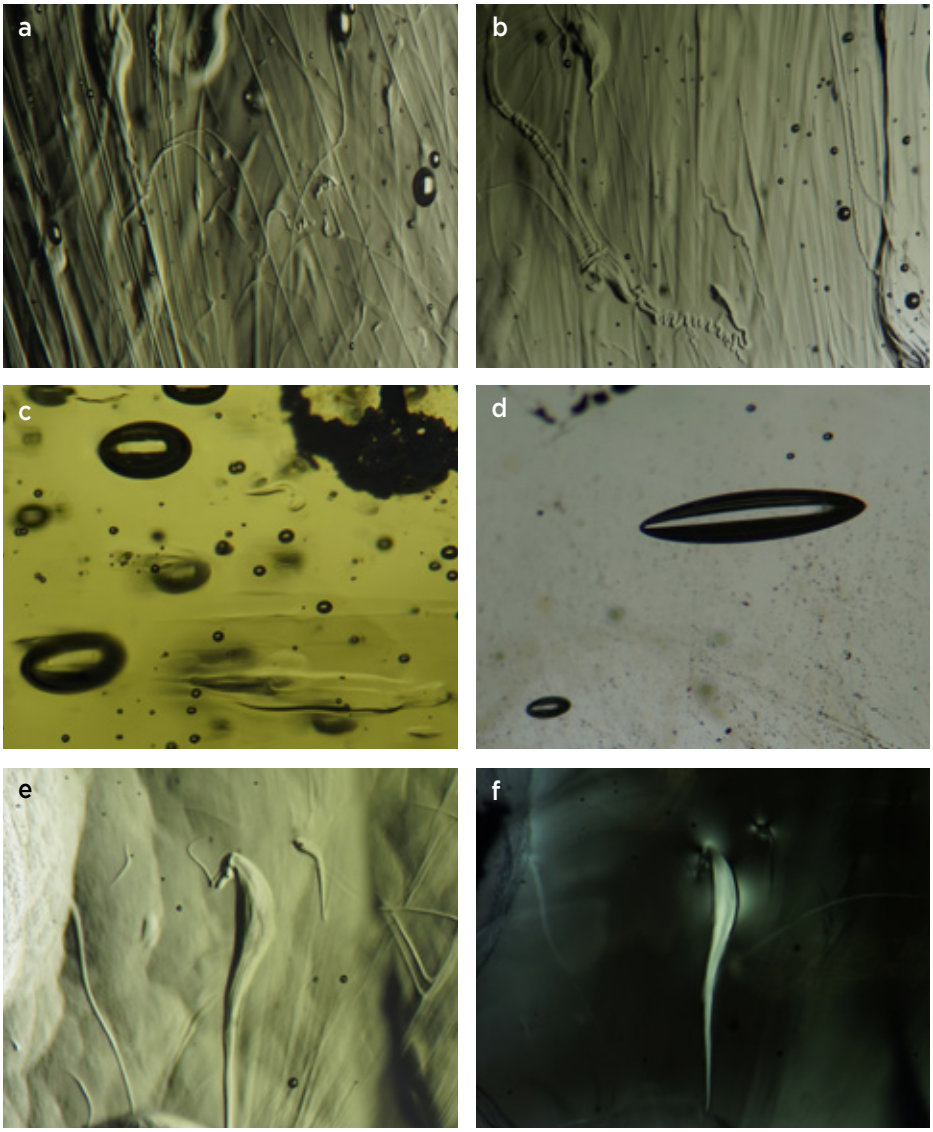

Figure 10: Typical inclusions in moldavite, photographed in the samples shown in Figure 9 that were collected by the authors, are: (**a**, **b**) round to oval gas bubbles, as well as straight or curved swirls (flow structures) and elongated lechatelierite inclusions showing high relief (both magnified 40×); (**c**) oval gas bubbles and lechatelierite inclusions (magnified 32×); (**d**) elongated, marquise-shaped gas bubbles (magnified 10×); and (**e**, **f**) a lechatelierite inclusion shown in plane-polarised (e) and cross-polarised light (f, surrounded by an anomalous extinction pattern; both magnified 20×). All images were taken in immersion. Photomicrographs by T. Stephan.

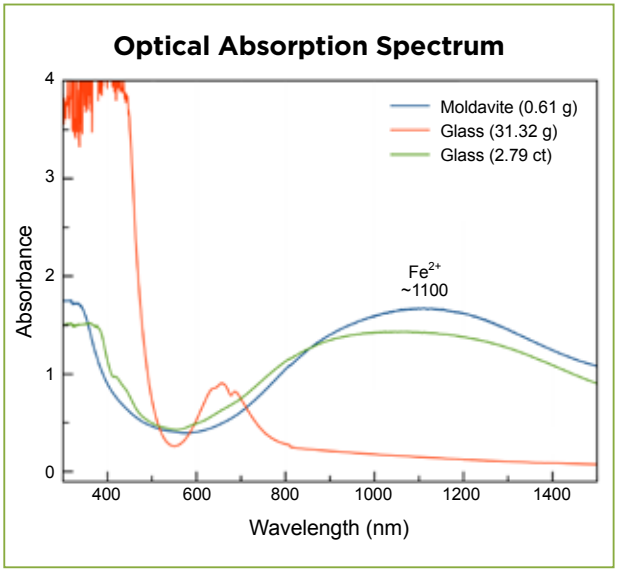

Figure 11: The optical absorption spectrum of moldavite is shown in comparison with spectra obtained from two artificial glasses, one of which shows features quite similar to moldavite.

Chemical Analysis

Table I shows the results of EDXRF chemical analysis of the moldavites analysed for this study, along with the compositions of the green artificial glasses and slag glasses shown in Figure 9.

Tektites such as moldavite typically have a chemical composition similar to that of granite, with high SiO_2 and Al_2O_3, lower K_2O, CaO, MgO and Fe_2O_3, and traces of Na_2O. However, the artificial glasses and slag glasses analysed for this study possessed a distinctly different compositional range. The artificial glasses were of the soda-lime (crown) type and had higher CaO and Na_2O contents than moldavite, while the slag glasses were highly enriched in CaO. The compositions of the artificial glasses and slag glasses obtained for this study are consistent with unpublished reference data from the databases of DGemG and the German Foundation for Gemstone Research.

Table I: Chemical composition of moldavite, artificial glass and slag glass from the DGemG reference collection.*

Sample type	Moldavite		Artificial glass		Slag glass
Description	Rough (from Chlum)	Faceted	Rough and cut	Cut 'green obsidian'	Rough
Oxide (wt.%)					
SiO_2	62.37–76.57	76.69–77.38	61.33–70.81	69.69	40.63–40.93
Al_2O_3	10.33–12.57	11.41–11.60	1.04–7.86	2.24	17.84–17.97
K_2O	3.30–3.93	2.92–3.14	2.95–6.59	0.66	2.08–2.10
CaO	2.63–3.21	2.77–3.32	8.65–11.02	8.93	23.77–24.21
Na_2O	0.33–0.51	bdl	11.27–12.79	15.39	0.60–0.67
MgO	2.37–2.68	2.70–3.27	0.35–2.16	0.91	7.12–8.22
Fe_2O_3	1.81–2.14	1.58–1.65	0.02–1.68	0.82	0.21–0.32

* The samples are shown in Figure 9. Abbreviation: bdl = below detection limit.

CONCLUSION

Moldavite (tektite glass) was produced by a spectacular meteorite impact event, and this origin adds to the contemporary popularity of moldavite (and other tektites). A resurgence in demand for moldavite began in the 1950s and has been growing steadily since then. In its rough state, moldavite is sought-after by collectors. In addition, natural uncut moldavite is often set in silver or gold, and faceted material is sometimes mounted in jewellery with Czech pyrope (e.g. Figure 12). Moldavite is especially popular in tourist jewellery.

Gemmologically, moldavite can be identified by a combination of RI and SG values, and it is easily differentiated from artificial glasses by its characteristic inclusion pattern. In cases of doubt, the absorption spectrum can be helpful, and clear identification is also possible by chemical analysis.

Figure 12: (**a**) Natural uncut moldavite is set in this silver ring. (**b**) Faceted moldavite is commonly mounted in jewellery with Czech pyrope. Rings by Granát Turnov, the largest producer of Czech garnet jewellery; photos by L. Aranyosiová, www.

It is likely that the sand-and-gravel layers in the Chlum-Besednice area of the Czech Republic will continue to supply the market with moldavite for the next several years.

REFERENCES

Bayer, J. 1921. Ein Moldavit aus dem Diluvium der Gudenushöhle [A moldavite from the alluvium of the Gundenus cave]. *Mittheilungen der Anthropologischen Gesellschaft in Wien*, **51**, 160.

Böhme, M., Gregor, H.-J. & Heissig, K. 2002. The Ries and Steinheim meteorite impacts and their effect on environmental conditions in time and space. *In*: Buffetaut, E. & Koeberl, C. (eds) *Geological and Biological Effects of Impact Events*. Springer, Berlin, Germany, 217–235, https://doi.org/10.1007/978-3-642-59388-8_10.

Bouška, V. & Konta, J. 1999. *Moldavites—Vltavíny*. Acta Universitatis Carolinae, Geologica series. Universita Karlova, Prague, Czech Republic, 128 pp.

Bouška, V., Frydrych, M. & Turnovec, I. 1985. Moldavites as precious stones. *Zeitschrift der Deutschen Gemmologischen Gesellschaft*, **34**(3/4), 83–91.

Brachaniec, T., Szopa, K. & Karwowski, Ł. 2014. Discovery of the most distal Ries tektites found in Lower Silesia, southwestern Poland. *Meteoritics & Planetary Science*, **49**(8), 1315–1322, https://doi.org/10.1111/maps.12311.

Di Vincenzo, G. & Skála, R. 2009. ^{40}Ar–^{39}Ar laser dating of tektites from the Cheb Basin (Czech Republic): Evidence for coevality with moldavites and influence of the dating standard on the age of the Ries impact. *Geochimica et Cosmochimica Acta*, **73**(2), 493–513, https://doi.org/10.1016/j.gca.2008.10.002.

Gentner, W. 1971. Cogenesis of the Ries crater and moldavites and the origin of tektites. *Meteoritics*, **6**, 274–275.

Graup, G., Horn, P., Köhler, H. & Möller-Sohnius, D. 1981. Source material for moldavites and bentonites. *Naturwissenschaften*, **68**(12), 616–617, https://doi.org/10.1007/bf00398615.

Hanus, R. 2016. *Moldavite: Mysterious Tears from Heaven*. Granit, Prague, Czech Republic, 136 pp.

Hanus, R. & Hyršl, J. 2018. Distinguishing "synthetic" and natural moldavite. *Journal of Gems & Gemmology*, **20**(1), 14–25.

Henn, U., Stephan, T. & Milisenda, C.C. 2020. *Gemmological Tables for the Identification of Gemstones, Synthetic Stones, Artificial Products and Imitations/Gemmologische Tabellen zur Bestimmung von Edelsteinen, Synthesen, künstlichen Produkten und Imitationen*. Deutsche Gemmologische Gesellschaft e.V. and German Gemmological Association, Idar-Oberstein, Germany, 42 pp.

Hyršl, J. 2015. Gem News International: Moldavites: natural or fake? *Gems & Gemology*, **51**(1), 103–104.

Okrusch, M. & Matthes, S. 2014. *Mineralogie: Eine Einführung in die spezielle Mineralogie, Petrologie und Lagerstättenkunde*. Springer, Berlin, Germany, xx + 728 pp., https://doi.org/10.1007/978-3-642-34660-6.

Pösges, G. & Schieber, M. 2009. *Das Rieskrater-Museum Nördlingen: Museumsführer und Empfehlungen zur Gestaltung eines Aufenthalts im Ries*. Verlag Dr. Friedrich Pfeil, Munich, Germany, 128 pp.

Schmieder, M., Kennedy, T., Jourdan, F., Buchner, E. & Reimold, W.U. 2018. A high-precision $^{40}Ar/^{39}Ar$ age for the Nördlinger Ries impact crater, Germany, and implications for the accurate dating of terrestrial impact events. *Geochimica et Cosmochimica Acta*, **220**, 146–157, https://doi.org/10.1016/j.gca.2017.09.036.

Schwarz, W.H., Hanel, M. & Trieloff, M. 2020. U-Pb dating of zircons from an impact melt of the Nördlinger Ries crater. *Meteoritics & Planetary Science*, **55**(2), 312–325, https://doi.org/10.1111/maps.13437.

Stöffler, D., Artemieva, N.A., Wünnemann, K., Reimold, W.U., Jacob, J., Hansen, B.K. & Summerson, I.A.T. 2013. Ries crater and suevite revisited—Observations and modelling. Part I: Observations. *Meteoritics & Planetary Science*, **48**(4), 515–589, https://doi.org/10.1111/maps.12086.

Tay, T.S. 2007. From a Singaporean gem laboratory—Moldavite: natural vs imitation? *Australian Gemmologist*, **23**(2), 76–78.

Tay, T.S., Atichat, W., Sriprasert, B. & Leelawatanasuk, T. 2008. Moldavite: Natural or imitation. *GIT2008: Proceedings of the 2nd International Gem and Jewelry Conference*, Bangkok, Thailand, 9–12 March, 80–85.

Trnka, M. & Houzar, S. 2002. Moldavites: A review. *Bulletin of the Czech Geological Survey*, **77**(4), 283–302.

Velebil, D. 2020. Sbírka tektitů Národního muzea. *Minerál*, **28**(3), 231–243.

Žák, K., Skála, R., Řanda, Z. & Mizera, J. 2012. A review of volatile compounds in tektites, and carbon content and isotopic composition of moldavite glass. *Meteoritics & Planetary Science*, **47**(6), 1010–1028, https://doi.org/10.1111/j.1945-5100.2012.01369.x.

The Authors

Dr Tom Stephan
German Gemmological Association,
Prof.-Schlossmacher-Str. 1,
D-55743 Idar-Oberstein, Germany
Email: t.stephan@dgemg.com

Stěpán Jaroměřský
Faculty of Science, Charles University,
128 43 Prague 2, Czech Republic

Lukáš Zahradníček
National Museum, Cirkusová 1740,
Prague 9 – Horní Počernice, Czech Republic

Stefan Müller
German Foundation for Gemstone Research – DSEF German Gem Lab, Prof.-Schlossmacher-Str. 1, D-55743 Idar-Oberstein, Germany

Origin of the Colour and Dichroism in Laurentthomasite

Isabella Pignatelli, Cristiano Ferraris and Dominik Schaniel

ABSTRACT: In 2020, laurentthomasite was described as a new gem material presenting remarkable dichroism. Here its polarised optical absorption spectra are interpreted on the basis of compositional and structural data, indicating the presence of transition-metal ions (Fe^{2+}, Fe^{3+} and Mn^{2+}) in different sites. Their possible contribution to colouration is discussed, but the spectral anisotropy suggests that both the colour and dichroism of laurentthomasite arise from intervalence charge transfer (IVCT) between Fe^{2+} and Fe^{3+}. Similar anisotropy has been observed in the polarised spectra of other Fe-bearing silicates with comparable optical properties and IVCT colour causes such as beryl, cordierite and bazzite. Possible confusion with other blue-coloured gem materials is also discussed, as well as the main differences useful for the rapid and correct identification of laurentthomasite.

The Journal of Gemmology, **38**(7), 2023, pp. 708–716, https://doi.org/10.15506/JoG.2023.38.7.708

Laurentthomasite, $Mg_2K(Be_2Al)Si_{12}O_{30}$, is a relatively new and rare gem material that was shown for the first time at the Tucson gem and mineral shows in 2020, where both rough and faceted samples were exhibited (e.g. Figure 1). This complex silicate is of particular gemmological interest due to its deep blue colour and strong dichroism (Figure 2). It was approved as a new mineral species in 2019 by the International Mineralogical Association, following a proposal submitted by Ferraris *et al.* (2019). It is named in honour of French geologist and mineral dealer Laurent Thomas, who collected it in Madagascar. The name 'thomasite' was initially proposed, but since it could have been confused with thaumasite (especially in French), the name was amended to laurentthomasite in order to acknowledge his discovery of this new species.

Given the rarity of laurentthomasite, only a few studies of it have been published. Ferraris *et al.* (2020) described its physical properties, chemical composition and structure, and they deposited the holotype at the Muséum National d'Histoire Naturelle (MNHN) in Paris. Ounorn *et al.* (2020) published the results of standard gemmological testing on two oval mixed-cut gems and provided polarised ultraviolet-visible-near infrared

Figure 1: These rough and cut samples of laurentthomasite were seen at one of the Tucson gem and mineral shows in 2020. The faceted stones weigh 0.73, 0.94 and 0.76 ct (from left to right), and the crystal is 2.2 cm in height. Photo by Jeff Scovil.

(UV-Vis-NIR) spectra, but they did not discuss the spectral features. JGGL (2020) presented gemmological, chemical and spectral data on laurentthomasite, and compared it to grandidierite (another rare blue gem material from Madagascar).

In this study, we recorded polarised absorption spectra in order to understand the origin of colour and dichroism of laurentthomasite, taking into account the structural description given by Ferraris *et al*. (2020) and the spectra of other silicates having similar optical properties (e.g. beryl, cordierite and bazzite).

CRYSTAL CHEMISTRY OF LAURENTTHOMASITE

Laurentthomasite is a Be-bearing mineral, and the presence of this element was first confirmed by laser-induced breakdown spectroscopy. Then inductively coupled plasma mass spectrometry, as well as inductively coupled plasma optical emission spectrometry, were used to quantify the contents of Be, major oxides, trace elements and rare-earth elements (Ferraris *et al*. 2020). The resulting chemical data (see Table I) indicate the presence of four transition-metal ions—Fe^{2+}, Fe^{3+}, Mn^{2+} and Sc^{3+}—but only the first three of these can affect the colour and dichroism of laurentthomasite. Although Sc^{3+} is a transition metal of the *d*-block, it has no *d* electrons left over. For this reason, scandium absorbs no visible light and does not play a role in the colouration of minerals.

To better understand the relationships between the locations and occupancies of cationic sites and associated spectroscopic data, here we briefly explain the structure of laurentthomasite (Figure 3). It crystallises in the hexagonal system (space group *P6/mcc*, cell dimensions a = 9.9580(1) Å and c = 14.1492(1) Å), and it has a structure built up of double six-membered rings $[T(1)_{12}O_{30}]$. Thus, it is a cyclosilicate, and it belongs to the milarite group. The rings are stacked along the *c*-axis, forming channels. Each T(1) tetrahedron of the rings shares three corners with adjacent T(1) tetrahedra and one corner with a T(2) tetrahedron. The latter shares all corners with T(1) tetrahedra and two edges with A octahedra, giving rise to a framework. B sites are sandwiched between adjacent A octahedra and are vacant in laurentthomasite. C sites are surrounded by 12 oxygen atoms that occur at the centre of the channel formed by the $[T(1)_{12}O_{30}]$ rings. Chemical analyses coupled to the structural refinement indicate that: (1) T(1) tetrahedra are occupied by Si, whereas T(2) tetrahedra are mainly occupied by Be and Al; (2) A sites contain Mg, Sc, Fe and Mn; and (3) C sites essentially contain K with low amounts of Na, Ca and Ba. Mössbauer spectroscopy revealed the presence of both Fe^{2+} and Fe^{3+} located in the A and T(2) sites, respectively (Ferraris *et al*. 2020).

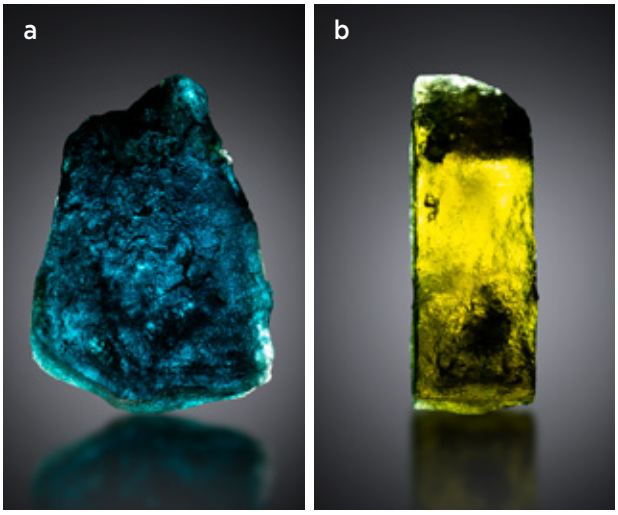

Figure 2: This crystal specimen of laurentthomasite displays striking dichroism in deep blue looking down the *c*-axis and yellow in directions perpendicular to it. Photos by Jeff Scovil.

Considering that the general formula of milarite-group minerals is $A_2B_2C[T(2)_3T(1)_{12}O_{30}](H_2O)_x$ (with $0 < x < 2$), the empirical formula of laurentthomasite calculated on 30 oxygen atoms can be written as $(Mg_{0.86}Sc_{0.54}Fe^{2+}_{0.34}Mn_{0.26})(K_{0.89}Na_{0.05}Y_{0.02}Ca_{0.01}Ba_{0.01})[(Be_{2.35}Al_{0.50}Mg_{0.11}Fe^{3+}_{0.03})(Si_{11.90}Al_{0.10})O_{30}](H_2O)_x$. Reports about water content are controversial, because it is not clearly understood where water occurs in the structure of minerals belonging to the milarite group. Some research has shown that H_2O is an important constituent at the B sites, but H_2O can also be occluded and not bonded directly to any cation (Hawthorne *et al*. 1991; Hawthorne 1992; Gagné & Hawthorne 2016). Moreover, water content can vary from one sample to another;

Table I: Chemical composition (in wt.%) of laurentthomasite.*

SiO_2	73.10	**MgO**	4.01
Al_2O_3	3.11	**ZnO**	0.04
Sc_2O_3	3.78	**CaO**	0.07
Y_2O_3	0.22	**BaO**	0.16
TiO_2	0.02	**BeO**	6.02
FeO	2.69	**Na_2O**	0.15
Fe_2O_3	0.19	**K_2O**	4.30
MnO	1.91	**Total**	99.77

* Data from Ferraris *et al*. (2020); Fe_2O_3 recalculated from Mössbauer data.

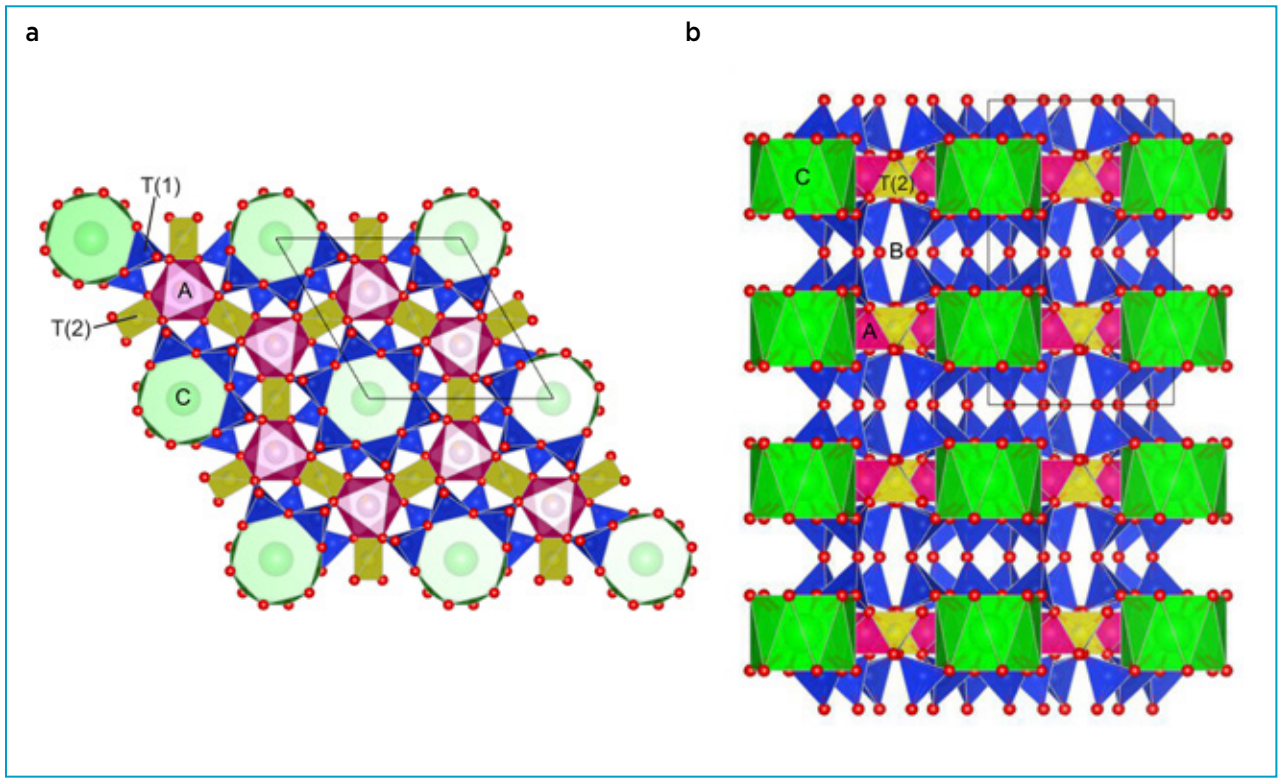

Figure 3: Two diagrams depict the crystal structure of laurentthomasite projected down (**a**) the *c*-axis and (**b**) the *a*-axis. The different cationic sites are labelled T(1), T(2), A, B and C; oxygen atoms are in red. These drawings were made using VESTA software (Momma & Izumi 2011).

Ferraris *et al.* (2020) did not detect water in their sample, whereas the FTIR spectra provided by JGGL (2020) and Ounorn *et al.* (2020) revealed weak absorption bands at approximately 3550, 3447 and 3253 cm^{-1}. Although the cited authors did not explain these spectral bands in their publications, they are probably related to the presence of water. This difference in results is not surprising, because some samples of milarite-group minerals are anhydrous, while others contain small amounts of water (Gagné & Hawthorne 2016).

GEOLOGICAL SETTING

To date, laurentthomasite occurs at only one locality, about 40 km east of the village of Betroka, within Toliara Province in southern Madagascar. The mine is situated in a rural area called Beravina, close to the small village of Ambaro (23°21′00″ S, 46°25′00″ E).

This area is underlain by migmatitic paragneisses and orthogneisses containing lenses of granites and marbles (Rakotonandrasana *et al.* 2010). Laurentthomasite formed in a granitic pegmatite hosted within high-grade metamorphic rocks such as amphibolites and migmatites. The pegmatites in this area are enriched in Sc, which explains the remarkable content of this element in laurentthomasite (3.78 wt.% Sc_2O_3; see Table I). Scandium is quite rare in terrestrial minerals and, above all, in gems.

Only very limited areas of the pegmatite contain laurentthomasite, which has been found together with orthoclase (up to 5 cm), quartz and rare green apatite. Also present were rare tabular crystals of grey-tan corundum that were less than 1 cm long (Ferraris *et al.* 2020).

MATERIALS AND METHODS

Six crystals of laurentthomasite were obtained by Laurent Thomas in Madagascar and deposited at the MNHN in Paris. One of them was analysed for this study (Figure 4). It is 4.41 mm tall with a width of 3.35 mm. Its hexagonal prismatic habit is not complete, with only relict prismatic faces and one pinacoidal face. We chose to obtain UV-Vis-NIR spectra from this sample because it was less included than the others and easier to orient, thanks to the faces. The sample was neither sliced nor embedded in resin in order to be used in further investigations.

Polarised optical absorption spectra were recorded in two directions in the 350–1700 nm range at room

temperature using a Shimadzu 3600 spectrometer. The spectra were taken with the electric field vector E of the incident light perpendicular (E⊥*c*) and parallel (E||*c*) to the *c*-axis (i.e. the beam was directed parallel and perpendicular to the *c*-axis, respectively). The measurements were carried out with a spectral slit width of 2 nm and a step size of 0.1 nm.

RESULTS AND DISCUSSION

The examined crystal showed dissolution marks, in particular hexagonal etch pits visible on the pinacoid (Figure 5a), as described by Koivula and Renfro (2022). It also contained eye-visible orangey brown inclusions of Fe-bearing minerals not yet identified (Ferraris *et al.* 2020; see, e.g., Figure 5b).

Laurentthomasite is characterised by strong pleochroism (Figures 2 and 4). Being uniaxial, it can have only two pleochroic colours (dichroism). The optic sign of laurentthomasite is positive, so its optical indicatrix is an ellipsoid, where the optic axis coincides with the crystallographic *c*-axis. As shown in Figure 4, it appears blue in the ordinary ray (ω), which defines the circular section of the indicatrix in the plane perpendicular to the optic axis, and yellow in the extraordinary ray (ε, i.e. in the oval section of the indicatrix in the plane parallel to the optic axis).

The optical absorption spectra of laurentthomasite show a broad absorption in the yellow-to-red portion of the visible range in the E⊥*c* direction, in comparison to the weaker visible-range absorption in the E||*c* spectrum (Figure 6). This explains the intense blue colour of this mineral and its dichroism.

E⊥c Spectrum

The E⊥*c* spectrum (Figure 6) has a steep UV absorption edge extending into the violet portion of the visible range. This feature could be attributed to O^{2-}–Fe^{3+} charge transfer or point defects (Fritsch & Rossman 1988; Shang *et al.* 2022 and references therein). The spectrum also shows a broad, intense absorption covering the near-infrared and part of the visible range, decreasing to a minimum around 500 nm. Thus, combined with the absorption in the violet spectral range, the mineral appears blue. A tentative deconvolution of the spectrum with Gaussian bands is available in *The Journal*'s online data depository to support the following discussion.

In the near-infrared range, two bands appear at around

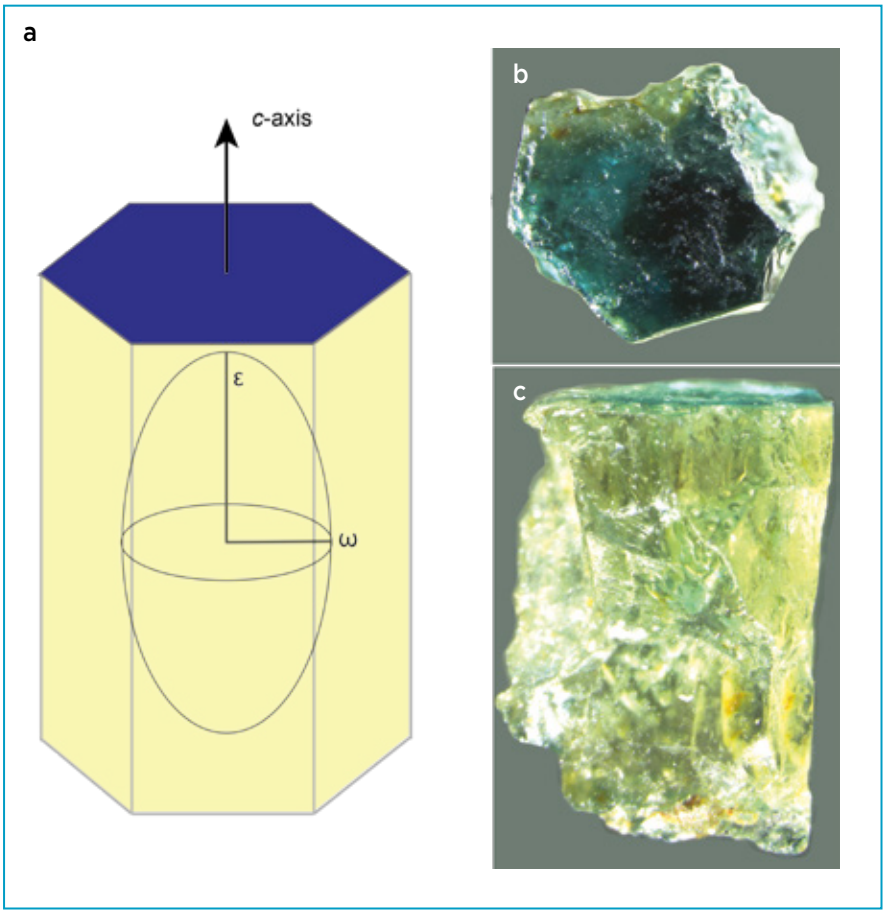

Figure 4: (**a**) A crystal diagram for laurentthomasite shows the relationships between habit, optical indicatrix and the strong dichroism, which appears (**b**) blue for the ordinary ray (ω, i.e. viewed parallel to the *c*-axis) and (**c**) yellow for the extraordinary ray (ε, i.e. viewed perpendicular to the *c*-axis). Both images are of the same sample (4.41 × 2.85 × 3.35 mm), which was analysed for this study. Photos by Emmanuel Wenger.

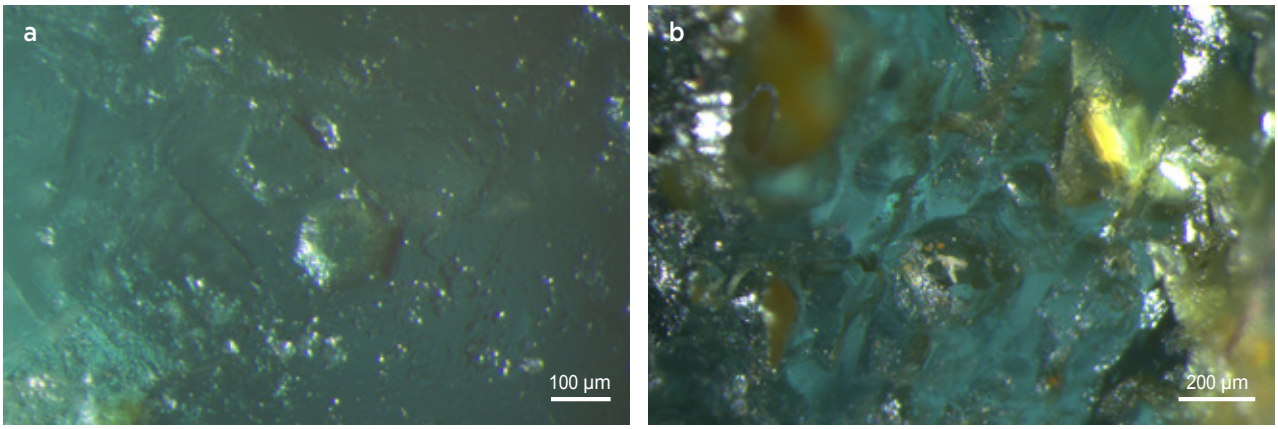

Figure 5: (**a**) Hexagonal etch pits are visible on the pinacoidal face of the analysed laurentthomasite sample. (**b**) Orangey brown inclusions of Fe-bearing minerals are shown here in another, more-included sample of laurentthomasite. Photomicrographs by Emmanuel Wenger.

909 and 1300 nm. (Note that the absorption between 750 and 1000 nm is saturated due to the thickness of the crystal used, so the peak position at 909 nm was derived from the spectral deconvolution, as described in *The Journal*'s online data depository.) According to the literature (Goldman *et al.* 1977; Amthauer & Rossman 1984), these two bands correspond to crystal-field transitions due to the E_g states of octahedral Fe^{2+}, as in Fe-rich cordierite. By comparison with Fe-bearing blue beryl, the strong absorption maximum around 909 nm can be attributed to octahedral Fe^{2+}, but it is outside the visible region, so it does not contribute to colour in laurentthomasite (Groat *et al.* 2010; Shang *et al.* 2022 and references therein).

The broad tail that extends through the yellow-to-red part of the spectrum (i.e. between 570 and 780 nm) was deconvoluted into two bands at 694 and 588 nm, before reaching the minimum at approximately 500 nm. According to their positions and widths, the two bands are ascribed to Fe^{2+}–Fe^{3+} intervalence charge transfer (IVCT), as observed in other minerals (Amthauer & Rossman 1984; Mattson & Rossman 1987; Burns 1993). IVCT is directional and causes strong pleochroism, as previously documented in beryl, cordierite, lazulite, bazzite etc. (Fritsch & Rossman 1988; Taran & Rossman 2001; Taran *et al.* 2017). Taking into account the anisotropy of the absorption spectra, the vector between the cations involved in IVCT should be oriented perpendicular to the *c*-axis.

According to the Mössbauer analysis and structural description given by Ferraris *et al.* (2020), Fe^{2+} is in octahedral coordination in the A sites, whereas Fe^{3+} occupies the neighbouring tetrahedral T(2) sites. This confirms that the Fe^{2+}–Fe^{3+} charge transfer takes place in the plane perpendicular to the *c*-axis (Figure 3). Moreover, each T(2) site shares two edges with two adjacent A sites, and the A–T(2) distance is 2.87 Å. This proximity favours Fe^{2+}–Fe^{3+} IVCT processes, which have low probability of occurring in structures with relatively long distances between cationic sites, such as in garnet (Taran *et al.* 2007).

Following the procedure applied by Groat *et al.* (2010) for dark blue aquamarine and beryl, it is possible to estimate the amount of Fe involved in the IVCT process. This amount is determined using the intensity of the IVCT band and the Beer-Lambert law. From the experimental data and deconvolution, the IVCT band at 694 nm has an absorbance of 0.71 for a sample thickness of 4.41 mm. The molar coefficient for IVCT interaction in laurentthomasite is unknown, as in beryl. For this reason, we used a typical molar absorption coefficient for IVCT in silicate minerals (i.e. 150) as previously done by Groat *et al.* (2010). Using the density of laurentthomasite (2.66 g/cm^3), we calculated 0.011 moles per litre of Fe pairs (i.e. 0.045 wt.% Fe) were involved in the IVCT interactions.

The minor shoulders at 377, 424 and 442 nm were also reported by Ounorn *et al.* (2020) and can be attributed to Fe^{3+} in octahedral sites (Amthauer & Rossman 1984; Taran & Rossman 2001; Groat *et al.* 2010; Liu & Guo 2022; Shang *et al.* 2022). Thus, the presence of these three bands suggests that Fe^{3+} can occupy both octahedral and tetrahedral sites, even though the Mössbauer study shown by Ferraris *et al.* (2020) on a bigger sample revealed only the presence of $^{IV}Fe^{3+}$. (It should be noted that Mössbauer data were not recorded on the sample analysed in this study because of the sample's small size and the presence of Fe-bearing inclusions.) However, the bands at 424 and 442 nm could be caused by a combination of Fe^{3+} and Mn^{2+}

(Webster 1983; Liu & Guo 2022). In fact, they have also been observed in the spectra of Mn-bearing synthetic spinels (Webster 1983). However, Fe^{3+} and Mn^{2+} do not contribute significantly to the colour of laurentthomasite because their absorptions are too weak and/or too close to the UV region (Liu & Guo 2022; Shang *et al.* 2022). The effect of IVCT on the colour of laurentthomasite is more important than that caused by these cations when they are isolated (Fritsch & Rossman 1988).

E||c Spectrum

The E||*c* spectrum (Figure 6) has an absorption edge in the UV range that extends into the blue end of the visible region and, in the absence of other strong absorptions in the visible range, leads to the yellow colour attributed to O^{2-}–Fe^{3+} charge transfer, as in heliodor (Fritsch & Rossman 1988).

The pair of bands in the IR region near 1110 and 1308 nm look similar to those of Fe^{2+}-bearing silicates (e.g. cordierite and bazzite), but they are shifted towards higher wavelengths (Taran *et al.* 2017). They can be attributed to octahedral Fe^{2+} (Goldman *et al.* 1977; Khomenko *et al.* 2001; Taran & Rossman 2001; Taran *et al.* 2017), and their shift could be due to the larger octahedral site in laurentthomasite (cf. Taran *et al.* 2017).

Role of Sc

Although laurentthomasite also contains Sc, it cannot affect colour, as mentioned above. This is also the case in another Sc-rich cyclosilicate (i.e. bazzite). Its structure is an analogue to that of beryl in which nearly half the octahedral sites are occupied by Sc^{3+} replacing Al (Armbruster *et al.* 1995). Like laurentthomasite, bazzite shows strong dichroism (ω = greenish yellow

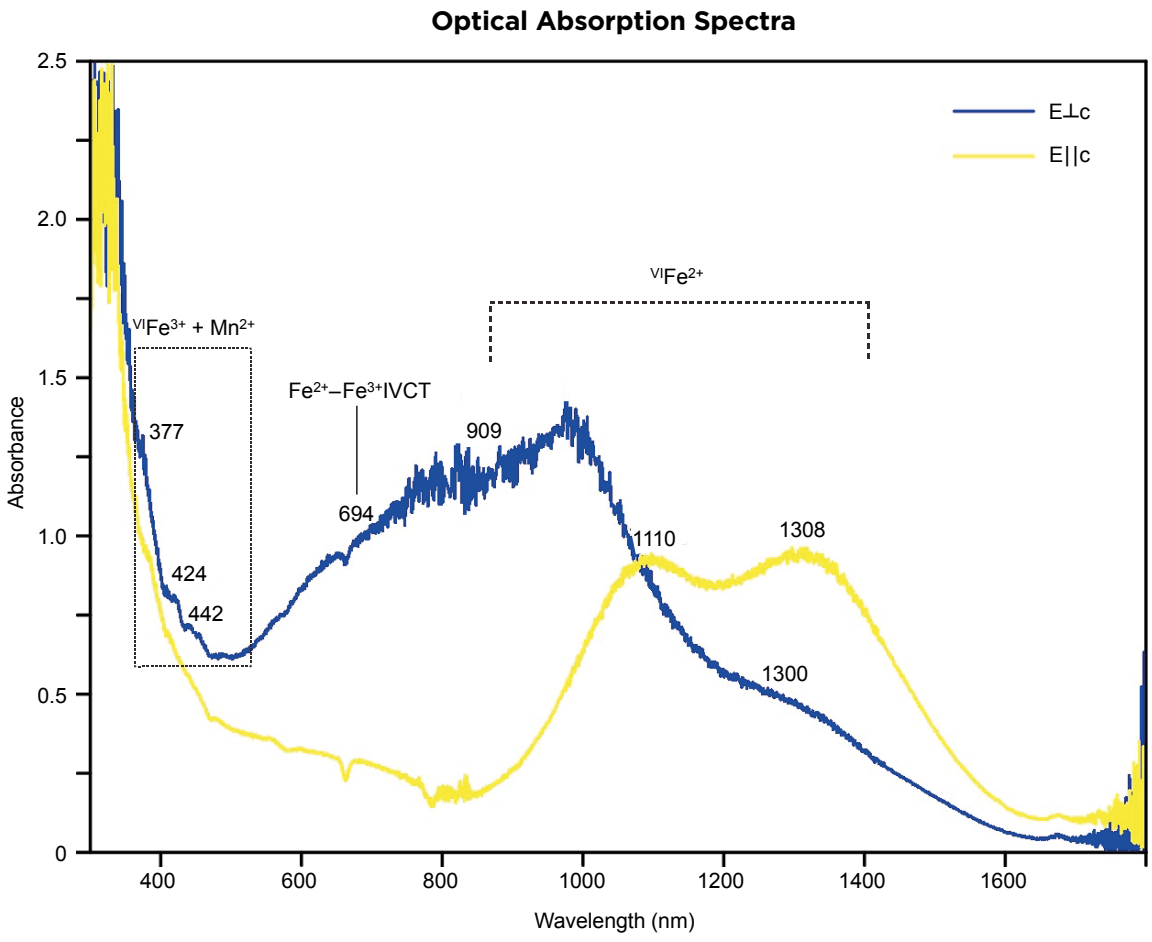

Figure 6: Polarised UV-Vis-NIR absorption spectra of laurentthomasite are characterised by a strong dichroic (E⊥*c* >> E||*c*) absorption in the visible range, which is caused by IVCT transition between Fe^{2+} and Fe^{3+}. The path length of the beam was 3.35 mm for E||c and 4.41 mm for E⊥c.

and ε = blue) that is not due to Sc but to IVCT between Fe^{2+} and Fe^{3+} occupying different cation sites (Taran *et al.* 2017).

Comparison with Other Blue Gemstones Showing Pleochroism

At first glance, laurentthomasite may be confused with cordierite (iolite), which is more often found in Madagascar. With careful analysis, it is possible to distinguish them easily. Although cordierite occurs as pseudo-hexagonal prisms, and its density is close to that of laurentthomasite, these two minerals have three main differences. (1) Their pleochroism differs. Due to their different symmetries, laurentthomasite is dichroic, while cordierite is trichroic and shows colourless-to-pale yellow, violet and light blue colours for the three crystallographic directions. (2) Their optical properties also differ. The crystal system of cordierite is orthorhombic, so it is a biaxial mineral, whereas laurentthomasite is uniaxial. (3) Their hardness can be useful to distinguish them rapidly with a simple scratch test when appropriate. Cordierite has a Mohs hardness of 7–7½, while laurentthomasite's hardness is 6. They can also be distinguished by comparing their Raman spectra; that of laurentthomasite is presented in Ferraris *et al.* (2020).

In addition, it is possible that laurentthomasite could be confused with blue sapphire (also found in southern Madagascar), but sapphire shows only weak pleochroism (ω = slightly violetish blue, ε = slightly greenish blue; Hughes 1997). The higher density and hardness of corundum are the main features facilitating its distinction from laurentthomasite.

Another blue gem material from southern Madagascar is grandidierite. Compared to laurentthomasite, it has a greater hardness (7½) and density (2.85–3.09 g/cm^3; JGGL 2020). Moreover, grandidierite is orthorhombic, so it is biaxial and trichroic in bluish green, deep green and colourless (Sun *et al.* 2019). In addition, grandidierite has perfect cleavage on {100} and {010}, and the crystals are usually anhedral, elongated and strongly corroded.

Laurentthomasite could appear similar to benitoite, especially after cutting, because the different crystal habits that are helpful for recognising them in the field are not present. These minerals have other common features: both have a Mohs hardness of 6; both are hexagonal and, thus, optically uniaxial (with a positive sign) and display dichroism. However, the dichroic colours for benitoite are ω = colourless and ε = blue to violetish blue. Benitoite and laurentthomasite are also easily differentiated by their density (3.68 vs 2.66 g/cm^3), RIs (1.757–1.804 vs 1.555–1.560) and birefringence (0.046 vs 0.005).

Tanzanite is another blue mineral with strong pleochroism. Being orthorhombic, it is biaxial and trichroic. Thus, its optical properties and habit preclude confusion with laurentthomasite. Moreover, its higher density (> 3 g/cm^3) is the main distinctive feature of tanzanite in comparison with laurentthomasite.

Bazzite (from Norway and Kazakhstan) and Santa Maria aquamarine (from Brazil) have dichroism similar to that of laurentthomasite (cf. Segura & Fritsch 2013; Taran *et al.* 2017). They are all hexagonal and uniaxial, but they can be differentiated by optic sign and RI values. In addition, the density and hardness of laurentthomasite are lower than those of bazzite and Santa Maria aquamarine. Another difference that may be useful in the field is morphology. All of them develop a hexagonal prismatic habit, but laurentthomasite crystals appear stubby, with variable height that usually does not exceed 2.5 cm (Ferraris *et al.* 2020).

CONCLUSIONS

Polarised optical spectroscopy indicates that Fe is the most important chromophore in laurentthomasite, although it also contains Mn. The spectra show strong dichroic ($E\perp c >> E||c$) absorption in the visible range caused by IVCT transition between Fe^{2+} and Fe^{3+}. This anisotropy explains why laurentthomasite appears blue for $E\perp c$ and yellow for $E||c$, and suggests that the vector between the ions involved must be oriented perpendicular to the *c*-axis. The vector that fulfils this conditions is that between Fe^{2+} in octahedral A sites and Fe^{3+} in tetrahedral T(2) sites. However, weak bands in the sample we analysed at 377, 424 and 442 nm indicate that Fe^{3+} can also occupy octahedral A sites. Calculations indicate that the concentration of Fe involved in the IVCT process is 0.045 wt.%, which corresponds to about 2% of the total Fe in laurentthomasite.

After cutting, laurentthomasite can look similar to other blue gemstones, especially ones with strong pleochroism, such as grandidierite or Santa Maria aquamarine. For this reason, it is important to perform standard gemmological tests and analyse accurately the optical properties (e.g. optic sign and RI values) in order to unambiguously identify a stone.

REFERENCES

Amthauer, G. & Rossman, G.R. 1984. Mixed valence of iron in minerals with cation clusters. *Physics and Chemistry of Minerals*, **11**(1), 37–51, https://doi.org/10.1007/bf00309374.

Armbruster, T., Libowitzky, E., Auernhammer, M., Bauerhansl, P., Hoffmann, C., Irran, E., Kurka, A., Rosenstingl, H. *et al*. 1995. Crystal chemistry and optics of bazzite from Furkabasistunnel (Switzerland). *Mineralogy and Petrology*, **52**(1–2), 113–126, https://doi.org/10.1007/bf01163130.

Burns, R.G. 1993. *Mineralogical Applications of Crystal Field Theory*. Cambridge University Press, Cambridge, Massachusetts, USA, 551 pp., https://doi.org/10.1017/cbo9780511524899.

Ferraris, C., Pignatelli, I., Cámara, F., Ponti, S., Schreyer, M., Parodi, G.C. & Wei, F. 2019. IMA No. 2018-157: Laurentthomasite $Mg_2K(Be_2Al)Si_{12}O_{30}$. IMA Commission on New Minerals, Nomenclature and Classification (CNMNC) newsletter 49: New minerals and nomenclature modifications approved in 2019. *Mineralogical Magazine*, **83**(3), 480, https://doi.org/10.1180/mgm.2019.35.

Ferraris, C., Pignatelli, I., Cámara, F., Parodi, G., Pont, S., Schreyer, M. & Wei, F. 2020. Laurentthomasite, $Mg_2K(Be_2Al)Si_{12}O_{30}$: A new milarite-group-type member from the Ihorombe region, Fianarantsoa Province, Madagascar. *European Journal of Mineralogy*, **32**(3), 355–365, https://doi.org/10.5194/ejm-32-355-2020.

Fritsch, E. & Rossman, G.R. 1988. An update on color in gems. Part 2: Colors involving multiple atoms and color centers. *Gems & Gemology*, **24**(1), 3–15, https://doi.org/10.5741/gems.24.1.3.

Gagné, O.C. & Hawthorne, F.C. 2016. Chemographic exploration of the milarite-type structure. *Canadian Mineralogist*, **54**(5), 1229–1247, https://doi.org/10.3749/canmin.1500088.

Goldman, D.S., Rossman, G.R. & Dollase, W.A. 1977. Channel constituents in cordierite. *American Mineralogist*, **62**(11–12), 1144–1157.

Groat, L.A., Rossman, G.R., Dyar, M.D., Turner, D., Piccoli, P.M.B., Schultz, A.J. & Ottolini, L. 2010. Crystal chemistry of dark blue aquamarine from the True Blue showing, Yukon Territory, Canada. *Canadian Mineralogist*, **48**(3), 597–613, https://doi.org/10.3749/canmin.48.3.597.

Hawthorne, F.C. 1992. The role of OH and H_2O in oxide and oxysalt minerals. *Zeitschrift für Kristallographie – Crystalline Materials*, **201**(3–4), 183–206, https://doi.org/10.1524/zkri.1992.201.3-4.183.

Hawthorne, F.C., Kimata, M., Černý, P., Ball, N., Rossman, G.R. & Grice, J.D. 1991. The crystal chemistry of the milarite-group minerals. *American Mineralogist*, **76**(11–12), 1836–1856.

Hughes, R.W. 1997. *Ruby & Sapphire*. RWH Publishing, Bangkok, Thailand, 511 pp.

Japan Germany Gemmological Laboratory (JGGL) 2020. Laurentthomasite: New gemstone and its comparison with grandidierite. https://www.sapphire.co.jp/jggl/1608.htm, 28 June, accessed 9 April 2023.

Khomenko, V.M., Langer, K. & Geiger, C.A. 2001. Structural locations of the iron ions in cordierite: A spectroscopic study. *Contributions to Mineralogy and Petrology*, **141**(4), 381–396, https://doi.org/10.1007/s004100100234.

Koivula, J.I. & Renfro, N. 2022. *G&G* Micro-World: Quarterly crystal: Etching on laurentthomasite. *Gems & Gemology*, **58**(4), 492–493.

Liu, X. & Guo, Y. 2022. Study on the color-influencing factors of blue iolite. *Minerals*, **12**(11), article 1356, https://doi.org/10.3390/min12111356.

Mattson, S.M. & Rossman, G.R. 1987. Identifying characteristics of charge transfer transitions in minerals. *Physics and Chemistry of Minerals*, **14**(1), 94–99, https://doi.org/10.1007/bf00311152.

Momma, K. & Izumi, F. 2011. VESTA 3 for three-dimensional visualization of crystal, volumetric and morphology data. *Journal of Applied Crystallography*, **44**(6), 1272–1276, https://doi.org/10.1107/s0021889811038970.

Ounorn, P., Srisataporn, B. & Suphan, C. 2020. Gem Notes: Laurentthomasite, a new gem mineral. *Journal of Gemmology*, **37**(2), 136–139, https://doi.org/10.15506/JoG.2020.37.2.136.

Rakotonandrasana, N.O.T., Arima, M., Miyawaki, R. & Rambeloson, R.A. 2010. Widespread occurrences of högbomite-2*N*2*S* in UHT metapelites from the Betroka Belt, southern Madagascar: Implications on melt or fluid activity during regional metamorphism. *Journal of Petrology*, **51**(4), 869–895, https://doi.org/10.1093/petrology/egq004.

Segura, O. & Fritsch, E. 2013. The Santa Maria variety of aquamarine: Never heated. *InColor*, No. 23, 34–35.

Shang, Y., Guo, Y. & Tang, J. 2022. Spectroscopy and chromaticity characterization of yellow to light-blue iron-containing beryl. *Scientific Reports*, **12**(1), article 10765, https://doi.org/10.1038/s41598-022-11916-z.

Sun, N., Li, G., Li, X. & Zhang, B. 2019. Gemmological characteristic of grandidierite from Madagascar. *Journal of Gems & Gemmology*, **21**(3), 37–41, https://doi.org/10.15964/j.cnki.027jgg.2019.03.005.

Taran, M.N. & Rossman, G.R. 2001. Optical spectroscopic study of tuhualite and a re-examination of the beryl, cordierite, and osumilite spectra. *American Mineralogist*, **86**(9), 973–980, https://doi.org/10.2138/am-2001-8-903.

Taran, M.N., Dyar, M.D. & Matsyuk, S.S. 2007. Optical absorption study of natural garnets of almandine-skiagite composition showing intervalence $Fe^{2+}+Fe^{3+}\rightarrow Fe^{3+}+Fe^{2+}$ charge-transfer transition. *American Mineralogist*, **92**(5–6), 753–760, https://doi.org/10.2138/am.2007.2163.

Taran, M.N., Dyar, M.D., Khomenko, V.M. & Boesenberg, J.S. 2017. Optical absorption, Mössbauer, and FTIR spectroscopic studies of two blue bazzites. *Physics and Chemistry of Minerals*, **44**(7), 497–507, https://doi.org/10.1007/s00269-017-0877-2.

Webster, R. 1983. *Gems: Their Sources, Descriptions and Identification*, 4th edn. Butterworths & Co., London, 1,044 pp.

The Authors

Dr Isabella Pignatelli
Université de Lorraine, Georessources UMR 7359 UL-CNRS, BP 70239, 54506 Vandœuvre-lès-Nancy cedex, France
Email: isabella.pignatelli@univ-lorraine.fr

Dr Cristiano Ferraris
Institut de Minéralogie, de Physique des Matériaux et de Cosmochimie, UMR 7590, Muséum National d'Histoire Naturelle, CP 52, 61 rue Buffon, 75005 Paris, France

Dr Dominik Schaniel
Université de Lorraine, Laboratoire de Cristallographie, Résonance Magnétique et Modélisation (CRM2) UMR 7036 UL-CNRS, BP 70239, 54506 Vandœuvre-lès-Nancy cedex, France

Acknowledgements

The authors are grateful to Dr Emmanuel Wenger for photos of laurentthomasite, as well as to Prof. Gaston Giuliani for helpful discussions.

Gem-A
INSTRUMENTS

OVER **100** PRODUCTS AVAILABLE

Buy Gem-A Instruments online!

View the full collection at:
shop.gem-a.com

GEM-A MEMBERS!

Log in to the Gem-A Instruments website and gain instant access to discounted rates. You must log in before adding products to your basket.

Username is your membership number.
Password is your surname with a capitalised first letter.

We recommend changing your password in the account settings.

Conferences

5TH ITALIAN NATIONAL CONFERENCE OF GEMMOLOGY

Italy's 5th National Conference of Gemmology took place on 26–27 June 2023 at Sapienza University of Rome (Figure 1). It was organised by **Drs Giovanni B. Andreozzi**, **Ferdinando Bosi** and **Michele Macrì** of Sapienza University of Rome, and also by **Paolo Minieri** of *IGR – Rivista Italiana di Gemmologia/Italian Gemological Review*. More than 220 participants registered for the two-day event, which had a theme of 'Yesterday, Today, Tomorrow: Gemmology between Research, Market and Politics'. Most of the presentations were in English, and simultaneous translations were provided in Italian or English. The event was accompanied by an exhibition of fine gemstones crafted by master cutter **Luigi Mariani** (Figure 2).

The conference began with several introductory addresses by dignitaries and the conference organisers, during which attendees learned that Italy's inaugural National Conference of Gemmology occurred in 2010 in Bari, and subsequent events took place in Florence, Naples and Ferrara.

Three presentations offered general reviews of gemmological topics. **Dr Thomas Hainschwang** (GGTL Laboratories, Balzers, Liechtenstein) discussed current challenges faced by gemmological laboratories. For coloured stones, these include: authenticating melee-sized gems in parcels; identifying low-temperature heating of ruby, sapphire, aquamarine, Imperial topaz, spinel and tanzanite; detecting Be-diffusion treatment in parcels of melee-sized corundum; quantifying clarity treatment in emerald; and detecting irradiation-related colour treatment of topaz, tourmaline, morganite, etc. For diamonds, the challenges include: detecting synthetics in melee-sized parcels of coloured diamonds; identifying HPHT treatment in colourless,

Figure 1: Participants at the 5th National Conference of Gemmology gather in the lecture hall of the Department of Earth Sciences at Sapienza University of Rome. This image was taken during the round-table discussion at the end of the conference. Photo by B. M. Laurs.

Figure 2: A portion of the fine gemstones exhibited during the conference by gem cutter Luigi Mariani are shown here. Photo by B. M. Laurs.

pink and blue type IIa and IIb stones; and identifying irradiation-related colour treatments, particularly for green to greenish blue diamonds. He also mentioned that country-of-origin determination is problematic for coloured stones (particularly blue sapphire) and is impossible for diamond. **Dr Loredana Prosperi** (Italian Gemological Institute, Milan, Italy) chronicled gemmological developments seen by laboratories over the past 35 years. She described how gemmologists initially had only a few simple tools that were used to deal with relatively straightforward identification problems, but as time went on the challenges became more complicated and so did the technology needed to address them. She ended by questioning the role of gemmologists in the future as artificial intelligence becomes more widespread in its application to gem analysis. **This author** reviewed important gemmological developments of the past decade, including: progress in the growth and characterisation of synthetic diamonds; the proliferation of diamond verification devices for the screening and detection of these synthetics (and simulants); age dating of inclusions to assist with the geographic origin determination of sapphire; research on the unstable colouration (photochromism) of pink, padparadscha, orange and yellow sapphires; detection of low-temperature heat treatment of ruby and sapphire; progress on the geographic origin determination of ruby, blue sapphire, emerald, Cu-bearing tourmaline and alexandrite; and refinements in instrumentation and analytical techniques (especially portable Raman and EDXRF spectroscopy).

Dr Emmanuel Fritsch (University of Nantes, France) compared two types of hollow inclusions in gems. The first, dissolved dislocations, form in a variety of gems and result from preferential chemical etching along defects such as edge and screw dislocations, resulting in surface-reaching, tapered, straight or curved hollow tubes that commonly have a polygonal cross-section. The second, rose channels, form in diamond, corundum and calcite, and occur at the intersection of twin lamellae where the migration of vacancies results in straight, hollow channels with a constant lozenge-shaped cross-section.

Diamonds were the topic of three presentations. **Sergio Sorrentino** (E-motion Diamond, Marcianise, Italy) looked at various aspects of the diamond trade, particularly marketing and sustainability issues and the increasing availability of synthetics. He emphasised that in order to maintain consumer confidence, transparency is particularly critical when dealing with synthetic diamonds—such as explaining their much lower value and difficulty in reselling them as compared to natural diamonds. **Dr Fabrizio Nestola** (University of Padova, Italy) examined the depth at which superdeep diamonds form. The most abundant inclusion in these diamonds is 'ferropericlase' (or 'magnesiowüstite'), a variety of periclase with the formula (Mg,Fe)O. He reviewed the use of this inclusion to determine the depth of cogenetic diamond crystallisation, and also examined the enigmatic occurrence of Fe-rich periclase

inclusions in these diamonds. **Giulia Marras** (with **Dr Vincenzo Stagno** from Sapienza University of Rome) discussed recent research on diamond inclusions using multiple advanced techniques, and also covered current growth techniques for synthetic diamonds, including fluid-driven diamond synthesis in a rotating multi-anvil press.

Coloured stones were the topic of several presentations. **Dr Federico Pezzotta** (Mozambique Mining, Milan, Italy) examined the geology, mining and heat treatment of Cu-bearing tourmaline from Mavuco, Mozambique. An average of 500 tonnes of material are processed daily from this residual deposit, yielding around 200–300 g of coloured tourmaline, of which approximately 100 g are Cu bearing. The largest cut stone produced in 2022 weighed 49 ct (Figure 3). **Dr Alessandra Altieri** (Sapienza University of Rome) reviewed the causes of colour in tourmaline, and then explored the genesis of colour zoning in gem crystals from Italy (Elba Island) and Mozambique (Mavuco). The dark-coloured termination on a tourmaline from Elba Island was found to be caused by Fe^{2+} that was derived from the leaching of biotite in the outer zone of the pegmatite, whereas the 'leek-green' (actually greenish yellow) colouration of a sample from another pegmatite on Elba Island was due to Mn^{2+}–Ti^{4+} intervalence charge transfer in the absence of iron. A multi-coloured tourmaline fragment from Mavuco recorded a complex history of enrichment in Mn^{2+}, Mn^{3+}, Cu^{2+}, Fe^{2+} and Fe^{3+} that showed an overall increase in oxidising conditions during crystallisation. **Dr Nicola Precisvalle** and colleagues (University of Ferrara, Italy) studied Imperial topaz from Brazil and Pakistan, and found that the most important trace element in this type of topaz is Cr (associated with V). He noted parallels with the nomenclature of Paraíba tourmaline (i.e. a colour variety regardless of locality). **Dr Isabella Pignatelli** (University of Lorraine, Vandoeuvre-lès-Nancy cedex, France) described her research on the blue/yellow dichroism of laurentthomasite (see article on pp. 708–716 of this issue of *The Journal*), as well as the possible presence of H_2O in this nominally anhydrous mineral. **Dr Marco Campos-Venuti** (Seville, Spain) discussed the likely microbial origin of epigenetic dendritic inclusions in quartz (e.g. pyrite/limonite aggregates, Mn-oxide colloform structures, 'koi fish' banded structures, etc.). The best evidence for their microbial origin is provided by similarities in the morphological structures of bacterial colonies.

Presentations on biogenic gem materials covered pearls and coral. **Piero De Stefano** (Studio De Stefano Gemmologi Associati, Rome) reviewed the current status of the cultured pearl industry. He noted the following trends: (1) production in Japan is way down, and the price has increased by 40–50%, with 80% of these cultured pearls going to China; (2) there is good availability of South Sea cultured pearls, but only in sizes up to 18 mm, and prices are increasing; and (3) freshwater cultured pearls are widely available, and there is large demand for higher quality to compensate for the lack of Japanese cultured pearls and the high cost of South Sea products. **Francesco Sequino** (International Gemological Institute, Naples, Italy) described his studies of coral treatments in order to differentiate between untreated

Figure 3: This image includes a selection of the finest Cu-bearing tourmaline gemstones from Mavuco, Mozambique, that were produced in 2022. The largest stone weighs 49 ct. Photo © Elliott/Mozambique Mining LLC.

coral and material subjected to surface oiling/waxing, filling of fractures or cavities with foreign substances, and impregnating with coloured plastic or similar substances. Useful tools included a hot point, a strong UV lamp (to detect the presence and amount of fillers) and Raman spectroscopy.

Instrumentation and analytical techniques were profiled in three presentations. **Dr Gioacchino Tempesta** (with co-author **Dr Giovanna Agrosì**, both of the University of Bari Aldo Moro, Italy) reviewed the application in gemmology of portable laser-induced breakdown spectroscopy (LIBS) and Raman spectroscopy. LIBS is a qualitative (rather than quantitative) chemical analysis technique that requires statistical methods or artificial intelligence to be employed in data processing in order to identify a sample's mineral group, whereas Raman spectroscopy is used in conjunction with well-established databases (e.g. https://rruff.info) for identification of specific minerals and is capable of differentiating between polymorphs. **Dr Danilo Bersani** (University of Parma, Italy) performed Raman characterisation of zoisite and other sorosilicates. He found that samples of yellow zoisite showed the same Raman features regardless of locality (Tanzania and the Alps), consistent with a lack of V. He also used Raman spectroscopy to distinguish between different members of the epidote group and measure the composition of specimens in the epidote-clinozoisite series. **Dr Gabriele Giuli** (University of Camerino, Italy) and colleagues reported the results of EPR and XAS spectroscopy to investigate the cause of colour in tanzanite. They found that the main chromophores are V^{3+} and Fe^{3+}, but that no simple mechanism is able to explain tanzanite's violetish blue colouration.

The study of gems from antiquity and in cultural heritage objects was the focus of three presentations. **Flavio Butini** (Istituto Gemmologico Nazionale, Rome) examined 43 engraved cabochons of 'prase' (Cr-bearing chalcedony). Gemmological and EDXRF chemical characterisation showed a high degree of homogeneity for all of these samples, and also some clear differences from 'modern' Cr-bearing chalcedony. This suggests a single source for archaeological Cr-bearing chalcedony. Currently known sources of this gem material include Australia, Zimbabwe, Bolivia, Tanzania and Turkey, but Pliny also mentioned Cyprus (now exhausted). **Dr Maura Fugazzotto** and colleagues (University of Catania, Italy) described recent research on gemstones in historical liturgical ornaments in Sicily using portable EDXRF and Raman spectroscopy. The objects were found to contain emerald, ruby, diamond, amethyst, rock crystal, citrine, garnet, spinel and artificial glass. It is likely that stones lost or removed during past handling and cleaning of the objects were replaced by substitutes that were different from the original materials (e.g. rock crystal for diamond). **Marco Torelli** (Masterstones Gemmological Analysis Center, Rome) examined and photographed an unusual ring owned by Pope Leo XII (who served in 1823–1829), which contains an approximately 2 ct 'green transmitter' diamond surrounded by 25 'rubies' (two of which proved to be red spinel) that were mounted on a slab of malachite. To photograph the ring, he used focus stacking to improve the depth of field, and then he processed the photos into a three-dimensional image that could be rotated by a viewer in the metaverse.

There was one presentation related to jewellery manufacturing, in which **Rocco Gay** delivered a talk for **Alessia Crivelli** (Gruppo Aziende Orafe di Confindustria Alessandria, Italy) on the Mani Intelligenti Foundation, which seeks to make the small municipality of Valenza attractive for the training and employment of young goldsmiths.

Towards the end of the conference was a session titled 'Speed Presentations' that featured four-minute talks on a variety of subjects by eight speakers: **Antonio Angellotti** (mineral inclusions in superdeep diamonds from Juina, Brazil), **Sara Monico** (synchrotron X-ray powder diffraction of Aquaprase chalcedony), **Marco Palumbo** (archaeological glasses from Roman antiquity), **Lorenzo Pasetti** (Raman spectroscopy of tourmaline gemstones), **Chiemi Sasajima** (new developments pertaining to Japanese coral), **Flavio Butini** for **Rose Marie Scappin** (three-dimensional elastomeric measurements of glyptic gems) and **Marilisa Yolanda Spironello** (Sicilian coral in fifteenth- to sixteenth-century masterworks). Most of these speakers also presented their research in a poster session during the conference.

The conference closed with a round-table discussion coordinated by **Dr Eugenio Scandale** (Accademia Pugliese delle Scienze, Bari) and moderated by **Dr Giovanni Andreozzi**, which partially focused on answering the question, 'What is a gem?' Although there is an accepted definition by the International Mineralogical Association (IMA) for what constitutes a mineral (a solid chemical substance formed as a result of geological processes), this is not the case for a gem. Based on the feedback obtained during the discussion, the group plans to submit a proposed definition of a gem to the IMA.

Brendan M. Laurs FGA

Gem-A Notices

MESSAGE FROM GEM-A CEO ALAN HART

Welcome to this issue of *The Journal of Gemmology*. This summer, Gem-A's headquarters has been buzzing with activities and projects, which we will be presenting in the coming months, including a brand-new website and online Member's area. In the meantime, as we release the results from the June 2023 exams, we are also thrilled to welcome our new students to Ely Place—and our distance-learning students online—for the new term starting this autumn. Later in October we will commence our membership renewal process for the year 2024. More information on how to renew your membership will be provided in due course.

Looking further ahead, I am thrilled to announce that the Gem-A Conference will be held in London this autumn on Sunday 5 November. Registration is now open for the conference and gala dinner, and I personally look forward to offering a warm welcome to many of our members, colleagues and partners. We have an excellent line-up of six international speakers who will deliver sessions on a wide range of gemmological and related topics.

I would like to extend my sincerest thanks once again for your ongoing support. I hope you enjoy this issue of *The Journal*, and I look forward to seeing many of you again soon.

REGISTER NOW FOR THE GEM-A CONFERENCE

The Gem-A Conference will make an in-person return on Sunday 5 November at etc.venues County Hall, which overlooks the River Thames and the Houses of Parliament in London. This year's event will feature a very full day with six expert speakers and will conclude with the much-anticipated Conference Dinner at the Tower of London (including a private tour of the new crown jewels exhibit), which will provide a fantastic opportunity to network with other gemmologists and jewellery professionals. Registrations for the conference and gala dinner are now open. More information and a link to register is available at https://gem-a.com/event/conference-2023. On Monday 6 November and Tuesday 7 November, attendees will have the option to attend a series of workshops and field trips to make the most of their visit to London.

GEM-A GRADUATION AND PRESENTATION OF AWARDS

The Gem-A Graduation and Presentation of Awards ceremony will be held at Goldsmiths' Hall in London on Monday 6 November. This important event will celebrate the achievements of our most recent graduating class, including special awards and prize winners. Goldsmiths' Hall, positioned at the junction of Foster Lane and Gresham Street, opened in 1835 and is one of London's hidden treasures. The Livery Hall is an awe-inspiring space and a magnificently proportioned room with Corinthian columns and a richly moulded ceiling decorated with gold leaf.

OBITUARY

Erik Schoonhoven, Amsterdam, The Netherlands, passed away on 10 August 2023. He was a cultural and literary historian who authored and reviewed articles for *The Journal*.

2023 ANNUAL GENERAL MEETING

This year, the Gem-A Annual General Meeting (AGM) will be held on 18 October at 17:00 at Gem-A's headquarters on Ely Place. To encourage participation from our global Membership base, voting on the resolutions will take place prior to the AGM using Civica Election Services. More information on the voting platform and access to the AGM documentation will be provided to Members via our email newsletters.

GIFTS TO THE ASSOCIATION

Gem-A is most grateful to the following for their generous donations that will support continued research and teaching:

Gaye Haselden, United Kingdom, for a rough specimen of white coral.

Roy Huddlestone, United Kingdom, for donating his entire collection of Lennix synthetic emeralds, which were the first synthetic emeralds to be grown in London.

Michal Kosior, Poland, for 14 rough pieces of Baltic amber and one specimen of Baltic amber sitting on the matrix on which it was found.

Enzo Liverino, CIBJO, Italy, for an important reference collection of different varieties of coral, both rough and polished.

Iona Pettit, United Kingdom, for donating her late husband's (Brian Pettit, gemmologist and jeweller) entire gemmology library of 78 books.

Mark Sandum, United Kingdom, for a 0.20 ct round-brilliant-cut diamond with a burned surface resulting from overheating during jewellery repair.

Sally Spencer, United Kingdom, for a copy of her book, *Jewellers' Quick Reference Guide to Working with Gemstones*.

Solly Solomons, United Kingdom, for four faceted fluorite specimens.

Learning Opportunities

CONFERENCES AND SEMINARS

CIBJO Congress 2023
3–5 October 2023
Jaipur, India
https://www.cibjo.org/congress2023

17th International Conference on Applied Mineralogy and Minerals (ICAMM 2023)
9–10 October 2023
New York, New York, USA
https://waset.org/applied-mineralogy-and-minerals-conference-in-october-2023-in-new-york
Theme of interest: Industrial Minerals, Gems, Ores, and Mineral Exploration

International Society of Appraisers 2023 Gems & Jewelry Symposium
13 October 2023
Online
https://www.isa-appraisers.org/courses/course/1513

Geological Society of America Annual Meeting (GSA Connects 2023)
15–18 October 2023
Pittsburgh, Pennsylvania, USA
https://community.geosociety.org/gsa2023/home
Session of interest: Gemological Research in the 21st Century—Gem Minerals and Localities

65th Anniversary Canadian Gemmological Association (CGA) Gem Conference
20–22 October 2023
Vancouver, British Columbia, Canada
https://canadiangemmological.com/2023-cga-conference-2

2023 Canadian Jewellers Association Industry Summit
23 October 2023
Vancouver, British Columbia, Canada
https://canadianjewellers.com/events/2023-cja-industry-summit

37th International Gemmological Conference
23–27 October 2023
Tokyo, Japan
https://www.igc-gemmology.org/igc-2023
Note: There will be a pre-conference jadeite excursion and a post-conference pearl excursion.

Gem-A Conference
5 November 2023
London
https://gem-a.com/event/conference-2023
Note: Workshops and field trips (and a graduation ceremony for Gem-A students) will take place on 6 November, and additional workshops will be held on 7 November.

GemGenève
2–5 November 2023
Geneva, Switzerland
https://gemgeneve.com
Note: Includes a seminar programme

New Mexico Mineral Symposium
10–12 November 2023
Socorro, New Mexico, USA
https://geoinfo.nmt.edu/museum/nmms/home.cfml

24th Federation for European Education in Gemmology (FEEG) Symposium
13 January 2024
Barcelona, Spain
http://www.feeg-education.com/symposium

NAJA 61st Winter Education Conference
28–29 January 2024
Tucson, Arizona, USA
https://najaappraisers.com/event/61st-annual-aceit-winter-education-conference

AGTA GemFair Tucson
30 January–4 February 2024
Tucson, Arizona, USA
https://agta.org/agta-gem-fair-tucson

Accredited Gemologists Association (AGA) Tucson Conference
31 January 2024
Tucson, Arizona, USA
https://accreditedgemologists.org

Tucson Gem and Mineral Show
8–11 February 2024
Tucson, Arizona, USA
https://www.tgms.org/show
Note: The theme of the seminar programme is 'Pegmatites: Crystals Big & Beautiful'.

Inhorgenta Munich
16–19 February 2024
Munich, Germany
https://inhorgenta.com/en
Note: Includes a seminar programme

Hasselt Diamond Workshop 2024 (SBDD XXVIII)
28 February–1 March 2024
Hasselt, Belgium
https://www.uhasselt.be/SBDD#anch-bce-sbdd-xxviii

Independent Jewelers Organization (IJO) Conference
9–12 March 2024
Dallas, Texas, USA
https://www.ijo.com/events/conferences

MJSA Expo
10–12 March 2024
New York, New York, USA
https://www.mjsa.org/events/mjsa-expo

American Gem Society Conclave
15–17 April 2024
Austin, Texas, USA
https://www.americangemsociety.org/conclave-2024

Jewellery & Gem ASEAN Bangkok
1–4 May 2024
Bangkok, Thailand
https://aseanbangkok.exhibitions.jewellerynet.com
Note: Includes a seminar programme

Scottish Gemmological Association Conference
3–6 May 2024
Location TBA
https://www.scottishgemmology.org/conference-2023

7th Mediterranean Gem and Jewellery Conference
7–11 May 2024
Cavalese, Italy and Piran, Slovenia
https://www.gemconference.com
Note: Workshops will take place 7–9 May in Italy and the conference will occur on 11 May in Slovenia. Pre- and post-conference tours are also available.

OTHER EDUCATIONAL OPPORTUNITIES

Gem-A Workshops and Courses
Gem-A, London
https://gem-a.com/education

Diplôme Universitaire de Gemmologie (DUG; University Diploma in Gemmology)
25 March–3 June 2024
https://sciences-techniques.univ-nantes.fr/formations/du-gemmologie
Note: The course will be taught in English at the University of Nantes in France. An information booklet in English can be downloaded at https://tinyurl.com/mr3b4639.

Gemstone Safari to Tanzania
10–27 January 2024 and 3–20 July 2024
https://www.free-form.ch/tanzania/gemstonesafari.html

Lectures with The Society of Jewellery Historians
Society of Antiquaries of London, Burlington House
https://www.societyofjewelleryhistorians.ac.uk/current_lectures (lists lectures up to November 2024)

- Cordelia Donohue—New Research on Tuareg Jewellery
  and
  Kathleen Walker-Meikle—Pet Bling: Jewelled Animal Accessories in the Late Medieval and Early Modern Period
  24 October 2023

- John Benjamin—Jewellery from Anglesey Abbey
  28 November 2023

- Sarah Laurenson—For a Banquet of Vampires: Scottish Stones in Jewellery
  23 January 2024

New Media

Amber Art: A Journey Between Science and Beauty

By Enrico Bonino, 2022. Self-published, https://enrico-bonino.eu/paleontology-publications, 300 pages, illus., ISBN 978-2960243611. EUR75.00 hardcover.

There is something magical about life forms captured in amber or other types of fossilised resin found around the globe. This fascination probably extends back to the origin of humanity. Imagine a group of Neanderthals holding pieces of amber up to the light and wondering how such creatures could have entered this 'stone' without breaking it into small pieces. While written accounts of such early events may not exist, actual amber pieces carved by our ancestors depicting animals and ancient tools have been recovered.

Creatures in amber are so well preserved, one may imagine they are still alive. This is what makes amber inclusions so attractive to humans: a desire to live forever. Just look at the attempts that have been made to use cryonic procedures to preserve humans so they could be brought back after death. Even the Egyptians covered their mummies with cloth soaked in resin to preserve them for a better afterlife.

Enrico Bonino is not the first to visualize amber art. Combining the artistic and scientific aspects of amber has been provided previously to English-language readers with Rosa Hunger's *The Magic of Amber* (1977) and Jamey D. Allen's *The Mysteries of Amber* (1990). Polish readers have the book *Tajemnice Bursztynem* (*Amber Secrets*) by Barbara Kosmowska-Ceranowicz and Tomasze Konart (1989). In German is Günter and Brigitte Krumbiegel's 2001 book *Faszination Bernstein* (*Fascination Amber*), and Chinese readers have *Wonders in Amber* by Yi-Jen Huang (2008) and *Amber—Lives Through Time and Space* by Fangyuan Xia *et al.* (2015).

The present work, *Amber Art*, has a similar theme to the abovementioned books in that it shows how artistic amber inclusions can be when examined with the right lighting. While the table of contents arranges the illustrations under several higher insect taxa, it is their photographic presentation that is stressed as the 'artistic' part of the book. Amber inclusions, like human art, retain their fascination and emotional suspense in timeless fashion. A current example of such art is Ossip Zadkine's *The Destroyed City*, a statue of a damaged figure arising from the rubble of Rotterdam after it was bombed in the Second World War.

What makes *Amber Art* unique is the use of a special camera to examine minute structures in the fossilised resin, including those of entombed animals and plants—aspects that only appear as specks to the general viewer. These excellent photos of amber specimens are the result of what the author calls 'macro-extreme photography', with the camera attached to an extension tube and the use of a microscopic objective. A wide range of lighting was employed, and focus-stacking was done to obtain a wide depth of field. Many of the photos in this book display details that can be used scientifically to establish new genera and species. All these features allow the reader to see a microworld rarely available to the public. These amazing advancements in the field of photomicrography reveal fine details previously rivalled only by images obtained with a scanning electron microscope.

While a number of amber sources are listed in the front of the book, most of the 333 specimens depicted in *Amber Art* consist of Baltic amber. In fact, Baltic, Dominican and Burmese amber specimens together represent about 95% of the amber sources photographed. Some viewers examining mid-Cretaceous Burmese amber fossils may not realize that these species co-existed—and possibly even had some physical contact—with dinosaurs.

With its captivating photographs, *Amber Art* is a very enjoyable book to read.

Dr George Poinar Jr
Oregon State University
Corvallis, Oregon, USA

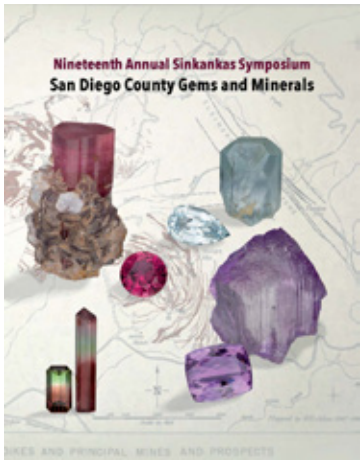

Nineteenth Annual Sinkankas Symposium: San Diego County Gems and Minerals

Ed. by Stuart Overlin, 2023. Pala International Inc., Fallbrook, California, USA, https://sinkankas.dpidirect.com/category/symposium-volumes, 97 pages, illus., ISBN 978-0991532070. Approximately USD42.50 softcover or free PDF.*

The Nineteenth Annual Sinkankas Symposium, held in April 2023 at the Gemological Institute of America (GIA) in Carlsbad, California, USA, focused on the gems and minerals of San Diego County, California. The event was co-hosted by GIA and the Gemological Society of San Diego.

After a dedication, acknowledgements, and speaker and author biographies, the abstracts of the symposium presentations begin with 'Tales from the Pala Chief mine' by Dr Raquel Alonzo-Perez of Harvard University, followed by 'Cutting the gems of San Diego County' by lapidary artist Meg Berry, 'Eureka! My love affair with the gems of Southern California' by jewellery designer Paula Crevoshay, 'Using gems to illuminate art and science' by Dr Aaron Celestian of the Natural History Museum of Los Angeles, 'The microfeatures of gems and minerals from San Diego County' by GIA's Nathan Renfro, 'Tourmaline crystallography' by William B. 'Skip' Simmons of the Maine Mineral and Gem Museum, and 'The causes of color of the San Diego County gem minerals' by Drs George Rossman of the California Institute of Technology and Aaron Palke of GIA.

Two previously published articles included in the proceedings are 'Spessartine garnet from Ramona, San Diego County, California' by Brendan M. Laurs and Kimberly Knox (originally published in the Winter 2001 issue of *Gems & Gemology*) and 'Pala pink and Mesa Grande mauve' by Ryan Bowling (from *Rubellite—Tourmaline Rouge*, Lithographie Mineral Monograph No. 20, 2019). Also included is a previously unpublished manuscript, 'Himalaya mine: Mesa Grande, California', written in 1992 by Bill Larson and John Sinkankas.

Next is an 'Image Gallery' that includes 15 additional illustrations. The volume concludes with a bibliography compiled by GIA librarian Sheryl Elen.

Abstracts were not provided for four of the symposium presentations: 'San Diego County mines and minerals' by mineral dealer Cal Graeber, 'The great tourmalines of the Pala mining district' by Bill Larson of Pala International, 'Himalaya mine treasures' by Will Larson of Pala International, and 'Geology of San Diego County pegmatites' by Brendan M. Laurs, editor-in-chief of *The Journal of Gemmology*.

The overall quality of this volume is very good. The paper stock, printing and colour reproduction of the images—lavishly distributed throughout the book—measure up to the importance of the book's theme. The wraparound cover, with its many colourful images of fine San Diego County gems and minerals shown over a geological map of the Pala District, beckons you to open to the contents. The abstracts and image gallery provide a wealth of diagrams, charts, historical images and, of course, photos of minerals, gems and jewellery. Bill Larson provided the specimens shown in many of the images, including those on the cover. The book contains photos by Jeff Scovil, Robert Weldon, Orasa Weldon, Mia Dixon, Emily Lane, Paula Crevoshay and others. Finally, the calibre of the speakers and authors would be hard to beat for the topic.

I have little to criticise and much to recommend about this unique book to mineral enthusiasts, gemmologists, lapidaries, jewellers and anyone, like myself, who loves the minerals, gems, geology and history of San Diego County pegmatite mines, which began producing over a century ago.

Michael T. Evans
Fallbrook Gem and Mineral Museum
Fallbrook, California, USA

* *Editor's note*: Hardcopies of this and previous Sinkankas Symposium volumes are available annually in March through DPI Direct's print-on-demand service (https://sinkankas.dpidirect.com/category/root). The exact pricing depends on the cost of materials at the time. Downloadable PDF files of this and the two previous Sinkankas Symposium volumes are freely available at https://independent.academia.edu/SinkankasSymposium.

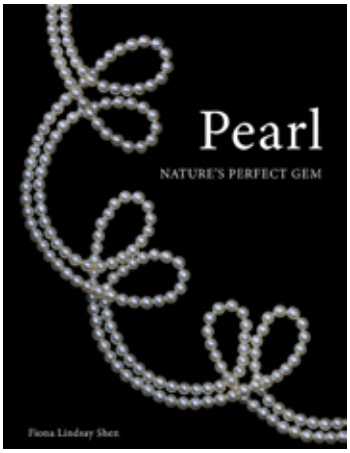

Pearl: Nature's Perfect Gem

By Fiona Lindsay Shen, 2022. Reaktion Books, London, https://reaktionbooks.co.uk/work/pearl, 287 pages, illus., ISBN 978-1789146219 or e-ISBN 978-1789146226. GBP25.00 hardcover or eBook.

Pearl: Nature's Perfect Gem elaborates on subjects regarding pearls that I had not seen in previous books. Most publications I have read on pearls focus heavily on the science, formation and localities of pearls. This book discusses those subjects, but it also details in an original way the sociological and historical impacts of pearls and the pearl trade on humanity and global culture.

The first chapter, 'The Oyster's Autobiography', predictably begins with a discussion of pearl formation, origins and traditional localities. Common myths and fables involving pearls through history are reviewed, along with references in popular literature. In the second chapter, 'Harvest', the reader starts to see the human cost of the pearl trade. Pearls have been harvested from the Persian Gulf for most of human history, and the lesson to be learned here is that very rarely were those who dove for the pearls able to reap the rewards of this dangerous activity. Descriptions of boats and their crews that set out along the Gulf during pearling season, even up to the 1960s, accompany accounts of the cycle of financial ruin that followed the pearl divers. Enslaved people from Africa—some kidnapped, others born into slavery—were used during the pearl boom of the nineteenth and early twentieth centuries. By 1929, roughly 20,000 enslaved divers worked the oyster banks of the Persian Gulf each season. The chapter also covers pearling activities in the Caribbean, Scotland and northern Europe.

The next chapter, titled 'Culturing Pearls, Capturing Markets, Cultivating Brands', details the creation, marketing and branding of cultured pearls. The first round pearls were cultured in Europe by none other than Carl Linnaeus, the father of modern taxonomy. Unfortunately for him, his plan to cultivate pearls in Lapland failed. Tavernier noted in the seventeenth century that Japan did not especially value pearls, but subsequently in the first part of the twentieth century Kokichi Mikimoto was the first person instrumental to the successful growth, branding and marketing of cultured pearls, not just in Japan, but worldwide. Less known but just as important were Tatsuhei Mise and Tokichi Nishikawa, who developed advanced culturing techniques, some of which are still used today for saltwater cultured pearls. Japan retained an absolute hold on the cultured pearl market until after World War II, when European colonists started targeting the rich oyster beds of the north-west Kimberley Coast of Australia, initially for high-quality pearl shells, and subsequently for the pearls. In what had become commonplace, colonists conscripted Aboriginal free divers to collect the shells in conditions comparable to slavery. After legislation was passed in the 1870s to curb the worst of these abuses, the colonists started importing indentured servants from Southeast Asia, a practice that persisted into the 1970s.

This chapter also covers the environmental cost of cultivating literally tonnes of cultured pearls, with warnings as early as 1970 predicting the collapse of the industry. In 1996 a massive die-off of saltwater pearl-culturing molluscs began, and by year's end almost two-thirds of Japan's oyster stock had died. However, since the 1990s freshwater cultured pearl farms in China have been booming, due in part to the *Hyriopsis cumingii* mussel's ability to tolerate water pollution that saltwater oysters could not.

The chapter titled 'The Seven Pearly Sins' covers the negative effects of pearls as they relate to lust, pride, wrath, gluttony, envy, greed and sloth in the human condition, with some surprising insights. The following chapter, 'And Seven Virtues', covers the positive aspects of pearls in terms of chastity, humility, patience, temperance, kindness, generosity and diligence. The fickleness of human perception knows no bounds!

The book closes with 'Embodied', a discussion of pearls in art and popular culture, both ancient and modern. Painted jewellery boxes of Roman Egypt (ca. first to third century CE) depict the upper classes commonly wearing *crotalia* (bar-and-pendant earring designs, also called castanet earrings, often with pearls), which help historians understand the culture of the time. The portraits were probably painted post-mortem to help the subject 'stay alive' for eternity. Mantegna of

Mantua (who had a reputation as a gem expert as well as an artist) was the first to depict in his ca. 1460 painting *The Adoration of the Magi* an independent (rather than 'owned') man of colour, Balthazar, as an ambassador wearing his own pearls. Vermeer's 1665 painting *Girl with a Pearl Earring* demonstrates how such a perfect illustration of a pearl was achieved by using no less than four different types of lead-white pigment to produce convincing 'pearliness' on a two-dimensional surface.

Depictions of pearls in art were not confined to northern European art. Mughal miniatures were often painted in opaque watercolours with organic and inorganic chemical bases, and lead white again was used to depict pearls. Some of the best miniatures use real seed pearls and gemstones instead of paint. In both Chinese and Japanese cultures, mother-of-pearl was often employed as wafer-thin pieces to depict scenes such as plum blossoms in moonlight. A lovely platter depicts, in mother-of-pearl, two dragons chasing the mythical 'Flaming Pearl'.

The 'Embodied' chapter ends with a description of how, in modern times, Catherine Opie photographed items belonging to the late actress Elizabeth Taylor. The resulting book, *700 Nimes Road*, has some images of Taylor's fabled jewellery collection, including the famous *La Peregrina* pearl. An historic pearl with a hazy past, Opie's artistic image of *La Peregrina* is purposefully blurred to convey the idea of a jewel rather than a photograph.

I highly recommend this book to anyone interested in pearls, if only for its unique perspective on how pearls and the pearl industry have influenced both ancient and modern culture. This book is well researched, and offers copious chapter notes and an excellent bibliography. It is also richly illustrated with historical paintings, modern photos and other images that enhance the text.

Jo Ellen Cole
Cole Appraisal Services
Los Angeles, California, USA

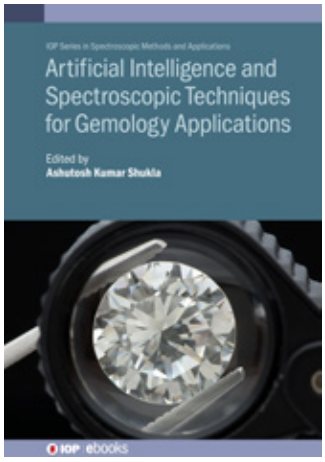

Artificial Intelligence and Spectroscopic Techniques for Gemology Applications

Ed. by Ashutosh Kumar Shukla, 2022. IOP Publishing Ltd, Glassfields, Bristol, 167 pages, illus., ISBN 978-0750339254 or e-ISBN 978-0750339278, https://doi.org/10.1088/978-0-7503-3927-8. GBP120.00 hardcover or GBP99.00 eBook.

This book is a five-chapter work that explores various analytical methods, including laser-induced breakdown spectroscopy (LIBS), Raman spectroscopy, Fourier-transform infrared spectroscopy (FTIR), optical tomography and X-ray fluorescence (XRF) spectroscopy in the context of gem analysis. Drawn in by the title, I anticipated a deep dive into the application of artificial intelligence (AI) within the realm of spectroscopic data, and its subsequent utilisation for more accurate identification of gem materials, treatments and geographical origins, all of which are of significant relevance to contemporary gemmological studies. However, if you are similarly intrigued by the mention of 'artificial intelligence' in the title, you may find the content of the book somewhat disappointing. The term is essentially used in the title alone, with most of the content having no direct connection to AI. The chapters primarily introduce the respective analytical techniques and illustrate examples of their applications in gemmology. The closest part to AI is perhaps chapter 3.9 ('Application of machine learning algorithm to gemstone classification'), yet the discussion remains largely theoretical, lacks details and does not offer concrete examples.

Chapter 1 opens with a discussion of LIBS used for gem analysis, with a considerable portion focusing on the theory behind the technique and the formula deduction for calibration-free LIBS. The method is particularly appealing for being quick and cost-effective while leaving minimal markings on samples. Section 1.3 includes some background from the literature, from the detection of Be diffusion-treated corundum in the early 2000s to the classification of beryl of various colours. The authors then provide additional examples

from the literature that use more advanced LIBS-based techniques, such as calibration-free LIBS, double-pulse LIBS and nanoparticle-enhanced LIBS. In terms of multivariate statistical analysis of the LIBS spectra, the authors briefly introduce research by Kochelek *et al*. (2015) using partial least-squares regression to reach a high accuracy (>95%) in the geographical origin classification of ruby and sapphire. A study by Eum *et al*. (2018) using a hierarchical support vector machine approach to combined Raman and LIBS data also showed high accuracy (>90%).

Chapter 2 covers gem analysis using Raman spectroscopy. After introducing the technique, the authors compare benchtop and mobile instrumentation. The latter extends the capability of the Raman technique outside of the lab environment, such as in geological fieldwork or on-site in museums. In the following section, the authors showcase some studies on various gems and jewelled artefacts, including garnet, jade, beryl, corundum, glass, pearl, coral and simulants. A short section also covers photoluminescence analysis using a Raman system. This technique can provide complementary information that is measured at the same time as Raman analysis.

Chapter 3 begins with an introduction to the concept of FTIR spectroscopy. It provides not only a brief theoretical background but also an extended comparison of different sampling techniques for the FTIR analysis of gems. Then the authors describe how FTIR spectroscopy can help the identification of various gem materials. Starting with diamond, the chapter covers type classification, characterisation of synthetic and treated diamonds, and the detection of simulants. A similar approach is taken for other gems, such as corundum, emerald, quartz, jade and turquoise. In discussing the origin determination of emerald, the authors stress the importance of combining complementary analytical techniques. Section 3.9 describes a path for gem classification via machine learning. However, this section feels somewhat disjointed from the previous ones, as it consists of many techniques other than FTIR. While the authors' perspectives may be trendy, in my view many of the methods mentioned seem oversimplified compared to the realities of their implementation. The absence of any tangible examples lends the section a promotional tone, and it comes across as somewhat unconvincing. Nevertheless, in general, this chapter provides useful 'fingerprint' information for gem applications.

Chapter 4 describes the use of optical tomography for ruby clarity grading. However, the authors wrote this section in a way I found hard to understand. Unlike the better-known X-ray tomography, this technique uses a red laser diode as an emission source and a CCD plate as a detector. It then employs an image-reconstruction process, but there is no three-dimensional tomogram of the ruby shown after the calculation, which I found puzzling. For X-ray tomography to work properly, an X-ray penetrates the sample and largely keeps its direction before reaching the detector. In optical tomography, it is necessary to consider the refraction of light in the gemstone, but there is no mention of how this is handled. In addition, the authors indicate that 'Due to the overly complex mathematical model, light scattering and the diffraction effect were elected to be disregarded in this study's calculations' (p. 4-4), which sounds debatable. Moreover, the last two sentences of the chapter's conclusion (p. 4-13) may not be true in many cases: 'A ruby stone with better clarity is considerably more expensive in comparison to a ruby stone with lower clarity. In other words, a ruby stone with a lower refractive index indicates that it commands a higher price compared to a ruby stone with a higher refractive index.' Readers would be better off not assuming these to be universal truths.

Chapter 5 introduces trace-element analysis of gems using XRF. It begins with some basic principles of the technique, followed by a comparison of advantages over other trace-element techniques. A large portion of the chapter then presents some case studies in which XRF was potentially helpful. These examples include garnet (distinguishing tsavorite from demantoid), tourmaline (determining the colouring agents in blue and 'watermelon' tourmalines), pearl (separating freshwater from saltwater origin, and colour-treatment detection) and ruby (fluorescence intensity variations related to Cr:Fe ratio). The authors further discuss 'big data applications in gemology' in section 5.4, with two examples of geographical origin determination for ruby and spinel. The chapter illustrates a bivariate scatter plot (Figure 5.22) and score plot (Figure 5.29) using linear discrimination analysis to distinguish a few countries of origin for ruby and spinel. Unfortunately, the term 'big data' is not adequately supported by the content, and it is not convincing that the authors consider an XRF spectroscopy dataset, which can be handled with an Excel spreadsheet, as 'big'.

In conclusion, this book provides some useful information about the analysis of gem materials using various spectroscopic techniques. Each chapter begins with an introduction to the technique, and most chapters offer actual examples. However, it would have been beneficial if the book had dedicated a section to ultraviolet-visible-near infrared spectroscopy, a crucial

spectroscopic tool for coloured-stone testing. Secondly, the book clearly lacks AI-related content, while certain buzzwords related to machine learning and big data are overused. Thus, the notion of AI as a 'silver bullet' to aid gemmologists in gem testing or address challenges in gemmological research may be premature. I am awaiting a contribution that can demonstrate the power of AI to assist gemmological work. Regrettably, this book isn't it.

Dr Hao A. O. Wang FGA
Swiss Gemmological Institute SSEF
Basel, Switzerland

Other Book Titles

CULTURAL HERITAGE

The Bone and Ivory Objects from Gordion
By Phoebe A. Sheftel, 2023. University of Pennsylvania Press, Philadelphia, Pennsylvania, USA, 584 pages, ISBN 978-1949057171 or e-ISBN 978-1949057188. USD120.00 hardcover or eBook.

The Gordion Excavations, 1950–1973: Final Reports Volume II—The Lesser Phrygian Tumuli Part 2: The Cremations
By Ellen L. Kohler and Elspeth R. M. Dusinberre, 2023. University of Pennsylvania Press, Philadelphia, Pennsylvania, USA, 792 pages, ISBN 978-1949057157 or e-ISBN 978-1949057164. USD120.00 hardcover or eBook.

The Magnificent Kunlun Jade: The Songzhutang Collection of Ming and Qing Jade
By Thomas Fok, 2023. CA Book Publishing, Hong Kong, 190 pages, ISBN 978-9887608936. HKD800.00 hardcover.

INSTRUMENTATION

Chemometrics and Numerical Methods in LIBS
By Vincenzo Palleschi, 2023. John Wiley & Sons, Hoboken, New Jersey, USA, xviii + 360 pages, ISBN 978-1119759584 or e-ISBN 978-1119759614, https://doi.org/10.1002/9781119759614. USD165.00 hardcover or eBook.

Laser Induced Breakdown Spectroscopy (LIBS): Concepts, Instrumentation, Data Analysis and Applications
Ed. by Vivek K. Singh, Durgesh Kumar Tripathi, Yoshihiro Deguchi and Zhenzhen Wang, 2023. John Wiley & Sons, Hoboken, New Jersey, USA, 1,008 pages, ISBN 978-1119758402 or e-ISBN 978-1119758426, https://doi.org/10.1002/9781119758396. USD395.00 hardcover or eBook (two-volume set).

JEWELLERY HISTORY

The Material Landscapes of Scotland's Jewellery Craft, 1780–1914
By Sarah Laurenson, 2023. Bloomsbury Publishing, London, 272 pages, ISBN 978-1501358005, e-ISBN 978-1501357985 (PDF) or 978-1501357992 (ePub). GBP90.00 hardcover or GBP81.00 eBook.

Speculum Lapidum: A Renaissance Treatise on the Healing Properties of Gemstones
By Camillo Leonardi (transl. with an introduction by Liliana Leopardi), 2023. Penn State University Press, University Park, Pennsylvania, USA, 240 pages, ISBN 978-0271095394. USD39.95 hardcover.

JEWELLERY AND *OBJETS D'ART*

Jakob Bengel, Oberstein: From Art Industry to Jewellery Design
Ed. by Jakob Bengel-Stiftung, 2023. Arnoldsche Art Publishers, Stuttgart, Germany, 152 pages, ISBN 978-3897906952 (in English and German). EUR28.00 hardcover.

Liber Amicorum in Honour of Diana Scarisbrick: A Life in Jewels
By Beatriz Chadour-Sampson, Sandra Hindman and Carla van de Puttelaar, 2022. Ad Ilissvm, London, 280 pages, ISBN 978-1915401021. GBP35.00 hardcover.

Therese Hilbert—RED: 1966–2020 Jewelry
By Heike Endter, Warwick Freeman, Petra Hölscher, Otto Künzli, Ellen Maurer Zilioli, Pravu Mazumdar and Angelika Nollert, 2023. Arnoldsche Art

Publishers, Stuttgart, Germany, 360 pages, ISBN 978-3897906235 (in English and German). EUR38.00 hardcover.

A Touch of Gold: The Reminiscences of Geoffrey Munn
By Geoffrey Munn, 2023. ACC Art Books, Woodbridge, Suffolk, 208 pages, ISBN 978-1788841979. GBP25.00 hardcover.

Walid Akkad: Bestiaire
By Michael Jakob, 2023. Silvana Editoriale, Milan, Italy, 96 pages, ISBN 978-8836653164. EUR35.00 hardcover.

Windows at Tiffany & Co.
By Christopher Young, 2023. Assouline Publishing, New York, New York, USA, 148 pages, ISBN 978-1649802224. USD85.00 hardcover.

MISCELLANEOUS

The Chatham Legacy: An American Story
By Thomas H. Chatham, 2023. Thomas H. Chatham, Half Moon Bay, California, 219 pages, ISBN 979-8987916100. USD90.00 hardcover.

King of Diamonds: Harry Winston—The Definitive Biography of an American Icon
By Ronald Winston & William Stadiem, 2023. Skyhorse Publishing Inc., New York, New York, USA, 336 pages, ISBN 978-1510775602 or ASIN B0B6WKFL1M. USD28.99 hardcover or USD17.99 Kindle edn.

PEARLS

The Story of the Pearl
By Caroline Young, 2023. OH! (Orange Hippo/ Welbeck Publishing Group), London, 160 pages, ISBN 978-1838611422. GBP14.99 hardcover or GBP7.99 eBook.

SOCIAL STUDIES

Under Pressure: Diamond Mining and Everyday Life in Northern Canada
By Lindsay A. Bell, 2023. University of Toronto Press, Toronto, Ontario, Canada, 188 pages, ISBN 978-1487548278 (hardcover), 978-1487548216 (softcover), e-ISBN 978-1487548872 (ePub) or 978-1487548575 (PDF). CAD75.00 hardcover, CAD26.95 softcover or CAD21.95 eBook.

Literature of Interest

COLOURED STONES

Agates from Mesoproterozoic volcanics (Pasha–Ladoga basin, NW Russia): Characteristics and proposed origin. E.N. Svetova and S.A. Svetov, *Minerals*, **13**(1), 2022, article 62 (26 pp.), https://doi.org/10.3390/min13010062.*

Amethyst, the national stone of Korea. B. Koo, *Wooshin Gem Lab Magazine*, **10**, 2023, 12–17, https://tinyurl.com/mv5cjpdb.*

Atomic and microstructural origin of banded colours in purple-blue variety of agate from Yozgat Province, Turkey. R. Lorenzi, A. Zullino, V. Gagliardi, L. Prosperi, A. Paleari and I. Adamo, *Physics and Chemistry of Minerals*, **49**(8), 2022, article 33 (8 pp.), https://doi.org/10.1007/s00269-022-01208-3.*

Characteristics of channel-water in blue-green beryl and its influence on colour. H. Wang, T. Shu, J. Chen and Y. Guo, *Crystals*, **12**(3), 2022, article 435 (13 pp.), https://doi.org/10.3390/cryst12030435.*

Chromatographic study of blue-violet tanzanite's color appearance. L. Qiu, Y. Guo, B. Yuan, Y.S. Su and Y.H. Qi, *Science of Advanced Materials*, **14**(6), 2022, 1032–1040, https://doi.org/10.1166/sam.2022.4288.

Cobalt spinel from Mahenge. *J.G.G.L. Gem Information*, **49**, 2023, 8–9 (in Japanese with English abstract).

Color coordination of emerald on CIE color space based on first-principles calculations. M. Novita, R.M.D. Ujianti, F. Nurdyansyah, S. Supriyadi, D. Marlina, R.A.S. Lestari, B. Walker, N.I. Binti Mohd Razip *et al.*, *Optical Materials: X*, **16**, 2022, article 100184 (9 pp.), https://doi.org/10.1016/j.omx.2022.100184.*

Color effects of Cu nanoparticles in Cu-bearing plagioclase feldspars. S. Jin, Z. Sun and A.C. Palke, *American Mineralogist*, **107**(12), 2022, 2188–2200, https://doi.org/10.2138/am-2022-8325.

Colored Stones Unearthed: Gems formed in metamorphic rocks. A.C. Palke and J.E. Shigley, *Gems & Gemology*, **59**(2), 2023, 232–241, https://tinyurl.com/yxtb3u65.*

Combining rare earth element analysis and chemometric method to determine the geographical origin of nephrite. Y. Su and M. Yang, *Minerals*, **12**(11), 2022, article 1399 (14 pp.), https://doi.org/10.3390/min12111399.*

The covariation of color and orange fluorescence instabilities in yellow sapphires. Y. Yang, C. Wang, C. Wang, X. Shen, K. Yin, T. Chen, A.H. Shen, T.J. Algeo *et al.*, *Minerals*, **13**(5), 2023, article 663 (14 pp.), https://doi.org/10.3390/min13050663.*

Fascinating structures within slices from dark tourmaline crystals. P. Rustemeyer, *Rocks & Minerals*, **98**(5), 2023, 418–437, https://doi.org/10.1080/00357529.2023.2213151.

Fire obsidian's beguiling spectrum. R. Weldon and N. Renfro, *Gems & Gemology*, **59**(2), 2023, 260–266, https://www.gia.edu/gems-gemology/summer-2023-in-the-spotlight.*

Gemmological and mineralogical characteristics of light blue-green phosphophyllite from Bolivia. X. Chen, J. Wang, Y. Chen and S. Gao, *Journal of Gems & Gemmology*, **24**(4), 2022, 18–25, https://tinyurl.com/yc5p5z78 (in Chinese with English abstract).*

Gemological characteristics of Lvwen stone and its color genesis. Z. Liu, W. Wang, K. Yin, H. Hong, T.J. Algeo, Z. Yin, Y. Pan, Z. Lu *et al.*, *Minerals*, **12**(12), 2022, article 1584 (14 pp.), https://doi.org/10.3390/min12121584.*

Gemological and mineralogical studies of greenish blue apatite in Madagascar. Z.Y. Zhang, B. Xu, P.Y. Yuan and Z.X. Wang, *Crystals*, **12**(8), 2022, article 1067 (19 pp.), https://doi.org/10.3390/cryst12081067.*

Gemological and spectral characteristics of emeralds from Swat Valley, Pakistan. S. Cao, H. Dai, C. Wang, L. Yu, R. Zuo, F. Wang and L. Guo, *Spectroscopy and Spectral Analysis*, **42**(11), 2022, 3533–3540, http://www.gpxygpfx.com/EN/Y2022/V42/I11/3533 (in Chinese with English abstract).*

Gemological and spectroscopic characteristics of "Jedi" spinel from Man Sin, Myanmar. L. Zhao, G. Li and L. Weng, *Minerals*, **12**(11), 2022, article 1359 (13 pp.), https://doi.org/10.3390/min12111359.*

Gemstone inclusion study by 3D Raman-mapping and high-resolution X-ray computed tomography: The case of trapiche emerald from Swat, Pakistan. Y. Gao, M. He, X. Li, M. Lin, X. Sun and Y. Zhang, *Crystals*, **12**(12), 2022, article 1829 (18 pp.), https://doi.org/10.3390/cryst12121829.*

Gemstone occurrences and ancient circular impact-scars: The gemmology tail wags the geology dog. J.M. Saul, *Australian Gemmologist*, **28**(3), 2023, 130–135.

***Gota de aceite*: Emerald's secret attraction.** R. Ringsrud, *Rivista Italiana de Gemmologia/Italian Gemological Review*, No. 16, 2023, 58–63.

Identification of the origin of bluish white nephrite based on laser-induced breakdown spectroscopy and artificial neural network model. P. Bao, Q. Chen, A. Zhao and Y. Ren, *Spectroscopy and Spectral Analysis*, **43**(1), 2023, 25–30, http://www.gpxygpfx.com/EN/Y2023/V43/I01/25 (in Chinese with English abstract).*

The impact of Munsell neutral grey backgrounds on tsavorite's color and study on the evaluation method of color gem cutting. Y. Ma and Y. Guo, *Applied Sciences*, **13**(3), 2023, article 1673 (14 pp.), https://doi.org/10.3390/app13031673.*

Le métamorphisme hydrothermal : la genèse des émeraudes [Hydrothermal metamorphism: The genesis of emeralds]. M. Mahfoufi, *Revue de Gemmologie A.F.G.*, No. 220, 2023, 10–13 (in French).

Mineral component and genesis of high-grade green jadeite jade from Guatemala. L. Wang, H. Zhang, J. Liu, L. Wang, Q. Ouyang, D. Liu and W. Liu, *Journal of Gems & Gemmology*, **24**(5), 2022, 11–30, https://tinyurl.com/5n7cxkab (in Chinese with English abstract).*

Minor elements and color causing role in spinel: Multi-analytical approaches. T. Pluthametwisute, B. Wanthanachaisaeng, C. Saiyasombat and C. Sutthirat, *Minerals*, **12**(8), 2022, article 928 (19 pp.), https://doi.org/10.3390/min12080928.*

New finds of cobalt-bearing spinel near Mahenge, Tanzania. T. Stephan, U. Henn and S. Muller, *Australian Gemmologist*, **28**(3), 2023, 136–142.

Non-destructive study of Egyptian emeralds preserved in the collection of the museum of the Ecole des Mines. M. Nikopoulou, S. Karampelas, E. Gaillou, U. Hennebois, F. Maouche, A. Herreweghe, L. Papadopoulou, V. Melfos *et al.*, *Minerals*, **13**(2), 2023, article 158 (15 pp.), https://doi.org/10.3390/min13020158.*

Opal pineapples from White Cliffs, New South Wales, Australia. P. Carr, M. Southwood, B. Jones and G. Dowton, *Rocks & Minerals*, **98**(5), 2023, 404–417, https://doi.org/10.1080/00357529.2023.2213150.

Optical properties of sulfur bearing sodalite. S.K. Lee, *Wooshin Gem Lab Magazine*, **9**, 2022, 2–5, https://tinyurl.com/4nuyb7jh.*

Origin of blue-water jadeite jades from Myanmar and Guatemala: Differentiation by non-destructive spectroscopic techniques. Y. Zhang and G. Shi, *Crystals*, **12**(10), 2022, article 1448 (16 pp.), https://doi.org/10.3390/cryst12101448.*

Our friends the inclusions. The detective at the party of inclusions. Fourteenth episode [corundum]. L. Costantini and C. Russo, *Rivista Italiana de Gemmologia/Italian Gemological Review*, No. 16, 2023, 7–13.

Photomicrographies d'une opale d'Éthiopie [Photomicrographs of an Ethiopian opal]. M. Bouvier, *Revue de Gemmologie A.F.G.*, No. 219, 2023, 33 (in French).

Pink to purple sapphires from Ilakaka, Madagascar: Insights to separate unheated from heated samples. S. Karampelas, U. Hennebois, J.-Y. Mevellec, V. Pardieu, A. Delaunay and E. Fritsch, *Minerals*, **13**(5),

2023, article 704 (14 pp.), https://doi.org/10.3390/min13050704.*

Purple chalcedony from Ethiopia. *J.G.G.L. Gem Information*, **49**, 2023, 1–2 (in Japanese with English abstract).

Quantitative study on colour and spectral characteristics of Beihong agate. Y. Zhou, Z. Liu, Z. Zhao and Y. Guo, *Minerals*, **12**(6), 2022, article 1448 (16 pp.), https://doi.org/10.3390/min12060677.*

Quelques éclaircissements sur la labradorescence. Partie 2 : Exemple des labradorites de Madagascar [Some clarifications on labradorescence. Part 2: Example of labradorites from Madagascar]. M. Cagnon-Trouche, J.-C. Boulliard, I. Estève and P. Giura, *Revue de Gemmologie A.F.G.*, No. 219, 2023, 5–14 (in French with English abstract).

Raman analysis of the characteristics of chrysoberyl containing an excessive amount of iron. S. Noh, *Wooshin Gem Lab Magazine*, **9**, 2022, 12–15, https://tinyurl.com/4nuyb7jh.*

Raman spectroscopic study on inclusion in sapphire from Azad-Kashmir. T. Huang, Y. Gao, X. Sun and Q. Han, *Journal of Gems & Gemmology*, **24**(5), 2022, 101–108, https://tinyurl.com/3mvfb7xh (in Chinese with English abstract).*

Rapid screening of a photochromic padparadscha-like sapphire using absorption spectroscopy. Z. Wang, T.H. Tsai and H. Takahashi, *Applied Optics*, **61**(27), 2022, article 8108 (7 pp.), https://doi.org/10.1364/ao.460718.*

A research of emeralds from Panjshir Valley, Afghanistan. Q. Chen, P. Bao, Y. Li, A.H. Shen, R. Gao, Y. Bai, X. Gong and X. Liu, *Minerals*, **13**(1), 2022, article 63 (22 pp.), https://doi.org/10.3390/min13010063.*

Reversible photochromic effect in natural gemstone sapphires. T.H. Tsai, Z. Wang and H. Takahashi, *Optics Letters*, **47**(22), 2022, article 5805 (4 pp.), https://doi.org/10.1364/ol.474838.*

Silicate gems. M. Mauthner, *Rocks & Minerals*, **98**(1), 2023, 28–43, https://doi.org/10.1080/00357529.2023.2126698.

Spectroscopic study on the species and color differences of gem-quality red garnets from Malawi. M. Li and K.S.V. Krishna Rao, *Journal of Spectroscopy*, **2022**, 2022, article 1638042 (9 pp.), https://doi.org/10.1155/2022/1638042.*

Spectroscopy characteristics of emerald from Swat Valley, Pakistan. P. Bao, Q. Chen, Y. Wu, X. Li and A. Zhao, *Spectroscopy and Spectral Analysis*, **43**(1), 2023, 213–219, http://www.gpxygpfx.com/EN/abstract/abstract13115.shtml (in Chinese with English abstract).*

The story behind the Smithsonian's newest gem: The exquisite Lion of Merelani. J. Tamisiea, *Smithsonian Magazine*, 20 April 2023, https://tinyurl.com/yaffkz6h.*

The structural origin of the efficient photochromism in natural minerals. P. Colinet, H. Byron, S. Vuori, J.P. Lehtiö, P. Laukkanen, L. Van Goethem, M. Lastusaari and T. Le Bahers, *Proceedings of the National Academy of Sciences*, **119**(23), 2022, article e2202487119 (7 pp.), https://doi.org/10.1073/pnas.2202487119.

Study on the chemical composition and spectroscopy characteristics of emeralds from Bahia mining area, Brazil. J. Hua and J. Di, *Journal of Gems & Gemmology*, **24**(5), 2022, 109–117, https://tinyurl.com/3hz4e9w8 (in Chinese with English abstract).*

Study on the color-influencing factors of blue iolite. X. Liu and Y. Guo, *Minerals*, **12**(11), 2022, article 1356 (10 pp.), https://doi.org/10.3390/min12111356.*

Study on fluorescence properties of green-blue apatite. Q. Yan, Z. Liu and Y. Guo, *Crystals*, **12**(6), 2022, article 866 (15 pp.), https://doi.org/10.3390/cryst12060866.*

Study on the spectral characteristics and the color-change effect of spinel. Z. Wang, X. Mao, Z. Yin, C. Chen and T. Cheng, *Spectroscopy and Spectral Analysis*, **42**(11), 2022, 3541–3545, http://www.gpxygpfx.com/EN/Y2022/V42/I11/3541 (in Chinese with English abstract).*

Study on spectral characteristics of gem grade cassiterite in Yunnan. R. Zhang, G. Yang and Y. Bai, *Superhard Material Engineering*, **34**(2), 2022, 58–62, https://tinyurl.com/2p86p8uk (in Chinese with English abstract).

Tenebrescent zircon. *J.G.G.L. Gem Information*, **49**, 2023, 5–6 (in Japanese with English abstract).

True jades, false friends. G.L. Barnes, *Tectonic Archaeology*. Archaeopress Publishing Ltd, Oxford, 2022, 338–372, https://doi.org/10.2307/j.ctv35n89zf.20.

Variation in gemological characteristics in tsavorites with different tones from East Africa. Y. Ma and Y. Guo, *Crystals*, **12**(11), 2022, article 1677 (14 pp.), https://doi.org/10.3390/cryst12111677.*

Water characterization and structural attribution of different colored opals. N. Li, Q. Guo, Q. Wang and L. Liao, *RSC Advances*, **12**(47), 2022, 30416–30425, https://doi.org/10.1039/d2ra04197a.*

Zultanite: Trick or treat? N. Zolotukhina, *Gemmology Today*, June 2023, 69–73, https://tinyurl.com/8fnw3ktt.*

CULTURAL HERITAGE

The Amsterdam diamond 'marketplace' and the Jewish experience. K. Hofmeester, *Jewish Culture and History*, **24**(1), 2023, 50–75, https://doi.org/10.1080/1462169x.2022.2156189.

Escarboucles & dragons, lexicologie des gemmes rouges [Carbuncles & dragons, lexicology of red gems]. N. Zylberman, *Revue de Gemmologie A.F.G.*, No. 219, 2023, 27–32 (in French with English abstract).

Les grenats dits « de Perpignan » [The so-called 'Perpignan' garnets]. M. Errera, I. Fordebras, A. La Viose and A.-M. Moigne, *Revue de Gemmologie A.F.G.*, No. 219, 2023, 15–26 (in French with English abstract).

A luxe for the ears. Roman earrings in Augusta Emerita (Mérida) and the province of Lusitania. N.B. Martín, in L.P. Pujol & J.P. González, Eds., *De Luxuria Propagata Romana Aetate – Roman Luxury in Its Many Forms*. Archaeopress Publishing Ltd, Oxford, 2023, 109–136, https://doi.org/10.2307/jj.1357306.12.

Un « miroir » préhispanique en obsidienne de l'expédition géodésique sur l'équateur (1735–1743) découvert dans les collections de minéralogie du Muséum national d'Histoire naturelle [A pre-Hispanic obsidian 'mirror' from the geodesic expedition to the equator (1735–1743) discovered in the mineralogy collections of the National Museum of Natural History]. F. Gendron, *Revue de Gemmologie A.F.G.*, No. 220, 2023, 14–17 (in French with English abstract).

Pearls, beryls, and priestesses in the Latin West: Pearls and gems as symbols of female power and devotion, as well as impiety and irreverence. A.S. Morales, in L.P. Pujol & J.P. González, Eds., *De Luxuria Propagata Romana Aetate – Roman Luxury in Its Many Forms*. Archaeopress Publishing Ltd, Oxford, 2023, 137–166, https://doi.org/10.2307/jj.1357306.13.

Raman spectroscopic characteristic of red coral artifact and its communication between China and the West before the 19th century. T. Lin, Y. Yuan, Y. Xu and Q. Liu, *Journal of Gems & Gemmology*, **24**(6), 2022, 141–151, https://tinyurl.com/msc52v97 (in Chinese with English abstract).*

DIAMONDS

Botswana, le nouveau géant du diamant [Botswana, the new diamond giant]. É. Gonthier and M. Valentin, *Revue de Gemmologie A.F.G.*, No. 220, 2023, 18–21 (in French with English abstract).

Crystallogenetic causes of the unique shape of the Matryoshka diamond: The effect of capturing a diamond inclusion of twin diamond crystals. A.D. Pavlushin and D.V. Konogorova, *Geochemistry International*, **61**(3), 2023, 252–264, https://doi.org/10.1134/s0016702923030102.

Electron probe microanalysis and microscopy of polishing-exposed solid-phase mineral inclusions in Fuxian kimberlite diamonds. D. Zhao, *Minerals*, **12**(7), 2022, article 844 (36 pp.), https://doi.org/10.3390/min12070844.*

From the lithosphere to the lower mantle: An aqueous-rich metal-bearing growth environment to form type IIb blue diamonds. L. Daver, H. Bureau, É. Boulard, É. Gaillou, P. Cartigny, D.L. Pinti, O. Belhadj, N. Guignot *et al.*, *Chemical Geology*, **613**, 2022, article 121163 (18 pp.), https://doi.org/10.1016/j.chemgeo.2022.121163.

Gemmological and spectroscopic characteristic of a natural type IIa colorless diamond with strong phosphorescence. S. Xu, Y. Xie and B. Wang, *Superhard Material Engineering*, **34**(5), 2022, 54–58, https://tinyurl.com/4cx2rvvb (in Chinese with English abstract).

Growth story of one diamond: A window to the lithospheric mantle. V. Afanasiev, S. Ugapeva, Y. Babich, V. Sonin, A. Logvinova, A. Yelisseyev, S. Goryainov, A. Agashev *et al.*, *Minerals*, **12**(8), 2022, article 1048 (18 pp.), https://doi.org/10.3390/min12081048.*

Low-temperature annealing and kinetics of radiation stains in natural diamond. S. Eaton-Magaña, C.M. Breeding and R. Bassoo, *Diamond and Related Materials*, **132**, 2023, article 109649 (13 pp.), https://doi.org/10.1016/j.diamond.2022.109649.

Morphological features and spectral comparisons of diamonds from three kimberlite belts in Mengyin, China. C.-F. Zhang, F. Liu, Q. Lv, Y. Wang and J.-S. Yang, *Minerals*, **12**(10), 2022, article 1185 (15 pp.), https://doi.org/10.3390/min12101185.*

Morphological and surface microtopographic features of HPHT-grown diamond crystals with contact twinning. K. Sun, T. Lu, M. He, Z. Song, J. Zhang and J. Ke, *Crystals*, **12**(9), 2022, article 1264 (15 pp.), https://doi.org/10.3390/cryst12091264.*

Optimal direction and propagation of mid-IR light inside rough and polished diamonds for highly-sensitive transmission measurements of nitrogen content. R.A. Khmelnitsky, O.E. Kovalchuk, Y.S. Gulina, A.A. Nastulyavichus, G.Y. Kriulina, N.Y. Boldyrev, S.I. Kudryashov, A.O. Levchenko *et al.*, *Diamond and Related Materials*, **128**, 2022, article 109278 (9 pp.), https://doi.org/10.1016/j.diamond.2022.109278.

Orientational dependences of diamonds grown in the NiMnCo–silicate–H_2O–C system under HPHT conditions and implications to natural diamonds. Z. Lu, Z. Wang, S. Wang, H. Zhao, Z. Cai, Y. Wang, H. Ma, L. Chen *et al.*, *ACS Earth and Space Chemistry*, **6**(4), 2022, 987–998, https://doi.org/10.1021/acsearthspacechem.1c00381.

Raman spectroscopy study on the surface of high temperature and high pressure diamond crystal in geology, rock and minerals. L. Shi, H. Chi, W. Wang and Y. Yu, *Highlights in Science, Engineering and Technology*, **17**, 2022, 142–147, https://doi.org/10.54097/hset.v17i.2562.*

A review on cut proportion of diamond learned from the experiences at a diamond cutting factory. H. Yano, *Journal of The Gemmological Society of Japan*, **36**(1–4), 2022, 10–18, https://doi.org/10.14915/gsjapan.36.1-4_10 (in Japanese with English abstract).

FAIR TRADE

Averting your gaze with sustainable, green marketing claims: A critique of luxury commodity production sustainability claims, with evidence from the diamond industry. M.J. Lynch, M.A. Long and P.B. Stretesky, *Sociological Spectrum*, **42**(4–6), 2022, 278–293, https://doi.org/10.1080/02732173.2022.2148797.

Critical "loupe" holes: Conflict diamonds and security threats arising from weaknesses in the Kimberley Process. M.E. Crouse, *National Security Law Journal*, **10**(1), 2023, 76–119, https://tinyurl.com/etjr4krs.*

The dynamics of the illegal ivory trade and the need for stronger global governance. Z. Miao, Q. Wang, X. Cui, K. Conrad, W. Ji, W. Zhang, X. Zhou and D.C. MacMillan, *Journal of International Wildlife Law & Policy*, **25**(1), 2022, 84–96, https://doi.org/10.1080/13880292.2022.2077393.

Fighting silicosis in Bahia, Brazil. B. Cook and J.-L. Archuleta, *Gems&Jewellery*, **32**(2), 2023, 24–27.

Five decades of wildlife protection: An introduction to CITES. J. Barzdo, *Gems&Jewellery*, **32**(1), 2023, 22–25.

Peace, hope and prosperity through diamond cutting in Sierra Leone. M. de Witte and F. Lebbie, *Gems&Jewellery*, **32**(2), 2023, 36–39.

Sustainable coastal business strategies for cultured pearl sectors: Agenda development for coast-area actors' collaboration. H. Oe and Y. Yamaoka, *Coasts*, **2**(4), 2022, 341–354, https://doi.org/10.3390/coasts2040017.*

GEM LOCALITIES

Corundum genesis at the Blue Jay sapphire occurrence (British Columbia, Canada) as a record of metamorphism and partial melting in the Monashee complex. L. Abdale, P.M. Belley, L.A. Groat, J. Cempírek, R. Škoda and C. Wall, *Lithos*, **438–439**, 2023, article 106992 (23 pp.), https://doi.org/10.1016/j.lithos.2022.106992.

Formation of the nephrite deposit with five mineral assemblage zones in the central western Kunlun Mountains, China. X. Zhang, G. Shi, X. Zhang and K. Gao, *Journal of Petrology*, **63**(11), 2022, article egac117 (16 pp.), https://doi.org/10.1093/petrology/egac117.*

Gem-quality augite from Dong Nai, Vietnam. Le Ngoc Nang, Lam Vinh Phat, Pham Minh Tien, Pham Trung Hieu, K. Kawaguchi and Pham Minh, *Gems & Gemology*, **59**(2), 2023, 182–194, https://doi.org/10.5741/gems.59.2.182.*

In search of *sakura ishi*: Cherry blossom stones [cerasite] from Kameoka, Japan. A. Mathys, *Gems&Jewellery*, **32**(1), 2023, 50–51.

In situ U–Th–Pb dating of parisite: Implication for the age of mineralization of Colombian emeralds. U. Altenberger, Y. Rojas-Agramonte, Y. Yang, J. Fernández-Lamus, T. Häger, C. Guenter, A. Gonzalez-Pinzón, F. Charris-Leal *et al.*, *Minerals*, **12**(10), 2022, article 1232 (14 pp.), https://doi.org/10.3390/min12101232.*

Mining Blue John in 2023. E. Turner and J.-L. Archuleta, *Gems&Jewellery*, **32**(2), 2023, 32–34.

Nurturing resilience: Overcoming challenges in the sapphire fields of Australia. D.J. Baral, *Gems&Jewellery*, **32**(2), 2023, 20–23.

Occurrences and genesis of emerald and other beryls mineralization in Egypt: A review. F.M. Khaleal, G.M. Saleh, E.S.R. Lasheen and D.R. Lentz, *Physics and Chemistry of the Earth, Parts A/B/C*, **128**, 2022, article 103266 (14 pp.), https://doi.org/10.1016/j.pce.2022.103266.

Petrology, geothermobarometry and geochemistry of granulite facies wall rocks and hosting gneiss of gemstone deposits from the Mogok area (Myanmar). M.M. Phyo, L. Franz, R.L. Romer, C. de Capitani, W.A. Balmer and M.S. Krzemnicki, *Journal of Asian Earth Sciences: X*, **9**, 2023, article 100132 (16 pp.), https://doi.org/10.1016/j.jaesx.2022.100132.*

The restart of demantoid from Madagascar and its twinning fire. *J.G.G.L. Gem Information*, **49**, 2023, 15–17 (in Japanese with English abstract).

INSTRUMENTATION AND TECHNOLOGY

Basics of LA-ICP-MS analysis. K. Emori, *Journal of The Gemmological Society of Japan*, **36**(1–4), 2022, 19–29, https://doi.org/10.14915/gsjapan.36.1-4_19 (in Japanese with English abstract).

Development of mid-infrared absorption spectroscopy for gemstone analysis. Z. Wang and H. Takahashi, *Minerals*, **13**(5), 2023, article 625 (9 pp.), https://doi.org/10.3390/min13050625.

Development of UV-Vis-NIR-MIR absorption spectroscopy for gemstone analysis. Z. Wang and H. Takahashi, *Novel Optical Systems, Methods, and Applications XXV*, **12216**, 3 October 2022, paper 122160R (7 pp. + poster), https://doi.org/10.1117/12.2624632.

Discussion on detection method of jewelry and jade by EDXRF. Y. Cheng, H. Zhu, C. Fan, X. Ma, S. Chen, Y. Huang, J. Gao and W. Wang, *Superhard Material Engineering*, **34**(4), 2022, 59–66, https://tinyurl.com/yzmebevd (in Chinese with English abstract).

Imaging-assisted Raman and photoluminescence spectroscopy for diamond jewelry identification and evaluation. T.-H. Tsai, *Applied Optics*, **62**(10), 2023, article 2587 (8 pp.), https://doi.org/10.1364/ao.484366.*

LED for gemstone and jewelry. *J.G.G.L. Gem Information*, **49**, 2023, 18–21 (in Japanese with English abstract).

A polynomial interactive reconstruction method based on spectral morphological features for the classification of gem minerals using portable LIBS.

J. Yan, Q. Li, F. Qin, L. Xiao and X. Li, *Journal of Analytical Atomic Spectrometry*, **37**(9), 2022, 1862–1868, https://doi.org/10.1039/d2ja00010e.

Study of 405 nm laser-induced time-resolved photoluminescence spectroscopy on spinel and alexandrite. W. Xu, T.-H. Tsai and A. Palke, *Minerals*, **13**(3), 2023, article 419 (15 pp.), https://doi.org/10.3390/min13030419.*

MISCELLANEOUS

The colourful success of the Gemfields' auction system. R.G. Sikri, *Gems&Jewellery*, **32**(1), 2023, 56–59.

Describing color: A fool's guide. R.W. Hughes, *GemGuide*, **42**(3), 2023, 4–10.

Diamond investments – Is the market free from multiple price bubbles? M. Potrykus, *International Review of Financial Analysis*, **83**, 2022, article 102329 (9 pp.), https://doi.org/10.1016/j.irfa.2022.102329.*

Empire builders: The art of branding. G. Dominy, L. Lauren, H. McCracken, P. Ati and K. Jones, *Gemmology Today*, June 2023, 6–13, https://tinyurl.com/bdn598nc.*

An interesting pair of earrings. L. Rennie, F. Payette and M. Blackwell, *Australian Gemmologist*, **28**(3), 2023, 152–153.

The new minerals exhibition at the Australian Museum. R. Pogson, *Australian Gemmologist*, **28**(3), 2023, 146–149.

The regalia of the coronation. C. Blatherwick, *Gems&Jewellery*, **32**(1), 2023, 38–41.

The Turquoise Museum in Albuquerque, New Mexico: A rich repository of all things turquoise! J. Lowry, *Rocks & Minerals*, **98**(5), 2023, 449–454, https://doi.org/10.1080/00357529.2023.2213154.

NEWS PRESS

The 10 most iconic jewels through history. D. Woodward, BBC News, 24 February 2023, https://tinyurl.com/vf8cyhsz.*

Chelmsford: Roman Apollo ring with links to Snettisham Hoard found. BBC News, 8 April 2023, https://www.bbc.com/news/uk-england-essex-65202077.*

How more sanctions on Russian diamonds could affect the global market. E. Paton, *New York Times*, 28 August 2023, https://tinyurl.com/26xyz8c5.

Inside the emerald mines that make Colombia a global giant of the green gem. J. Otis, NPR, 11 March 2023, https://tinyurl.com/yvdc3vdd.*

Mourning jewelry leaves the Victorian era behind: Lab-grown diamonds made with cremation ashes are just one way people are honoring their loved ones. A.R. Esman, *New York Times*, 26 May 2023, https://tinyurl.com/2p84mphc.

Precious metals, gems, ivory found in artifact-laden tombs unearthed in Cyprus. S. Shafiq, *USA Today*, 7 July 2023, https://tinyurl.com/47kk2fxd.*

The revolution underway in India's diamond industry. P. Gupta and B. Morris, BBC News, 17 March 2023, https://www.bbc.com/news/business-64783843.*

ORGANIC/BIOGENIC GEMS

The fossil resins of Europe. M. Kazubski, *Bursztynisko (The Amber Magazine)*, No. 47, 2023, 86–87, https://www.calameo.com/read/007323557a467cf9a10df (in English and Polish).*

Origin of fossil resins. A. Matuszewska, *Bursztynisko (The Amber Magazine)*, No. 47, 2023, 80–84, https://www.calameo.com/read/007323557a467cf9a10df (in English and Polish).*

Origins of color in brown mammoth ivory. Z. Huang, T. Chen, J. Zheng, D. Wang and X. Xu, *Gems & Gemology*, **59**(2), 2023, 196–209, https://doi.org/10.5741/gems.59.2.196.*

Preliminary study on infrared holographic imaging of amber from the Baltic Sea. Y. Yao, H. Huang, X. Chen, Y. Gui, B. Yang and Z. Zheng, *Journal of Gems & Gemmology*, **25**(1), 2023, 36–44, https://tinyurl.com/3dj37w54 (in Chinese with English abstract).*

A review for the gemmological research on amber. Y. Wang, Y. Li, Z. Shi, F. Liu, F. Liu and Z. Zhang, *Journal of Gems & Gemmology*, **24**(5), 2022, 55–68, https://tinyurl.com/4y9punee (in Chinese with English abstract).*

Spectral and colour characteristics of red series amber from Myanmar. L. Dong, *Journal of Gems & Gemmology*, **24**(5), 2022, 87–93, https://tinyurl.com/4pe8bbrj (in Chinese with English abstract).*

PEARLS

Change of optical properties of akoya pearls with treatment. S. Tazawa, *Journal of The Gemmological Society of Japan*, **36**(1–4), 2022, 30–31, https://doi.org/10.14915/gsjapan.36.1-4_30 (in Japanese with English abstract).

Cultured pearls soar: High prices and higher demand. B. Branstrator, *GemGuide*, **42**(4), 2023, 4–7.

Deciphering the color origin of pink conch pearl using nondestructive spectroscopies and DFT calculations. C. Chen, J. Yu, X. Ye and A.H. Shen, *Minerals*, **13**(6), 2023, article 811 (14 pp.), https://doi.org/10.3390/min13060811.*

Dynamic microstructural characteristics of Edison pearls cultured in *Hyriopsis cumingii*. X. Yan, J. Zhang, J. Sheng, Q. Sun, T. Chen, Y. Zhou, J. Wang, C. Jia *et al.*, *Journal of Materials Science*, **57**(43), 2022, 20138–20155, https://doi.org/10.1007/s10853-022-07905-2.

An idea of evaluation of nacre thickness of nucleated cultured pearls. E. Ito, *Journal of The Gemmological Society of Japan*, **36**(1–4), 2022, 37–41, https://doi.org/10.14915/gsjapan.36.1-4_37 (in Japanese with English abstract).

Nature of pigments in orange and purple coloured Chinese freshwater cultured pearls: Insights from experimental Raman spectroscopy and DFT calculations. C. Chen, J. Yu, C. Zhang, X. Ye and A.H. Shen, *Minerals*, **13**(7), 2023, article 959 (14 pp.), https://doi.org/10.3390/min13070959.*

Synchrotron radiation μ-XRF imaging reveals Mn zoning in freshwater pearls. J. Gao, J. Zhang, W. Wu, C.K. Yen and W. Su, *Journal of Physical Chemistry C*, **126**(50), 2022, 21381–21389, https://doi.org/10.1021/acs.jpcc.2c05988.

Synchrotron radiation μ-XRF imaging reveals oscillatory zoning of freshwater pearls. J. Gao, J. Zhang and C. Yen, *Journal of Gems & Gemmology*, **25**(1), 2023, 28–35, https://tinyurl.com/5xrh9x8e (in Chinese with English abstract).*

Synchrotron-based HR-fluorescence and mineralogical mapping of the initial growth stages of Polynesian cultivated pearls disprove the 'reversed shell' concept. J.-P. Cuif, Y. Dauphin, C. Lo, K. Medjoubi, D. Saulnier and A. Somogyi, *Minerals*, **12**(2), 2022, article 172 (15 pp.), https://doi.org/10.3390/min12020172.*

The types of UV-Vis diffuse reflectance spectra of common gray pearls and their coloring mechanism. S. Fang, Y. Jiang, J. Yan, X. Yan, Y. Zhou and J. Zhang, *Spectroscopy and Spectral Analysis*, **42**(12), 2022, 3703–3708, http://www.gpxygpfx.com/EN/Y2022/V42/I12/3703 (in Chinese with English abstract).*

UV light resistance test of pearls. R. Wakatsuki, *Journal of The Gemmological Society of Japan*, **36**(1–4), 2022, 32–36, https://doi.org/10.14915/gsjapan.36.1-4_32 (in Japanese with English abstract).

Visiting the home of Japan's cultured pearl farms. A. Naito, *Gems&Jewellery*, **32**(2), 2023, 28–31.

SIMULANTS

A comparison of the optical and chemical characteristics of lapis lazuli with attractive color and its imitation stones. B. Koo, *Wooshin Gem Lab Magazine*, **9**, 2022, 6–11, https://tinyurl.com/4nuyb7jh.*

Development of glass-ceramics from soda lime silica glass waste with addition of kaolin and coloring oxide for turquoise's imitation. D. Bootkul and S. Intarasiri, *Vibrational Spectroscopy*, **123**, 2022, article 103467 (9 pp.), https://doi.org/10.1016/j.vibspec.2022.103467.

Preparation and basic properties of praseodymium-neodymium-chromium containing imitation gemstone glass. S. Zhang, K. Li, J. Pu and W. Ni, *Materials*, **15**(20), 2022, article 7341 (11 pp.), https://doi.org/10.3390/ma15207341.*

Synthetic resins in mining simulate amber. A. Krumbiegel, M. Kazubski, E. Wagner-Wysiecka and R. Wimmer, *Bursztynisko (The Amber Magazine)*, No. 47, 2023, 88–91, https://www.calameo.com/read/007323557a467cf9a10df (in English and Polish).*

SYNTHETICS

Chemical composition and spectra characteristics of hydrothermal synthetic sapphire. Y. Lü, J. Pei and Y. Zhang, *Spectroscopy and Spectral Analysis*, **42**(11), 2022, 3546–3551, http://www.gpxygpfx.com/EN/Y2022/V42/I11/3546 (in Chinese with English abstract).*

Chinese colorless HPHT synthetic diamond inclusion features and identification. Y. Ma, Z. Qiu, X. Deng, T. Ding, H. Li, T. Lu, Z. Song, W. Zhu *et al.*, *Crystals*, **12**(9), 2022, article 1266 (12 pp.), https://doi.org/10.3390/cryst12091266.*

Comparative study of mineralogical characteristics of natural and synthetic amethyst and smoky quartz. K. Liu and Y. Guo, *Crystals*, **12**(12), 2022, article 1735 (8 pp.), https://doi.org/10.3390/cryst12121735.*

Comparative study on the quality of HTHP and CVD single crystal diamond substrates. Y. Yang, X. Han, X. Hu, B. Li, Y. Peng, X. Wang, X. Hu, X. Xu *et al.*, *Journal of Synthetic Crystals*, **51**(9–10), 2022, 1777–1784, http://rgjtxb.jtxb.cn/EN/Y2022/V51/I9-10/1777 (in Chinese with English abstract).*

Evaluating the defects in CVD diamonds: A statistical approach to spectroscopy. M.F. Hardman, S.C. Eaton-Magaña, C.M. Breeding, T. Ardon and U.F.S. D'Haenens-Johansson, *Diamond and Related Materials*, **130**, 2022, article 109508 (22 pp.), https://doi.org/10.1016/j.diamond.2022.109508.

Giorgia Spezia and the hydrothermal quartz. E. Costa and R. Navone, *Rivista Italiana de Gemmologia/Italian Gemological Review,* No. 16, 2023, 51–55.

Not just a pretty face: The history of HPHT synthetic diamonds. B. West, *Gems&Jewellery*, **32**(1), 2023, 42–45.

Spectroscopic properties of CVD lab-grown diamond and a typical example: Lightbox. S. Noh, *Wooshin Gem Lab Magazine*, **10**, 2023, 2–8, https://tinyurl.com/mv5cjpdb.*

Synthetic diamond identification under X-ray excitation. L. Cheng, Y. Zhu, R. Lin, Y. Ding, X. Ouyang and W. Zheng, *Cell Reports Physical Science*, **4**(1), 2023, article 101208 (15 pp.), https://doi.org/10.1016/j.xcrp.2022.101208.*

Synthetic morganite: The long journey of hydrothermal pink beryl. A. Malossi, *Rivista Italiana de Gemmologia/Italian Gemological Review*, No. 16, 2023, 33–44.

TREATMENTS

Application of high-temperature copper diffusion in surface recoloring of faceted labradorites. Q. Zhou, C. Wang and A.H. Shen, *Minerals*, **12**(8), 2022, article 920 (13 pp.), https://doi.org/10.3390/min12080920.*

Chemical composition and spectroscopic characteristics of heat-treated rubies from Madagascar, Mozambique and Tanzania. L. Yang, Q. Lu, D. Ma, H. Zheng, R. Hu, Z. Shi and B. Qin, *Crystals*, **13**(7), 2023, article 1051 (16 pp.), https://doi.org/10.3390/cryst13071051.*

Color modification of spinel by nickel diffusion: A new treatment. M. Jollands, A. Ludlam, A.C. Palke, W. Vertriest, S. Jin, P. Cevallos, S. Arden, E. Myagkaya *et al.*, *Gems & Gemology*, **59**(2), 2023, 164–181, https://doi.org/10.5741/gems.59.2.164.*

Detecting corundum fillers with the long-wave UV torch. E.B. Hughes, *Australian Gemmologist*, **28**(3), 2023, 150–151.

Difference of lattice radiation damage and spectroscopic characterization in natural and artificial radiation green diamonds. L. Qi, Z. Zhou, B. Zhao, C. Zeng and C. Xiang, *Journal of Gems & Gemmology*, **24**(5), 2022, 1–10, https://tinyurl.com/4pn32epe (in Chinese with English abstract).*

Enhancement of Paraiba tourmaline. *J.G.G.L. Gem Information*, **49**, 2023, 11–14 (in Japanese with English abstract).

Gemstone testing during the jewelry manufacturing process. Lead-glass filled ruby. D. Romanelli and S. Coppola, *Rivista Italiana de Gemmologia/Italian Gemological Review*, No. 16, 2023, 25–31.

Identification method of glue-filled aquamarine. N. Cao, T. Chen, J. Zheng, X. Chen, Y. Zhuang and Z. Wang, *Journal of Gems & Gemmology*, **25**(1), 2023, 45–51, https://tinyurl.com/bdepj8y5 (in Chinese with English abstract).*

Mechanism of Be-thermodiffusion in rutile inclusions of fancy sapphires. M. Rossi, R. Biondi, R. Rizzi, N. Corriero, F. Sequino and A. Vergara, *Crystal Growth & Design*, **22**(11), 2022, 6493–6503, https://doi.org/10.1021/acs.cgd.2c00700.*

Optimized conditions for cobalt diffusion in Sri Lankan colorless topaz and coloration mechanism elucidation through spectro-chemical investigation. C.P. Udawatte, S. Abeyweera, L.R.K. Perera, S. Illangasinghe, C. Weerasooriya, C. Sutthirat, N. Jayasinghe, T. Dharmaratne *et al.*, *Journal of Metals, Materials and Minerals*, **33**(1), 2023, 73–81, https://doi.org/10.55713/jmmm.v33i1.1596.*

Les saphirs chauffés à haute temperature et leurs inclusions identifiables en gemmologie classique [Sapphires heated at high temperatures and their identifiable inclusions in classical gemology]. M. Bouvier, *Revue de Gemmologie A.F.G.*, No. 220, 2023, 22–23 (in French).

The spectroscopy study of different filling materials in tourmaline. J. Sui, *Superhard Material Engineering*, **34**(5), 2022, 59–65, https://tinyurl.com/ycmne9p4 (in Chinese with English abstract).

Study on the common effect of heat treatment, dyeing or irradiation treatment on UV-Vis diffuse reflectance spectra of pearls. J. Yan, S. Fang, X. Yan, J. Sheng, J. Xu, C. Xu and J. Zhang, *Spectroscopy and Spectral Analysis*, **42**(12), 2022, 3697–3702, http://www.gpxygpfx.com/EN/Y2022/V42/I12/3697 (in Chinese with English abstract).*

Update of andesine diffusion. *J.G.G.L. Gem Information*, **49**, 2023, 7 (in Japanese with English abstract).

COMPILATIONS

***G&G* Micro-World.** Aquamarine from Xinjiang, China • Clinochlore and muscovite in quartz from Colorado, USA • Iridescent 'insect wing' in diamond • Patchy yellow trigon on diamond • 'Rainbow mountain' in diamond • Musical note symbol in diamond • Snail-shaped pyrope-diopside inclusion in diamond • Metal sulfide(?) in garnet • Graphite in pink sapphire • Night sky scene in yellow sapphire • 'Eye' on a Tridacninae pearl • Thread-like inclusions of serpentine in brown peridot • Metallic platelets in Paraíba tourmaline • Triplite inclusions in Chinese quartz • Geocronite in fluorite. *Gems & Gemology*, **59**(2), 2023, 222–231, https://tinyurl.com/jv9rnphm.*

Gem News International. Suite of Colombian emerald-and-matrix cabochons • Calcite in a pearl from *Pinctada maculata* • Unusual metallic core in a natural *P. radiata* pearl • Saltwater clamshell beads in freshwater cultured pearls • Quartz with 'rabbit hair' inclusions • Heat-treated rubies from Greenland • Treatment for creating phantom structure in opal • Spring 2023 auction highlights • 2023 Sinkankas Symposium • Sustainability panels at JCK Las Vegas. *Gems & Gemology*, **59**(2), 2023, 242–258, https://tinyurl.com/yy2p3rh2.*

Lab Notes. Star aquamarine • Faceted brucite • Natural diamond with CVD-like fluorescence pattern • Yellow zoning in pink diamonds • Glass imitation of cat's-eye chrysoberyl • 34.59 ct CVD synthetic diamond • CVD synthetic diamonds with invisible markings • Two pearls of Indian cultural significance • 19+ mm South Sea bead-cultured pearl • Linear structures in non-bead cultured pearls • Plastic imitations of emerald • Pink zektzerite. *Gems & Gemology*, **59**(2), 2023, 210–222, https://tinyurl.com/mrxr4cd9.*

**Article freely available for download, as of press time*

Gem-A

THE GEMMOLOGICAL ASSOCIATION OF GREAT BRITAIN

Gem-A Conference 2023

BOOK NOW!

November 5

etc.venues County Hall, London

Bringing together the greatest minds in Gemmology

This year's Conference boasts an incredible line-up of six expert speakers and is a must-attend event for anyone interested in gemmology. The Conference will be held at etc.venues County Hall, which overlooks the River Thames and the Houses of Parliament.

REASONS TO ATTEND

- Amazing line-up of six experts in their respective fields.
- Enjoy a rare opportunity to network with fellow gemmologists and industry professionals in a relaxed environment.
- Enhance your knowledge and stay up-to-date with developments in our evolving sectors.
- Exclusive workshops and tours including private viewings.
- Add to the Conference experience by joining us for the Gem-A Conference dinner on the evening of November 5.

▶ To register and buy tickets visit: gem-a.com/event/conference-2023